UNIVERSITY OF SOUTHAMPTON

The epoch and environmental dependence of radio-loud active galaxy feedback

by

Judith Ineson

Thesis for the degree of Doctor of Philosophy

in the

FACULTY OF PHYSICAL SCIENCES AND ENGINEERING

Department of Physics and Astronomy

June 2016

UNIVERSITY OF SOUTHAMPTON

ABSTRACT

FACULTY OF PHYSICAL SCIENCES AND ENGINEERING
Department of Physics and Astronomy

Doctor of Philosophy

THE EPOCH AND ENVIRONMENTAL DEPENDENCE OF RADIO-LOUD ACTIVE GALAXY FEEDBACK

by Judith Ineson

This thesis contains the first systematic X-ray investigation of the relationships between the properties of different types of radio-loud AGN and their large-scale environments, using samples at two distinct redshifts to isolate the effects of evolution. I used X-ray observations of the galaxy clusters hosting the radio galaxies to characterise the properties of the environments and compared them with the low-frequency radio properties of the AGN. I found a strong relationship between radio luminosity and ICM richness for low-excitation radio galaxies (LERGs) but not for high-excitation radio galaxies (HERGs), and tentative evidence of evolution of the environment for HERGs, but not for LERGs.

I then used the X-ray emission from the lobes of the FRII galaxies in the samples to calculate their internal pressures, finding them to be at slightly higher pressures than predicted by equipartition and near pressure balance with their external environment at the lobe mid-points. I made the first estimates of lower limits for lobe-tip Mach numbers for a large sample of lobes; suggesting that about half the lobe tips were driving strong shocks.

Finally I verified that the correlation between LERG radio luminosity and cluster X-ray luminosity is not caused by a common correlation with black hole mass, and also found no evidence that HERG properties are affected by ICM richness, adding evidence for theories of local fuelling for HERGs. I found evidence that HERGs should have a strong relationship between jet power and radio luminosity, but that LERG jet power must be subject to factors additional to black hole mass. I also found evidence that the same mass black hole is associated with lower radio luminosities in FRI morphology galaxies than in FRIIs, perhaps as a result of the higher proton content of FRI jets leading to lower radiative efficiency.

Contents

List of Figures

List of Tables

Declaration of Authorship

I, Judith Ineson, declare that this thesis titled, 'The epoch and environmental dependence of radio-loud active galaxy feedback' and the work presented in it are my own. I confirm that:

- This work was done wholly or mainly while in candidature for a research degree at this University.
- Where any part of this thesis has previously been submitted for a degree or any other qualification at this University or any other institution, this has been clearly stated.
- Where I have consulted the published work of others, this is always clearly attributed.
- Where I have quoted from the work of others, the source is always given. With the exception of such quotations, this thesis is entirely my own work.
- I have acknowledged all main sources of help.
- Where the thesis is based on work done by myself jointly with others, I have made clear exactly what was done by others and what I have contributed myself.

Acknowledgements

I acknowledge the support of the South-East Physics Network (SEPnet).

The scientific results reported in this thesis are based on observations made with the *Chandra* X-ray observatory and on observations obtained with *XMM-Newton*, an ESA science mission with instruments and contributions directly funded by ESA Member States and NASA. This research has made use of software provided by the *Chandra* X-ray Center (CXC) in the application packages CIAO and CHIPS, and of the *XMM-Newton* Science Analysis Software (SAS).

This research also made use of the University of Hertfordshire high-performance computing facility (http://stri-cluster.herts.ac.uk/), and thanks are due to Martin Hardcastle for providing IT assistance and access to his software.

Figures were plotted using the *veusz* package (http://home.gna.org/veusz/).

My immense gratitude goes to my supervisor, Judith Croston, for her knowledge, support and encouragement, and for being so good-natured and such a pleasure to work with. I would also like to thank Ian McHardy and Martin Hardcastle for taking over when Judith was unavailable, my assistant supervisors Rob Fender and Anna Scaife, and Simon Harris for his always good-natured IT support.

Finally, I would like to express my thanks to the University of Southampton Astronomy group as a whole, for being such a thoroughly nice group of people.

Chapter 1

Introduction

1.1 Radio galaxies

1.1.1 General

The discovery of the wide variety of strange objects that became known collectively as Active Galactic Nuclei (AGN) is a story of disbelief in the incredible power of these objects followed by a gradual acceptance as the emission mechanisms were deduced. The short history I give here of the radio-loud subgroup of AGN is taken largely from the reviews of Shields (1999) and Kellermann (2015).

Radio astronomy began with Karl Jansky's hunt for the source of the static affecting long-distance radio communications and his discovery that one type changed in direction with the Earth's movements, leading him to the conclusion that the radiation was of stellar origin (Jansky 1935). The first map of radio maxima was published by Reber (1940), using a home-built reflector in his back yard. This showed energy peaks coming from the directions of the Andromeda Galaxy and the Milky Way – the first radio observation of what would be later be named Cygnus A. After World War II, work began in earnest on investigating Cyg A and other, similar radio sources. In 1949, Bolton et al. reported the discovery of three strong, discrete sources, but although two of them appeared to be associated with galaxies, the immense luminosity that would be needed for such bright sources to be extragalactic led them to publish the sources as probably stellar but with no observed optical sources (Bolton et al. 1949).

Baade and Minkowski (1954) found that the optical counterparts to the radio observations of Cyg A and two other objects were galaxies, and so the objects must be extragalactic. They also noted that their optical spectra resembled those of the Seyfert

galaxies studied in the 1940s. As radio telescopes improved, the maps became more accurate and detailed and astronomers began to see structure in the radio sources. Jennison and Das Gupta (1953) discovered that Cyg A had two components, and this structure was found to be common amongst the extragalactic radio sources. Eventually these objects were found to have radio jets ending in plumes or lobes, as described in Section 1.1.2.1 below. Figure 1.1 shows an early photograph of Cyg A with the positions of the radio lobes superimposed alongside a modern equivalent.

During the next few years, some of the point sources that had become known as quasi-stellar radio sources (now known as radio-loud QSOs) were found to have what were thought to be impossibly high redshifts and in some cases were misidentified as stellar objects. It was finally accepted that these high redshifts were correct (eg Minkowski 1960; Greenstein and Matthews 1963). Assuming the redshift was cosmological, the optical luminosities of these objects were so great that there was no current theory that could explain the energy production. A number of alternative theories were suggested to explain the high recession velocity, for example that the objects that had been expelled violently from the Milky Way, but this process would itself have required an incredible amount of power.

Two decades of work looking at the emission lines of the early QSO discoveries followed, leading to the suggestion of separate Broad and Narrow line emission regions (see Section 1.1.2.3). Oke and Sargent (1968) derived a central mass of $\sim 10^5 M_\odot$ for a Seyfert galaxy, and after the development of reverberation mapping eventually enabled limits to be set on the sizes of the different emission regions, the realisation finally came that the central mass must be a black hole.

The source of the incredible luminosity of these objects generated some interesting suggestions; for example that matter falling into a black hole went down a worm-hole and emerged as a white hole – the QSO. The first suggestions that accretion onto a supermassive black hole could release sufficient energy to power a QSO came as early as 1964 (Salpeter 1964; Zeldovich 1964), but received little attention. However, once the first galactic black holes were identified in the early 1970's and Shakura and Sunyaev (1973) had published their detailed analysis of accretion disc physics the theory began to be applied to QSOs and the model began to gain acceptance. Accretion onto a supermassive black hole is now assumed to be the power source of all AGN. There were by this time a wide variety of powerful objects, both radio-loud and radio-quiet, that were so luminous that this was the only known method of producing sufficient power.

The unified model of AGN, described in Section 1.1.2.3 below, brought the majority of the different types of AGN into a single type of object viewed from different angles. Most types of radio-loud and radio-quiet AGN have similar optical and ultra-violet

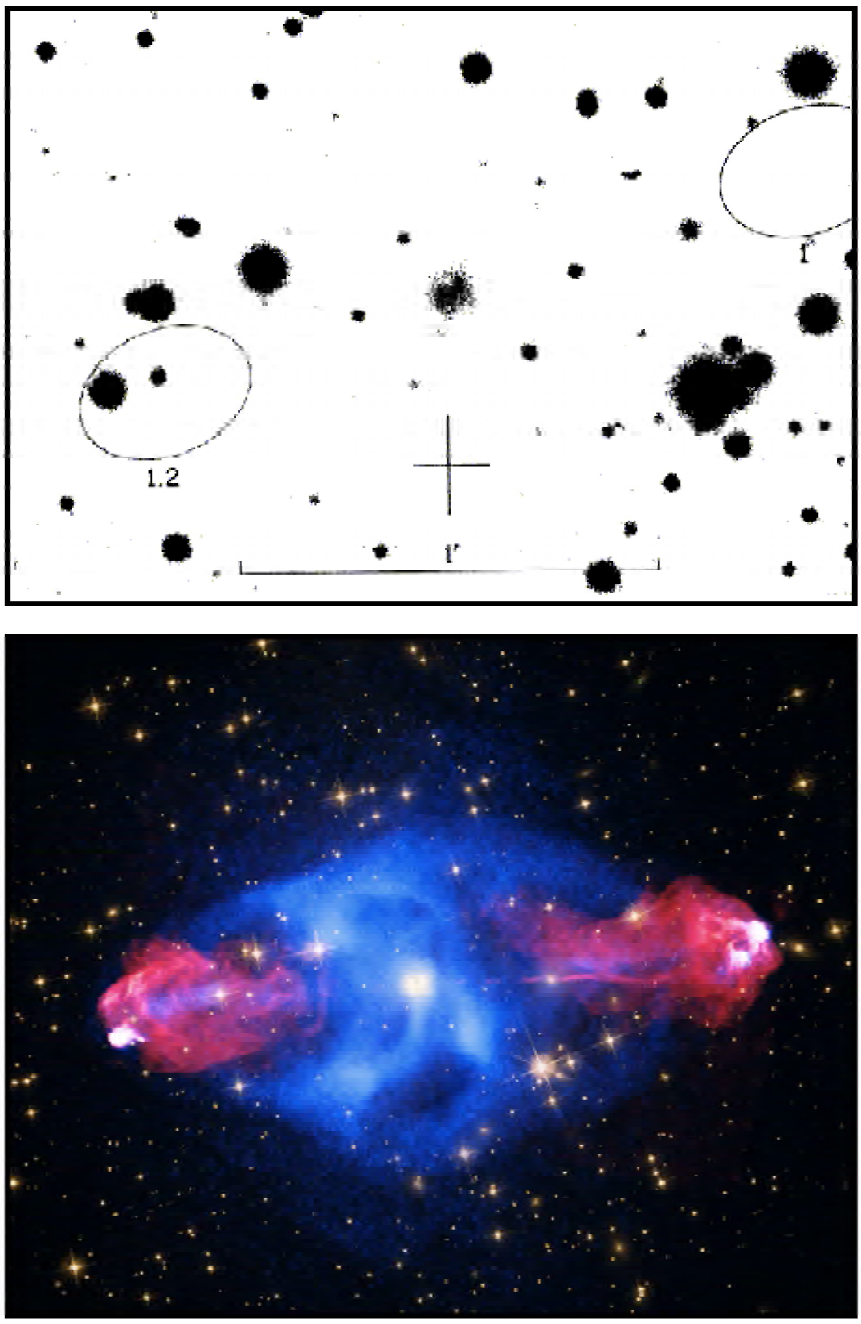

FIGURE 1.1: Top: an early photograph of Cygnus A with the interferometer positions of the radio lobes superimposed (Matthews et al. 1964). Bottom: a modern optical image (NASA/STScI) overlaid with the radio lobes in red (NSF/NRAO/AUI/VLA) and the X-ray emission from the intra-cluster medium in blue (NASA/CXC/SAO).

spectra and central X-ray features, and so the majority of radio-loud AGN spectra fit into this model. There is however a group of radio-loud AGN that have some different spectral features and do not fit into the unified model – these will also be discussed in Section 1.1.2.3.

The category of radio-loud is defined by the relative proportions of optical and radio emission – an AGN is defined as radio-loud if the ratio of the 5 GHz radio flux to B-band optical flux is greater than 10 (Kellermann et al. 1989). The difference between the two is a little fuzzy – radio-quiet AGN are not radio silent and objects classified as radio-quiet may still have weak or short jets (eg Mezcua and Prieto 2014). In this thesis I will however only be concerned with AGN falling within the traditional definition of radio-loud.

A galaxy can be isolated, or it can occupy a region of space where a number of galaxies are gravitationally bound into a structure consisting of anything from a few to thousands of galaxies – galaxy groups and clusters (see Section 1.2). The general population of radio-quiet AGN are commonly hosted by galaxies residing in any density of environment from isolated through to cluster (eg Kauffmann et al. 2004). Radio-loud AGN, however, appear not to be hosted by isolated galaxies, as will be seen in the literature review in Section 1.3.1 and in the radio galaxy samples used in this thesis, but for the most part inhabit relatively low density galaxy groups and clusters.

Radio-loud AGN send massive amounts of energy into their environments. Disturbances of the cluster environment by the radio jets can be seen in detailed studies of nearby radio galaxies (eg Kraft et al. 2003; Fabian et al. 2003; Forman et al. 2005; Croston et al. 2009) and the processes involved are described in the review by McNamara and Nulsen (2007). As can be seen from the cavities carved out of the intra-cluster medium (ICM) by the radio lobes in Figure 1.1, the radio jets transport energy from the centre of the system for a considerable distance into their galaxy cluster. The jets can themselves be modified in speed, shape and direction by the density variations of the ICM (eg NGC 1265 in Figure 1.10).

Understanding how the properties of radio-loud AGN relate to their cluster environments is crucial for our understanding of the role of this type of energy input in galaxy evolution. For example, the theoretical cooling time for the ICM was expected to result in star formation in the cool gas falling into the cluster centre, but this was not observed (eg Peterson et al. 2003; Peterson and Fabian 2006). Simulations can be reconciled with observations if they include energy transport by AGN (eg Croton et al. 2006; McNamara and Nulsen 2007; Gitti et al. 2012).

AGN feedback – the self-regulated cycle of energy transfer between the AGN and its environment – via radio jets is therefore a complex, two-way process, and the relationship between the radio-loud AGN and environment and how this relationship evolves with epoch is as yet poorly understood. The aim of this thesis is to investigate the relationship between radio galaxies and their large-scale environment, using radio and X-ray observations of samples of radio-loud AGN and their surrounding ICM at two distinct redshifts.

In the rest of this introduction I will describe radio galaxies in more detail, looking at their morphology and spectral characteristics and the emission processes that produce the radiative features that I will use during my analysis. I will then give an outline of differences that have been found between two major classes of radio galaxy and current theories of how these differences might arise from different accretion modes. Finally I will introduce the main topics of my thesis and give an overview of historical and more recent research in this area and why further work is needed.

1.1.2 Types of radio galaxy

As mentioned in the brief history of AGN above, there are a number of different types of radio galaxy. Two common classification methods use radio luminosity and physical appearance of the radio jets and the optical spectra. I describe first the morphology of the radio galaxies and the emission processes responsible for their large-scale appearance. I then go on discuss the nuclear multiwavelength spectra of the different types of radio galaxy, how they relate to the processes going on nearer the heart of the systems, and give a brief overview of possible accretion modes for the two major spectral classes of radio galaxy.

1.1.2.1 Morphological classification

Radio galaxies typically have twin jets which either flare out rapidly into a lobe or plume or stay collimated for a long distance and terminate in a lobe (Figure 1.2). Fanaroff and Riley (1974) classified the two morphologies by the positions of the regions of brightest emission – whether they were near the nucleus or the lobe tip – and found a fairly clear difference in radio luminosity between the two morphologies. Those that are brightest near the nucleus are known as FRI galaxies. They generally have a 178 MHz luminosity below about 2×10^{25} W Hz^{-1} sr^{-1}, although the luminosity break varies with host galaxy mass (Owen and Ledlow 1994).

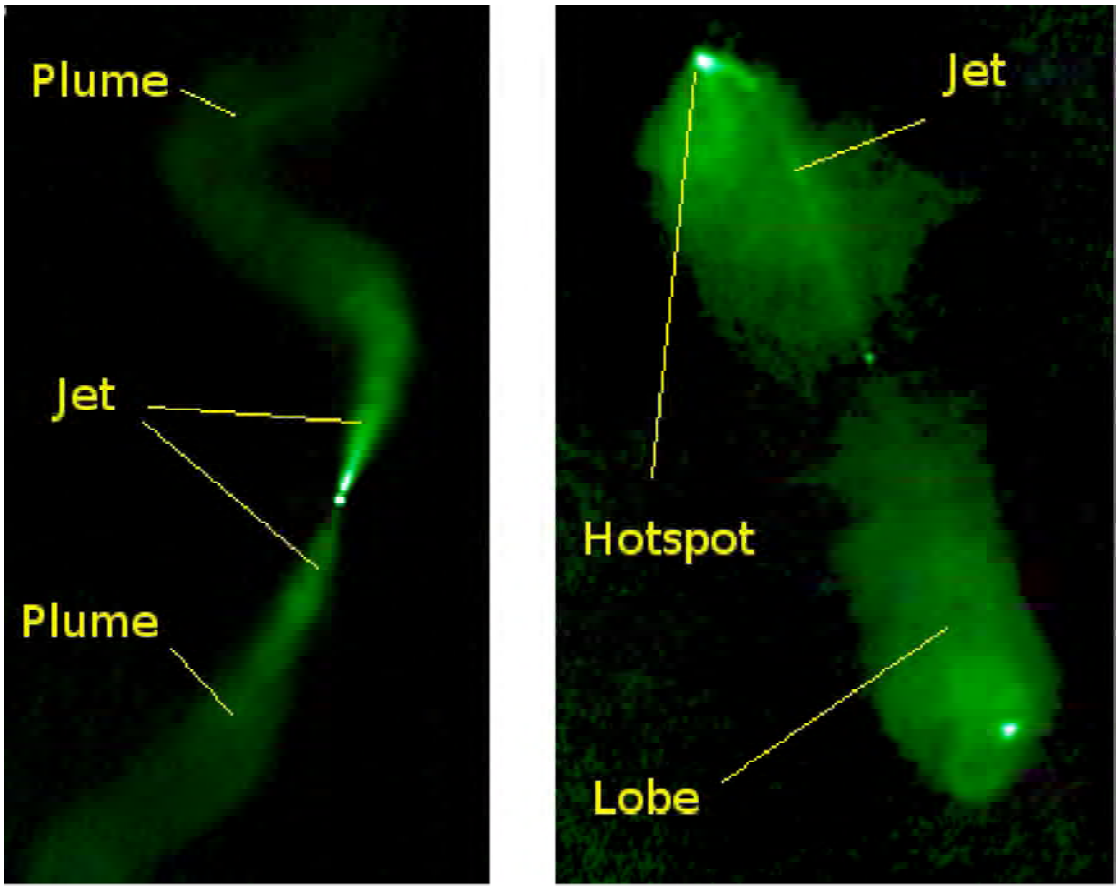

FIGURE 1.2: Examples of an FRI galaxy (left) and FRII galaxy (right). Images courtesy of M. Hardcastle.

FRI jets are emitted at relativistic speeds but decelerate quite rapidly and become turbulent, expanding into a plume or lobe extending for perhaps several hundred kpc. They are brightest near the nucleus where the jets are decelerating. The jets are thought to be turbulent and to entrain material from the environment, thus losing energy. Canvin and Laing (2004), for example, measured jet decelerations from $\sim 0.8c$ near the nucleus down to $\lesssim 0.2c$ in less than 10 kpc.

The lobes that are brightest at the tips – the FRII galaxies – have higher radio luminosities. Their jets stay relativistic for immense distances – in some cases a few Mpc – so relativistic beaming usually results in only the near-side jet being visible. The jets terminate in a hot-spot with material spreading out from behind the hot-spot in a lobe. They are brightest at the hot-spots and the edges of the lobes.

One as yet unsolved problem is why some AGN should develop powerful relativistic jets while the majority do not. Various suggestions have been made over the years; for example that the property is related to host galaxy type (eg Smith et al. 1986), or to black hole spin (eg Wilson and Colbert 1995). More recently it has been suggested that

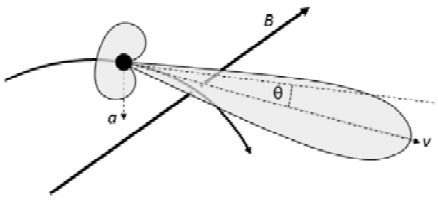

FIGURE 1.3: Synchrotron radiation. Emission from a relativistic particle spiralling around a magnetic field line beams in the direction of motion of the particle. a is the acceleration vector, v the velocity vector, B the magnetic field and θ, the half-power cone of the beam, is $\pi/2\gamma$.

whether the spin is prograde or retrograde with respect to the accreting material might enable the formation of powerful relativistic jets (eg Garofalo et al. 2010).

It has long been suggested that there should be a continuum of jet power down to quite low values, and also that there should be young sources with small jets. Gallimore et al. (2006), looking at a sample of 43 radio-quiet LINERs (Low-Ionisation Nuclear Emission-line Region galaxies) and Seyfert galaxies, found that 19 had radio jets at least 1 kpc long. Baldi et al. (2015), in a pilot study looking at a small sample of radio-loud compact sources, found some with jets extending to only a few kpc. Whether these are newly activated FRI galaxies or are naturally weak jets is not yet known.

1.1.2.2 Emission processes

The features described above all produce radio emission, and some features also have optical and/or X-ray counterparts. In the following sections I give a brief description of the two processes responsible for most of the observed radio and X-ray radiation in the radio jets and lobes.

Synchrotron emission

The jets of radio galaxies consist of particles spiralling around magnetic field lines. The emission mechanism is synchrotron (Figure 1.3), emitted across a range of radio frequencies as the particles spiral, radiating as they accelerate. Burbidge (1956) first made calculations of the magnetic field and particle energies required to produce synchrotron emission using observations of the jet of M87, and Perley et al. (1984) showed the complexity of the magnetic fields constraining the inner parts of the jet in their detailed study of the FRI radio galaxy NGC 6251.

For the following discussion of synchrotron radiation, I follow Longair (2011), Chapters 8 and 16.

Spiralling electrons lose energy at a rate:

$$-\frac{dE}{dt} = \frac{4}{3}\sigma_T c U_B \left(\frac{v}{c}\right)^2 \gamma^2 \tag{1.1}$$

where σ_T is the Thomson cross-section of the electron, c the speed of light, U_B the energy density of the magnetic field, v the electron velocity, and the Lorentz factor $\gamma = 1/\sqrt{1 - v^2/c^2}$.

Because the particles are highly relativistic, the radiation is beamed in the direction of motion of the electron. The observer sees a pulse of radiation as the beam sweeps past, with a pulse duration Δt that is much shorter than the gyration period and inversely related to γ^2. For an electron of mass m_e and charge e circling normal to the magnetic field, the bulk of the radiation is emitted at the critical frequency $\nu_c \sim 1/\Delta t \sim \gamma^2 \nu_g$, where $\nu_g = eB/(2\pi m_e)$ is the non-relativistic gyration frequency at magnetic field strength B.

Thus for an electron with energy $E = \gamma m_e c^2$,

$$\nu_c \approx \left(\frac{E}{m_e c^2}\right)^2 \frac{eB}{2\pi m_e} \tag{1.2}$$

Because of the inverse dependence on mass, electrons (and/or positrons) dominate the synchrotron emission and so synchrotron radiation cannot be used to look at the proton content of the jet.

Figure 1.4 shows the spectrum of synchrotron radiation from an electron in linear and logarithmic form. The emission has a broad maximum near the critical frequency.

Assuming $v \sim c$ and using $U_B = B^2/2\mu_0$, where μ_0 is the permeability of the vacuum, we can rewrite the energy loss equation (1.1) in terms of the electron energy and the magnetic field strength:

$$-\frac{dE}{dt} = \frac{4}{3}\sigma_T c \left(\frac{E}{m_e c^2}\right)^2 \frac{B^2}{2\mu_0} \tag{1.3}$$

An electron's radiative lifetime can be expressed as $E/\frac{dE}{dt}$, and so is inversely proportional to the electron energy. Thus the highest energy electrons, which produce the highest energy radiation, lose energy fastest and are short-lived.

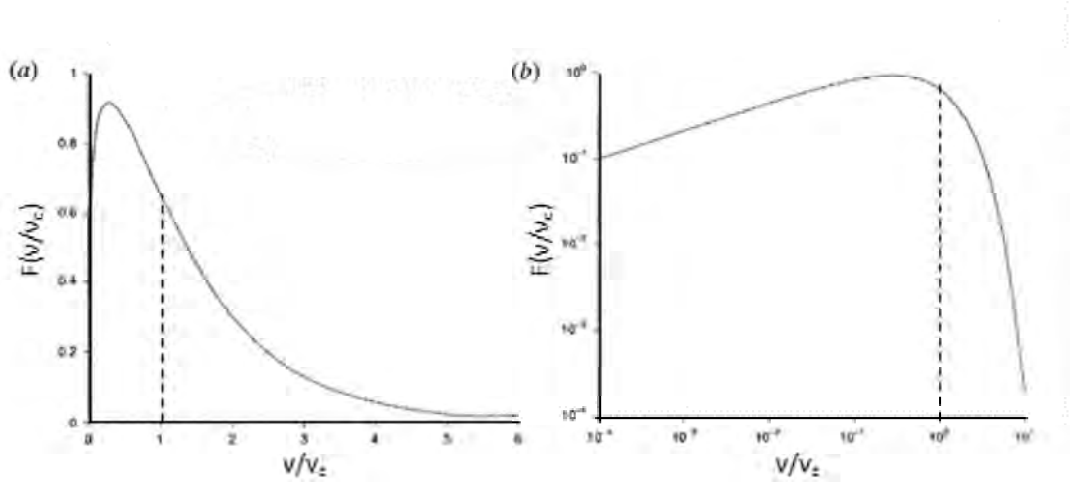

FIGURE 1.4: The spectrum of synchrotron radiation from an electron, taken from Longair (2011), Figure 8.8. The frequency ν is scaled by the critical frequency ν_c and the spectrum is shown using linear axes (left) and logarithmic axes (right). The vertical lines show ν_c.

Assuming particle acceleration by ultra-relativistic shocks, the number density of electrons $N(E)$ with energy E reduces as energy increases as a power law (eg Achterberg et al. 2001), so $N(E) = N_0 E^{-m}$ where m is the electron index. m is typically $\sim 2.2-2.3$ (Achterberg et al. 2001), but will however steepen where energy losses are important (Worrall and Birkinshaw 2006).

The emitted spectrum $J(\nu)$ for a distribution of electrons consists of the sum of the individual electron pulses, taken between the maximum and minimum electron energies E_{max} and E_{min}.

$$J(\nu)d\nu = \int_{E_{min}}^{E_{max}} j(\nu)N(E)dE \tag{1.4}$$

If we assume that $j(\nu)$ is a delta function at the critical frequency, we obtain

$$J(\nu)d\nu = -\frac{dE}{dt}N(E)dE \tag{1.5}$$

giving

$$J(\nu) = N_0 B^{(m+1)/2}\nu^{-(m-1)/2} \tag{1.6}$$

or $J(\nu) = N_0 B^{\alpha+1}\nu^{-\alpha}$, where $\alpha = (m-1)/2$ is the spectral index.

The observed flux thus depends on both the particle density and the magnetic field strength.

The total energy density is the sum of the energy densities of the magnetic field and the particles. Assuming the particles to be electrons, the total energy W_T within a volume V is:

$$W_T = V\frac{B^2}{2\mu_0} + V\int_{E_{min}}^{Emax} EN(E)dE \tag{1.7}$$

which gives

$$W_T = V\frac{B^2}{2\mu_0} + V\frac{N_0}{2-m}\left[E_{max}^{(2-m)} - E_{min}^{(2-m)}\right] \tag{1.8}$$

If we use $\nu = CE^2B$ (where C is constant) to replace E_{max} and E_{min} and equation 1.6 to eliminate N_0, we obtain

$$W_T = V\frac{B^2}{2\mu_0} + G(\alpha)J(\nu)B^{-3/2} \tag{1.9}$$

where $G(\alpha) = \frac{C^{(m-2)/2}}{(2-m)}V\nu^{(m-1)/2}\left[\nu_{max}^{(2-m)/2} - \nu_{min}^{(2-m)/2}\right]$ and has, for a typical spectral index of ~ 0.75, a weak dependence on m, ν_{max} and ν_{min}.

Figure 1.5 shows the variation of total energy with magnetic field strength, showing the contributions from the particle and magnetic field energies. The particle contribution decreases with magnetic field strength while the magnetic field energy increases, giving a minimum for the total energy. So when neither the magnetic field strength or the electron number density are known, we can calculate the minimum energy densities that can account for the observed synchrotron flux. Using Equation 1.9, we can differentiate with respect to B to obtain the minimum magnetic field for a given emissivity and frequency:

$$B_{min} = \left[\frac{3\mu_0}{2}\frac{G(\alpha)J(\nu)}{V}\right]^{2/7} \tag{1.10}$$

This gives a lower bound on the energy densities in the lobe.

In Figure 1.5, there is also a point near the energy minimum where the energy densities of the magnetic field and electrons are the same, so:

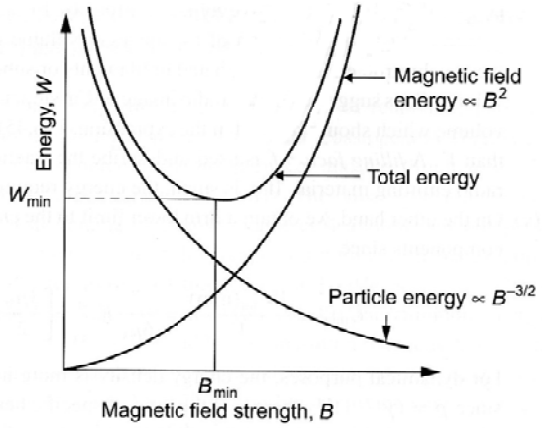

FIGURE 1.5: Total energy, particle energy and magnetic field energy plotted against magnetic field strength, showing the minimum energy condition (W_min, B_{min}) and the equipartition condition where the particle and magnetic field energy curves cross. Plot taken from Longair (2011), Figure 16.7.

$$\frac{B^2}{2\mu_0} = \int_{E_{min}}^{Emax} EN(E)dE \tag{1.11}$$

Putting in the minimum magnetic flux density B_{min}, this gives a magnetic field energy of 3/4 of the electron energy, and so the equipartition condition is similar to the minimum energy condition. Thus we can estimate the electron density and magnetic field strength for the minimum energy within a radio lobe from its volume, flux and spectral index by assuming equipartition.

It is important to note that if there is a significant contribution from relativistic protons, a factor needs to be included to take account of their energy contribution since it will raise the energy density above the minimum.

Inverse Compton emission

Regions of X-ray emission are often seen in radio jets and lobes. In FRI sources they occur mainly in the inner jets and knots but are rarely seen in the lobes and plumes. In FRII sources, however, X-ray emission is often visible much further out from the nucleus, in the hot-spots where the jets terminate in the ICM and at a lower level throughout the lobes.

Some features, such as the FRI jets and some of the knots and also some FRII hot-spots, are dominated by, or have measurable contributions from high energy synchrotron emission (Hardcastle et al. 2001, 2002b, 2004; Kataoka and Stawarz 2005). Otherwise, the bulk of the X-ray emission is attributed to inverse Compton (IC) scattering (Hardcastle et al. 2002a; Croston et al. 2005b; Kataoka and Stawarz 2005), where photons' energies

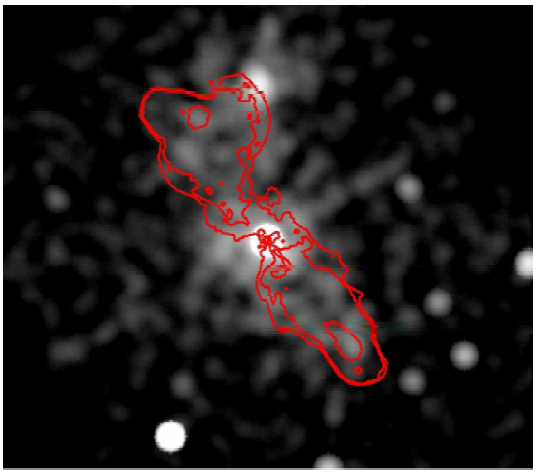

FIGURE 1.6: 3C 219, one of the sources analysed in Chapter 5. The X-ray emission (grey) is overlaid by the radio lobe contours (red), and inverse Compton emission is visible extending along the lobes.

are boosted during collisions with the relativistic electrons generating the synchrotron emission. In Figure 1.6, IC X-ray emission can be seen extending along the lobes, brighter than the surrounding ICM.

For a low energy, isotropic photon field of energy density U_{rad}, the rate of energy loss for IC is (Longair 2011, equation 9.42):

$$-\frac{dE}{dt} = \frac{4}{3}\sigma_T c U_{rad} \left(\frac{v}{c}\right)^2 \gamma^2 \tag{1.12}$$

Comparing this with Equation 1.1, we can see that for a population of electrons losing energy by both synchrotron and IC emission the ratio of powers of the two emission mechanisms P_{IC}/P_{sync} is simply the ratio of the photon and magnetic field energy densities U_{rad}/U_B.

Consider an isotropic photon field of initial frequency ν_0. From Rybicki and Lightman (1979), Section 7.3 and Longair (2011) Equation 9.43, we can give the spectral emissivity $I(\nu)$ of the IC scattered photons by:

$$I(\nu)d\nu = \frac{3\sigma_T c}{4\gamma^2} N(\nu_0) \frac{\nu}{\nu_0} f(x) d\nu \tag{1.13}$$

where $N(\nu_0)$ is the number density of the initial photon field, $x = \nu/(4\gamma^2\nu_0)$, and $f(x) = 2xlnx + x + 1 - 2x^2$

For low frequencies, x is small, $f(x)$ tends to a constant, and the spectrum $I(\nu) \propto \nu$.

FRII lobes (excluding compact regions such as hot-spots) have no known mechanism for accelerating electrons sufficiently to emit X-ray photons by the synchrotron process, so we can assume that the X-ray emission seen in the lobes comes from IC scattering. The observed X-ray flux can then be used to find the energy density of the electrons and, when combined with the radio synchrotron emission, to obtain the magnetic field strength and total energy budget (assuming that proton content of the lobes is low).

From this electron density, we can also obtain the lobe pressure and compare it with conditions in the external medium. This density is however based on the electron content of the lobe and so if there is a population of protons present this will not be taken into account.

There are three potential sources of high flux density, low energy photons available in the lobe for IC scattering. In a compact source, the electrons producing radio emission by synchrotron radiation also collide with these photons and boost them up to X-ray energies. This is known as synchrotron self-Compton emission (SSC), and has been observed by Kataoka and Stawarz (2005) and Hardcastle et al. (2004) as the dominant process in some FRII hot-spots and FRI knots where the electron density is high, and also in some small, bright lobes such as Cygnus A (eg Hardcastle and Croston 2010).

A second, omnipresent source of photons is the cosmic microwave background (CMB), which becomes a significant source of energy loss for electrons with $\gamma \approx 1000$ (Hardcastle and Croston 2010). This is the dominant process in FRII lobes (Hardcastle et al. 2002a), where the electron density is lower than in the hot-spots and so SSC emission is lower.

Both these fields are approximately isotropic and so calculating their emissivities is relatively straightforward. The third potential photon field comes from the hidden AGN nucleus (Nuclear Inverse Compton emission; NIC). In this case the photons are coming from a discrete source and so are not isotropic and the computations are more complex (Brunetti 2000). Croston et al. (2004), Belsole et al. (2004) and Croston et al. (2005b) looked at the size of the NIC contribution in three individual sources and found the contribution to the overall lobe flux to be small. Croston et al. (2005b) conclude that nuclear IC is not generally a dominant source of X-ray emission in lobes and I therefore do not include it in my estimates of lobe pressure.

Taking the SSC contribution first, Band and Grindlay (1985) give the number density of the synchrotron photons in a sphere of radius R as

$$n_{SSC}(\nu_i)d\nu_i = \frac{3}{4c}R\frac{J(\nu_i)d\nu_i}{h\nu_i} \tag{1.14}$$

where $J(\nu_i)$ is the synchrotron emissivity giving photons of frequency ν_i.

Combining this with the emission function (Equation 1.13), we can obtain the emissivity resulting from SSC scattering from the full electron energy range:

$$J_{SSC}(\nu_s) = \frac{9}{16} m_e^2 c^4 \nu_s \sigma_T R \int_{E_{min}}^{E_{max}} \int_{\nu_{min}}^{\nu_{max}} \frac{N(E) J(\nu_i)}{E^2 \nu_i^2} f(x) d\nu_i dE \tag{1.15}$$

where $N(E)$ is the synchrotron electron number density described above.

The CMB is a black body, so the photon number density comes from Planck's law:

$$n_{CMB}(\nu_i) d\nu_i = \frac{8\pi \nu_i^2 d\nu_i}{c^3 (e^{\frac{h\nu_i}{kT}} - 1)} \tag{1.16}$$

giving an emissivity of:

$$J_{CMB}(\nu_s) = 6\pi h m_e^2 c^2 \nu_s \sigma_T \int_{E_{min}}^{E_{max}} \int_{\nu_{min}}^{\nu_{max}} \frac{N(E) \nu_i}{E^2 (e^{\frac{h\nu_i}{kT}} - 1)} f(x) d\nu_i dE \tag{1.17}$$

These two equations then allow us to find the electron energy density from the X-ray flux in the FRII lobes.

Figure 1.7 shows an example of a model fit to a observations of PKS 0227 showing the synchrotron emission and the contributions of inverse Compton scattering of different photon fields. At the X-ray wavelengths of 1 to 10 keV, IC emission is dominated by CMB scattering. As can be seen from the figure, starlight also provides a photon field for IC scattering, but being higher energy the photons are scattered beyond the 1 to 10 keV range, and its contribution overall is small compared with CMB scattering.

1.1.2.3 Spectral classification

The second common method of classification of radio-loud AGN is by their optical spectral features, in particular whether or not the object has strong emission lines (eg Hine and Longair 1979; Laing et al. 1994). Figure 1.8 shows optical spectra of three different classes of AGN.

Narrow-Line Radio Galaxies (NLRGs, eg 3C 223, Figure 1.8), have strong, narrow emission lines indicating low velocity material. The presence of forbidden lines indicate that the material is low density. Broad-Line Radio Galaxies (BLRGs, eg 3C 219) have the same narrow lines as the NLRGs, but also broad lines indicating faster moving material. Some of the broad lines overlay narrow lines, indicating elements in common with the

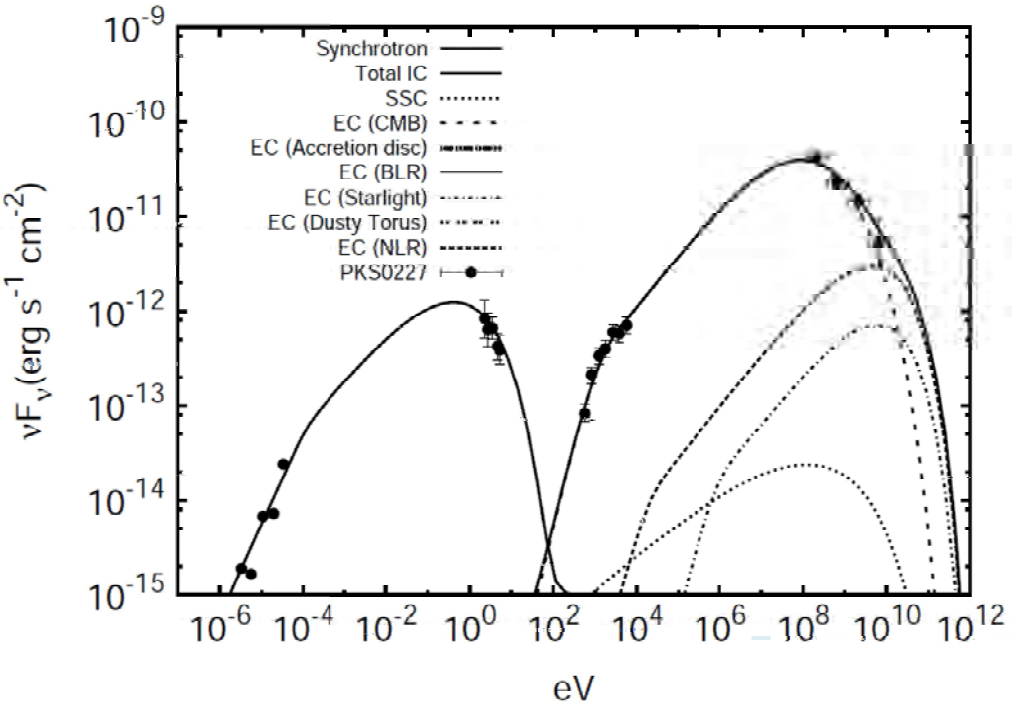

FIGURE 1.7: An example spectrum of synchrotron and inverse Compton from the jet of PKS 0227 taken from Potter and Cotter (2013), showing the IC contributions from different photon fields.

slower moving material, but none of the broad lines are forbidden so the material must be more dense than that producing the narrow lines.

The third spectrum (3C 31) is completely different. Low Excitation Radio Galaxies (LERGs or LEGs) are a class of radio galaxy which does not have the strong broad and narrow emission lines seen in the other types of radio galaxy described above, but has strong absorption features not seen in the other galaxies and few, weak emission lines from galactic gas and dust. Note that what appears to be a broad Hα emission line in 3C 31 in fact the sum of three narrow lines.

Discussions of AGN unification (eg Antonucci 1993; Laing et al. 1994; Urry and Padovani 1995) recognized that radio-loud QSOs, BLRGs and NLRGs could be interpreted as the same class of object viewed at different orientations. The standard model of these AGN (Figure 1.9, left) contains a central black hole (giving high energy radiation from matter falling towards the black hole), some form of accretion disc (giving black body emission), a region of fast-rotating material relatively close to the nucleus which re-emits the nuclear radiation as broad lines, and a region of material further out from the nucleus responsible for the narrow emission lines. Beyond the broad-line region, there is a dense region of material which has become known as the dusty torus, which re-emits the central radiation in the infra-red. The inner features are progressively obscured as

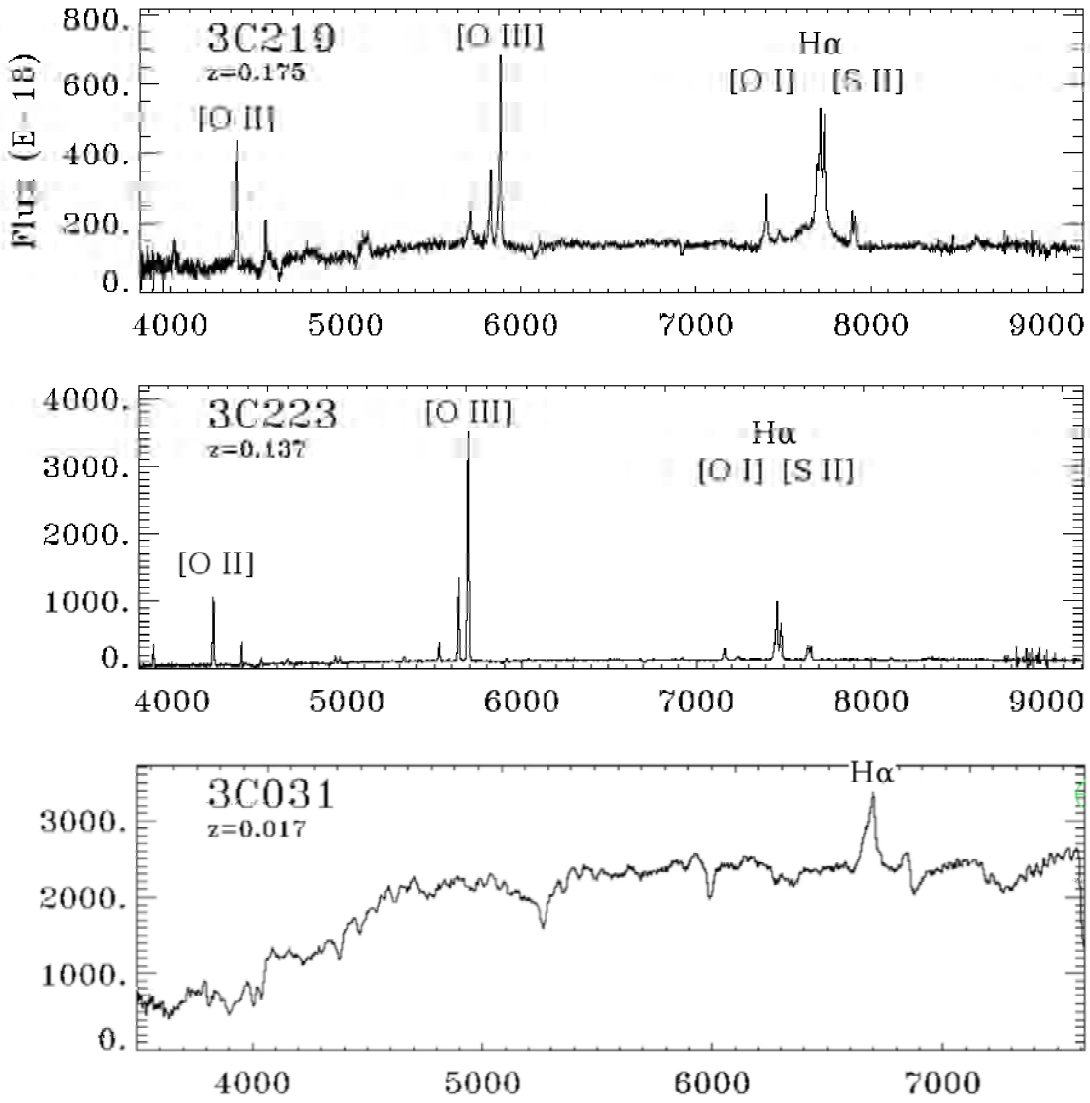

FIGURE 1.8: Optical spectra of three types of radio-loud AGN, from Buttiglione et al. (2009). 3C 219 (top) is a broad line RG and 3C 223 (middle) a narrow line RG. These are both high excitation radio galaxies with strong emission lines. 3C 31 (bottom) is a low excitation radio galaxy with strong absorption features but few emission lines.

the viewing angle increases, giving the spectra of the different types of radio galaxy. When viewed along the jet, the strength of the beamed emission obscures most or all of the other features, giving the strong, flat spectrum of the Flat Spectrum Radio Quasar (FSRQ) sub-class of blazar. These types of radio galaxy are often known collectively as High Excitation Radio Galaxies (HERGs or HEGs) or radiative-mode AGN.

This model does not however include the LERGs (eg Hardcastle et al. 2006). Their spectra tend to have weaker nuclear X-ray emission than the HERGs, suggesting a lower accretion rate. They do not have the range of spectra of the HERGs, suggesting that there is no torus to obscure the edge-on view of the nucleus, so the only orientation effect comes when the jet is viewed end-on, giving the spectrum of the BL Lac class of blazar.

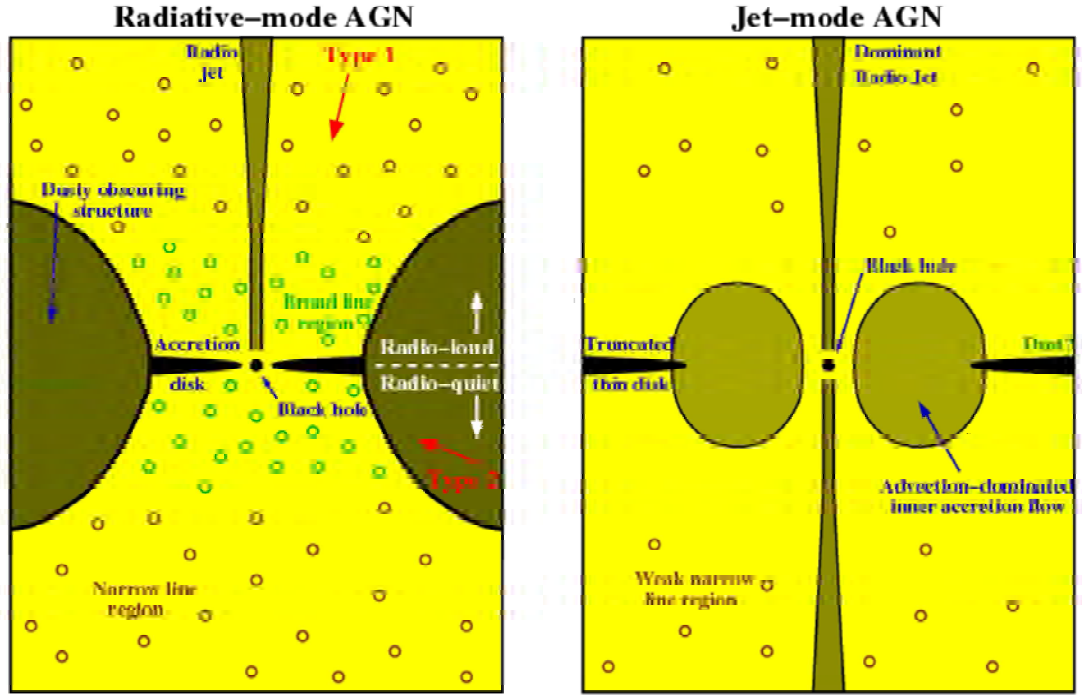

FIGURE 1.9: Two models of AGN structure, from Heckman and Best (2014). To the left is a schematic of the radiative mode (also known as HERG or HEG). This is the standard unified model with the black hole accreting from a thin disc and surrounded by an obscuring structure. Within the dusty torus is a relatively dense, fast-moving inner region of gas which emits broad emission lines, and further out there is a less dense, slow-moving cloud that emits narrow lines. The visibility of the different features depends on whether they are hidden by the torus. On the right is the Jet-mode model (LERG or LEG), where the inner accretion disc and broad line region are replaced by a geometrically thick advection-dominated accretion flow.

As well as lacking strong emission lines and an obscuring feature, the LERGs also do not show the spectral components expected from a hot accretion disc. So although the large-scale physical appearance of the two classes of galaxy are the same, they appear to be fundamentally different at their hearts.

More recently, as telescopes have improved, researchers have started to examine the different properties of HERGs and LERGs. There is now strong evidence that they have different accretion rates (e.g. Best and Heckman 2012; Son et al. 2012; Mingo et al. 2014; Gürkan et al. 2014; Fernandes et al. 2015), with the majority of HERGs having Eddington ratios (see Section 1.1.2.4) above ∼1% and LERGs below ∼1%, albeit with some overlap. HERGs, together with their radio-quiet counterparts, are therefore classified as Radiative-mode AGN while the LERGs are classified as Jet-mode AGN (a somewhat confusing name as the FRI and FRII jets discussed in Section 1.1.2.1 above are seen in both HERGs and LERGs).

There are also differences in the host galaxies of HERGs and LERGs. They display a

different evolutionary phase, with HERGs tending to have lower mass than LERGs (e.g. Tasse et al. 2008; Smolčić 2009; Best and Heckman 2012), to be bluer (e.g. Smolčić 2009; Janssen et al. 2012; Herbert et al. 2010), and to have ongoing star formation (eg. Hardcastle et al. 2013).

1.1.2.4 Accretion physics

In this section I give a very brief overview of the basics of accretion physics and some the different modes of accretion postulated for AGN, following Netzer (2006).

For a particle to accrete from a distance r onto a source of luminosity L and black hole mass M_{BH}, the gravitational force acting on the particle must be greater than the radiative force coming out from the source. Thus if we assume a non-turbulent, spherical system where the only source of scattering is Compton emission, we obtain

$$\frac{\sigma_T L}{4\pi c r^2} \leq \frac{G M_{BH} M_p}{r^2} \tag{1.18}$$

where σ_T is the Thomson cross-section of the electron, c is the speed of light and M_p is the proton mass.

This gives a maximum luminosity that can be powered by spherical accretion – the Eddington luminosity or limit, $L_{Edd} \sim 1.26 \times 10^{38} (M_{BH}/M_\odot)$ erg s^{-1}. The Eddington ratio for a source of luminosity L is $\lambda = L/L_{Edd}$.

If we assume that the energy available from a mass M is $\eta M c^2$ where η is the accretion efficiency, then the mass accretion rate $\dot{M}$ is given by $\dot{M} = L/(\eta c^2)$. Correspondingly the Eddington accretion rate – the mass accretion rate required to maintain the Eddington luminosity – is $\dot{M_{Edd}} = L_{Edd}/(\eta c^2) \sim 2.2 \times 10^8 (M_{BH}/M_\odot)$ per year.

The simplest theory of accretion (Bondi 1952) assumes that the accreting gas has no radial motion and comes in from a large radius. Most of the radiation comes from particle collisions rather than gravitational energy and so the Eddington ratio follows a different relationship: $\lambda \sim 10^{-4} (\dot{M}/\dot{M_{Edd}})^2$.

The most efficient form of accretion is via an optically thick, geometrically thin accretion disc – such discs are a natural consequence of matter which is rotating about the host galaxy losing angular momentum and falling towards the centre of the system. If the disc is sufficiently dense, matter moves gradually towards the disc centre as it loses angular momentum and eventually accretes onto the black hole. Matter accretes in the equatorial plane, but the radiation is largely emitted in the direction of the disc axis

and so the Eddington limit can be exceeded. In practice, the accretion rate is limited by the rate at which angular momentum can be lost and for radio-loud AGN it is typically $\sim 1 - 10\%$.

Most of the gravitational energy is carried by protons, while the electrons are responsible for most of the cooling and electromagnetic emission. If the accretion rate is low, a two-temperature ionised system can form – an ion torus – with the protons being hotter than the electrons. This results in Advection Dominated Accretion Flow (ADAF) where the hotter protons are then advected into the black hole, taking in the bulk of the gravitational energy but giving little emission. This has been suggested as a possible mechanism for producing jets, since the magnetic field could be anchored to the rapidly rotating ion torus.

1.1.2.5 HERG and LERG accretion modes

The dichotomy in accretion rate supports the suggestion that the two types of radio galaxy have different accretion modes. HERGs, in common with radio-quiet radiative mode AGN, are thought to be fuelled by cold interstellar gas which builds some form of accretion disc and gives rise to radiatively efficient accretion (Shakura and Sunyaev 1973). Cold fuel is channelled into the galaxy centre, and because the host galaxies have a plentiful supply of cold gas (Tadhunter et al. 2014 found large reservoirs of gas at $\sim$ 40 K in their sample of HERGs), there is also fuel available for star formation. The gas and dust form a torus around the black hole heated to a maximum of 1500 K, this being the sublimation temperature of the silicon in the dust. The dust and gas fall into the accretion disc, which has a black body spectrum of $\sim 10^4 - 10^5$ K, emitting in UV and optical wavelengths. The radiation from the accretion disc indirectly gives rise to X-ray emission from the nucleus and IR from the surrounding dusty torus. The high accretion rate adds mass to the black hole, and radiative mode AGN are thought to contribute to black hole growth and the bulge-black hole mass relation (e.g. Ishibashi and Fabian 2012).

Galaxy mergers and interactions are thought to be a major source of new gas for HERGs, and perhaps to provide the stimulus for triggering the jet. Hopkins et al. (2008) predicted galaxy merger rates, and these reproduced the observed population properties of QSOs – luminosity functions, fractions and clustering – suggesting that mergers and interactions could be a triggering and fuelling mechanism. Ramos Almeida et al. (2012) looked for signs of interactions in HERGs and comparable quiescent galaxies and found a substantially higher proportion of HERGs than quiescent galaxies with comparably bright interaction features (90 per cent vs 50 per cent), implying that interactions are

likely to be part of the triggering process. (Since interaction features endure for substantially longer than the active phase of a HERG, they calculated that we should expect HERGs in 1-10 per cent of disturbed ellipticals.) Tadhunter et al. (2014) estimated that gas reservoirs of around $10^9 M_\odot$ are required to sustain activity over the expected duty cycle of a HERG. They found that this matched observed HERG gas reservoirs whereas the reservoirs for quiescent galaxies are, on average, lower. The fact that there are also quiescent galaxies with large gas reservoirs suggests that the size of the reservoir alone is not sufficient to trigger activity, and that gas distribution and kinematics also play a part.

The fuelling mechanism for LERGs is more uncertain. They do not show the characteristic optical and X-ray features of radiatively efficient accretion seen in radiative mode AGN, and it is likely that they are fuelled by a hot, radiatively inefficient flow or advection dominated accretion flow (ADAF, e.g. Narayan and Yi 1994). Bondi accretion of hot gas from the ICM (typically $\sim 10^7$ K at the accretion radius) could provide enough energy for the lower luminosity population (Allen et al. 2006; Hardcastle et al. 2007a), so such sources could be fuelled by a form of hot flow, but this is probably insufficient for the more luminous sources (Russell et al. 2013, – although this is disputed by Fujita et al. 2014). A number of researchers (e.g. Pizzolato and Soker 2005; Gaspari et al. 2012, 2013; Voit and Donahue 2015) discuss a process of chaotic accretion of cool gas clouds, which they find to be capable of releasing more than sufficient energy for the most powerful sources. In this model, filaments and blobs of cooling gas are channelled in from the ICM at large radii to form a central, rotating torus of gas clumps at about 10^4 K, and these gas clumps then collide and accrete, with both processes releasing energy. The cycle is controlled by the central entropy, which when high reduces the gas movement into the centre. It then drops again as the gas in the centre is accreted and removed by the jets, allowing the gas inflow to increase. Temperatures, accretion rates and jet powers thus vary (and in the case of lower power systems may turn off) during a well-regulated cycle that can be maintained for perhaps 10^8 years.

Cooling flows from the inner, more dense regions of the ICM are expected as the bremsstrahlung emission increases with density squared, but another potential source of fuel comes from the gas displaced by the radio lobes. Simulations of lobe growth through the ICM (Hardcastle and Krause 2013) have shown the gas being channelled back towards the centre of the cluster, and this could bring in fuel from more distant regions than the bremsstrahlung cooling flows.

1.2 Galaxy groups and clusters

Having described the different types of radio galaxy and their emission processes, in this section I discuss the large-scale environment surrounding the radio galaxies and some of the different ways of measuring its properties.

Assemblies of galaxies that are bound together by gravity are called galaxy groups or clusters, depending on the size of the structure. That groups and clusters appear to contain more mass than is contained in the galaxies has been noted for some time: Zwicky (1937) estimated the energy contained within the Coma cluster and found that the cluster should be unstable, and Kahn and Woltjer (1959) suggested that the Local Group could only be dynamically stable if there were an appreciable amount of intergalactic material. Mitchell et al. (1976) obtained an X-ray spectrum of the Perseus cluster with the *Ariel 5* satellite. They found iron emission lines at ~ 7 keV and a spectrum shape consistent with thermal radiation from hot gas, suggesting the presence of hot plasma consisting of gas ejected from stars. Further similar spectra were obtained from rich clusters, but it was not until the *ROSAT* and *ASCA* telescopes were launched in the 1990s that the Intra-Cluster Medium (ICM) was found to be ubiquitous. Even taking account of the ICM, the total baryon mass was still much less than the estimated mass of the systems, and it was suggested that the majority of the mass is dark matter (eg Mulchaey et al. 1993; Ponman and Bertram 1993).

The proportions of the different components vary – see Sun (2012) for a review – but the galaxies typically contain $\sim 1\%$ of the mass of the structure. The ICM, which is a hot plasma consisting mainly of ionised hydrogen and helium with small quantities of heavier metals (eg Balestra et al. 2007), contains $\sim 9\%$ of the total mass of the cluster. The remaining $\sim 90\%$ of the cluster mass is assumed to be dark matter, binding the cluster into a single structure.

The total mass of galaxy groups and clusters ranges from about $10^{12} - 10^{15} \mathrm{M}_{\odot}$, and the radius from 0.1–2 Mpc.

1.2.1 Galaxy content

Abell (1958) defined a rich cluster as a system containing 50 or more galaxies not more than 2 magnitudes fainter than the third brightest member within ~ 2 Mpc. There is no clear-cut dividing line between groups and clusters; typically groups are defined as structures containing three or more galaxies, and clusters as containing more than 30–50 galaxies.

Optical measures of cluster richness are based on galaxy counts. Abell's straightforward method of classes based on galaxy counts has no method other than visual of excluding background galaxies. The $N_{0.5}$ measure (Bahcall 1977) is similar to Abell's method, but does an initial background subtraction, using a radius of $0.5h_{50}^{-1}$ Mpc around the target galaxy and counting galaxies within two magnitudes of the third-faintest cluster member.

These methods take no account of galaxy separations and so a loose cluster has the same classification as a tight cluster with a similar number of galaxies. Nearest neighbour methods take as their basis the assumption that the richness of a galaxy cluster is related to how close neighbouring galaxies are. For the 10th nearest neighbour, for example, the method centres on the galaxy of interest and finds the radius containing the nearest 10 neighbouring galaxies. In its basic form, the method is two-dimensional and so takes no account of chance alignments in the third dimension, but there are a number of variations which improve on the basic method.

Muldrew et al. (2012) compared a number of different fixed aperture and nearest neighbour measures of cluster richness. They found that the aperture-based methods tend to be a better indicator of the total cluster mass, but that nearest neighbour methods, particularly ones using a small neighbour number, are a better indicator of the internal properties of the dark matter halo.

One of the most popular cluster measures, which uses a fixed aperture but also takes into account the spatial clustering of the galaxies, is the galaxy-galaxy spatial covariance function B_{gg} (eg Longair and Seldner 1979). This takes as its basic assumption that galaxies are randomly distributed, and given one randomly selected galaxy, determines the probability of finding a second galaxy within a given distance. The cross-correlation function w_{ab} is defined by the joint probability δP of finding an object of type a in an element of solid angle $\delta\Omega_1$ at an angular distance θ from an object of type b in an element of solid angle $\delta\Omega_2$:

$$\delta P = N_a N_b [1 + w_{ab}(\theta)]\delta\Omega_1\delta\Omega_2 \tag{1.19}$$

where N_a and N_b are the mean density of objects of type a and b.

Following Longair and Seldner (1979), ring counts of galaxies about a radio galaxy can thus be described by an angular correlation function:

$$N(\theta)d\Omega = N_g[1 + w(\theta)]d\Omega \tag{1.20}$$

where $N(\theta)d\Omega$ is the number of galaxies in solid angle $d\Omega$ at an angular distance θ from the radio galaxy and N_g is the average surface density of galaxies. From the Lick galaxy counts, Seldner and Peebles (1978) obtained a power law for the cross-correlation function of the form $w(\theta) = A_{gg}\theta^{-0.77}$.

Converting this from angular distances, we obtain the spatial cross-correlation function ξ:

$$n(r)dV = \rho_g[1 + \xi(r)]dV \tag{1.21}$$

where $n(r)$ is the number of galaxies in volume dV at distance r from the radio galaxy, ρ_g is the average space density of galaxies and $\xi(r) = B_{gg}r^{-0.77}$.

The parameter B_{gg} is then a measure of the degree of clustering of galaxies about the radio galaxy.

Note that B_{gg} is sometimes known as B_{gq} (galaxy-quasar spatial covariance function) or B_{gc} (galaxy-cluster centre spatial covariance function).

These methods of measuring cluster richness all correlate to some extent, so results derived using different optical measures are usually comparable even if translations between measures for individual clusters are imprecise. However, one important factor that needs to be taken into account when comparing results is the size of the galaxy count regions. This is usually determined by the field of view of the observations, but as can be seen in Tasse et al. (2008), clusters hosting different types of radio galaxy have different richnesses within narrow and wide radii, and so studies using galaxy count regions with large and small radii may be capturing different effects. This reflects the findings of Muldrew et al. (2012) of the differences between aperture and nearest-neighbour methods.

1.2.2 Intra-cluster medium

The gas of the ICM contains most of the baryonic mass of the group or cluster – Figure 1.1 (bottom) shows X-ray emission from the ICM in blue. To simplify modelling, clusters are often assumed to be spherically symmetric, with the ICM in hydrostatic equilibrium within the total mass (baryonic and dark matter) of the cluster. Balancing the gravitational force with the outward pressure gives:

$$\frac{dP}{dr} = -\frac{GM(<r)\rho(r)}{r^2} \tag{1.22}$$

where P is the gas pressure, G the gravitational constant, $M(< r)$ the mass within radius r and $\rho(r)$ is the gas density at radius r. For an ideal gas,

$$P = \frac{\rho k T}{\mu m_p} \tag{1.23}$$

where k is Boltzmann's constant, T the gas temperature, μ the mean molecular weight and m_p the proton mass. So the total mass of the cluster is related to the ICM temperature.

Assuming the ICM is isothermal, the surface brightness and density profiles of galaxy clusters can be approximated by the β model (eg Cavaliere and Fusco-Femiano 1976; Jones and Forman 1984), based on the King (1962) and King (1972) approximation for an isothermal sphere:

$$\rho(r) = \rho_0 \left(1 + \left(\frac{r}{r_c}\right)^2\right)^{-3\beta/2} \tag{1.24}$$

and

$$S(R) = S_0 \left(1 + \left(\frac{r}{r_c}\right)^2\right)^{-3\beta+0.5} \tag{1.25}$$

where $\rho(r)$ is the density at spherical radius r, $S(R)$ is the surface brightness at projected radius R as viewed in the plane of the sky, and ρ_0 and S_0 are the corresponding normalisations. β is the ratio of the specific energies of galaxies and gas within the cluster, and r_c (the core radius) is a scale length. For rich clusters, β is typically $\sim$0.7, but tends to be lower for galaxy groups (eg Mulchaey 2000). r_c for a rich cluster is generally a few hundred kpc.

The King profile is no longer considered a good description of a galaxy cluster and the assumption that the ICM is isothermal is no longer considered valid. Similarly, galaxy clusters, and more frequently groups, can show signs of irregularities (particularly when hosting radio-loud AGN, as can be seen in Figure 1.1) and so the assumption of hydrostatic equilibrium can also be incorrect. Nevertheless, if β and r_c are treated as empirical parameters rather than as physical quantities, they can be tailored to make a profile shape that fits the observation. The surface brightness profile can then be integrated to give the overall ICM X-ray luminosity within a given radius. This method works for comparatively low resolution data, but better quality profiles often show more detail and, as discussed in Section 2.2.2, may need additional parameters to fit the shape.

The ICM plasma consists mainly of ionised hydrogen, with small quantities of heavier elements. It is shock-heated as it falls into the potential well of the cluster's dark matter halo and emits in X-ray via bremsstrahlung, with some line emission from the heavier elements. The gas gains energy from the gravitational potential energy of the halo, and so the average temperature of the ICM therefore reflects the total mass of the cluster.

bremsstrahlung, or braking radiation, is emission from unbound electrons passing through the electrostatic fields of the nuclei of an ionised gas. An electron is deflected and accelerates in an ion's field, and then radiates at a frequency related to its distance from the ion and the ion's charge. As the electron passes through the gas, it is accelerated by ions at different distances and so produces a series of pulses of different strengths and frequency, resulting in white noise. The spectrum is therefore roughly flat until it reaches a cut-off frequency related to the durations of the individual pulses. The pulse duration is related to the electron energy, and consequently to the temperature of the plasma. Thus we can obtain the temperature of the ICM from its X-ray spectrum.

Temperatures for clusters typically range from about 2 keV to 9 keV (although radio galaxies are rarely housed by rich clusters – see Section 1.3) and for groups $\sim 0.5 - 2$ keV. The ICM density is low – $\sim 10^{-3}$ particles per cm^3 (eg Sarazin 1986).

For an individual electron in a hydrogen plasma, the intensity spectrum $I(\nu)$ below the cut-off is given by (Longair 2011, equation 6.39):

$$I(\nu) \propto N \frac{1}{v} ln \left(\frac{b_{max}}{b_{min}} \right) \tag{1.26}$$

where N is the ion density, v the electron velocity and b_{max} and b_{min} the maximum and minimum interaction distances.

Taking b_{min} as the position uncertainty for an electron of velocity v, we can integrate 1.26 to obtain the electron energy loss rate:

$$- \frac{dE}{dt} \propto Nv \tag{1.27}$$

so the energy loss rate is related to the square root of the electron's kinetic energy.

The ICM is a thermal plasma, so will have a Maxwell-Boltzmann distribution of electron velocities. To find the ICM energy loss rate we need to integrate Equation 1.26 over the velocity range as well as the collision parameters, and for a hydrogen plasma of temperature T this gives (Longair 2011, Section 6.5):

$$I(\nu) \propto N^2 \left(\frac{m_e}{kT}\right)^{1/2} g(\nu, T) \tag{1.28}$$

where $g(\nu, T)$ is the Gaunt factor, which has a weak dependence on frequency.

Integrating 1.28 over the frequency range then gives the energy loss rate for the ICM:

$$-\frac{dE}{dt} \propto T^{1/2} N^2 \bar{g} \tag{1.29}$$

$\bar{g}$ is the frequency averaged Gaunt factor, which lies between 1.1 and 1.5.

Thus the ICM luminosity is related to its density (and consequently its mass) and, more weakly, its temperature.

We can obtain the mass-temperature scaling relation from the virial theorem, which relates the gravitational and kinetic energies for the ICM. If R_Δ is the radius at which the cluster density is Δ times the critical density of the universe, then we can relate M_Δ, the mass within R_Δ, to the cluster temperature T by $kT \propto M_\Delta / R_\Delta$:

The density of the cluster at R_Δ is related to the square of the Hubble parameter H, and in a flat universe the redshift dependence of the Hubble parameter is given by $H = h(z)H_0$ where

$$h^2(z) = \Omega_m (1+z)^3 + \Omega_\Lambda \tag{1.30}$$

Ω_m and Ω_Λ are the mass density and dark energy density respectively.

Following Gitti et al. (2012), the density at R_Δ is then proportional to $M_\Delta / (\Delta R_\Delta^3 h^2(z))$. This gives us the $M - T$ scaling relation:

$$M \propto T^{3/2} h(z)^{-1} \tag{1.31}$$

which leads to the $L_X - T$ scaling relation relating the ICM X-ray luminosity to its temperature:

$$L_X \propto T^2 h(z) \tag{1.32}$$

Observations show a steeper $L_X - T$ relationship than theory, so there must be other processes involved. The richness of the galaxy cluster and whether or not it has a

cool-core and/or a radio galaxy are all factors which have been found to modify the $L_X - T$ relation (e.g. Helsdon and Ponman 2000; Croston et al. 2005a; Chen et al. 2007; Magliocchetti and Brüggen 2007; Pratt et al. 2009; Eckmiller et al. 2011; Stott et al. 2012; Bharadwaj et al. 2015). In addition, selection biases (in particular the Malmquist bias, which ensures that for a given temperature, the most luminous objects are preferentially selected) can have a strong effect on the slope of the $L_X - T$ relation (e.g. Eckmiller et al. 2011; Bharadwaj et al. 2015). Also, the choice of evolution parameter (the power of $h(z)$, usually assumed to be unity for the $L_X - T$ relation) is likely to be affected by the break in self-similarity in the $L_X - T$ relation (Maughan 2014).

Since the ICM temperature is related to both ICM luminosity and cluster mass, ICM luminosity can be used as a proxy for cluster mass, providing an alternative to the optical measures of cluster richness described in Section 1.2.1 above. As with the $L_X - T$ relation, the assumptions made about cluster structure and the processes that might disrupt the idealised model give considerable scatter to the relationship (eg Andreon et al. 2015). Nevertheless, the ICM contains the bulk of the baryonic mass of the system and is distributed throughout the system, and provides a better proxy for total mass than galaxy counts (eg Vikhlinin et al. 2006; Pratt et al. 2009).

1.3 Radio galaxy interactions with the environment

Figure 1.10 shows some examples of the complex interactions between radio-loud AGN and their large-scale environment. Radio galaxy jets transport energy a considerable distance into the surrounding galaxy group or cluster, and cavities carved in the ICM by the jets have been observed in clusters out to redshifts greater than 0.5 (Hlavacek-Larrondo et al. 2012). Detailed studies of local sources have shown complex substructures in the ICM (eg Karovska et al. 2002; Fabian et al. 2003) and shock fronts driven by the lobe expansion (eg Croston et al. 2009; Shelton 2011). Gas belts have been observed between the nucleus and lobe end of some systems (Worrall et al. 2007; Hardcastle et al. 2007b), dense enough to drive the lobe away from the nucleus. These may have been at least partly formed from displaced ICM gas from the lobe tip being compressed and falling in towards the nucleus (Worrall et al. 2007; Hardcastle and Krause 2013; Duffy et al. 2016), and could be helping to fuel the AGN.

So we have direct evidence that the radio jets are disturbing the ICM on a large scale, and this can be used to make estimates of the energy being put into the cluster by the AGN. I will discuss this later in Section 1.3.3. But the ICM in its turn exerts pressure on the radio jets and on the central regions of the system, so do the properties of the large-scale cluster environment in their turn affect the feedback loop maintaining the

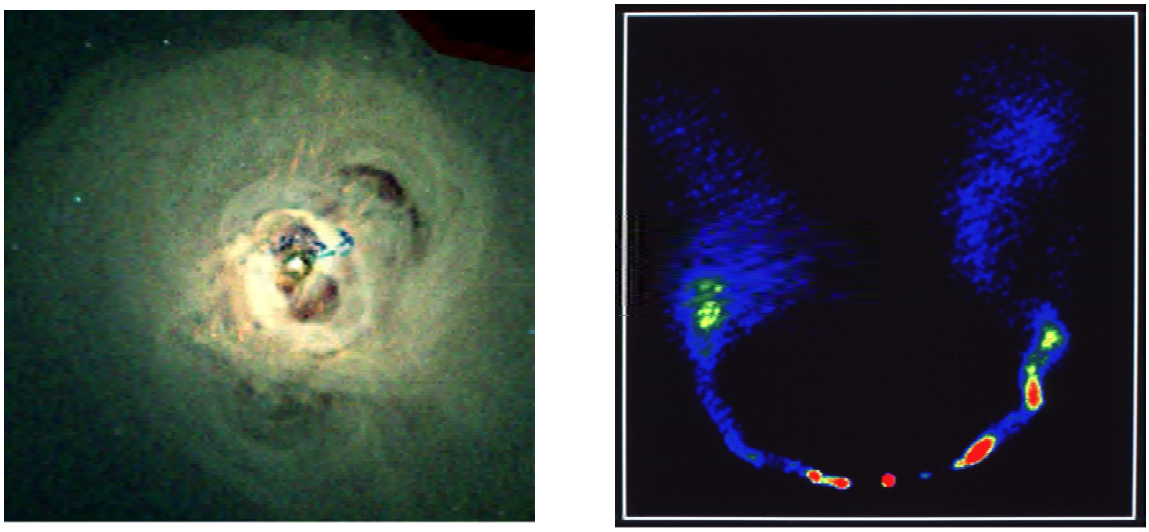

FIGURE 1.10: On the left, energy from the central AGN of the Perseus cluster being transferred to the surrounding ICM, showing lobe cavities and what are thought to be sound waves propagating though the ICM (Image courtesy of NASA/CXC/IoA/A.Fabian et al.). On the right, NGC 1265 – another inhabitant of the Perseus cluster whose jets have been bent by the ram pressure exerted by the external gas (Image courtesy of NRAO/AUI and C. O'Dea & F. Owen).

AGN, or are the AGN properties solely determined by the more local environment of the host galaxy? And how does this disruption of the cluster environment affect its evolution?

These questions have been under consideration for some time. In the following sections I review existing studies looking at the environments of radio galaxies, noting results that are generally accepted and areas that require further research.

1.3.1 The environments of radio-loud AGN

At low redshifts, it has long been known that FRI galaxies appear to inhabit richer clusters than the more luminous FRII galaxies (eg Longair and Seldner 1979; Prestage and Peacock 1988). However, Prestage & Peacock found that although there was a clear difference in average environment richness, the range of environments was large with both types of galaxy having examples at similar extremes. Hill and Lilly (1991) extended this work by comparing the low redshift results with a flux-limited sample at $z \sim 0.5$. They found that at the higher redshift range, the FRII galaxies were spread more evenly over a wider range of cluster richnesses than at low redshift, raising the possibility that the environments of FRII galaxies evolve.

Note that very few of the radio galaxies reside in rich clusters and most are in galaxy groups. In Hill and Lilly (1991)'s $z \sim 0.5$ sample the majority are below Abell richness 1 and in their low redshift sample the majority are below Abell richness 0.

More modern facilities have enabled researchers to examine the differences between the spectral types. Looking at relatively low redshift samples ($z < 0.4$), Best (2004) and Hardcastle (2004) both found that the different types of HERG (BLRGs, NLRGs and radio-loud QSOs) all inhabit poor environments, but that LERGs are spread across a broader range of environments. Furthermore, the environments of the different types of HERG were all similar, as would be expected if they were different aspects of the same class of object. Gendre et al. (2013) obtained similar results for HERGs and LERGs at $z < 0.3$, as did Ramos Almeida et al. (2013) using a wider redshift range of $0.05 < z < 0.7$.

At higher redshifts, Harvanek et al. (2001) found QSOs at $0.4 < z < 0.65$ in richer environments than at $z < 0.4$, and Belsole et al. (2007), using a sample of FRII galaxies that were mostly HERGs ($0.45 < z < 1.0$), also found them inhabiting relatively rich environments. Since HERGs are mostly FRII galaxies and LERGs are both FRI and FRIIs, these results are compatible with the results of Hill and Lilly (1991) for FRI and FRII galaxies. Ramos Almeida et al. (2013), however, comparing local FRII galaxies with the higher redshift FRIIs in their sample found no difference between their environments, so do not agree with Hill & Lilly's results.

Do these results imply that the environments of HERGs change with time, or, given the combination of the Malmquist bias and the paucity of high luminosity radio galaxies at low redshifts, does this imply that the environments of high luminosity sources are typically richer than those of low luminosity sources? Best (2004), using a sample with $z < 0.1$, found a strong correlation between radio luminosity and environment richness for LERGs, but not for HERGs. Belsole et al. (2007) found no correlation for their high-z FRII sample, but Wold et al. (2000) ($0.5 < z < 0.9$) and Falder et al. (2010) ($z \sim 1.0$) both found a correlation for high redshift, radio-loud QSOs. There is therefore some evidence that radio luminosity is related to the richness of the cluster environment for at least some classes of radio galaxy, but this does not exclude the possibility of evolution with epoch. However, Wold et al. (2000) and McLure and Dunlop (2001) both compared their samples with results from studies at different redshifts and found no evidence of a variation of environment with redshift – evidence supporting a link between environment and radio luminosity rather than epoch. So the picture of the relationship between radio-loud AGN and their large-scale cluster environments, and for the evolution of those environments, remains confused, and one of the key aims of this thesis is to clarify these issues.

1.3.2 Difficulties

Cluster richness has historically been quantified by optical methods based on galaxy numbers and density. However, as discussed in Section 1.2.2, the galaxies contain only a small proportion of the baryonic mass of the system and so, since X-ray observations became available, the luminosity of the ICM has been able to provide a better proxy for the total cluster mass.

The papers cited above use a number of different measures of cluster richness, so comparing results needs some caution. Belsole et al. (2007) used X-ray luminosity within R_{200} and in my work (Chapters 3 and 4) I used X-ray luminosity within R_{500} (R_Δ is the radius within which the mean density is Δ times the critical density at the cluster's redshift). The other studies all used optical methods – a variation on the 'nearest neighbours' method (Best 2004); galaxy counts above a specified magnitude within 1 Mpc radius (Gendre et al. 2013); and the galaxy-galaxy spatial covariance function B_{gg} calculated within a variety of radii depending on the image size (Harvanek et al. 2001; Hardcastle 2004; Wold et al. 2000 use 0.5 Mpc; McLure and Dunlop 2001 use 180 kpc; Ramos Almeida et al. 2013 use 170 kpc). The different measures of cluster richness correlate, (e.g. Wold et al. 2000; Yee and Ellingson 2003; Ledlow et al. 2003 and Sections 3.5.3 and 4.5.3 of this thesis), but with a large amount of scatter so conversion between the methods is unreliable.

The different sizes of galaxy count regions may also present a problem. Tasse et al. (2008) calculated galaxy overdensities within three different radii (75 kpc, 250 kpc and 450 kpc). Differences between 250 and 450 kpc were present but not strong, but the results for 75 kpc, which would capture interacting galaxies at the cluster centre, were strikingly different from the larger-scale radii. The HERG-dominated population in particular was very overdense compared with the background within 75 kpc, but underdense within the larger radii. Studies using galaxy count regions with large and small radii may therefore be capturing different effects.

Furthermore, if there is evolution of the environment, studies of environment richness at high and low redshift may not be directly comparable and studies covering a wide redshift range are at risk of confounding factors. In addition, the Malmquist bias in flux-limited samples, the changes in HERG and LERG populations with redshift and the paucity of powerful local sources mean that there is automatically a correlation between radio luminosity and redshift which needs to be taken into account during sample selection and data analysis. The studies cited above all agree on the differences between HERG and LERG environments at relatively low redshifts; the disagreements come when making comparisons across wider redshift ranges.

1.3.3 Lobe interactions with the ICM

At the start of this section, I briefly mentioned some observational evidence of the impact that radio lobes have on the ICM. The radio jets draw relativistic plasma out from the nucleus of a radio-loud AGN into the ICM where it forms into lobes, displacing the ICM. Estimates of the energy required to create the cavities around the lobes, and hence of energy to be dissipated into the ICM, vary with the method used (Gitti et al. 2012), but enthalpies tend to lie between 10^{55} and 10^{61} erg depending on the richness of the cluster (eg Bîrzan et al. 2004). The power in radio lobes has been estimated to be comparable to that required to offset the ICM cooling and star formation that is predicted by evolutionary models but not seen in observations (eg Dunn and Fabian 2006; Rafferty et al. 2006).

As mentioned above, shock fronts have also been seen around a few lobes, but the shocks are usually not strong (simulations, eg Heinz 2003; Gaspari et al. 2011; Perucho et al. 2014, suggest they are typically Mach 1-2) and so are difficult to observe. However, studies of nearby sources do show cavities edged with weak shocks – Sanders and Fabian (2007) have produced a detailed study of ripples propagating through the Perseus cluster. They suggest that 20–40% of the cavity power goes into sound waves which carry the energy outwards from the cavities and heat the ICM.

Detailed studies have of necessity concentrated on local sources, which are mainly low power, FRI sources. FRII sources are for the most part further away than FRIs and so are harder to study in detail, but shocks have been observed around some FRII lobes (eg Croston et al. 2011; Shelton et al. 2011) and these also must be be injecting energy into the ICM.

The formation of FRII radio lobes depends on the properties of the ICM. Scheuer (1974) discusses possible models for powerful radio sources; these models give different morphologies depending on the assumptions made about the relative pressures of the lobes and the external medium and the distribution of the external medium. He concludes that the model which fits the observed radio galaxy structures best (model C) consists of lobes near pressure balance with the ICM. The lobes form at the end of the jet as it moves outwards, leaving behind it a shell of expanding gas bounded by a weak shock. The lobe tip advance is supersonic, but because the energy density within the lobes is comparable with that of the ICM, the lateral lobe expansion is subsonic and the pressure within the lobe is uniform. Since the ICM pressure is greater near the nucleus, the lobes are under-pressured there and so are compressed by the ICM. This forces the lobes to expand nearer the tips, and gives the typical FRII lobe shape that we observe. Scheuer's

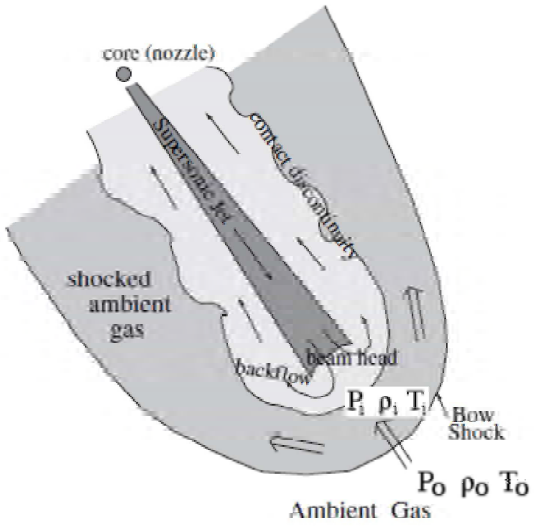

FIGURE 1.11: The bow shock around the lobe of a powerful radio source, taken from Worrall and Birkinshaw (2006).

alternative models, which assume the lobes are overpressured with respect to the environment, result in a uniform, elliptical or cylindrical lobe expanding supersonically. In these models, the bulk of the energy emission is focussed on the lobe tip rather than spread throughout the lobe, resulting in a single large lobe enclosing the source. Simulations of lobe evolution using assumptions compatible with Scheuer (1974)'s model C (eg Zanni et al. 2005; Hardcastle and Krause 2013; Perucho et al. 2014) found that the lobes develop morphologies, X-ray surface brightnesses and temperatures similar to those observed and that the shocks, although mild, are an important mechanism for transferring energy into the ICM.

The conditions on each side of a shock can be described by the Rankine-Huginiot conditions, which invoke the conservation of mass, momentum and energy across the discontinuity. Figure 1.11 shows a lobe surrounded by a shock, with the pressure P, density ρ and temperature T inside and outside the lobe denoted by the suffixes i and o.

Applying the conservation laws gives the Rankine-Huginiot conditions:

$$[\rho v]_i^o = \left[P + \rho v^2\right]_i^o = \left[\frac{v^2}{2} + \frac{\Gamma P}{(\Gamma - 1)\rho}\right]_i^o \tag{1.33}$$

where v is the velocity of the gas and Γ is the adiabatic index (5/3 for a monatomic gas).

Assuming Γ is the same before and after the shock, and using the equation for the speed of sound in an ideal gas ($a = \sqrt{\Gamma P/\rho}$), these can be rearranged to give the Mach number

of the shocked gas $\mathscr{M} = v/a$ in terms of the pressures in the shocked and unshocked gas:

$$\mathscr{M}^2 = \frac{1}{2\Gamma}\left((\Gamma+1)\frac{P_i}{P_o} - (1-\Gamma)\right) \tag{1.34}$$

This equation relates the pressure ratio between shocked and unshocked gas at the shock front to the Mach number.

Throughout this section, I have made two major assumptions, that the high energy particle content of the lobes is dominated by electrons and that the filling factor – the fraction of the lobe filled by synchrotron-emitting electrons – is unity. I discuss these assumptions briefly in the following two sections.

1.3.3.1 Particle content

Although the calculations of lobe emission and pressure assume that the lobes are predominantly filled with relativistic leptons, there is no direct way of determining the particle content. Some indication of particle content can however be inferred by looking at how well the calculated lobe fields and pressures relate to the external conditions.

IC X-ray emission has not been detected from FRI lobes and so their lobe pressures are generally calculated assuming equipartition. These pressures have generally been found to be less than that of the surrounding ICM (eg Hardcastle et al. 1998b; Worrall and Birkinshaw 2000; Dunn et al. 2005) which, since the lobes are long-lived, indicates the presence of a population of non-radiating particles to boost the pressure. Croston et al. (2008a) looked at the morphologies of different FRI galaxies and found that those where the jets were in direct contact with the ICM showed a larger pressure deficit, suggesting that the additional particles are likely to come from entrainment of material from the ICM. Bîrzan et al. (2008), comparing equipartition and ICM pressure, also found entrainment the most likely cause of the difference, with older systems having higher proportions of entrained material. Detailed studies of local sources (eg Hardcastle and Croston 2010; Croston and Hardcastle 2014) use upper limits on the lobe IC emission to place limits on the population of relativistic leptons. This is insufficient to provide the required lobe pressures, and so there must also be a significant population of baryons. Measurements of external and internal conditions along the jet show that these are most likely to come from entrainment.

FRII lobes also appear underpressured with respect to the environment when the pressure is estimated assuming equipartition (Hardcastle and Worrall 2000). Unlike FRI

lobes, however, many FRII lobes show X-ray emission indicative of IC emission and when this is taken into account FRII lobes tend to be close to pressure balance with their environment (eg Hardcastle et al. 2002a; Croston et al. 2004; Kataoka and Stawarz 2005; Croston et al. 2005b; Belsole et al. 2007). This suggests that the lobes are likely to be predominantly populated by relativistic electrons; there may still be some lower energy baryons present but they can only account for a small amount of the energy budget (eg Hardcastle and Croston 2010).

1.3.3.2 Filling factor

The filling factor is the fraction of the lobe that contains synchrotron-emitting particles. As discussed in Hardcastle and Worrall (2000), the effects of a lower filling factor depend on the content of the fluid interspersed with the synchrotron-emitting particles. If it contains low energy, non-radiating particles, the lobe internal pressure will be higher than calculated from the IC emission.

The effect of the uncertainty in the filling factor is discussed in Section 5.4.5.

1.4 Thesis aims

In this thesis I make a systematic examination of the relationship between radio galaxies and their large-scale environments. I use the ICM X-ray luminosity as a measure of cluster richness (see Section 1.2.2 above) and look at how it is related to low frequency radio luminosity. New X-ray observations made for this project allow me to generate representative samples in two narrow redshift ranges, allowing me to disentangle relationships due to environment and evolution. I also make use of the X-ray observations to calculate the internal pressures of the FRII radio lobes via combined inverse Compton and synchrotron modelling, enabling the first investigation of the relationships between lobes and their environments for a large sample.

In the next chapter, I describe the instruments used to collect the X-ray observations used for this work, and the data processing and analysis required to derive the ICM temperatures, luminosities and pressures, and the internal lobe fields and pressures. In Chapters 3 and 4 I use samples at redshifts ~ 0.5 and ~ 0.1 respectively to look for relationships between radio and ICM luminosity, looking also for differences between the different types of radio galaxy, and I compare the results at the two redshifts to look for evidence of evolution.

I compare my results with typical ICM properties of clusters which do not contain a radio galaxy, to see if there is any evidence of a systematic difference in the cluster properties, and also compare the ICM luminosities with other measures of cluster richness, to see if there is a useable relationship for combining results.

In Chapter 5 I look at the internal properties of the FRII lobes in the samples and how they relate to equipartition and their external environment. I look at the impact that the FRII lobes have on their environment, comparing the Mach numbers at the lobe tips with the radio and ICM properties. Then in Chapter 6 I look briefly at how the central properties of the AGN relate to their large-scale environment to see if the central properties could be a factor in the relationships found in the previous chapters.

Finally, in Chapter 7 I summarise my findings and discuss which aspects of the work require further exploration.

Throughout this thesis I use a cosmology in which $H_0 = 70$ km s^{-1} Mpc^{-1}, $\Omega_{\rm m} = 0.3$ and $\Omega_\Lambda = 0.7$. Unless otherwise stated, errors are quoted at the 1σ level.

Chapter 2

Instrumental details and data analysis

The aim of my work was to look for relationships between the properties of radio-loud AGN and the galaxy clusters that house them, using the X-ray luminosity of the ICM as a proxy for the total mass of the galaxy cluster. I therefore used X-ray observations of the galaxy clusters to extract and analyse spectra, measure the flux of the ICM and the radio lobes, and create surface brightness profiles of the ICM in order to obtain the ICM luminosity and estimates of the IC emission from the radio galaxy lobes.

For the radio emission, I used existing radio maps and published radio fluxes and luminosities from a variety of sources.

In this section I give a brief description of the instruments used to make the observations for my work and the data processing and analysis methods used to produce the results.

2.1 Instrumental details

2.1.1 X-ray telescopes

I used X-ray observations from two X-ray observatories – *Chandra* and *XMM-Newton*, both launched in 1999. The cameras provide images across similar energy ranges, but differ in field of view, spatial and energy resolution and PSF (point spread function) size.

2.1.1.1 Chandra

The *Chandra* X-Ray Observatory[1] has two focal plane instruments - ACIS (Advanced CCD Imaging Spectrometer) and HRC (High Resolution Camera), together with High and Low Energy Transmission Grating spectrometers (HETG and LETG) which can be used with the cameras. My observations used ACIS, which has better energy resolution than the HRC.

ACIS consists of 8 CCDs operating within 0.2–10 keV, arranged as shown in Figure 2.1 (left). The pixel size is 0.492 arcsec, giving a field of view of 8.3x8.3 arcmin per CCD. The mirror assembly PSF is similar to the pixel size (FWHM), but is dithered over 16 arcsec in a Lissajous pattern. This allows the system to smooth out differences in pixel quantum efficiencies, cover bad pixels and provide some coverage in the chip gaps. The effects of dither are removed in the post-processing. Figure 2.2 shows the simulated on-axis PSF on the ACIS-I detector.

The standard frame time for the ACIS CCDs is 3.2 s; this mode allows readout of the full chip areas and both spatial dimensions. In this mode there is a choice of three telemetry formats: these are GRADED, FAINT and VFAINT in order of reducing saturation limit. The extended emission for my sources is mostly faint and so the observations were taken in FAINT and VFAINT mode as appropriate.

Chips I0-I3 (ACIS-I) are arranged in a square to give a wide field of view; these are all front-illuminated CCDs with a maximum energy resolution of 130 eV at 1.49 keV. Chips S0-S5 are arranged in a strip, giving a long, narrow field. S1 and S3 are back-illuminated CCDs, more sensitive than the front-illuminated chips at lower energies and with a maximum energy resolution of 95 eV at 1.49 keV. The S3 chip is used as the aim point for sources with emission limited to a small visual field and the I3 chip for emission covering a wider field.

2.1.1.2 XMM-Newton

The *XMM-Newton* observatory[2] houses three telescopes, each with its own European Photon Imaging Camera (EPIC). These are shown in Figure 2.1 (right). The telescopes each have a 30 arcmin field of view and operate over 0.15–12.0 keV. The frame time for all cameras is 2.6 s. There is a choice of three filters for minimising optical light contamination – thick, medium and thin — depending on the optical properties of the

[1] `http://cxc.harvard.edu/`
[2] `http://xmm.esac.esa.int/`

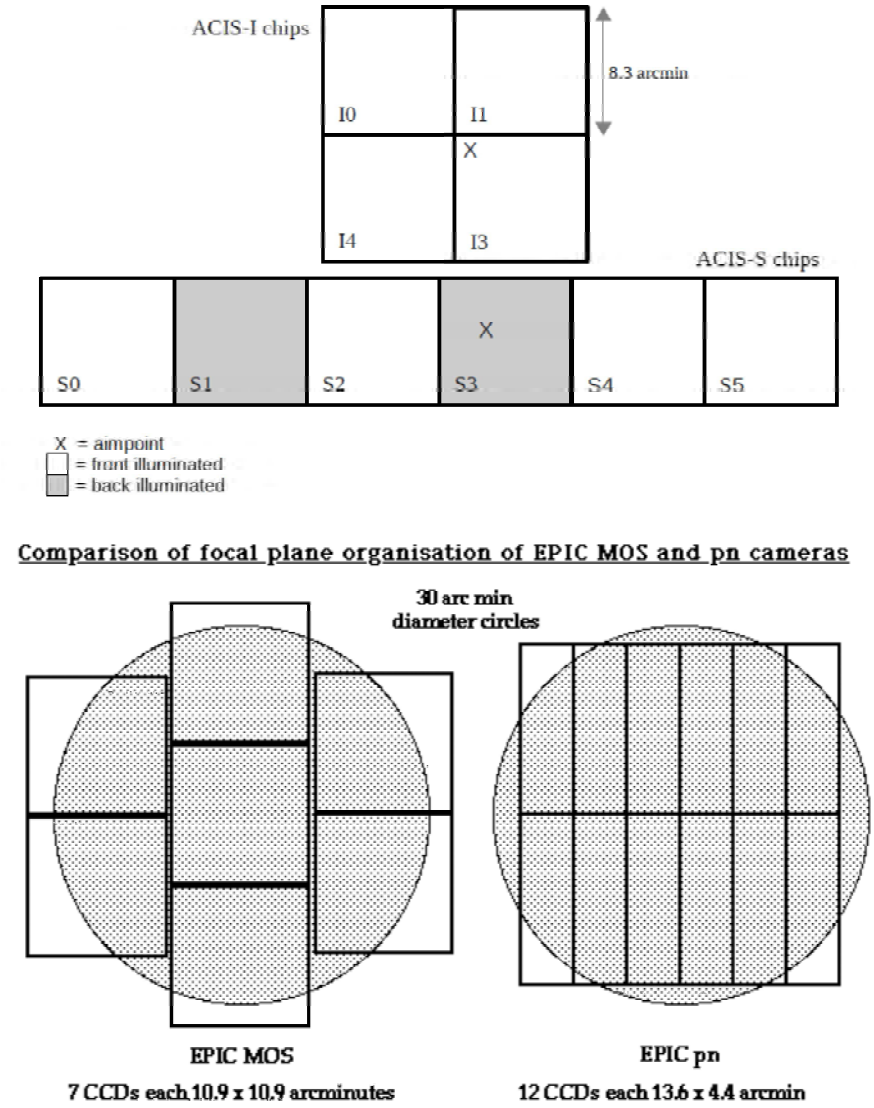

FIGURE 2.1: The *Chandra* ACIS (top) and *XMM-Newton* EPIC (bottom) X-ray detectors.

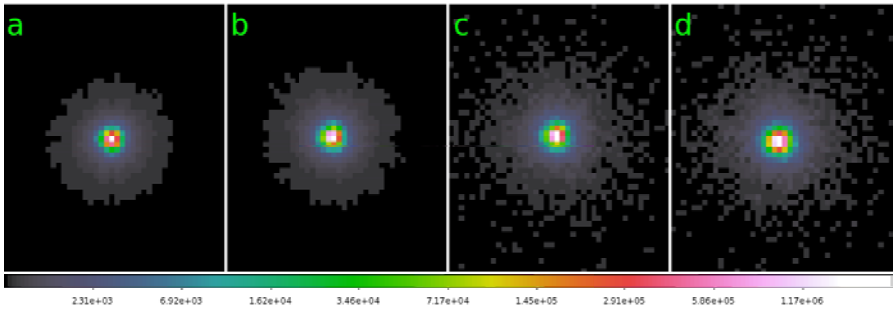

FIGURE 2.2: The simulated *Chandra* on-axis ACIS-I PSF, taken from `http://cxc.harvard.edu/ciao/PSFs/psf_central.htmlFigure1`. (a)The mirror assembly PSF. (b) The same PSF as detected by a perfect ACIS-I detector. (c) The ACIS-I PSF smeared and modified by detector effects. (d) The ACIS-I PSF with detector effects and spacecraft dithering. The pixel sizes are those of ACIS-I.

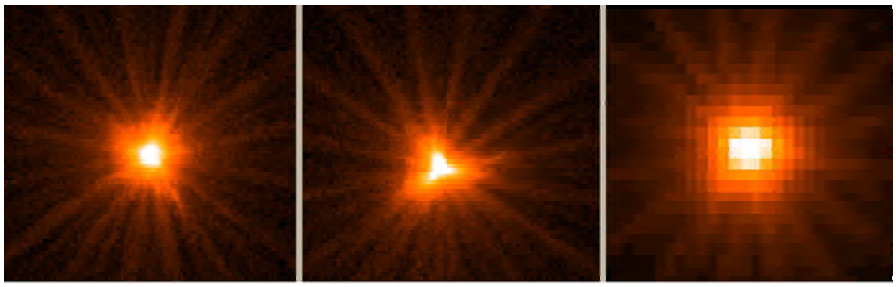

FIGURE 2.3: The *EPIC* on-axis PSFs for the MOS1 (left), MOS2 (centre) and pn (right) telescopes, taken from `https://heasarc.gsfc.nasa.gov/docs/xmm/uhb/Figure4`. The core is piled-up to show the PSF shape. The images are 100 arcsec wide, and with a square root scale to bring out the PSF wings. The star pattern comes from the mirror supports.

field and its surroundings and the optical brightness of the source. Medium or thin filters were used for my observations.

Two of the EPIC cameras are MOS cameras, each consisting of an array of seven 600x600 pixel chips. The pixel size is about 1.1 arcsec, the energy resolution is ∼70 eV and the on-axis PSF is 5 arcsec (FWHM) – see Figure 2.3.

The third telescope uses the EPIC-pn camera which has twelve 64x189 pixel CCDs with a pixel size of 4.1 arcsec. The energy resolution is ∼80 eV and the on-axis PSF (Figure 2.3) is 6 arcsec (FWHM). The pn camera is back-illuminated and has a quantum efficiency above ∼ 0.9 across about 0.4 to 9 keV; the MOS cameras are front-illuminated and less sensitive overall – the quantum efficiency peaks at ∼ 0.9 at 3 to 4 keV.

Two chips on the MOS1 camera have been damaged by what is thought to have been micro-meteoroid impacts – chip 6 in 2005 and chip 3 in 2012 (the top and bottom chips in Figure 2.1) – and these chips have been switched off. Most of my *XMM-Newton* observations were taken between the two events and so are missing one chip in the MOS1 camera. However, these observations are all of distant objects so the bulk of the cluster emission is on the central chip, and the emission is roughly symmetrical so the adjacent chips will give a good representation of the emission on the missing chip. Also the pn and MOS2 cameras are both still fully operational so the damage is unlikely to have had any impact on my results.

2.1.1.3 Telescope compatibility

There has for some time been discussion about an apparent difference between temperatures obtained from *Chandra* and *XMM-Newton* observations. Schmidt et al. (2001) and Majerowicz et al. (2002) obtained different temperature profiles for galaxy cluster

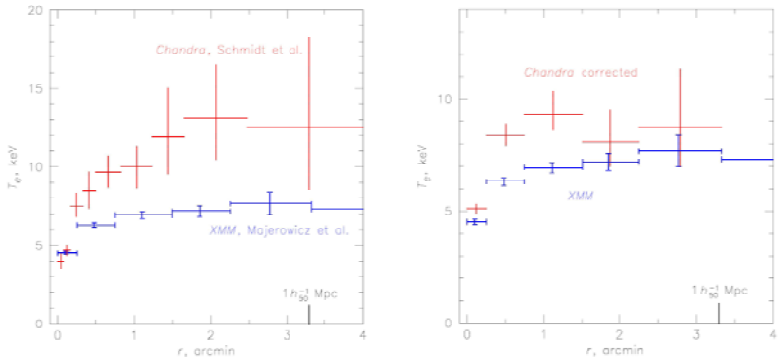

FIGURE 2.4: Temperature profiles of galaxy cluster A1835. On the left, the profiles from Schmidt et al. (2001) (*Chandra*) and Majerowicz et al. (2002) (*XMM-Newton*). On the right, the profile from the *Chandra* observation with improved background cleaning. Images taken from Markevitch (2002).

A1835 using *Chandra* and *XMM-Newton* observations respectively (Figure 2.4). Markevitch (2002), using meticulous background cleaning for the *Chandra* observation and modelling of the *XMM-Newton* PSF, reduced the maximum temperature difference from ~ 6 keV to less than 2 keV; nevertheless a small difference remained.

The International Astronomical Consortium for High Energy Calibration (IACHEC) has published a number of studies comparing properties of the different X-ray detectors [3]. For example, Nevalainen et al. (2010), comparing results for a small sample of nearby, relaxed galaxy clusters, reported uncertainties in the normalisations of the effective areas of the *Chandra* and *XMM-Newton* telescopes leading to differences in flux measurements in the higher energy bands and temperatures in the lower energy bands.

Schellenberger et al. (2015) made a systematic study of the temperatures of a much larger sample of galaxy clusters, comparing *Chandra* ACIS and the three *XMM-Newton* EPIC detectors. They found consistent differences increasing with temperature between the ACIS, EPIC-MOS and EPIC-pn detectors with ACIS giving the highest temperatures and EPIC-pn the lowest. The differences increase with temperature, with little if any difference below 2 keV.

This study was published after my work on ICM temperatures was complete, but I checked to see if the instrument differences would affect my results. The majority of my sources were observed with *Chandra* and only three of the *XMM-Newton* observations gave ICM temperatures greater than 2 keV. The highest is $3.10^{+2.95}_{-1.00}$ keV; the 1-σ errors are much larger than the differences between the instruments at that temperature and none of the three sources are outliers in the luminosity-temperature relation. I therefore concluded that the differences between the instruments would not affect my results.

[3] `http://web.mit.edu/iachec/papers/index.html`

FIGURE 2.5: The VLA radio interferometer. Image from http://www.aoc.nrao.edu/.

2.1.2 Radio telescopes

I used radio maps to define the shapes of the radio lobes – I used existing radio maps and so did not reduce radio data myself. The maps were used to exclude X-ray emission from the radio lobes during spatial and spectral analysis of the ICM, measure the radio and X-ray flux emitted from the lobes and calculate the internal lobe pressures.

The radio observations for my work came from a variety of telescopes, and these are credited in Tables 3.2 and 4.2. The Very Large Array (VLA) in New Mexico, for example, was used for many of the 2Jy observations. The VLA (Figure 2.5) is an interferometer with 27 radio antennae, each of which uses a 25 m diameter dish. Each antenna has eight receivers covering frequency bands from 1 to 50 GHz. There are also low frequency receivers for 230-470 MHz and 54-86 MHz, but these are not recorded from all the antennae. The antennae are arranged in a Y-shape, but can be moved along the axes to alter their separations and are used in four main configurations. The A array has the largest antenna separations ($\sim$1-36 km), giving the smallest beam width (1.3 arcsec at 1.5 GHz) but also the lowest Large Angular Scale (LAS) limit (36 arcsec at 1.5 GHz). The D array has the smallest separations ($\sim$0.04-1 km), the largest beam width (46 arcsec at 1.5 GHz) and the largest LAS (97 arcsec at 1.5 GHz).

Most of my 3CRR observations were at $\sim$1.5 GHz, so where possible, I used observations at this frequency for the other sources. However, the observing frequencies ranged from 610 MHz to 8.5 GHz and the resolutions from about 1 to 50 arcsec so there are two areas of concern. When defining the lobe areas using high resolution maps with a low LAS, I could miss regions of diffuse flux, but when using low resolution maps I could overestimate the size of the lobe.

I also needed to exclude emission originating from the nucleus and hot-spots from the lobe regions. Where possible I used higher frequency maps for this since the hot-spot

emission dominates over the lobe emission at higher frequencies and also the resolution is better at higher frequencies thus enabling more accurate regions to be defined.

2.2 Data analysis

As discussed in Section 1.4, the aims of the analysis were to find the properties of the ICM emission in the galaxy clusters hosting the radio galaxies and the internal pressures of the FRII galaxy lobes. In this section I describe the initial data preparation for the X-ray observations (Section 2.2.1), the spatial analysis that was used to find the ICM luminosity, density and pressure (Section 2.2.2) and the spectral analysis used to find the ICM temperature and the lobe X-ray flux (Section 2.2.3).

2.2.1 Data preparation for the X-ray observations

2.2.1.1 Calibrations

A number of corrections need to be applied before the observations can be used, as described in the telescope handbooks[4,5]. The quantum efficiency of the pixels varies across the chip and with operating temperature, and may reduce with time – for example ACIS has developed a build-up of contaminants on the optical filters. Observations therefore need to be reprocessed using the correct calibration data for the observation date and filter. Corrections also need to be applied for vignetting, aspect, chip edges and gaps.

For the *Chandra* observations, I used the analysis package CIAO. I reprocessed the files using the CHANDRA_REPRO script, using the particle background cleaning facility for observations taken in the VFAINT mode. The sources at $z \sim 0.5$ only occupied a small area of the ACIS S3 chip and so did not need further correction, but the nearer sources had a larger angular visual angle, in some cases extending beyond the observing chip. For these sources, I created exposure maps using the FLUXIMAGE script to allow me to correct for vignetting, aspect, chip edges and gaps.

I used the SAS package to process the *XMM-Newton* data. The observations are broken into a series of separate exposures which need to be linked into a single data file per camera. The tasks CIFBUILD and ODFINGEST find the calibration and other instrumental housekeeping data relevant to the observation, and the data files are then linked using EMCHAIN for the MOS cameras and EPCHAIN for the pn camera. These give a single,

[4] `http://cxc.harvard.edu/proposer/POG/html/`
[5] `http://xmm.esac.esa.int/external/xmm_user_support/documentation/uhb_2.1/XMM_UHB.html`

calibrated data file per camera (filtered to remove bad pixels, bad columns etc) containing a list of events and associated quality data. These quality data flag multiple events in the same region – multiple events are likely to be due to particle background or flares. When the pre-processing was complete, I used EVIGWEIGHT to correct the events files for vignetting.

2.2.1.2 Particle background and flares

High energy cosmic rays interact with the telescope and detector, resulting in a fairly consistent level of particle background which needs to be removed using observations made with the cameras stowed. Charged particles can also be channelled down the telescope onto the detector causing intermittent flares which also need to be removed from the observations (Baganoff 1999; Read and Ponman 2003; Markevitch et al. 2003).

The particle background is removed using background files generated with closed filters (*XMM-Newton*) or blank sky files which are observations with the point and extended sources removed (*Chandra*). Particle background removal for *XMM-Newton* observations is a standard method described in detail in Croston et al. (2008a). The background observations are rotated to match the source observations and scaling factors are calculated by comparing the count rates of the source and background files at energies greater than those emitted by the source – 12–14 keV for the EPIC-pn camera and 10–12 keV for the EPIC-MOS cameras and ACIS chips. The closed filter data are then scaled by these factors before carrying out background subtraction when generating profiles and spectra.

I built the background files from the *Chandra* blank sky datasets for each observation using the method described in the CIAO threads[6]. I used ACIS_BKGRND_LOOKUP to list the appropriate background files for each chip in the corresponding source file. Then, having collected the files, I used DMMERGE to build them into single file and REPROJECT_EVENTS to rotate the background file to match the source observation. These files include galactic and extragalactic X-ray background as well as the particle background (see Section 2.2.1.4 below).

The particle background in the *XMM-Newton* sources was removed using closed filter files (supplied courtesy of E. Pointecouteau) that were processed, filtered and weighted in the same manner as the source data sets. Their coordinates were then transformed to match the source files using ATTCALC. These files contain particle background only.

[6] `http://cxc.harvard.edu/ciao/threads/acisbackground/`

I checked each events file for flares using the light curves at 10–12 keV for the ACIS and EPIC-MOS cameras and 12–14 keV for the EPIC-pn camera. For the *Chandra* observations, I extracted a light curve using DMEXTRACT and used CHIPS to look for periods where the count rate was more than 3σ above the mean. I then removed these using DEFLARE.

For the *XMM-Newton* observations, I looked at the count rate histogram using XMMSELECT to identify the quiescent background rate and used TABGTIGEN to create a good-time-interval (GTI) filter to select data where the light curve was within 20% of the quiescent level. I then used EVSELECT to filter the data. The pn camera data were also filtered to include only single and double events (PATTERN ≤ 4) and data from the MOS cameras were filtered using the standard pattern mask (PATTERN ≤ 12), which allows up to quadruple events.

In addition, the *XMM-Newton* instrument housings give rise to a number of fluorescence lines (Strüder et al. 2001). The 1.5 keV Al Kα line was visible in some of my observations. I therefore excluded the 1.4-1.6 keV energy band from all my *XMM-Newton* analysis.

2.2.1.3 Pile-up

Once the basic calibrations and corrections have been done, the observations need to be checked for pile-up, where multiple photons from a bright source are recorded together as a single photon of higher energy. This results in a distorted energy spectrum and an underestimated count rate. In my observations, since the sources are mostly faint, pile-up only occurred in a few $z \sim 0.1$ *Chandra* sources. I checked for pile-up by finding the maximum count rate per pixel at the peak of the emission, which I scaled to estimate %pile-up (Davis 2001, 2007). If pile-up was greater than 12%, I checked the maximum count rate per pixel at increasing radii until pile-up was less than 12%. I then excluded the central region out to this radius.

2.2.1.4 External X-ray background

Finally, the cosmic and Galactic X-ray backgrounds need to be excluded from the observations (Snowden et al. 1997; Markevitch et al. 2003). This varies with both direction and time. There are three potential components to the X-ray background, depending on pointing direction. The extragalactic X-ray background is thought to be due to distant AGN, which emit X-rays with a power law spectrum – I fixed this at 1.41 when modelling the background (Lumb et al. 2002). The local X-ray background is thermal

in origin and comes from the Milky Way (~ 0.25 keV) and/or the local bubble (~ 0.75 keV).

Background exclusion is best done by selecting an area representative of background close to the source – for the galaxy clusters I used an annulus surrounding the source just beyond its maximum detected radius. This annulus should then contain a similar X-ray background to the source. In addition, the *Chandra* blank sky files contain an X-ray background approximating to that of the area under observation. This can be used to make an initial correction to both the source and background regions, and is the only way of removing the background from sources extending beyond the observing chip. However, since the background varies with time, the blank sky files should where possible be used as a supplement to the usual background modelling rather than a replacement for it.

2.2.1.5 Removal of extraneous emission

For both the *Chandra* and *XMM-Newton* sources, I examined images of the sources using DS9, overlaying them with the radio contours. I identified point sources in the data sets and emission associated with nearby clusters which I excluded during subsequent analysis – I used RASS (ROSAT X-Ray All-Sky Survey) images to check for clusters that were centred outside the field of view of my observations. I also removed emission associated with the radio lobes when determining the ICM properties.

2.2.2 Spatial analysis

I obtained the ICM luminosity, density and pressure from the surface brightness profile, which I fitted with a β model (Section 1.2.2).

I extracted the radial surface brightness profile from the events file of each source by taking the average counts in annuli around the source centroid, extending to the maxiumum detected radius of the source. I used an outer annulus beyond the maximum detected radius as background.

I corrected for particle background, external X-ray background, vignetting etc. by subtracting from each annulus the relevant number of counts, scaled to match the source exposure time and the annulus area. For the *XMM-Newton* sources, the particle background counts came from the *XMM-Newton* closed filter files. For the *Chandra* sources of large angular extent, I used the *Chandra* blank sky files and exposure map. The X-ray background was then removed by subtracting the scaled counts from the outer annulus. Extraneous emission identified during data preparation was also removed and

the annulus areas adjusted to account for the excluded regions. I used an energy range of 0.4–7.0 keV, this being within the well calibrated range for the *Chandra* data. For the *XMM-Newton* sources, since the pn camera is more sensitive than the MOS cameras I created the pn profile first and then used the same annuli and background area for the MOS profiles. The three profiles were then scaled by their relative exposure times and added together. I used the FUNPROFILE software (written by M. Hardcastle and J. Croston) to build the profiles. I chose annulus radii such that each annulus contained at least 20 counts.

In addition to the ICM emission, the surface brightness profile also contained contributions from the nucleus (within the PSF) and, in the case of the nearer sources, the host galaxy.

Once I had extracted the surface brightness profiles, I fitted them with β models (Section 1.2.2), using the Markov-Chain Monte Carlo (MCMC) method described by Croston et al. (2008a) to explore the parameter space of these models and thus find Bayesian estimates of the core radii (r_c) and β values. This MCMC method uses the Metropolis-Hastings algorithm in a manner similar to the METRO code by Hobson and Baldwin (2004), but implemented to run on a cluster of multiple processors (Mullin and Hardcastle 2009).

The method I use here differs from the implementation of this method used by Croston et al. (2008a), in that I use a new fitting engine which allows the normalisations of the β model and point-source components to vary freely during the fits. Plausible ranges for the free parameters were estimated and used to define uniform (uninformative) priors for the MCMC method. For the normalisations and core radii, priors uniform in log space were used to avoid bias towards large values. The uncertainties corresponding to 1σ errors for 2 interesting parameters were determined using 1-dimensional projections of the minimal n-dimensional volume that encloses 68% of the posterior probability distribution as returned by the MCMC code. This code was also used to determine the luminosities as discussed below.

I initially used the appropriate instrument PSF alone to check whether this gave a satisfactory fit to the data. The *XMM-Newton* calibration files contain King profile model parameters for the PSF shapes of the three detectors as a function of energy and off-axis angle, although since all my observations were on-axis the corrections for off-axis distortions were not needed. These profiles were then weighted by the counts in the source profiles from the three detectors and combined to produce a singe, normalised PSF weighted by the energy distribution of the source. A similar process was used for the *Chandra* PSF, but in this case the PSF shape was provided by Prof. Worrall.

I then added a single β model to fit the extended emission from the ICM, convolved with the PSF. If, as was often the case with the $z \sim 0.1$ sources, the host galaxy was visible beyond the PSF I added a second β model as described in Croston et al. (2008a), so that I could describe the galaxy and cluster contributions separately and exclude the galaxy luminosity. In this model, the line-of-sight sum of the gas densities in the two components is given by

$$n(r) = n_0 \Big[\Big(1 + (\frac{r}{r_{c,in}})^2\Big)^{-3\beta_{in}/2} + N\Big(1 + (\frac{r}{r_c})^2\Big)^{-3\beta/2} \Big] \tag{2.1}$$

where N is the relative normalisation of the two beta models and the subscript in refers to the inner (galaxy) model.

The surface brightness profile, which is calculated numerically by the modelling code, is then

$$S(R) \propto \int_{-\infty}^{\infty} n^2(l, R) dl \tag{2.2}$$

where R is the distance in the plane of the sky, l is the cluster depth along the line of sight and the shperical radius $r = \sqrt{l^2 + R^2}$.

Since I was assuming the clusters and groups to be at least approximately relaxed, I limited β for the outer (ICM) model to the range 0.3 to 1.2 and r_c to a minimum of 1 kpc. I allowed more freedom in the parameters for the inner model, which describes the host galaxy, since the galaxy is ellipsoidal rather than spherical and could be at any orientation to the line of sight.

If there was no extended emission visible, or if the modelled emission did not extend beyond the host galaxy radius (taken from NED[7]), I used the observations of the source to derive an upper limit on cluster-scale emission. For these sources, I compared the net count rate from a region outside the host galaxy with a more distant background region. If the net counts were greater than three times the background error, I considered this to be a detection; otherwise I used three times the background error as the net counts for the upper limit.

Figure 2.6 contains examples of surface brightness profiles for distant and nearby *Chandra* and *XMM-Newton* sources, showing the contributions of the PSF, the host galaxy (for the nearby sources) and the ICM. They also show the difference in the size of the PSF of the two instruments.

Luminosity within the required radius was calculated by integrating the ICM β model profile using counts to flux conversion factors generated from the *apec* model. This was

[7] http://ned.ipac.caltech.edu/

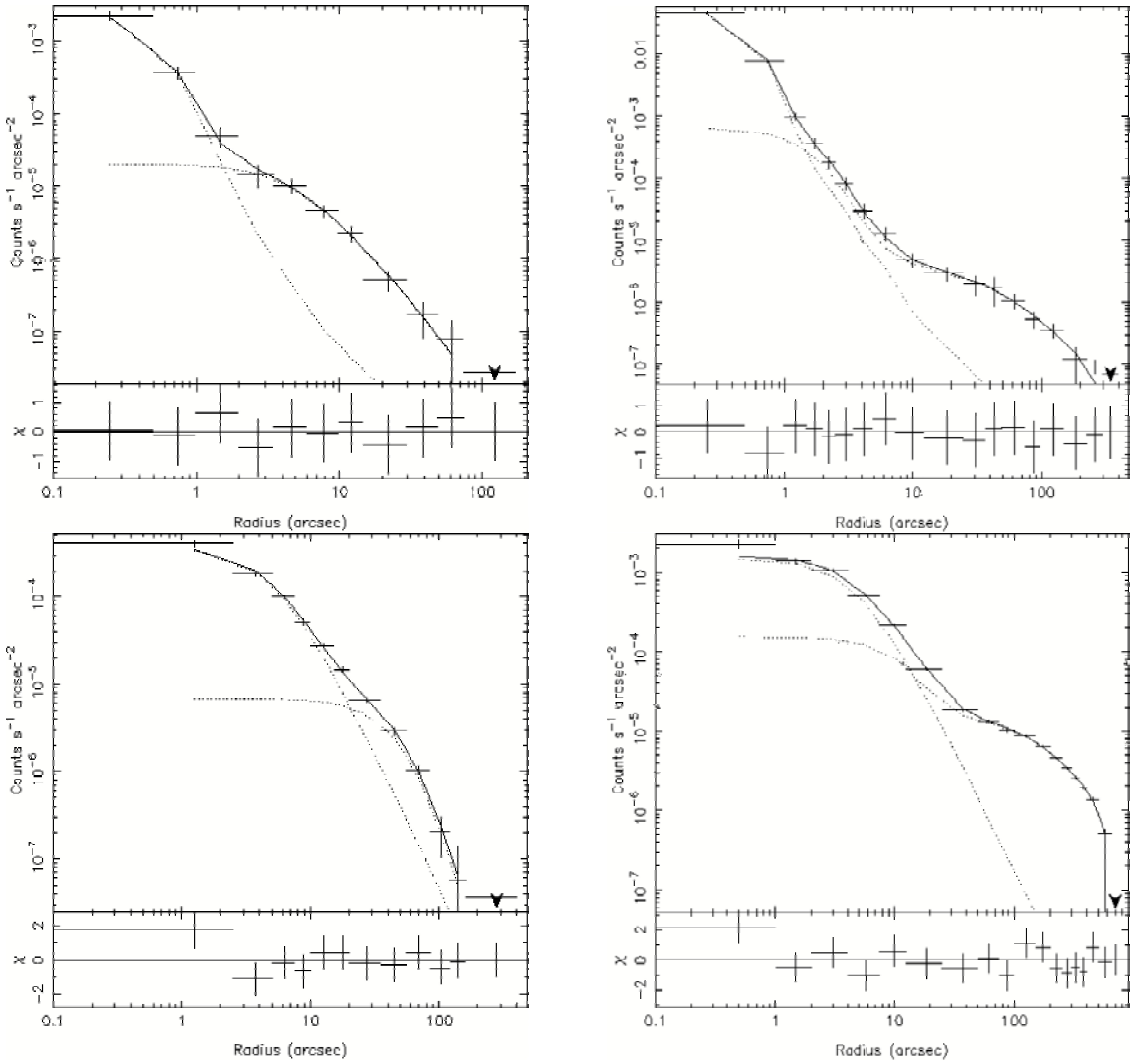

FIGURE 2.6: Examples of surface brightness profiles for *Chandra* sources (top) and *XMM-Newton* sources (bottom). 3C 330 (top left) is at redshift 0.55 and is modelled with a single beta model and the PSF. PKS 2356−61 (top right) is at redshift 0.1 and uses a double beta model and PSF. 6C 1200+3416 (bottom left) is at redshift 0.53 and is modelled with a single beta model and the PSF. 3C 66B (bottom right) is at redshift 0.02 and uses a double beta model and PSF.

done by calculating a luminosity for each sample of the output of the MCMC code, which provided a posterior probability distribution function over luminosity, marginalized over all other parameters. I used the median rather than the mean of the posterior probability distribution function as my luminosity estimate because the distributions were skewed for the fainter sources. My quoted uncertainties on the luminosity are credible intervals defined on this one-dimensional posterior probability distribution function such that 68 per cent of the probability is contained in the smallest luminosity range. The luminosity uncertainties take into account the (in some cases large) uncertainties on β and r_c.

Figure 2.7 shows the MCMC code output for the β model of a rich cluster environment.

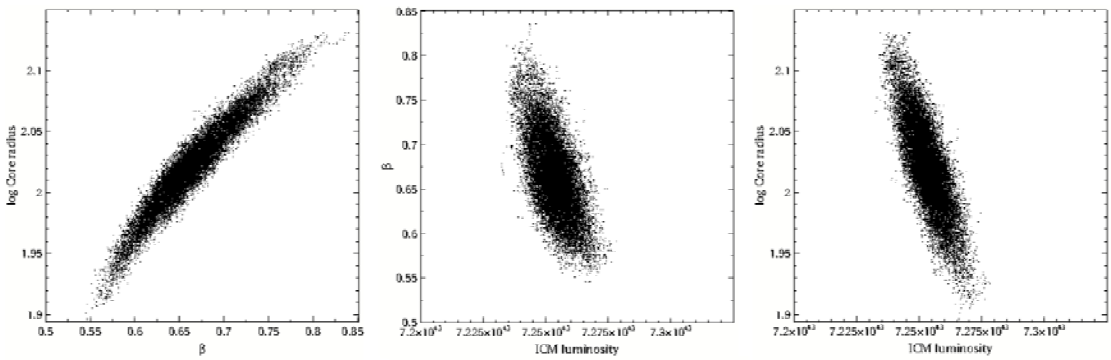

FIGURE 2.7: The relationships between β, core radius r_c and ICM luminosity for 3C 28, a source with a rich environment analysed in Chapter 4. On the left, β and r_c show a clear correlation. Centre and left, β and r_c are compared with the ICM luminosity, and any correlation is marginal.

The model parameters, β and the core radius r_c (Equation 1.25), are strongly related, but there is no such strong relationship between the cluster luminosity and either of the model parameters. This supports the assumption that, provided that β and r_c are chosen so that the β model fits the cluster surface brightness profile, the actual values of β and r_c do not have any great effect on the luminosity calculations.

To calculate the electron number density at radius r, I used the method described in Birkinshaw and Worrall (1993). The distance-normalised volume emission measure of the atmosphere per unit solid angle, $\mathscr{A}$, is:

$$\mathscr{A} = \frac{\int n_e n_p dV}{4\pi d\Omega D_L^2} \tag{2.3}$$

where n_e and n_p are the electron and proton densities, dV is a cylindrical volume element subtending a solid angle $d\Omega$ to the observer and D_L is the luminosity distance to the source.

Converting this to angular structure gives the emission measure in the same form as the surface brightness β model (Section 1.2.2):

$$\mathscr{A}(\theta) = \mathscr{A}_0 \left(1 + \left(\frac{\theta}{\theta_c}\right)^2\right)^{-3\beta+0.5} \tag{2.4}$$

where θ is the angular radius and θ_c the angular core radius of the cluster. The normalisation $\mathscr{A}_0$ is then given by:

$$\mathscr{A}_0 = \pi^{1/2} \frac{\Gamma(3\beta - 1/2)}{\Gamma(3\beta)} \eta n_{p0}^2 \frac{D_A^2}{4\pi D_L^2} r_c \tag{2.5}$$

where η is the electron-proton ratio (1.18 for cosmic abundances; Worrall and Birkinshaw 2006), and D_A and D_L are the angular diameter and luminosity distances respectively.

The *apec* model normalisation[8] is:

$$normalisation = \frac{10^{-14}}{4\pi[D_A(1+z)]^2} \int n_e n_p dV \tag{2.6}$$

So the β model normalisation can be obtained from the normalisation of the *apec* model used in the spectral analysis. I then used the normalisation to calculate the electron density at the required radius for each sample in the MCMC code output, using Equations 1.24 and 2.1 for the single and double β models respectively. The uncertainties were derived in the same manner as the luminosity uncertainties.

Pressure P at radius r was then obtained by converting the electron density $n_e(r)$ to gas density $\rho(r)$ and applying the ideal gas law:

$$P(r) = \frac{k_B T}{\mu m_H} \rho(r) \tag{2.7}$$

where k_B is Boltzman's constant, T the ICM temperature, μ the mass per particle (0.6 for cosmic abundances) and m_H the mass of a hydrogen atom.

2.2.3 ICM spectral analysis

The ICM temperatures and the lobe X-ray fluxes were obtained by spectral analysis using XSPEC. I used the *apec* thermal plasma model (Smith et al. 2001) for the ICM thermal bremsstrahlung. I combined this with the *wabs* photo-electric absorption model to take account of Galactic absorption.

For *Chandra* sources of small angular extent, I used a single subtraction method with the background region taken from the same observation as the source. For *Chandra* sources that extended beyond the imaging chip, I used single subtraction with the background region taken from the *Chandra* blank sky files. For the rest of the sources, I used double subtraction with the blank sky files (*Chandra*) or closed shutter files (*XMM-Newton*) providing backgrounds for both the source and background regions.

[8] `https://heasarc.gsfc.nasa.gov/xanadu/xspec/manual/manual.html`

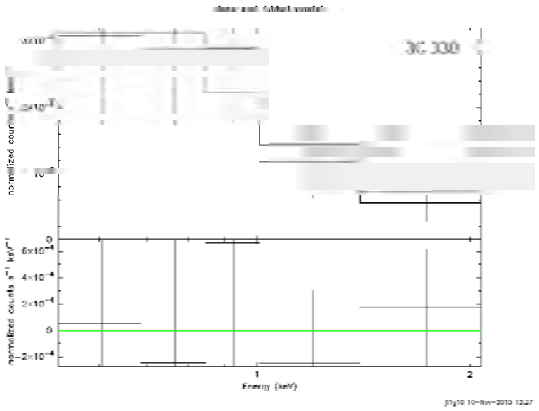

FIGURE 2.8: Example of a $z \sim 0.5$ spectrum with few bins, where single subtraction was appropriate. The source spectrum is at the top and the solid line shows the fitted model. The residuals are below.

2.2.3.1 Single subtraction, source background

For the ICM temperature of the *Chandra* sources of small angular extent, vignetting was not a problem and so the particle and external X-ray background were best modelled with a region local to the source rather than with the blank sky files. I initially defined the source region with a circle extending to the maximum detected radius, excluding the nucleus, lobes and extraneous emission. I used an annulus outside the source region for the background region, again excluding lobe and extraneous emission. I then used SPECEXTRACT to create the source and background spectra. I used FUNGROUP (written by M. Hardcastle) to bin the data so that there were at least 20 counts per bin after background subtraction.

For the *apec* model, I fixed the Galactic column density and redshift and initially fixed the metallicity at 0.3 solar, and then fitted for the temperature and normalisation. Clusters are usually cooler in the core, rise to a maximum and then drop off gradually as radius increases. For sources with rich environments, I made a temperature profile and selected an annulus excluding the cool core and outer regions of the temperature variation; otherwise I varied the source and nucleus region radii to find an annulus of representative temperature with low errors. Once I had a reasonable fit, I also tried to fit the metallicity. If it converged to a reasonable value (0.15 to 0.6 solar – Balestra et al. 2007), with errors smaller than this range, I used that value, otherwise I reverted to 0.3 solar.

Figure 2.8 shows an example of a single subtraction source of small angular extent.

2.2.3.2 Single subtraction, blank sky background

If the source was too large, there was no space left on the imaging chip to define a background region. This was only the case for a few rich *Chandra* sources. For these sources I defined the source region as above, and used the same region of the relevant blank sky file as background. I used MATHPHA to scale the background high energy count rate to match that of the source. The background then contained the particle background and a representative external X-ray background for the source region. I then binned the source spectrum and fit the *apec* model as above.

Because the X-ray background changes with time, the blank sky files may not always provide good background subtraction, but for a large source there is no alternative method.

2.2.3.3 Double subtraction

For the *XMM-Newton* sources and the *Chandra* sources of large angular extent but whose maximum detection radius lay at least partially within the ACIS-S3 or ACIS-I chips, I used a double subtraction method. The source and background regions were defined as in section 2.2.3.1 above, but spectra were generated for both regions and both regions were then modelled in XSPEC.

The source region spectrum was generated as in Section 2.2.3.2 above, using the blank sky files (*Chandra*) or closed filter files (*XMM-Newton*) for the spectrum background. The background region spectrum was generated in the same way, and the backgrounds for each spectrum were scaled to match the source high energy count rate. The two spectra were then binned to 20 counts.

The *XMM-Newton* background spectra then consist of the off-source X-ray background with the particle background removed. The *Chandra* background spectra have the particle background removed and the off-source X-ray background at least partially removed.

The X-ray background typically consists of the cosmic X-ray background and up to two Galactic thermal components (see Section 2.2.1.4). I therefore modelled the spectrum for the background region with a power law and up to two *apec* models, removing one or both *apec* models if those components were not visible in the spectrum.

The ICM was still modelled by the thermal *apec* model, but the components from the background spectrum were added as fixed components. The normalisations of the background were scaled by the ratio of the areas of the source and background regions. This was then fit for the ICM temperature and, if possible, the metallicity as described

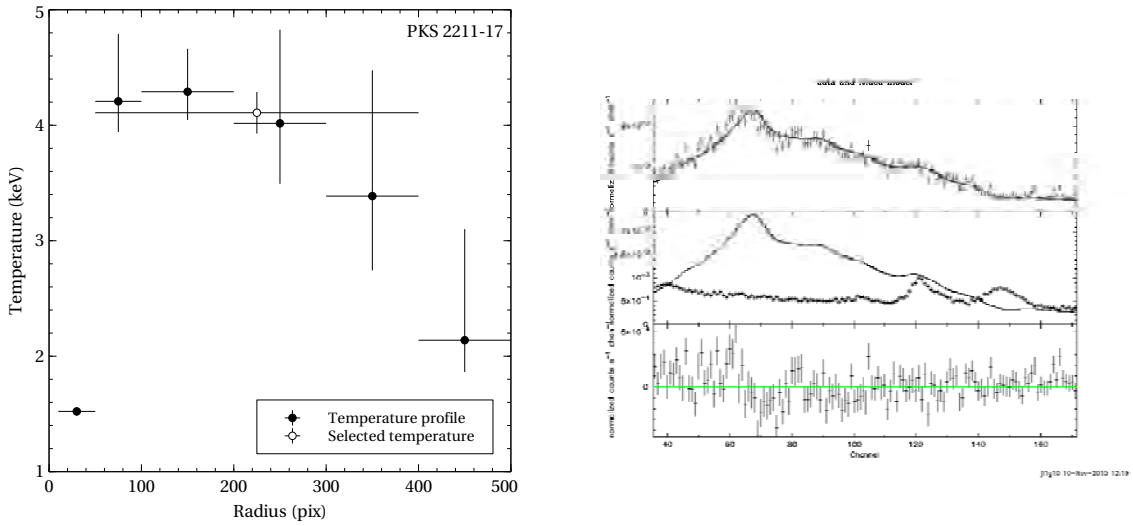

FIGURE 2.9: Examples of the temperature profile (left) and spectrum (right) of a source in a rich environment modelled using double subtraction. The temperature used in the analysis is shown as a white circle. The spectrum contains the background-subtracted source (top) with the model overlaying the data as a solid line. The background spectrum is shown in the middle and the residuals at the bottom.

in Section 2.2.3.1 above. Figure 2.9 contains the temperature profile and spectrum of a source in a rich environment where double subtraction was used.

2.2.3.4 Temperature estimates

For sources where there were insufficient counts in the spectrum to fit an *apec* model, I used the count rate within the maximum detected radius from the β model in the *apec* model with a starting temperature to find the corresponding luminosity. This was converted to temperature using the scaling relation of Pratt et al. (2009), which provided an initial estimate of R_{500} (see Section 3.4.2). Iterating the process gave new estimates of the counts within R_{500}, luminosity and temperature until the temperature converged.

For the fainter sources with a β model fit, I extracted a spectrum and used the count rate from the β model to estimate luminosity from the *apec* model, and then estimated the temperature as described above. For the *XMM-Newton* sources, I used counts from the pn camera only in this process.

For the sources without a β model fit, I used the 3σ upper limit on the counts and the median β model parameters to estimate an upper limit for the temperature.

2.2.3.5 FRII lobe X-ray flux

The FRII X-ray emission is inverse Compton, and follows a power law (Section 1.1.2.2). I used the single subtraction method (Section 2.2.3.1) for all the lobes. Having obtained the lobe shape and the jet and hot-spot exclusions from the radio maps, I also excluded the nucleus and extraneous emission using the X-ray image. This formed the source region. For the background, I needed to sample regions of the X-ray background and ICM representative of the lobe region, and in some cases, the wings of the AGN PSF. Where possible, I therefore used a rectangle of the same length as the lobe, starting at the same distance from the nucleus as the lobe and extending radially out from the nucleus. This method was suitable for well-defined lobes indented near the nucleus. For small lobes and lobes where the emission spread about the nucleus, I used an ellipse surrounding the lobe for the background.

To obtain the lobe X-ray flux density at 1 keV, I modelled the IC emission in XSPEC using a power law combined with the *wabs* photo-electric absorption model to take account of Galactic absorption. Since there are expected to be shocks at the lobe edges I also checked for thermal emission and included it in the model if present – 3C 452 for example is known to have thermal emission likely to be from the shock at the lobe tip (Shelton 2011). I then obtained the flux by refitting the model using the *cflux* component convolved with the power law model. Because the samples were at two widely separated redshifts, I corrected for redshift to find the emitted 1 keV flux density rather than observed flux.

2.2.4 FRII lobe fields and pressures

The synchrotron emission depends on the magnetic field strength and population of relativistic particles, and the relativistic particles also give rise to inverse Compton emission (Section 1.1.2.2). These processes must be modelled to find the pressures within the lobes.

I used the SYNCH code (Hardcastle et al. 1998a) to find the magnetic and electron energy densities within the lobes. SYNCH models the population of relativistic electrons expected from the input radio spectrum, calculating the equipartition conditions and the IC X-ray flux expected from the synchrotron and CMB photon fields as described in Section 1.1.2.2. Having defined the equipartition conditions, the user can then modify the lobe magnetic field until the predicted X-ray flux matches the observed flux within the lobe. The electron density from SYNCH then gives the internal lobe pressure.

As noted in Section 1.1.2.2, these calculations assume that particle content of the lobes is dominated by relativistic electrons.

2.2.5 FRII lobe Mach numbers

In Section 1.3.3, Equation 1.34 relates the Mach number to the pressure ratio of shocked and unshocked gas at the shock front. If we assume that the shell of shocked gas is in pressure balance with the lobe interior and is overpressured compared with the ICM, then we can estimate the Mach number from the pressure ratio between the lobe interior and the ICM and use the Mach number as an indicator of the amount of energy being transferred to the ICM. Note however that the effects of the jet ram pressure have not been included, so this estimate should be regarded as a lower limit.

It is relatively straightforward to obtain the ICM pressure from the β model (Section 1.2.2), but finding the pressure within the lobes is more complicated. An estimate can be made using the assumption of equipartition (Section 1.1.2.2), which, being close to the minimum energy condition, gives limits on the energy densities due to the magnetic field and electron content. However, as discussed in Hardcastle and Worrall (2000), these estimates tend to give lobe pressures lower than those of the surrounding ICM and so must underestimate the lobe energy densities. Inverse Compton observations (eg Croston et al. 2005b; Kataoka and Stawarz 2005) have shown that FRII lobes are typically not at equipartition, but that on average the electron energy density dominates the magnetic by a factor of ~ 5. This increases the total energy inferred for the lobes, and has been shown in individual cases and small samples to bring the lobes close to pressure balance or mildly overpressured with the ICM at mid-lobe and overpressured at the tip (eg Hardcastle et al. 2002a; Croston et al. 2004, 2005b; Belsole et al. 2007; Hardcastle and Krause 2013). Estimates of lobe internal pressure therefore need to model both synchrotron and IC emission from the radio and X-ray flux measurements as described in Section 2.2.4 above.

2.3 Summary

In this chapter, I gave a brief description of the instruments used to capture the data used for the research presented in this thesis and described the techniques used to carry out the data analysis. I discussed how the data from the X-ray observations were cleaned and calibrated and the removal of the X-ray background and other extraneous emission. I described how the ICM was modelled spatially and spectrally to obtain the luminosity,

pressure and temperature of the radio galaxy environments. I then gave a brief overview of the software used to find the conditions within the radio galaxy lobes.

In the next chapters I use these techniques to analyse X-ray observations of two samples, one at redshift 0.5 and one at redshift 0.1. In Chapters 3 and 4 I calculate the ICM luminosity and temperature to look at how the properties of the radio galaxies relate to their large-scale environments. In Chapter 5 I estimate the pressures of the radio lobes and the surrounding ICM, using these to look at the pressure balance between the lobes and their external environment and to estimate their advance speed through the ICM.

Chapter 3

Environments of radio-loud AGN at redshift 0.5

The contents of this chapter have been published in Astrophysical Journal as Ineson et al. (2013).

3.1 Introduction

There is evidence that different types of radio-loud AGN have different cluster environments; at lower redshifts ($z \lesssim 0.4$), high excitation radio galaxies tend to occupy galaxy groups while low excitation sources are spread across a wide range of environments (Hardcastle 2004; Best 2004; Gendre et al. 2013). There is also some evidence that, at least at low redshifts, the radio luminosity of LERGs is related to environment richness (Best 2004), but that this is not the case for HERGs.

As discussed in Section 1.3.1, the picture at higher redshifts is more confused with studies giving different results both when looking for a difference in the environment richness of HERGs with redshift (eg Harvanek et al. 2001; Belsole et al. 2007; Ramos Almeida et al. 2013; Wold et al. 2000; McLure and Dunlop 2001), and when looking for correlations between radio luminosity and environment richness (eg Belsole et al. 2007; Wold et al. 2000; Falder et al. 2010). In Section 1.3.2 I discussed some possible reasons for the disparities in results, namely the difficulty of distinguishing the effects of environment, evolution, measurement method and sample bias.

Relationships between the properties of radio galaxies and their environments need to be studied in narrow redshift bands to avoid contamination by any evolution of the environment, and the results then compared to look at evolution separately. The process

is made more difficult by both the Malmquist bias and the evolution of radio luminosity, so that local samples have little overlap in luminosity with high redshift samples. An additional problem is that the reduction in the numbers of LERGs with redshift also limits the maximum redshift for comparisons of galaxy types.

The work in this thesis provides the first systematic examination of the cluster environments of radio galaxies at distinct redshifts, separating out the effects of environment and evolution. It uses two samples separated far enough in redshift that evolutionary effects may be able to be seen, but with sufficient sources to make subsamples of the different galaxy types and a large enough overlap in radio luminosity for the results to be comparable. The environment richness is measured using ICM luminosity rather than a method based on galaxy counts/overdensities for two reasons – the ICM contains most of the baryonic mass of the cluster and so can be used as a proxy for total cluster mass, and radio galaxy interactions are with the ICM rather than the galaxies in the cluster.

In this chapter I present the results for the sample at the more distant redshift – $z \sim 0.5$. The aims of this work were:

- to compare radio luminosity with cluster richness for the different classes of radio galaxy, using the ICM X-ray luminosity as the measure of cluster richness;
- to look for differences between the cluster environments of radio galaxies and the general population of galaxy clusters;
- to see how my measurements of the ICM X-ray luminosity relate to existing measurements of cluster richness using the galaxy-galaxy spatial covariance function B_{gg}.

3.2 The sample

I made use of the ZP5 sample of McLure et al. (2004), which contains all narrow-line and low-excitation radio galaxies with redshifts between 0.4 and 0.6 from four flux-limited, spectroscopically complete, low-frequency radio surveys of the northern hemisphere – 3CRR (Laing et al. 1983), 6CE (Eales et al. 1997; Rawlings et al. 2001), 7CRS (Lacy et al. 1999; Willott et al. 2003), and TexOx-1000 (Hill and Rawlings 2003). This sample was ideal for comparing radio luminosity and environment richness without contamination by evolution. It covers three decades in radio luminosity in a small redshift range and is both distant enough to contain high luminosity radio galaxies and near enough for low luminosity galaxies still to be detectable and for X-ray observations of the ICM to be feasible with reasonable exposure times.

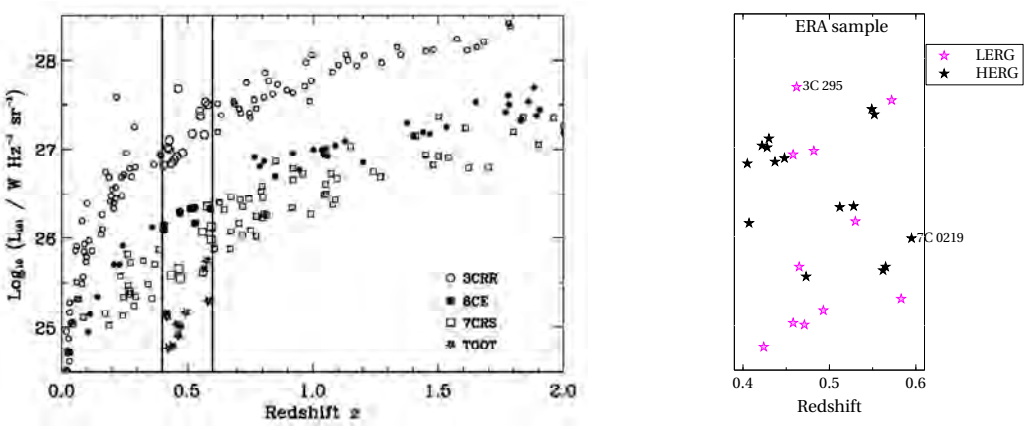

FIGURE 3.1: On the left, 151-MHz radio luminosity vs redshift for the narrow-line and low excitation radio galaxies in the 3CRR, 6CE and 7CRS samples, with galaxies from the TOOT survey added in the range $0.4 < z < 0.6$ (McLure et al. 2004). The McLure et al. sample is in the $0.4 < z < 0.6$ redshift interval. On the right, the ERA subsample used in this project. Black stars are HERGs and magenta stars are LERGs.

The luminosity and redshift range for the four surveys are shown on the left of Figure 3.1, with the McLure et al. (2004) ZP5 sample highlighted. The sample contains 41 sources and includes high- and low-excitation sources and a range of radio source morphologies. Host galaxy properties for the full sample were derived by McLure et al. from HST WFPC2 observations, and an optical environment study has recently been carried out by Herbert et al. (2015), using the spatial covariance function B_{gg}. Ten of the ZP5 sources had already been imaged in X-ray by *XMM-Newton* or *Chandra*. Because of the amount of X-ray observing time required, the entire ZP5 sample could not be imaged for this project so new *Chandra* observations (the Chandra Environments of Radio-loud AGN Large Project – ERA) and *XMM-Newton* observations were obtained for fourteen additional sources, making a representative subsample of 24 sources (Croston 2007, 2009). The ERA sample covered the full range of radio luminosity of the ZP5 sample and contained HERG and LERG spectral types and FRI and FRII morphologies. During the analysis phase, X-ray data for another two sources from the parent sample became available and were added to the sample. Figure 3.1 shows radio luminosity plotted against redshift for the ERA sample (right) alongside the ZP5 sample (left), and Figure 3.2 shows the coverage of the ERA sample.

Table 3.1 lists details of the 26 sources. Positions and redshifts were taken from McLure et al. (2004). For all galaxies except 3C 457, I obtained Galactic column densities from Dickey and Lockman (1990) via the HEASARC tools; for 3C 457, I used the higher column density found by Konar et al. (2009). Excitation type was taken from McLure et al. (2004), except for 3C 295. 3C 295 is classified as a LERG in the on-line 3CRR catalogue[1] based on the results of Lawrence et al. (1996), but this classification is questioned

[1] `http://3crr.extragalactic.info/`

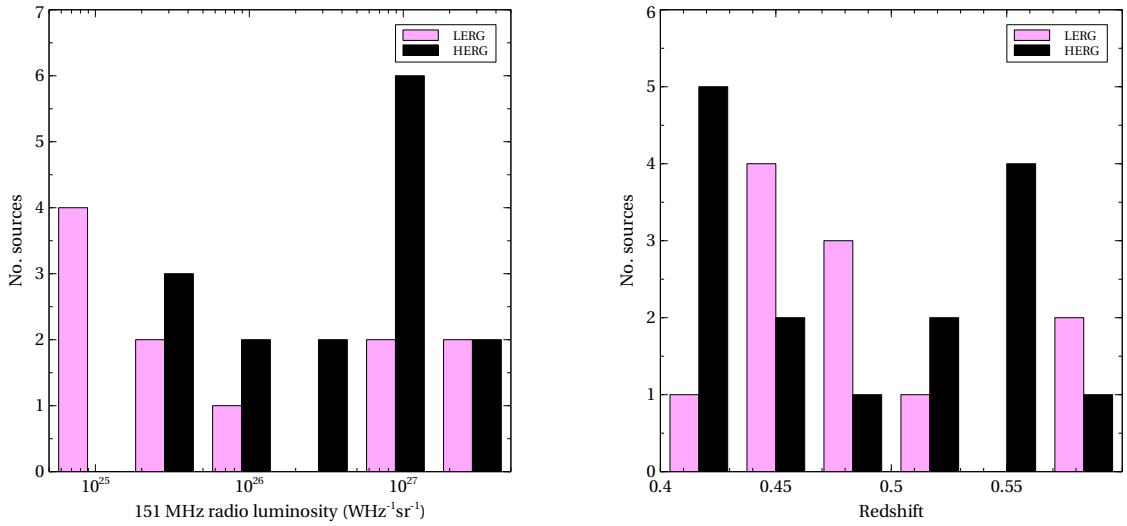

FIGURE 3.2: The ERA sample; Radio luminosity coverage (left) and redshift coverage (right). HERGs are shown in black and LERGs in magenta.

(Varano et al. 2004). I have here classified 3C 295 as a LERG, but where appropriate have analysed LERG subsamples with and without 3C 295. 7C 0219+3423's classification is also uncertain; I have followed McLure et al. (2004) in classifying it as a possible HERG.

3.3 Observations and data preparation

3.3.1 X-ray data

The X-ray observations for this study came from *Chandra* and *XMM-Newton*. The 3C sources had already been observed; the 6C, 7C and TOOT observations were made for this programme. The *XMM-Newton* observations used the three EPIC cameras with the medium filter and the *Chandra* observations used the ACIS-S3 chip in either FAINT or VFAINT mode. Observation IDs and times and screened observation times are given in Table 3.2.

3.3.2 Radio data

Radio maps were used to make the overlay images shown in Section 3.7 and to mask out the radio lobes so that any radio-related X-ray emission did not contaminate measurements of the cluster properties. In most cases I used existing maps, either from the 3CRR Atlas[2]; the Faint Images of the Radio Sky at Twenty Centimeters Survey

[2]http://www.jb.man.ac.uk/atlas

(FIRST, Becker et al. 1995); Hardcastle et al. (2002a); and Croston et al. (2005b). For some of the less luminous radio galaxies where adequate maps were not available from these sources, I used the 1.4-GHz observations of Mitchell (2005), which were taken in A and C configurations. These were obtained these from the VLA archive (Program ID AR477) and were reduced in AIPS in the standard manner by Dr. Hardcastle. Table 3.2 contains details of the radio maps used.

3.4 Analysis

The aim of the analysis was to find the temperature and X-ray luminosity of the ICM emission of the radio galaxies. Where possible, the temperature was obtained by spectral analysis; when there were insufficient counts, it was estimated from the count rate. The luminosity was determined by integrating the surface brightness profiles to the R_{500} radius (Section 3.4.2, Equation 3.1).

Initial data preparation followed the procedures described in Section 2.2.1. I used the analysis packages CIAO v4.2 and CALDB v3.3.0 for the *Chandra* observations and SAS v11.0.0 for the *XMM-Newton* events files. Screened observation times are included in Table 3.2. Since the *Chandra* sources were of small angular extent and fit well within the observing chip, I did not need to correct for vignetting or chip edges so did not build exposure maps.

3.4.1 Imaging

Section 3.7 contains images of the X-ray emission of each cluster in the 0.5–5 keV energy range, with the radio emission overlaid as contours. I generated images for the *XMM-Newton* sources using the method described in Croston et al. (2008a). An image was extracted for each of the three EPIC cameras using EVSELECT. The MOS images were then scaled to make their sensitivity equivalent to the pn camera image so that there would be no chip-gap artefacts when the three images were combined. I generated exposure maps for each camera using EEXPMAP, which were used to correct for the chip gaps, but not for vignetting as this leads to incorrect scaling of the particle background that dominates at large radii. The resulting images are therefore not vignetting corrected; they are purely pictorial and not used in any subsequent analysis.

For both *Chandra* and *XMM-Newton* sources, I used DMFILTH to replace point sources by Poission noise at the level of nearby regions, and then applied Gaussian smoothing using ACONVOLVE. I then used DS9 to display the X-ray emission and overlay the radio emission contours.

3.4.2 Spatial analysis

I prepared the surface brightness profiles as described in Section 2.2.2, using the single subtraction method for the distant *Chandra* sources and the standard double subtraction method for the *XMM-Newton* sources. For one source (3C 341), the extended emission was swamped by a bright nucleus, so I used an energy range of 0.4–2.0 keV to reduce the nuclear emission so that the profile could be modelled.

Table 3.3 contains the maximum detection radius and net counts within that radius for each of the sources.

Since the host galaxy was not visible beyond the PSF, I fit the surface brightness profiles with single β models using the Markov-Chain Monte Carlo (MCMC) method described by Croston et al. (2008a) and in Section 2.2.2. The goodness-of-fit and β model parameters are shown in Table 3.3 and Section 3.7 contains the surface brightness profiles overlaid with the PSF and β model profiles. Note that the limits on β and r_c mentioned in Section 2.2.1.5 were not used for this sample.

I could not obtain fits for six sources. TOOT 1630+4534 could not be detected above the background (neither nuclear or extended emission); TOOT 1301+3658, 7C 0213+3418 and 3C 16 had insufficient counts to create a profile, and 7C 0223+3415 and 7C 1731+6638 had a point-source detection, but no extended emission above the level of the PSF wings. For these sources I estimated a 3σ upper limit on the counts by obtaining the net counts within an estimated R_{500} overdensity radius (Equation 3.1). For the four faint sources, I used the median R_{500} of the 7C and TOOT sources; for 3C 16 I used the median of the 6C and 3C sources. If the net counts were greater than three times the error on the counts in the background area, I used the net counts plus three times the error for the upper limit on the counts; otherwise I used three times the background error. (Since 7C 1731+6638 has a strong PSF with no detectable extended emission, I used the background error method rather than the net counts method).

The distributions of β and the core radius (r_c) are shown in Figure 3.3. The majority of the β values are around 0.5, which is expected for groups and poor clusters (eg Helsdon and Ponman 2000), but there are three very high values of β (TOOT 1255+3556, 3C 46 and 3C 274.1 – these also have the three highest core radii) and two very low values (TOOT 1626+4523 and TOOT 1303+3334). The three TOOT sources are faint objects with low counts, so the model parameters are very poorly constrained, and McLure et al. (2004) identified the host galaxy of 3C 46 as having undergone a major merger so its ICM may not be in hydrostatic equilibrium. 3C 274.1, however, has an undisturbed host galaxy and so its steep profile is perhaps surprising. However, the profile fits the data well and since I was using the profile simply to obtain luminosity I was concerned only

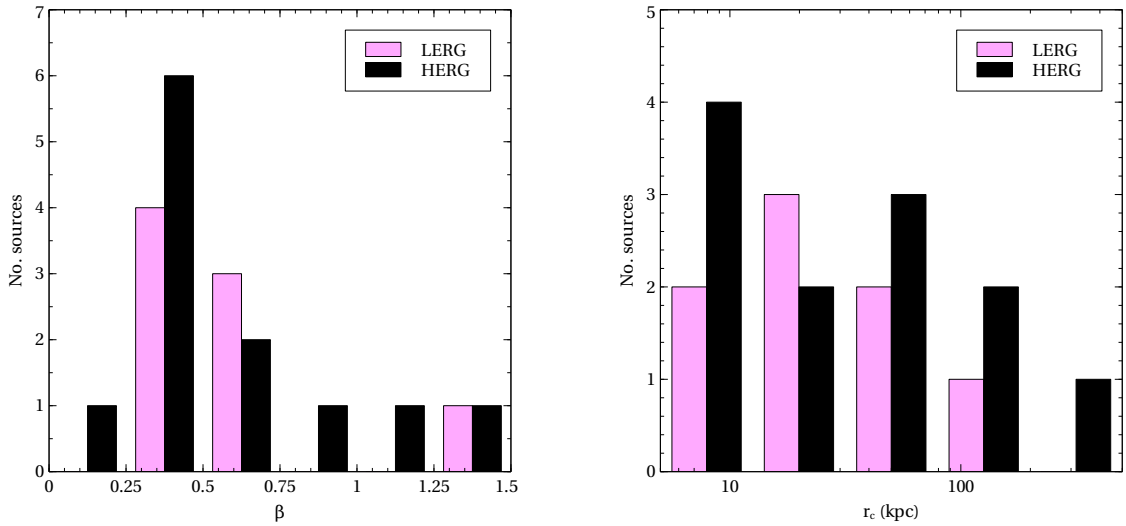

FIGURE 3.3: Distribution of the β model parameters; β (left) and core radius (right), separated into excitation classes. Symbols as in Figure 3.2.

with the shape of the profile and not the accuracy of the β model. The β and r_c values are degenerate and therefore not physically very meaningful, and the uncertainties on the extreme values are large and so cover more typical values.

Luminosity was calculated as described in Section 2.2.2, by integrating the β model profile to the R_{500} overdensity radius, using counts to flux conversion factors generated from the *apec* model. I extrapolated the β model to the R_{500} radius calculated using the $R-T$ relationship from Arnaud et al. (2005):

$$R_{500} = h(z)^{-1} B_{500} \left(\frac{kT}{5}\right)^{\beta} \tag{3.1}$$

where the redshift dependence of the Hubble constant, $h(z)$, is defined in Equation 1.30.

Table 3.4 contains four ICM X-ray luminosities (L_X) for each source: $L_X(0.4-0.7)$ is the luminosity within the 0.4 to 7.0 keV energy range out to the maximum detection radius (D_{rad}); $L_X(bol)$ is the bolometric luminosity within D_{rad}; $L_X(bol)$ is the bolometric luminosity within R_{500}; and $h(z)^{-1}L_X(bol)$ is the bolometric luminosity within R_{500} scaled by $h^{-1}(z)$ to correct for the critical density evolution.

Nine sources have R_{500} greater than D_{rad}. For these, the extrapolated counts for the luminosities within R_{500} are less than 30% greater than the observed counts for all but one source – TOOT 1626+4523 – which has a shallow surface brightness profile and R_{500} much larger than the maximum detection radius. Consequently the R_{500} luminosity for that source is more than twice the luminosity within the maximum detection radius. The mean extrapolation to R_{500} for the remaining eight sources is 12%.

3.4.3 Spectral analysis

Where possible, I used spectral analysis to obtain the ICM temperature, using the single subtraction method for the *Chandra* observations (Section 2.2.3.1) and the double subtraction method for the *XMM-Newton* observations (Section 2.2.3.3). When there were insufficient counts (10 sources) or the ICM could not be detected in the observation (6 sources), I estimated the temperature using the scaling relation of Pratt et al. (2009) (Section 2.2.3.4).

I used a metallicity of 0.3 solar (Balestra et al. 2007) for all sources except for 3C 295, 3C 330 and 3C 457, where metallicities had been calculated elsewhere (Belsole et al. 2007; Konar et al. 2009). These were 0.48, 0.2 and 0.35 respectively. I discuss the effect of varying metallicity in Section 3.5.1.

Table 3.5 contains the inner and outer radii of the annuli, the temperatures of the sources and the χ^2 for the temperatures obtained by spectral analysis. As expected, the temperatures are for the most part typical of groups and poor clusters with only three sources above 3 keV. The errors on most of the spectral temperatures are large, as is to be expected from such faint objects. Temperatures have been obtained for some of the clusters by other researchers (Belsole et al. 2007; Allen et al. 2001; Konar et al. 2009) and my values are compatible with their results.

I have not included any corrections for the reported difference between temperatures obtained by *Chandra* and *XMM-Newton* since the difference at 3 keV and less is slight (Schellenberger et al. 2012).

3.5 Results and discussion

3.5.1 Radio galaxy environments

In order to investigate the relationship between radio galaxies and their cluster environments, I compared radio luminosity and ICM luminosity for the full sample, for the different excitation classes and for the FR classes. These are plotted in Figures 3.4 and 3.5.

The majority of the sources have similar ICM luminosity. Although the radio luminosity covers three decades, 80% of the sources have ICM luminosity within the single decade from 10^{43} to 10^{44} erg s^{-1}. The five sources outside this range are all LERGs (with the possible exception of 3C 295), spreading over about 2.5 decades, and X-ray luminosity does appear to rise with radio luminosity for the LERGs. Since I had censored data, I

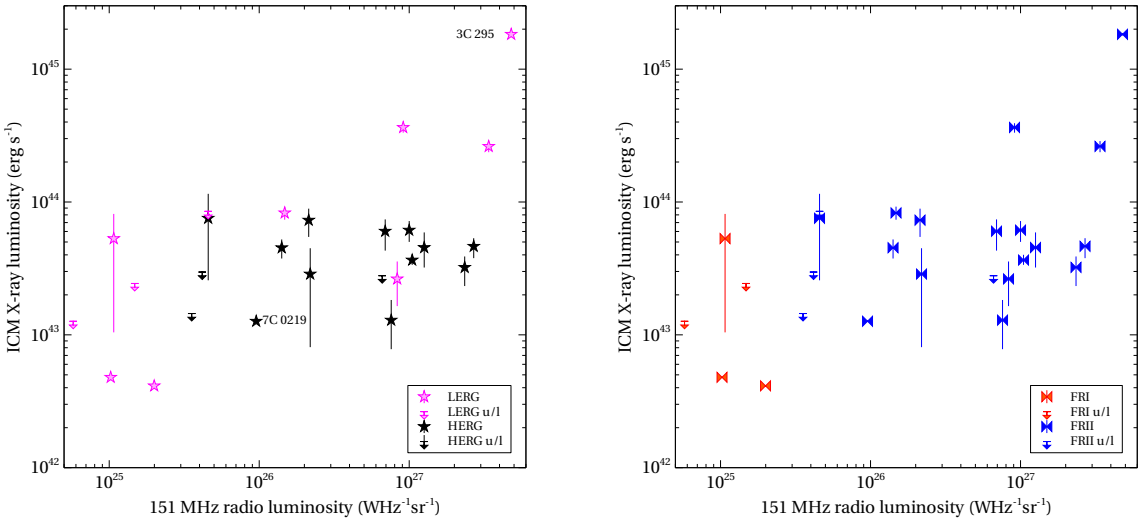

FIGURE 3.4: Radio luminosity vs ICM X-ray luminosity, separated into excitation classes (left), and FRI and FRII galaxies (right). In the left plot, magenta stars are LERGs, black stars are HERGs and arrows are upper limits. In the right plot, red ties are FRIs, blue ties are FRIIs and arrows are upper limits.

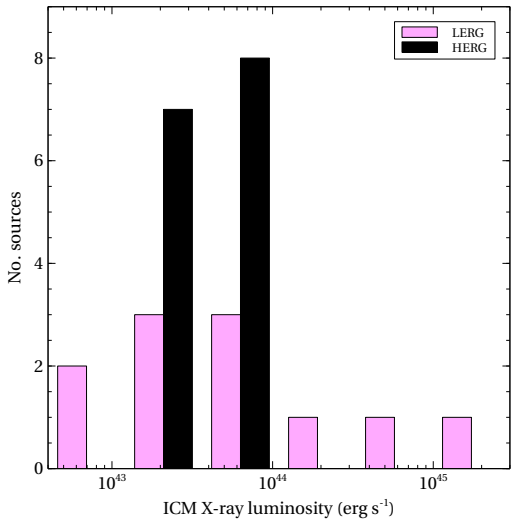

FIGURE 3.5: ICM X-ray luminosity coverage, separated into excitation classes. Symbols as in Figure 3.2.

checked for correlations using generalized Kendall's τ tests (Isobe et al. 1986), and the results are shown in Table 3.6. I found a correlation between radio luminosity and ICM luminosity for the full sample and for the LERG subsample, but not for the HERGs. The LERG result does however depend heavily on 3C 295; the correlation is considerably weaker when 3C 295 is removed from the LERG subsample.

Since the extrapolation of the luminosity to R_{500} depends on temperature, I checked the effect of propagating the temperature uncertainties through the calculations for some of the sources with large temperature errors and/or big differences between the maximum

detection radius and R_{500}. For most of the sources, the difference was slight, but there were big changes to the uncertainties for some of the sources with large errors on the temperatures. 3C 427.1 had the biggest change, with the 1σ range going from $28-30\times10^{43}$ erg s^{-1} to $19-54\times10^{43}$ erg s^{-1}. This however retains 3C 427.1's position as one of the most luminous clusters and radio galaxies and so the LERG correlation remained. 3C 457 had the next largest temperature errors and the upper limit on the luminosity potentially increases from 7×10^{43} to 11×10^{43} erg s^{-1}. Its position within Figure 3.4, however, means that an increase in luminosity would merely weaken the HERG correlation further. Overall, I found that propagating the temperature uncertainties through the calculations would not affect the results of the correlation tests.

A second potential source of error was my assumption of a metallicity of 0.3 solar for the majority of the sources. There were insufficient counts to allow metallicity to vary during modelling, so I recalculated the temperatures and luminosities of three of my sources with spectral temperatures (3C 427.1, 6C 1132+3439 and 6C 1200+3416) with metallicities of 0.1 and 0.5 solar, these being outside the rms bounds given by Balestra et al. (2007). The biggest change in luminosity was 4%, which was well within the luminosity errors of the sources. I also recalculated the luminosities for three of the sources with estimated temperatures. The biggest luminosity change was for the coolest source – TOOT 1255+3556 – where dropping the metallicity to 0.1 solar increased the luminosity by 12%. Again, this was well within the 1σ error bounds. I therefore concluded that inaccuracies in my metallicities were unlikely to affect my results.

As can be seen from the right-hand plot in Figure 3.4, any correlation for the FRII subgroup would be weak. The Kendall's τ test gave a weaker correlation than for the LERGs, even when 3C 295 was excluded. There were insufficient data to examine the FRI subgroup.

3.5.2 Comparison with general cluster environments

During the analysis, I used various assumptions based on the expectation that the cluster environments of my sample of radio-loud AGN are not markedly different from other clusters of similar luminosity. In particular I assumed that the X-ray cluster luminosity is a good proxy for gravitational mass and that the ICM follows the expected luminosity–temperature relation. There is evidence that radio-loud groups of a given X-ray luminosity are hotter than similar radio-quiet groups (Croston et al. 2005a), but this effect is small enough not to be seen at higher luminosities (Belsole et al. 2007).

I expected that the cluster environments, although relatively poor, would be sufficiently luminous for any disruption by feedback to be smaller than the experimental errors. I

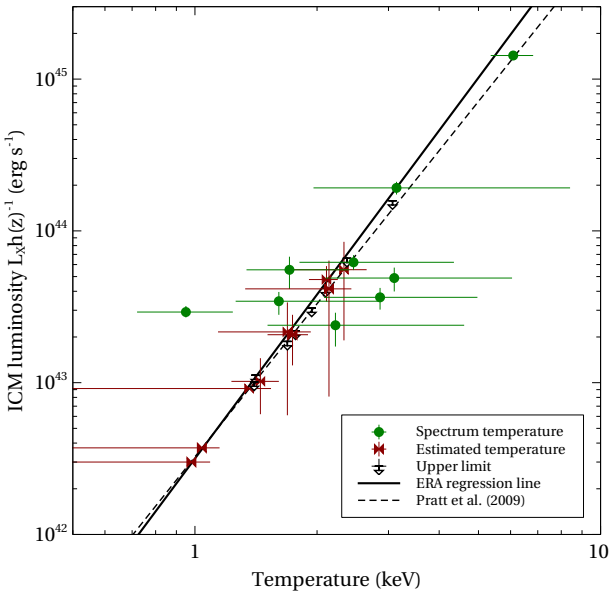

FIGURE 3.6: ICM luminosity vs temperature. Temperatures obtained by spectral analysis are shown by green circles, estimated temperatures by maroon ties and upper limits by arrows. The solid line shows the $L_X - T_X$ relationship from the ERA results (excluding upper limits) and the dashed line shows the Pratt et al. (2009) $L_X - T_X$ relation.

checked the validity of this assumption by looking at the $L_X - T_X$ relation, and the gravitational masses and the entropy of the clusters. Figure 3.6 plots ICM luminosity (corrected for redshift evolution) against temperature for the results obtained by spectral analysis, and Table 3.6 lists the results of the correlation tests. (Since the majority of the temperatures were estimated from the $L_X - T_X$ scaling relation (Pratt et al. 2009), it would be startling if there were not a strong correlation for the full data set.) The bulk of the scatter comes from the sources with temperatures derived from their spectra, and this is reflected in a weaker correlation for that subpopulation.

I used the orthogonal BCES method (Akritas and Bershady 1996) to obtain the $L_X - T_X$ regression line for the ERA sources excluding the upper limits: $log(L_X) = (3.59 \pm 0.33) log(T_X) + (42.5 \pm 0.19)$. This is shown by the solid line in Figure 3.6. The dashed line shows the Pratt et al. $L_X - T_X$ scaling relation that I used to obtain the estimated temperatures, which is, as expected, very similar.

Böhringer et al. (2012) predict a scaling relation slope of 2.70±0.04 and their review of the literature cites slopes of 2.6 to 3.7 for scaling relations derived from observations. My result is therefore compatible with existing observational results.

I estimated the total gravitational mass for each cluster via the assumption of hydrostatic equilibrium, using equation (5.113) from Sarazin (1986), having obtained the density gradient from the β model parameters (Birkinshaw and Worrall 1993). I then compared

these results with the $M-T$ scaling relation of Arnaud et al. (2005) and found them compatible within the 1σ errors.

I also calculated entropy S within $0.1R_{200}$ using $h^{4/3}(z)S = kT/n_e^{2/3}$ (Pratt et al. 2006), where R_{200} is the radius at an overdensity of 200 (Arnaud et al. 2005), kT is the ICM temperature and n_e is the electron density. I converted β model counts to electron density via the volume emission measure from the *apec* model (Equations 2.5 and 2.6). I compared my results with the scaling relation of Pratt et al. (2010) and again found them within the expected range.

I concluded that, within the experimental errors, the cluster environments of my sample of radio galaxies are comparable to those of other clusters of similar luminosity, and find no evidence (within the often large uncertainties, and bearing in mind that only ten of the cluster temperatures have been directly measured) that the radio sources have altered the global cluster properties.

3.5.3 Comparison with optical measures

Herbert et al. (2015) have calculated the galaxy-galaxy spatial covariance function B_{gg} at two radii (977 kpc and 564 kpc) for the McLure et al. (2004) sample, and I used these values to look for a scaling relation between ICM luminosity and B_{gg} (Figure 3.7, Table 3.6). There is only slight evidence of a relationship for the 977 kpc values, but the full 564 kpc data set shows a correlation. The Buckley-James linear regression method, which allows for censored data in the independent variable (Isobe et al. 1986), gives a scaling relation of $\log_{10}(L_X) = (0.0015 \pm 0.0004) \times B_{gg} + 43.12$ with a standard deviation of 0.52, and this is plotted in Figure 3.7.

Yee and Ellingson (2003) found a power law relation between B_{gg} calculated within 500 kpc, and ICM luminosity – since their sample is more luminous than the ERA sample, they have no negative values of B_{gg}. In order to compare my results with those of Yee and Ellingson, I removed the negative values from the 564 kpc data set and found a good correlation and a scaling relation of $log(L_X) = (1.67 \pm 0.47) log(B_{gg}) + 39.4$ with a standard deviation of 0.52. Figure 3.8 shows a log plot of the B_{gg} data overlaid with the two scaling relations. My line has a similar slope to that of Yee & Ellingson but a lower intercept, albeit within the $1-\sigma$ error. Their sample contains brighter sources over a larger redshift range than ours and their cluster richness measures are calculated within slightly different radii, so some difference in the regression lines is not unexpected.

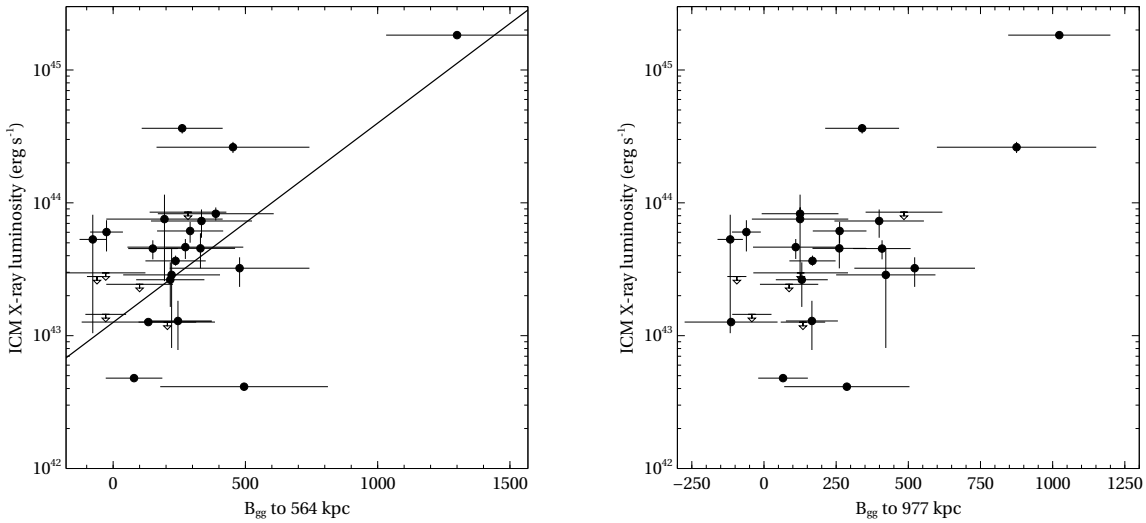

FIGURE 3.7: ICM luminosity vs the galaxy-galaxy spatial covariance function B_{gg} (values taken from Herbert et al. 2015). B_{gg} is calculated within 564 kpc (left) and 977 kpc (right). Upper limits are shown as arrows.

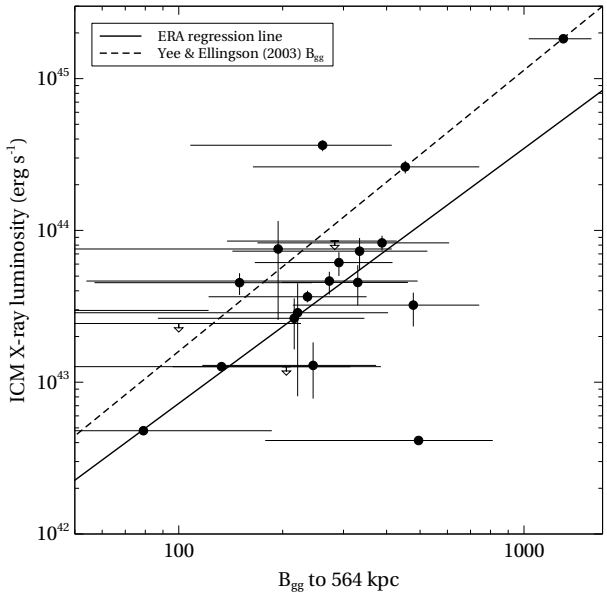

FIGURE 3.8: ICM luminosity vs $\log_{10} B_{gg}$ for all positive values of B_{gg} (calculated within 564 kpc) overlaid with the scaling relations from the ERA sample (solid line) and Yee and Ellingson (2003) (dashed line). Upper limits are shown as arrows. Note that Yee & Ellingson used B_{gg} calculated within 500 kpc.

3.5.4 Implications

Overall, I found a correlation, significant at the $\sim 99.5\%$ confidence level, between radio luminosity and cluster richness. This result is similar to that of Herbert et al. (2015), who calculated optical overdensity parameters for the McLure et al. (2004) ZP5 sample, and found a 98% significant correlation between radio luminosity and environmental overdensity within 564 kpc of the source. Thus for the sample as a whole, the optical and X-ray measures of environment richness yield a similar result.

Splitting the sample by spectral class, I found a slightly reduced probability of correlation between radio luminosity and cluster richness for LERGs compared with the full data set, but no correlation for HERGs, suggesting that the overall correlation is driven by the LERGs. This adds to the body of evidence that there are fundamental differences in the properties of the two classes of radio galaxy. The HERG clusters occupied a single decade of X-ray luminosity (10^{43} to 10^{44} erg s^{-1}), while the LERG clusters had a much wider range of luminosities. However, there is about an order of magnitude of scatter in the relationship, and large uncertainties at the lower end of the luminosity range where most of the upper limits are also situated. This, taken with the small sample size, makes any conclusions tentative.

Best (2004), Hardcastle (2004) and Gendre et al. (2013) all found that HERGs lay within a limited range of relatively low environment richnesses. Hardcastle used B_{gg} within 500 kpc to measure cluster richness. Bearing in mind the weakness of the correlation, the considerable scatter and the measurement radius of 564 kpc rather than 500 kpc, I can use the $L_X - B_{gg}$ relationship given in Section 3.5.3 to estimate that my clusters lie roughly within $-150 < B_{gg} < 400$, which is roughly compatible with the range occupied by the HERGs in Hardcastle's sample. McLure and Dunlop (2001) and Harvanek et al. (2001) report similar B_{gg} ranges for their QSOs at $z \sim 0.2$ and $z < 0.4$ respectively. For their QSOs in the $0.4 < z < 0.6$ region, however, Harvanek et al. found higher values of B_{gg}, roughly corresponding to cluster luminosities from 10^{43} to 10^{45} erg s^{-1}.

Looking at results for higher redshift radio galaxies, Belsole et al. (2007) and Wold et al. (2000) both find HERG cluster luminosities within similar ranges. This could hint that any evolution of the HERG environment is slight, but it would be unwise to draw any conclusions based on this cursory analysis. I look at evolution of the environment in Chapter 4.

Turning to the LERG subsample, the range of cluster luminosities is larger than for the HERGs, a result also reported by Hardcastle (2004), Best (2004) and Gendre et al. (2013). Best also found a 99.95% correlation between environment richness and radio luminosity; my correlation is weaker (99.2%) but supports his result. This suggests a

link between radio properties and the environment that does not appear to exist for HERGs. However, when 3C 295 is excluded, the LERG sources are all within about 0.5 dex of the HERG range so the difference between the samples is now slight and the LERG correlation between radio and environment luminosity becomes weaker.

The answer to the question posed in the introduction – whether the radio-galaxy luminosity is related to large-scale cluster environment – appears to be "Yes". There is, however, considerable scatter in the results, and the correlation is driven by a small number of sources. I also found tentative evidence that it may be the population of low-excitation radio galaxies driving this relationship, with no correlation found for the high-excitation subsample alone. In Chapter 6 I demonstrate that the correlation between L_R and environmental L_X (for the full sample) is not driven by a correlation between cluster X-ray luminosity and black hole mass.

Such a correlation between radio luminosity and environmental richness would be expected if jet properties are determined by the properties of the surrounding hot gas; however, there are many reasons why such a relationship may be expected to have considerable scatter, even for the narrow redshift range I consider here. An important source of scatter is the still poorly understood relationship between jet mechanical power and radio luminosity. Progress has been made in constraining this relationship observationally (eg Bîrzan et al. 2008; Cavagnolo et al. 2010; Godfrey and Shabala 2013), but there is scatter of one to two orders of magnitude. This on its own could be enough to explain the scatter I observe in the relationship between radio luminosity and environment, even if jet power and environmental richness were tightly correlated.

If, however, one of the sources of scatter in the jet power/radio luminosity relation is differences in the environment, this ought to tighten the $L_R - L_X$ relation rather than add scatter to it.

A second important source of scatter is the relationship between central cooling time and total ICM X-ray luminosity. If jet power is controlled by the properties of the hot gas environment, then it must be the central gas distribution that is important. Both cool core and unrelaxed clusters can be found at all luminosities, and the central gas density is uncorrelated with total ICM X-ray luminosity for the cluster population as a whole (eg Croston et al. 2008b). It has been found that low-power radio galaxies appear to require a cool core or dense galaxy corona (eg Hardcastle et al. 2001, 2002b; Sun 2009); however, it has not been observationally established whether this is the case for the FRII population that form the majority of my sample. It is therefore plausible that there is substantial scatter between my measured X-ray luminosities and the central hot gas properties that may drive jet behaviour (at least in part of the sample), which could be a major contributor to the scatter I observe between L_R and L_X.

3.6 Conclusions

I have made a comparison of low frequency radio luminosity and cluster environment richness for a sample of 26 radio-loud AGN. I excluded any effects of environment evolution by taking the sample from a narrow redshift range at $z \sim 0.5$. The sample covered three decades of radio luminosity and contained both high- and low-excitation sources. My measure of environment richness was ICM X-ray luminosity, obtained from *Chandra* and *XMM-Newton* observations.

My main findings are:

- Over the full sample, there is a correlation between radio luminosity and cluster richness, using ICM luminosity as the measure of cluster richness. There is however total scatter of about one order of magnitude in environment richness at a given radio luminosity, which is not much smaller than the total range of cluster richnesses.
- There is tentative evidence for a difference between high- and low-excitation sources – the HERGs occupy a slightly narrower range of cluster richnesses than the LERGs and show no sign of a correlation between radio luminosity and cluster richness whereas the LERGs have a similar strength correlation to the full sample. However, re-analysis without the brightest source, whose classification as a LERG is disputed, reduces the LERG correlation to only slightly above 95% significance.
- Evidence for a correlation between radio luminosity and ICM luminosity for the FRII subpopulation was weaker than that for the LERG population, even when the brightest source was excluded.
- My results were compatible with published ICM luminosity–temperature scaling relationships.
- I compared ICM luminosity and B_{gg} in the hope of finding a scaling relation between the two cluster measures. I found a correlation between $\log_{10} L_X$ and B_{gg} calculated to 564 kpc (Herbert et al. 2015) for FRII sources, and a power law relationship between L_X and B_{gg} that is broadly compatible with that of Yee and Ellingson (2003). Study results using the two measures should therefore be comparable, but the large scatter suggests that converting between the measures for individual sources is likely to be inaccurate.

Having examined a sample of radio-loud AGN at a single epoch, I found evidence for a correlation between radio luminosity and host cluster X-ray luminosity, as well as

tentative evidence that this correlation may be driven by the subpopulation of low-excitation radio galaxies. This is in keeping with previous studies showing different accretion efficiencies and host galaxy properties for the two types of radio galaxy. I also, in common with other researchers, found considerable scatter in the results, which may be a sign of more complex relationships between jet power and environment than are generally assumed.

In the next chapter, I report a similar analysis of a sample at redshift ~ 0.1, to see if the results at redshift ~ 0.5 also apply at lower redshifts. I then look for evidence of evolution of the environments of radio-loud AGN.

3.7 Images and surface brightness profiles

This section contains images (left) and surface brightness profiles (right) of the ERA sample in order of radio luminosity. The images are of the X-ray emission overlaid with radio contours. The dashed circles are the maximum detected radius and the solid circles show R_{500}.

Twenty-two sources had sufficient counts to create surface brightness profiles. The PSF and β model profiles are overlaid on the profiles. Although profiles were generated for 7C 0223+3415 and 7C 0213+3418, they had insufficient extended emission to fit a β model.

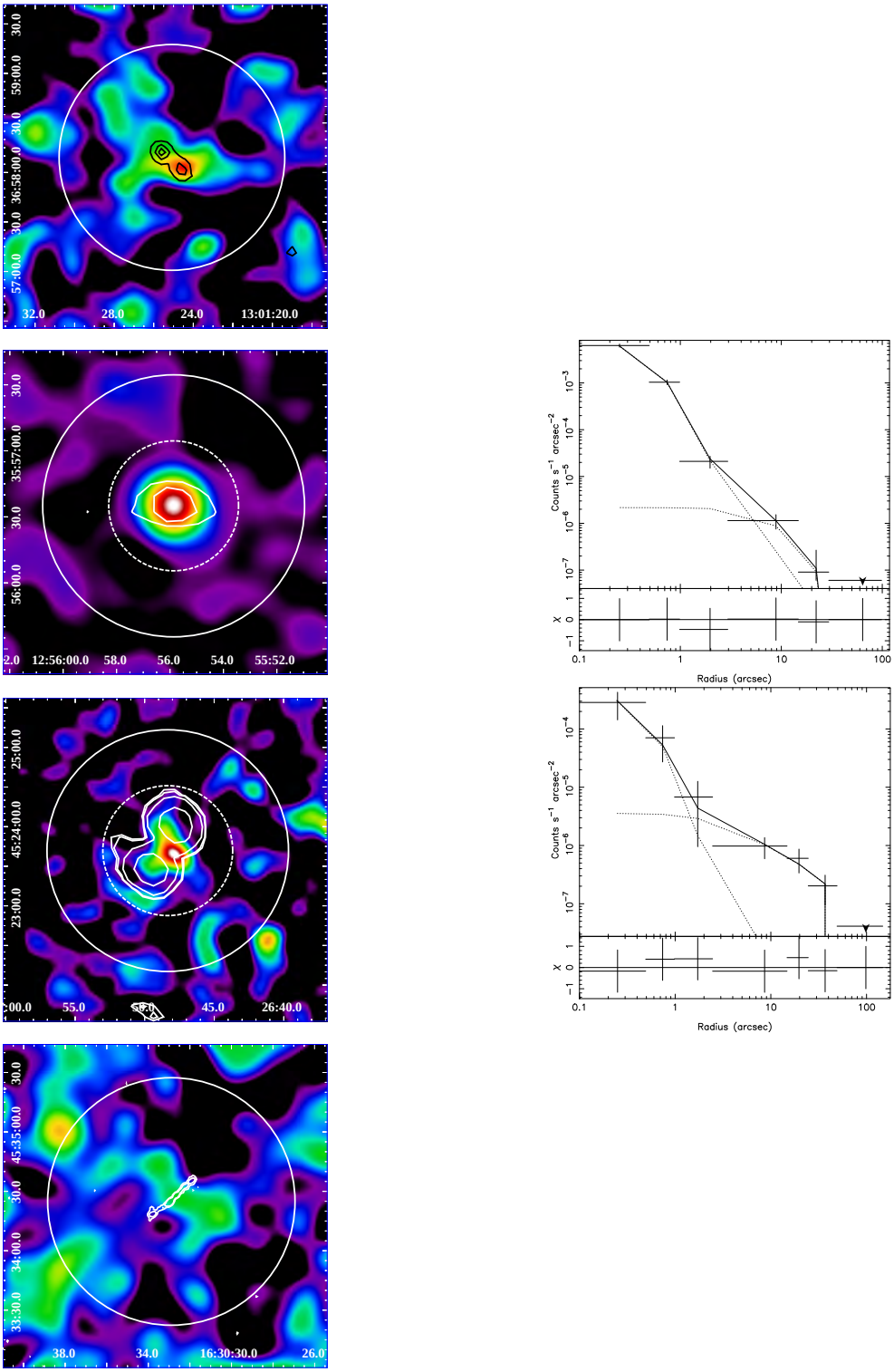

FIGURE 3.9: TOOT 1301+3658 (top), TOOT 1255+3556 (row 2), TOOT 1626+4523 (row 3), TOOT 1630+4534 (bottom)

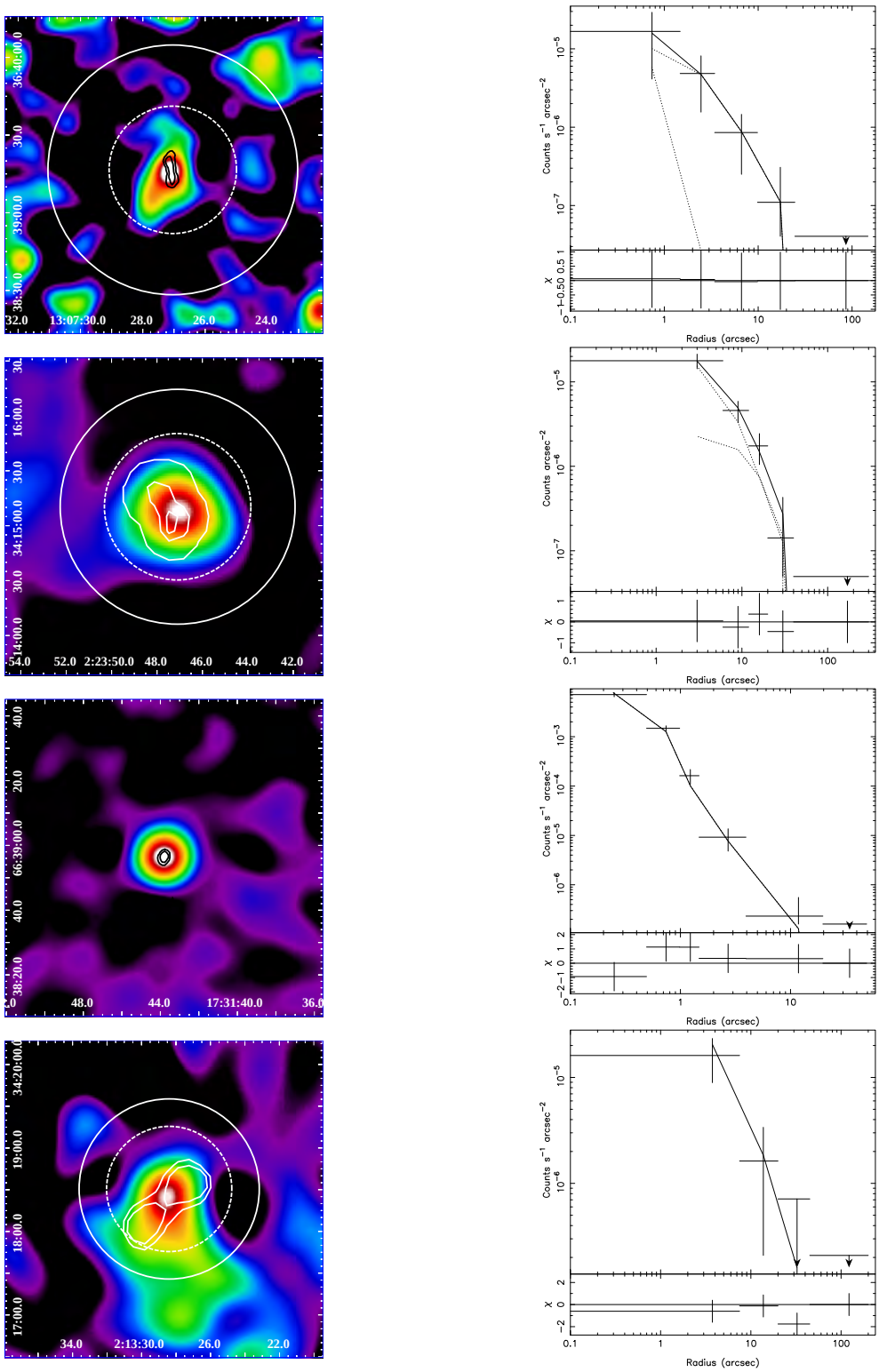

FIGURE 3.10: TOOT 1307+3639 (top), 7C 0223+3415 (row 2), 7C 1731+6638 (row 3), 7C 0213+3418 (bottom)

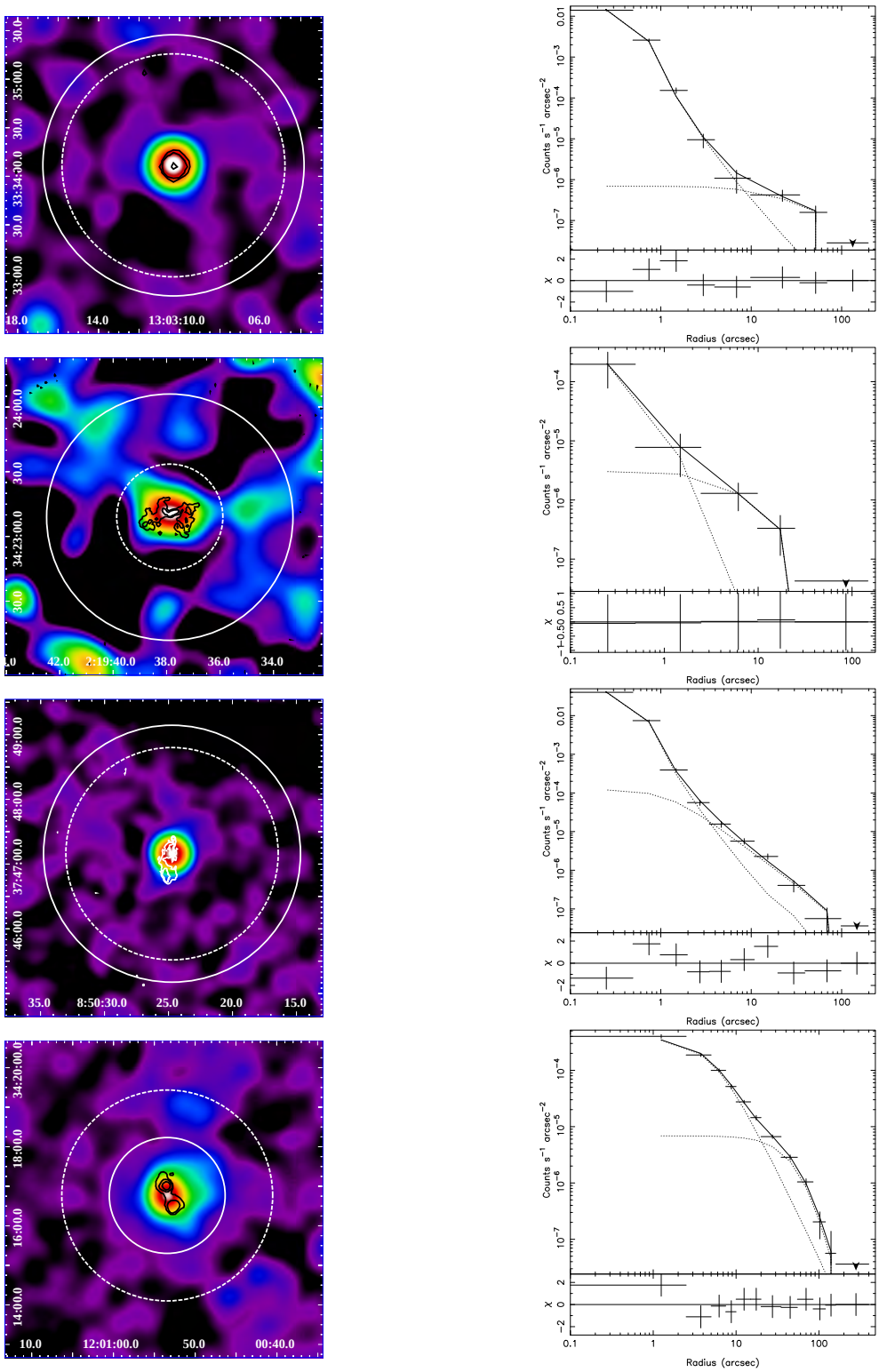

FIGURE 3.11: TOOT 1303+3334 (top), 7C 0219+3423 (row 2), 6C 0850+3747 (row 3), 6C 1200+3416 (bottom). The chip edge of 6C 0850+3747 was excluded for the analysis.

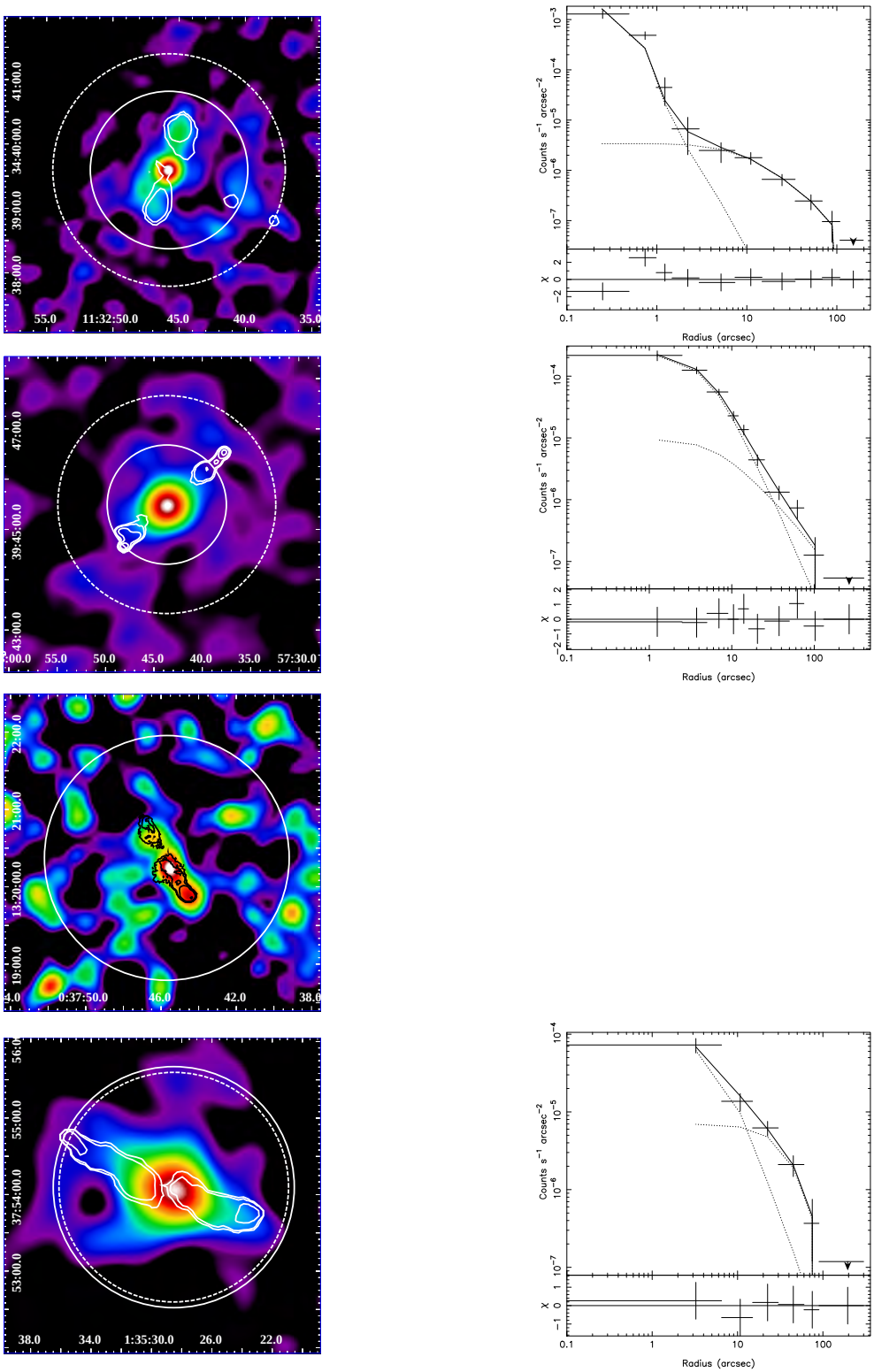

FIGURE 3.12: 6C 1132+3439 (top), 6C 0857+3945 (row 2), 3C 16 (row 3), 3C 46 (bottom). The chip edge of 6C 1132+3439 was excluded for the analysis.

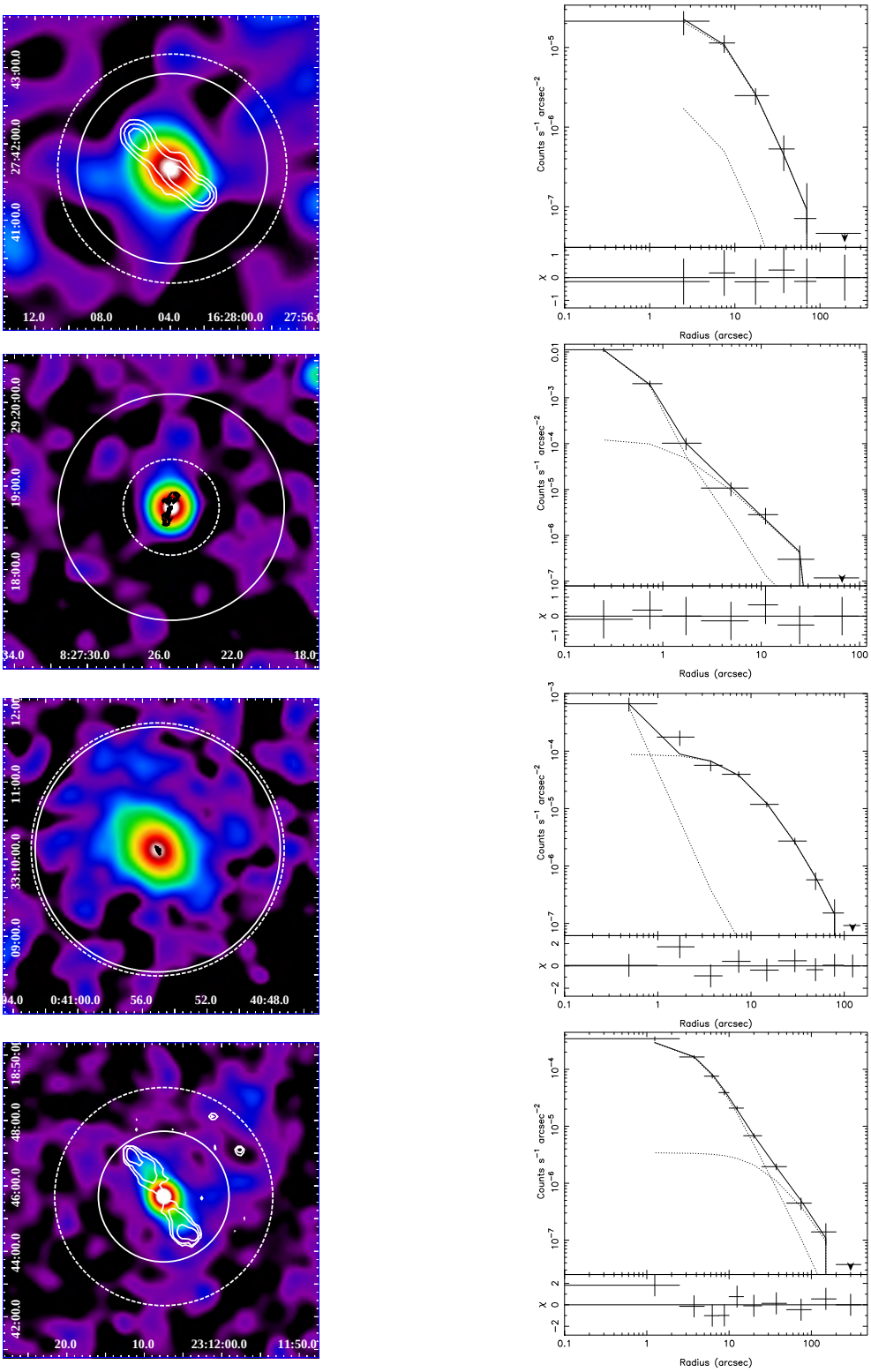

FIGURE 3.13: 3C 341 (top), 3C 200 (row 2), 3C 19 (row 3), 3C 457 (bottom)

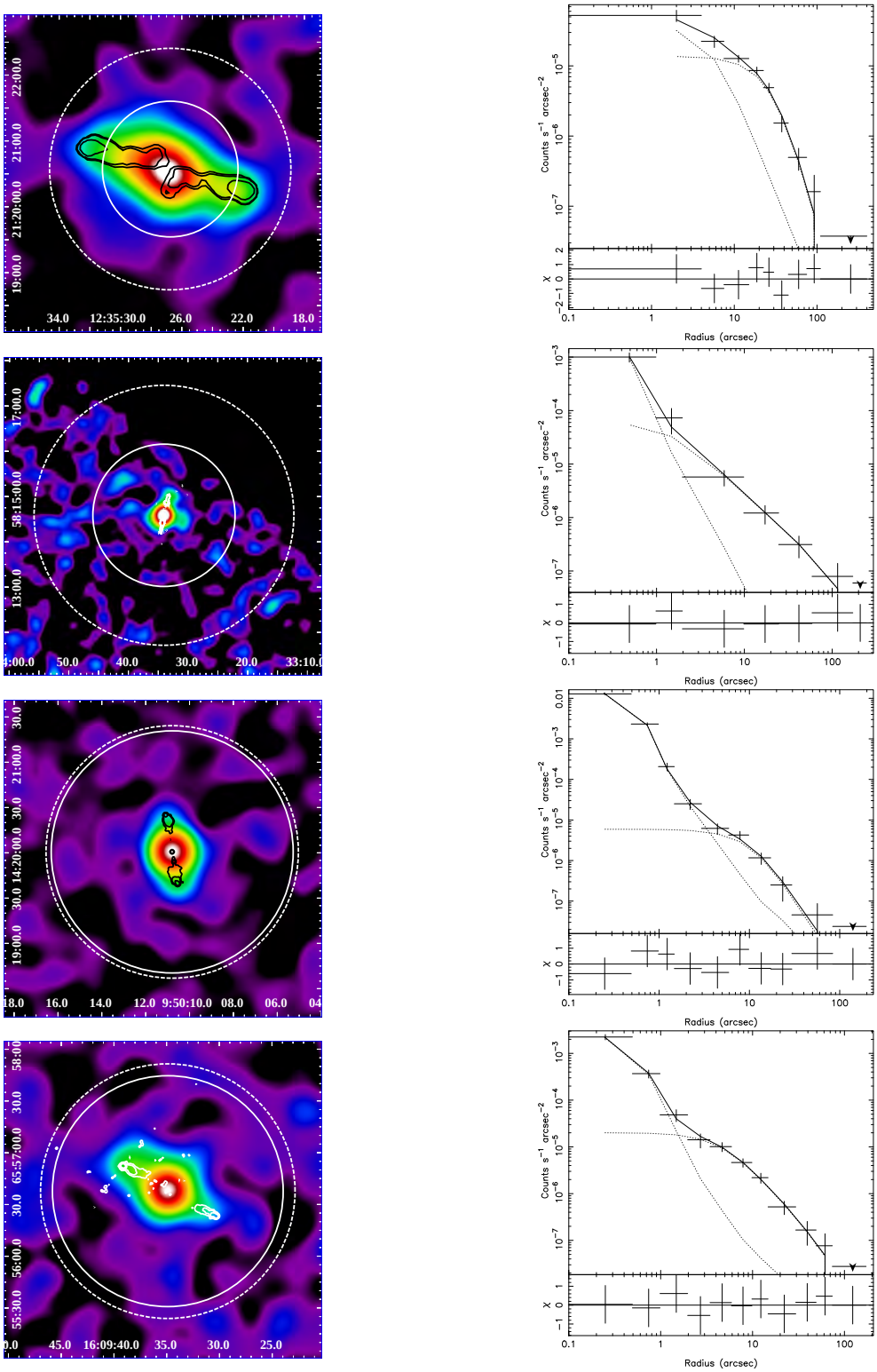

FIGURE 3.14: 3C 274.1 (top), 3C 244.1 (row 2), 3C 228 (row 3), 3C 330 (bottom). The chip edge of 3C 244.1 was excluded for the analysis.

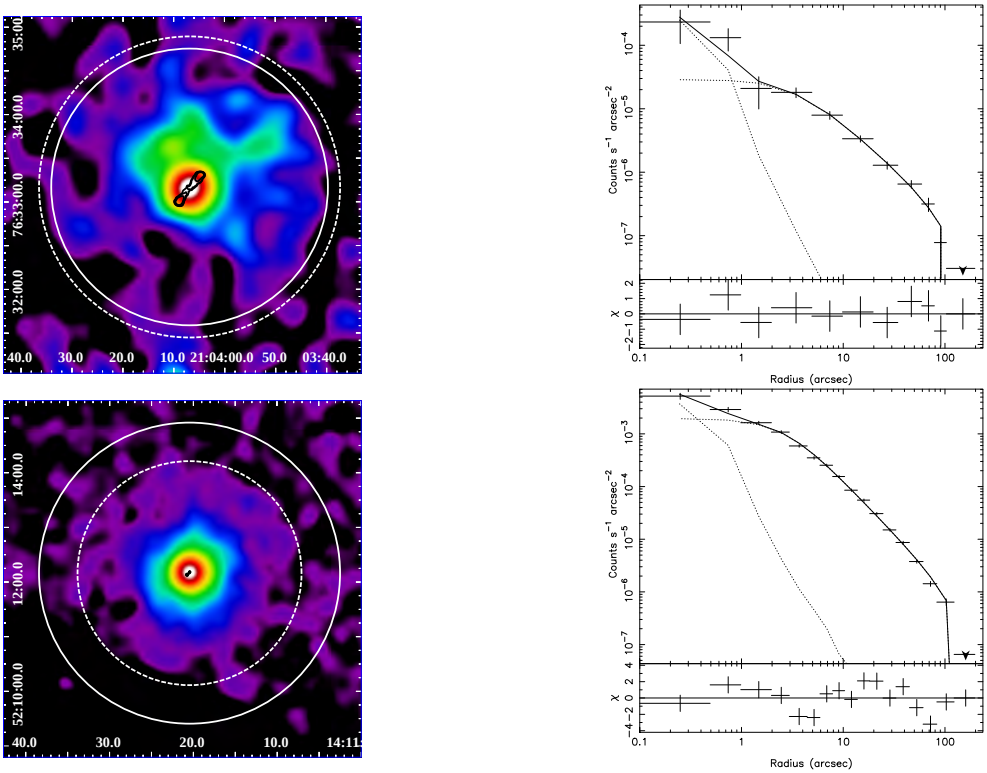

FIGURE 3.15: 3C 427.1 (top), 3C 295 (bottom)

TABLE 3.1: The ERA sample, in order of radio luminosity.

Source	RA (J2000) Dec		Redshift	Scale	$\log_{10}$ L_{151}	Type	FR	nH
	h m s	deg min sec		kpc as^{-1}	W Hz^{-1} sr^{-1}		Class	x10^{20} cm^{-2}
TOOT 1301+3658	13 01 25.03	+36 58 09.4	0.424	5.56	24.76	LERG	1	1.32
TOOT 1255+3556	12 55 55.83	+35 56 35.8	0.471	5.91	25.01	LERG	1	1.30
TOOT 1626+4523	16 26 48.5	+45 23 42.6	0.458	5.82	25.03	LERG	1	1.12
TOOT 1630+4534	16 30 32.8	+45 34 26.0	0.493	6.06	25.17	LERG	1	1.26
TOOT 1307+3639	13 07 27.07	+36 39 16.4	0.583	6.60	25.30	LERG	1	1.14
7C 0223+3415	02 23 47.24	+34 15 11.9	0.473	5.92	25.55	HERG	2	6.31
7C 1731+6638	17 31 43.84	+66 38 56.7	0.562	6.48	25.62	HERG	2	3.84
7C 0213+3418	02 13 28.39	+34 18 30.6	0.465	5.87	25.66	LERG	2	6.60
TOOT 1303+3334	13 03 10.29	+33 34 07.0	0.565	6.50	25.66	HERG	2	1.06
7C 0219+3423	02 19 37.83	+34 23 11.2	0.595	6.66	25.98	HERG?	2	6.30
6C 0850+3747	08 50 24.77	+37 47 09.1	0.407	5.43	26.15	HERG	2	2.95
6C 1200+3416	12 00 53.34	+34 16 47.3	0.530	6.29	26.17	LERG	2	1.62
6C 1132+3439	11 32 45.74	+34 39 36.2	0.512	6.18	26.33	HERG	2	2.14
6C 0857+3945	08 57 43.56	+39 45 29.0	0.528	6.28	26.34	HERG	2	2.64
3C 16	00 37 45.39	+13 20 09.6	0.405	5.41	26.82	HERG	2	4.48
3C 46	01 35 28.47	+37 54 05.7	0.437	5.66	26.84	HERG	2	5.66
3C 341	16 28 04.04	+27 41 39.3	0.448	5.74	26.88	HERG	2	3.26
3C 200	08 27 25.38	+29 18 45.5	0.458	5.82	26.92	LERG	2	3.74
3C 19	00 40 55.01	+33 10 07.3	0.482	5.98	26.96	LERG	2	5.82
3C 457	23 12 07.57	+18 45 41.4	0.428	5.59	27.00	HERG	2	22.3
3C 274.1	12 35 26.64	+21 20 34.7	0.422	5.55	27.02	HERG	2	2.00
3C 244.1	10 33 33.97	+58 14 35.8	0.430	5.61	27.10	HERG	2	0.58
3C 228	09 50 10.79	+14 20 00.9	0.552	6.42	27.37	HERG	2	3.18
3C 330	16 09 35.01	+65 56 37.7	0.549	6.41	27.43	HERG	2	2.81
3C 427.1	21 04 07.07	+76 33 10.8	0.572	6.54	27.53	LERG	2	10.90

Source	RA (J2000)	Dec	Redshift	Scale	$\log_{10}$ L_{151}	Type	FR	nH
3C 295	14 11 20.65	+52 12 09.0	0.462	5.85	27.68	LERG?	2	1.32

TABLE 3.2: Observation data for the ERA sample.

Source	X-ray[a] Instrument	Observation ID	Exposure[b] time (ks)	Screened[b] time (ks)	Radio map freq. (GHz)	Resolution (arcsec)	Ref.
TOOT 1301+3658	C	11568	39.5	39.5	1.4	5.4×5.4	1
TOOT 1255+3556	C	11569	39.5	39.5	1.4	5.4×5.4	1
TOOT 1626+4523	C	11570	36.7	36.4	1.4	17×13	2
TOOT 1630+4534	C	11571	20.8	20.8	1.4	1.3×1.3	2
TOOT 1307+3639	C	11572	39.5	39.5	1.4	1.3×1.3	2
7C 0223+3415	X	551630101	41.0	32.5	1.4	14.7×12.7	2
7C 1731+6638	C	11573	24.0	24.0	1.4	1.5×1.2	2
7C 0213+3418	X	0551630201	43.9	15.4	1.4	14.6×12.7	2
TOOT 1303+3334	C	11574	39.7	39.7	1.4	5.4×5.4	1
7C 0219+3423	C	11575	39.3	39.3	1.4	1.4×1.3	2
6C 0850+3747	C	11576	39.2	39.2	1.4	1.4×1.3	2
6C 1200+3416	X	0551630301	49.6	37.6	1.4	5.4×5.4	1
6C 1132+3439	C	11577	39.6	39.6	1.4	5.4×5.4	1
6C 0857+3945	X	551630601	24.9	10.0	1.4	5.4×5.4	1
3C 16	C	13879	11.9	11.9	1.4	1.2×1.2	3
3C 46	X	0600450501	17.9	5.5	1.5	4.2×4.2	3
3C 341	X	0600450601	16.7	13.3	1.4	1.3×1.3	3
3C 200	C	838	14.7	14.7	4.9	0.33×0.33	3
3C 19	C	13880	11.9	11.9	1.5	0.15×0.15	3
3C 457	X	0502500101	52.2	36.8	1.4	5.1×5.1	3
3C 274.1	X	0671640801	27.2	22.5	1.4	5.4×5.4	1
3C 244.1	C	13882	11.9	11.8	8.4	0.75×0.75	4
3C 228	C	2453/2095	10.6/13.8	24.4	8.4	1.2×1.2	4
3C 330	C	2127	44.2	44.0	1.5	1.5×1.5	5
3C 427.1	C	2194	39.5	39.5	1.5	1.8×1.1	6

Source	Instrument	Obs. ID	Exposure[b] time	Screened[b] time	Radio map freq.	Resolution	Ref.
3C 295	C	578	18.8	18.2	8.7	0.2×0.2	3

References: (1) Becker et al. (1995), (2) Mitchell (2005), (3) `http://www.jb.man.ac.uk/atlas`, (4) Mullin et al. (2008), (5) Hardcastle et al. (2002a), (6) Croston et al. (2005b)

[a] C=*Chandra*, X=*XMM-Newton*. [b] pn camera times for *XMM-Newton* sources.

TABLE 3.3: Radial profile modelling results for the ERA sample.

Source	R_{det} kpc	Counts[a]	PSF fit χ^2/dof	PSF+β fit χ^2/dof	β[b]	r_c[a] arcsec
TOOT 1301+3658		(< *94*)	*Low counts*		*0.49*	*5.58*
TOOT 1255+3556	174	340	5.4/5	0.23/2	$1.48^{+0.02}_{-1.15}$	$19.00^{+11.6}_{-16.5}$
TOOT 1626+4523	286	108	16/6	0.62/3	$0.30^{+0.19}_{-0.10}$	$2.10^{+7.89}_{-1.10}$
TOOT 1630+4534		(< *63*)	*Low counts*		*0.49*	*5.13*
TOOT 1307+3639	162	26	4.2/4	0.007/1	$0.53^{+1.08}_{-0.16}$	$1.91^{+7.89}_{-0.90}$
7C 0223+3415		(< *77*)	*Low counts*		*0.49*	*5.24*
7C 1731+6638		(< *63*)	*Low counts*		*0.49*	*4.79*
7C 0213+3418		(< *100*)	*Low counts*		*0.49*	*5.29*
TOOT 1303+3334	68.9	867	33/7	6.1/4	$0.22^{+0.13}_{-0.05}$	$7.82^{+2.17}_{-6.55}$
7C 0219+3423	164	46	6.0/4	0.008/1	$0.45^{+0.54}_{-0.24}$	$4.70^{+5.28}_{-3.70}$
6C 0850+3747	534	2351	84/9	10/6	$0.45^{+0.04}_{-0.02}$	$1.01^{+1.49}_{-0.01}$
6C 1200+3416	1007	1983	120/10	36/7	$0.41^{+0.03}_{-0.04}$	$6.22^{+0.07}_{-4.65}$
6C 1132+3439	669	389	55/10	9.3/7	$0.38^{+0.07}_{-0.09}$	$7.73^{+2.26}_{-6.73}$
6C 0857+3747	816	612	8.8/9	2.2/6	$0.41^{+0.15}_{-0.17}$	$1.12^{+15.80}_{-0.12}$
3C 16		(< *60*)	*Low counts*		*0.49*	*5.74*
3C 46	510	170	13/5	0.57/2	$1.49^{+0.01}_{-0.97}$	$66.3^{+18.0}_{-45.5}$
3C 341	517	214	20/5	0.25/2	$0.54^{+0.96}_{-0.10}$	$1.74^{+40.36}_{-0.23}$
3C 200	200	259	16/6	0.77/3	$0.48^{+0.15}_{-0.05}$	$1.10^{+1.78}_{-0.09}$
3C 19	589	503	294/8	4.4/5	$0.61^{+0.06}_{-0.05}$	$7.73^{+1.91}_{-1.67}$
3C 457	1119	2402	51/9	6.5/6	$0.45^{+0.21}_{-0.11}$	$18.3^{+29.6}_{-17.3}$
3C 274.1	610	678	121/8	3.8/5	$1.16^{+0.34}_{-0.41}$	$32.0^{+11.5}_{-13.4}$
3C 244.1	966	171	28/6	0.82/3	$0.41^{+0.04}_{-0.05}$	$1.03^{+2.13}_{-0.01}$
3C 228	537	768	32/9	3.3/6	$0.90^{+1.10}_{-0.33}$	$12.3^{+15.6}_{-6.2}$
3C 330	473	360	82/10	1.3/7	$0.56^{+0.11}_{-0.07}$	$4.80^{+2.65}_{-1.86}$
3C 427.1	675	721	288/10	4.7/7	$0.40^{+0.14}_{-0.02}$	$3.14^{+1.22}_{-1.18}$
3C 295	719	5308	3978/17	37/14	$0.50^{+0.005}_{-0.004}$	$2.52^{+0.19}_{-0.15}$

[a] Upper limits were obtained within estimated R_{500}. Counts for *XMM-Newton* sources are for the pn camera only. [b] Italics indicate median values used for sources with low counts.

TABLE 3.4: ICM X-ray luminosity for the ERA sample.

Source	$L_X(0.4-7.0keV)$ D_{rad} $\times 10^{43} erg.s^{-1}$	$L_X(bol)$ D_{rad} $\times 10^{43} erg.s^{-1}$	R_{500} kpc	$L_X(bol)$ R_{500} $\times 10^{43} erg.s^{-1}$	$h(z)^{-1}L_X(bol)$ R_{500} $\times 10^{43} erg.s^{-1}$
TOOT 1301+3658			380^a	< 0.772	< 0.7571
TOOT 1255+3556	$0.25^{+0.10}_{-0.24}$	$0.44^{+0.18}_{-0.42}$	351	$0.48^{+0.20}_{-0.47}$	0.37
TOOT 1626+4523	$1.61^{+0.70}_{-0.99}$	$2.45^{+1.07}_{-1.52}$	533	$5.30^{+2.83}_{-4.26}$	4.15
TOOT 1630+4534			380^a	< 2.44	< 1.87
TOOT 1307+3639	$0.23^{+0.11}_{-0.22}$	$0.40^{+0.20}_{-0.39}$	317	$0.41^{+0.20}_{-0.41}$	0.30
7C 0223+3415			380^a	< 1.45	< 1.12
7C 1731+6638			380^a	< 2.97	< 2.19
7C 0213+3418			380^a	< 8.51	< 6.60
TOOT 1303+3334	$3.92^{+1.89}_{-2.48}$	$6.00^{+2.90}_{-3.80}$	525	$7.54^{+3.98}_{-4.97}$	5.55
7C 0219+3423	$0.56^{+0.24}_{-0.53}$	$1.00^{+0.42}_{-0.95}$	380	$1.27^{+0.71}_{-1.25}$	0.92
6C 0850+3747	$2.95^{+0.42}_{-0.49}$	$4.22^{+0.60}_{-0.70}$	648	$4.53^{+0.70}_{-0.77}$	3.65
6C 1200+3416	$8.48^{+1.05}_{-1.04}$	$12.69^{+1.57}_{-1.55}$	553	$8.28^{+0.95}_{-0.92}$	6.21
6C 1132+3439	$6.61^{+1.81}_{-2.00}$	$10.89^{+2.98}_{-3.30}$	454	$7.30^{+1.61}_{-1.84}$	5.54
6C 0857+3945	$1.89^{+1.00}_{-1.42}$	$3.15^{+1.67}_{-2.35}$	447	$2.87^{+1.62}_{-2.06}$	2.16
3C 16			515^b	< 2.79	< 2.25
3C 46	$3.90^{+0.87}_{-1.09}$	$5.95^{+1.33}_{-1.67}$	535	$6.03^{+1.37}_{-1.72}$	4.79
3C 341	$0.79^{+0.34}_{-0.32}$	$1.33^{+0.57}_{-0.54}$	429	$1.29^{+0.51}_{-0.54}$	1.02
3C 200	$1.41^{+0.42}_{-0.41}$	$2.28^{+0.69}_{-0.67}$	474	$2.64^{+0.93}_{-0.99}$	2.07
3C 19	$24.643^{+1.90}_{-2.18}$	$36.589^{+2.82}_{-3.23}$	570	$36.4^{+2.8}_{-3.1}$	28.1
3C 457	$6.48^{+1.67}_{-1.48}$	$9.03^{+2.33}_{-2.06}$	670	$6.14^{+1.05}_{-1.13}$	4.89
3C 274.1	$2.25^{+0.22}_{-0.21}$	$3.82^{+0.38}_{-0.36}$	343	$3.66^{+0.35}_{-0.29}$	2.92
3C 244.1	$4.06^{+1.40}_{-1.55}$	$6.15^{+2.11}_{-2.35}$	529	$4.54^{+1.36}_{-1.33}$	3.61
3C 228	$2.09^{+0.44}_{-0.58}$	$3.22^{+0.67}_{-0.89}$	515	$3.22^{+0.67}_{-0.89}$	2.39
3C 330	$2.75^{+0.42}_{-0.55}$	$4.75^{+0.72}_{-0.95}$	430	$4.64^{+0.70}_{-0.86}$	3.44
3C 427.1	$19.5^{+1.8}_{-2.2}$	$27.9^{+2.5}_{-3.1}$	620	$26.2^{+2.5}_{-2.5}$	19.2
3C 295	125^{+2}_{-2}	171^{+3}_{-3}	966	183^{+4}_{-4}	143

L_X is the ICM X-ray luminosity, calculated within either the maximum detected radius D_{rad} or the R_{500} overdensity radius.

[a] Median R_{500} of 7C and TOOT sources. [b] Median R_{500} of 6C and 3C sources.

TABLE 3.5: ICM temperatures for the ERA sample.

Source	Method	Annulus radii kpc	Temperature keV	χ^2/dof[a]
TOOT 1301+3658	Upper limit		< 1.21	
TOOT 1255+3556	Estimate	15–174	$1.04^{+0.11}_{-0.63}$	
TOOT 1626+4523	Estimate	15–296	$2.14^{+0.29}_{-0.81}$	
TOOT 1630+4534	Upper limit		< 1.69	
TOOT 1307+3639	Estimate	16–162	$0.98^{+0.11}_{-0.67}$	
7C 0223+3415	Upper limit		< 1.41	
7C 1731+6638	Upper limit		< 1.77	
7C 0213+3418	Upper limit		< 2.37	
TOOT 1303+3334	Estimate	51–448	$2.33^{+0.32}_{-0.62}$	
7C 0219+3423	Estimate	17–164	$1.36^{+0.18}_{-0.91}$	
6C 0850+3747	Spectrum	21–160	$2.86^{+2.11}_{-0.78}$	3.77/4
6C 1200+3416	Spectrum	252–944	$2.46^{+1.89}_{-0.65}$	84.0/78
6C 1132+3439	Spectrum	15–486	$1.71^{+0.69}_{-0.37}$	4.16/5
6C 0857	Estimate	251–816	$1.69^{+0.24}_{-0.55}$	
3C 16	Upper limit		< 1.78	
3C 46	Estimate	170–510	$2.11^{+0.14}_{-0.20}$	
3C 341	Estimate	115-517	$1.45^{+0.16}_{-0.22}$	
3C 200	Estimate	15-215	$1.74^{+0.16}_{-0.23}$	
3C 19	Spectrum	29-383	$2.47^{+0.63}_{-0.38}$	4.78/11
3C 457	Spectrum	168–839	$3.10^{+2.95}_{-1.00}$	95.7/75
3C 274.1	Spectrum	166–555	$0.95^{+0.29}_{-0.25}$	9.99/12
3C 244.1	Estimate	14–966	$2.05^{+0.17}_{-0.19}$	
3C 228	Spectrum	31–316	$2.22^{+2.39}_{-0.71}$	1.06/4
3C 330	Spectrum	25–441	$1.61^{+1.26}_{-0.35}$	0.76/3
3C 427.1	Spectrum	32–193	$3.14^{+5.27}_{-1.18}$	2.86/4
3C 295	Spectrum	29–575	$6.09^{+0.73}_{-0.73}$	72.3/85

[a] For temperatures obtained using spectral analysis.

TABLE 3.6: Generalized Kendall's τ correlation tests

Subpopulation	Z	N	p
Radio luminosity vs ICM luminosity			
All data	2.841	26	0.0045
HERG	0.862	15	0.39
HERG–no 7C 0219	0.446	14	0.66
LERG	2.655	11	0.0079
LERG–no 3C 295	2.140	10	0.032
FRII	1.903	21	0.0571
Black hole mass vs ICM luminosity			
All data	1.539	26	0.12
HERG	1.470	15	0.14
LERG	1.202	11	0.23
ICM temperature vs luminosity			
All data	5.082	26	< 0.00005
Spectrum method	2.236	9	0.025
B_{gg}(977 kpc) vs ICM luminosity			
All data	1.965	26	0.049
HERG	0.963	15	0.34
LERG	1.456	11	0.15
FRII	2.064	21	0.039
B_{gg}(564 kpc) vs ICM luminosity			
All data	2.557	26	0.011
HERG	1.878	15	0.060
LERG	1.456	11	0.15
FRII	3.064	21	0.0022

Z is the correlation statistic; N is sample size; p is probability under the null hypothesis.

Chapter 4

Environments at redshift 0.1, and environment evolution

The contents of this chapter have been published in Monthly Notices of the Royal Astronomical Society as Ineson et al. (2015).

4.1 Introduction

In the previous chapter I reported a comparison of radio luminosity and cluster richness (as measured by ICM X-ray luminosity) within a limited redshift range ($0.4 < z < 0.6$), the aim of the work being to look for relationships between radio galaxies and their environments while excluding any evolution with epoch. I found that the low excitation radio galaxies occupied a wide range of environments covering over 2 decades of ICM luminosity, and that there was a correlation between radio luminosity and environment richness. In contrast, the high excitation sources occupied a only a single decade of ICM luminosity and showed no sign of a correlation.

As noted in Section 3.5.4 however, the spectral type of the LERG with the highest radio and ICM luminosities has been questioned. Removing this source weakens the LERG correlation and the results should therefore be considered tentative.

Previous studies have found different results when looking for changes in the cluster environment with redshift (eg Harvanek et al. 2001; Belsole et al. 2007; Ramos Almeida et al. 2013; Wold et al. 2000; McLure and Dunlop 2001) – these results are discussed in Section 1.3. In this chapter I therefore address the questions: do the findings at redshift 0.5 also apply to radio galaxies at other redshifts? and does the environment evolve with epoch?

This chapter contains the results of a similar analysis to that in Chapter 3 but using a low redshift comparison sample, to see if the results reflect those of the ERA sample and if so, whether the conclusions are strengthened by the use of a larger sample. The two samples are then compared to see if there is any evidence of environment change with epoch. I used a sample at $z \sim 0.1$ since it is well separated in redshift from the previous sample and there are sufficient radio galaxies in that redshift range with existing X-ray observations to create a large sample covering a range of radio luminosities that overlap with those of the ERA sample.

4.2 The sample

The new sample, hereafter referred to as the z0.1 sample, consists of all radio-loud AGN with radio lobes visible beyond the nucleus within the redshift range $0.01 \leq z \leq 0.2$ from two flux-limited radio surveys: the 3CRR survey (Laing et al. 1983) and the subsample of the 2Jy survey (Wall and Peacock 1985; Tadhunter et al. 1993) defined by Dicken et al. (2008). The initial sample contained 38 3CRR and 22 2Jy sources, but five sources were excluded. 3C 382 has currently no suitable *Chandra* or *XMM-Newton* observation, 3C 83.1B, 3C 264 and Abell 1552 all lie in the outskirts of richer clusters, so that their immediate environments could not be disentangled from those of the stronger sources for the spherical modelling, while the angular size of the cluster emission of 3C 84 (Perseus A) is so large that analysis was impractical. The final sample consists of 55 sources comprising 25 HERGs and 30 LERGS. 22 of the sources have FRI morphologies, and 33 are FRIIs.

The properties of the sources are listed in Table 4.1 and Figure 4.1 shows radio luminosity plotted against redshift. The ERA sample sources used in Chapter 3 are also shown in Figure 4.1. Positions, radio luminosities, spectral type and morphologies of the sources were taken from the on-line 3CRR catalogue[1] and from Mingo et al. (2014). Redshifts were taken from the most recent source cited in the 3CRR catalogue, Mingo et al. (2014), the NASA/IPAC Extragalactic Database (NED)[2] and the SIMBAD astronomical database[3]. Galactic column densities came from Dickey and Lockman (1990) via the HEASARC tools.

As can be seen in Figure 4.1, the z0.1 sample shows a strong relationship with redshift which is not present in the ERA sample. This needs to be accounted for in the statistical analysis.

[1] http://3crr.extragalactic.info/
[2] http://ned.ipac.caltech.edu/
[3] http://simbad.u-strasbg.fr/simbad/

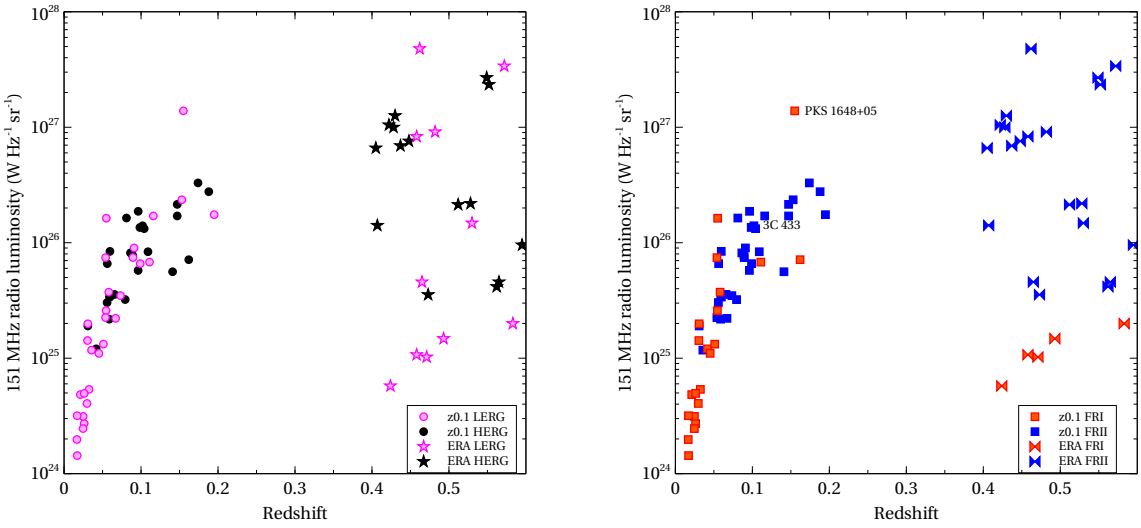

FIGURE 4.1: 151 MHz radio luminosity vs redshift for the z0.1 sample and the ERA ($z \sim 0.5$) sample used in Chapter 3. The left plot shows the HERG (black symbols) and LERG (magenta symbols) excitation classes and the right plot shows FRI (red symbols) and FRII (blue symbols) morphologies. 3C 433 and PKS 1648+05 have hybrid morphologies.

4.3 Observations and data preparation

4.3.1 X-ray data

All but two of the X-ray observations for the z0.1 sample came from the *Chandra* archive; for 3C 31 and 3C 66B I used observations from the *XMM-Newton* archive. The *XMM-Newton* observations used the three EPIC cameras with the medium filter and the *Chandra* observations used either the ACIS-S3 chip or the four ACIS-I chips. Observation IDs and times are given in Table 4.2.

I followed the procedures described in Section 2.2.1 for the initial data processing, using the *Chandra* analysis packages CIAO v4.5 and CALDB v4.5.8 for the *Chandra* observations and *XMM-Newton* SAS v11.0.0 for the *XMM-Newton* observations. Screened observation times are included in Table 4.2. Since the clusters and groups at $z \sim 0.1$ had a larger angular size than those from the ERA sample described in the previous chapter, in some cases extending beyond the observing chip, I built exposure maps and background files for the *Chandra* sources. These were used when generating surface brightness profiles and spectra.

I checked for pile-up, as described in Section 2.2.1.3. One source had severe pile-up (3C 390.3), and three had mild pile-up (3C 219, 3C 303 and NGC 6251). I also checked for extraneous emission (Section 2.2.1.5) which I excluded during subsequent analysis.

4.3.2 Radio data

Radio maps were used to mask out the radio lobes so that any radio-related X-ray emission did not contaminate my measurements of the cluster properties. All of the 3CRR radio maps except that of NGC 7385 were taken from the 3CRR Atlas[4]. I also used existing maps for the majority of the 2Jy sources. The remaining six maps were made using observations from the VLA and ATCA archives and reduced using AIPS in the standard manner by Dr. Hardcastle.

Table 4.2 contains the full details of the radio maps used, including references.

4.4 Analysis

The aim of the analysis was to find the temperature and X-ray luminosity of the ICM emission of the radio galaxies. Where possible, the temperature was obtained by spectral analysis; when there were insufficient counts, it was estimated from the count rate in a self-consistent way, as described in Section 4.4.1. The luminosity was determined by integrating the surface brightness profiles to the R_{500} overdensity radius (defined in Section 3.4.2).

Section 4.7 contains brief notes on the individual sources.

4.4.1 Spatial analysis

I extracted a radial surface brightness profile from the events file of each source using the methods described in Section 2.2.2. I used an energy range of 0.4-7.0 keV, this being the well calibrated range for the *Chandra* data.

For the *XMM-Newton* sources, I used the standard double subtraction method using the closed filter files. For the *Chandra* sources, when the maximum detection radius lay at least partially within the ACIS-S3 or ACIS-I chips I used the double subtraction method where the background in the blank sky files was subtracted from both the source and background regions before generating the profile. If the maximum detection radius was so extensive that I could not select a suitable background region, I used the appropriate *Chandra* blank sky files as the background.

Table 4.3 contains the maximum detection radius D_{rad} and the net counts within that radius for each of the sources. If the emission extends beyond the chip, the maximum detection radius is quoted as the distance to the chip edge.

[4]http://www.jb.man.ac.uk/atlas

I fitted the surface brightness profiles with β models, using the MCMC method described by Croston et al. (2008a) and in Section 2.2.2. Since these sources are nearer than those in the ERA sample, their host galaxies usually extend beyond the instrument PSF. In these cases, a second β model was added so that the inner and outer components of the profile were modelled individually.

If there was no extended emission visible, or if the modelled emission did not extend beyond the host galaxy radius, I derived an upper limit as described in Section 2.2.2. This was the case for seven sources.

The surface brightness profiles for each source are shown in Section 4.7. The goodness-of-fit and ICM β model parameters are shown in Table 4.3, and also the inner beta model parameters for the sources where the galaxy emission was discernible. The distributions of β and the core radius (r_c) for the ICM model are shown in Figure 4.2. Except for a few high values, the values of β are mostly lower than the values of typical clusters, as is expected for less rich environments (e.g. Mulchaey 2000). The overall median β for the z0.1 sample is 0.47, close to the value of 0.5 expected for groups. The ERA sample also has a median of 0.47, showing consistency between the two samples.

There are eight sources with high values of β compared with the rest of the sample and six sources with a very low core radius. 3C 442A and PKS 0915−11 (Hyd A) contain interacting galaxies which have sent shocks into the ICM. The disturbance is clearly visible in the surface brightness profiles. Both profiles contain sufficient counts to show that the outer ICM is well modelled. The other sources have very little emission detected beyond the host galaxy and so their models are poorly constrained. The profiles of the environments with high βs have ICM emission visible beyond the host, but because there are few bins the profiles look flat and wide and this is reflected in the model parameters (eg 3C 326). The outer emission of the sources with low core radii have the opposite problem, with the outer profile merging smoothly with that of the host galaxy so they are hard to differentiate (eg 3C 98).

For some of the inner β models, it was difficult to differentiate between the point source and the galaxy, and consequently some of the galaxy βs are very high. However, as I only wished to model the shapes in order to exclude them from the luminosity calculation, I did not expect this to be of concern provided the profile shape was well modelled. I tested this assumption using the sources with the two highest galaxy βs — 3C 98 and PKS 1559+02. I fixed the galaxy βs at the median value of 0.95, refitted the surface brightness profiles and recalculated the luminosities. They were both consistent with the luminosities calculated using the high values of β.

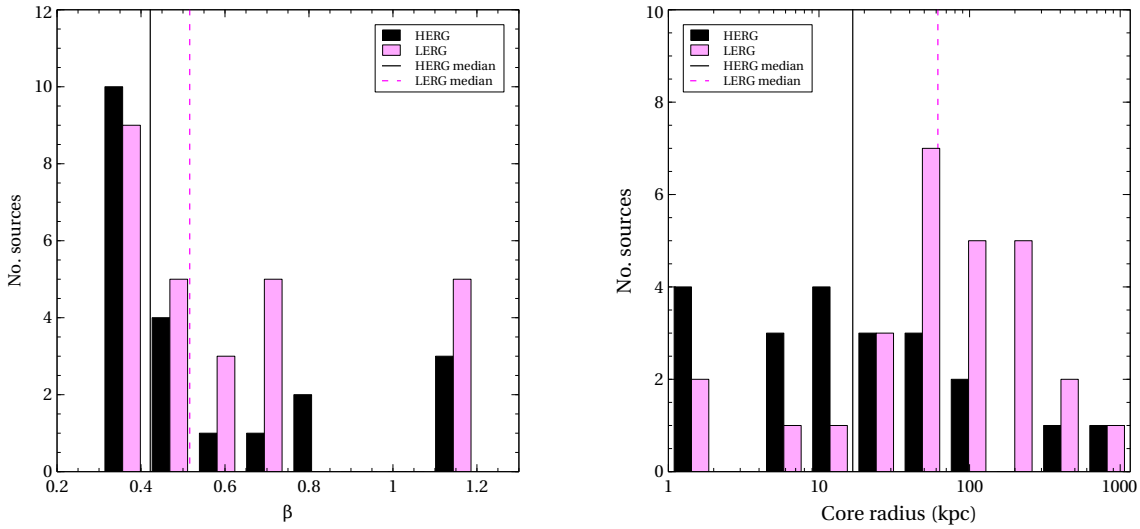

FIGURE 4.2: Distribution of the β model parameters for the z0.1 sample; β (left) and core radius (right). The LERGs are magenta and the HERGs black. Dashed lines show the LERG medians and solid lines the HERG medians.

Because the *Chandra* blank sky files may not model the background accurately, I looked for systematic differences between the profiles made using double and single background subtraction. All the single subtraction sources have a large number of counts and well-defined profiles, and the β model parameters cover a similar range to those of the double subtraction sources. All except PKS 1648+05 (Her A) are towards the low end of the redshift range, so would be expected to cover the chip if the environment was relatively rich and/or the observation long.

Luminosity within the R_{500} overdensity radius was calculated by integrating the ICM β model profile as described in Section 2.2.2, having extrapolated the β model profile to R_{500}. Luminosity upper limits were calculated within the median R_{500} (533 kpc), using the median β and r_c for the profile shapes and the count rate upper limits for the normalisations.

Table 4.4 contains three bolometric X-ray luminosities ($L_X(bol)$) for each source: within the maximum detection radius D_{rad}; within the R_{500} overdensity radius; and within R_{500} but scaled by $h^{-1}(z)$ to correct for the critical density evolution. Figure 4.3 shows the luminosity distribution; it can be seen that, as with the sample at redshift 0.5, the most luminous environments are occupied by LERGs.

The sources with emission extending beyond the chip have luminosities from 0.4×10^{43} to 61×10^{43} erg s^{-1}, so cover most of the luminosity range. Since their emission is so extensive, it is to be expected that they tend to be high luminosity. Five of the ten clusters with luminosity greater than 10^{44} erg s^{-1} are among this group, and they include four of the five most luminous clusters.

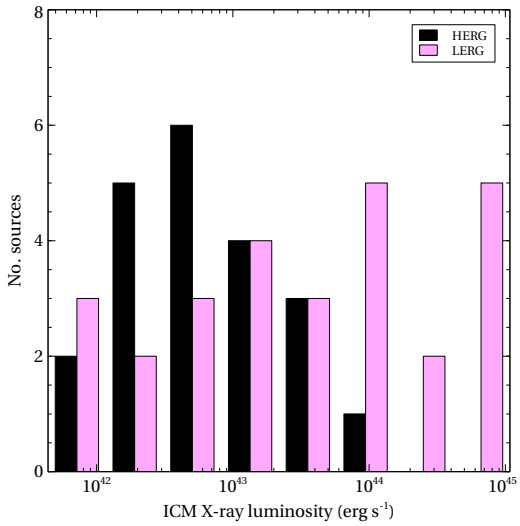

FIGURE 4.3: ICM X-ray luminosity distribution for the z0.1 sample, separated into excitation classes (upper limits excluded). Symbols as in Figure 4.2.

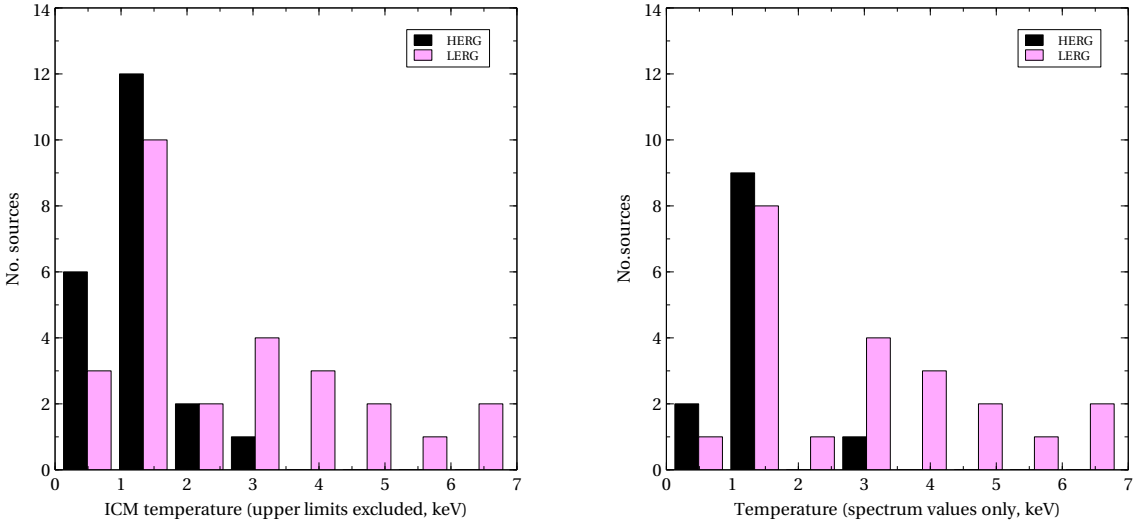

FIGURE 4.4: ICM temperature distribution for the z0.1 sample, separated into excitation classes (upper limits excluded). The left histogram includes all sources; the right histogram shows only those with temperatures obtained by spectral analysis. Symbols as in Figure 4.2.

I also wished to gain some idea of the central conditions of the radio galaxy environments so I calculated the environment density at a radius of $0.1R_{500}$; for all but two of the sources this was not much larger than the host galaxy radius and so was the closest radius to the source that I could measure the density. I used the method described in Birkinshaw and Worrall (1993) (Section 2.2.2, equation 2.3 on). I calculated the electron density at $0.1R_{500}$ for each sample in the MCMC code output, using the same method that I used for the luminosity calculations. The uncertainties were also derived in the same manner. The densities are included in Table 4.4.

4.4.2 Spectral analysis

When there were sufficient counts, I obtained the ICM temperature from spectral analysis, following the procedures in Section 2.2.3. I used the XSPEC package, using the *apec* model for the thermal bremsstrahlung from the ICM and the *wabs* photo-electric absorption model to take account of Galactic absorption. I reduced the energy range to 0.5 to 5.0 keV to reduce the PSF-scattered high energy emission from the nucleus and, where possible, I used a double subtraction method as described in Section 2.2.3.3, using a region from outside the maximum detected radius as the background for both the source and blank sky events files.

In some sources, the *Chandra* blank sky files matched the background from the source observation sufficiently well that there were very few counts left after the background subtraction. In these cases, I used single subtraction with a region from outside the maximum detected radius as the background for the spectrum (Section 2.2.3.1).

If the source emission was so extensive that there was no region of the source observation that could be used for background, I could not use double subtraction. In this case, single subtraction using the blank sky files as background was the only method available (Section 2.2.3.2). In addition to the ICM emission, the cosmic ray background and local thermal emission were modelled as in the double subtraction method, but were left as free parameters.

For 3C 31 and 3C 66B, I also excluded the 1.4 to 1.6 keV energy band from the spectrum to remove the *XMM-Newton* 1.5 keV instrumental aluminium fluorescence line (Strüder et al. 2001).

The spectra for 18 sources had insufficient counts to model the spectrum. For these sources I extracted a spectrum to the maximum detected radius and estimated the temperature as described in Section 2.2.3.4.

The distribution of temperatures is shown in Figure 4.4, and Table 4.4 contains the inner and outer radii of the annuli, the temperatures of the sources and the χ^2 for the temperatures obtained by spectral analysis. The temperatures range from 0.65 to 6.8 keV – a similar range to the ERA sample – and are for the most part typical of groups and poor clusters. The temperatures for the sources where the emission extended beyond the chip included the highest temperature (6.8 keV), but otherwise ranged from 1.38 keV to 4.43 keV, not concentrated in or dominating any temperature range. Although the distributions of both types of radio galaxy peak at low temperatures, the LERGs have a wider range of temperatures with the top of the range being occupied exclusively by LERGs.

In Section 4.7 I compare my results with previously published analyses of the sources.

4.5 Results and discussion

4.5.1 Radio galaxy environments

4.5.1.1 z0.1 sample results

I first compared radio and ICM luminosities for the z0.1 sample, to see if the results differed from those found for the ERA sample. As can be seen from Figure 4.5 (left), the HERG subsample tends to cluster in the lower, central region of the plot, while the LERG subsample forms a diagonal across the plot. Since there is a strong correlation between radio luminosity and redshift from the Malmquist bias and the lack of high luminosity local sources (see Figure 4.1), I used partial correlation Kendall's τ tests (Akritas and Siebert 1996) to look for correlations between the radio and ICM luminosities in the presence of a dependency on redshift, and found a weak correlation for the full sample, a strong correlation for the LERG subsample ($> 3\sigma$) and no correlation for the HERGs (Table 4.5). Figure 4.1 suggests a correlation between L_R and L_X for the HERGS; in order to check that this was due to the redshift correlation I also looked for a correlation between radio luminosity and redshift in the presence of a common correlation with ICM luminosity. As can be seen from Table 4.5, this gave a strong correlation.

These results strengthen those found with the ERA sample at $z \sim 0.5$ and demonstrate for the first time a clear relationship between the radio properties of the source and the ICM and the difference in the ICM properties of the subsamples.

Because the sources are relatively close, the maximum detected radius is on average only half of R_{500}. Consequently, the beta models needed to be extrapolated to calculate the luminosities for all but ten of the sources. I therefore also calculated the luminosity for each source within $0.5R_{500}$ (which was within the maximum detected radius for 80 per cent of the sources) to check that the statistical results were similar. This gave similar results for the partial correlation tests between the subsamples ($> 3\sigma$ for the LERGS, no correlation for the HERGs), implying that the extrapolation to R_{500} does not have a significant effect.

I also checked the LERG results for a subsample with $z > 0.03$, removing the bulk of the redshift dependence, which gave a weaker correlation ($> 2\sigma$). This was to be expected, since the scatter is proportionally greater over the reduced luminosity range.

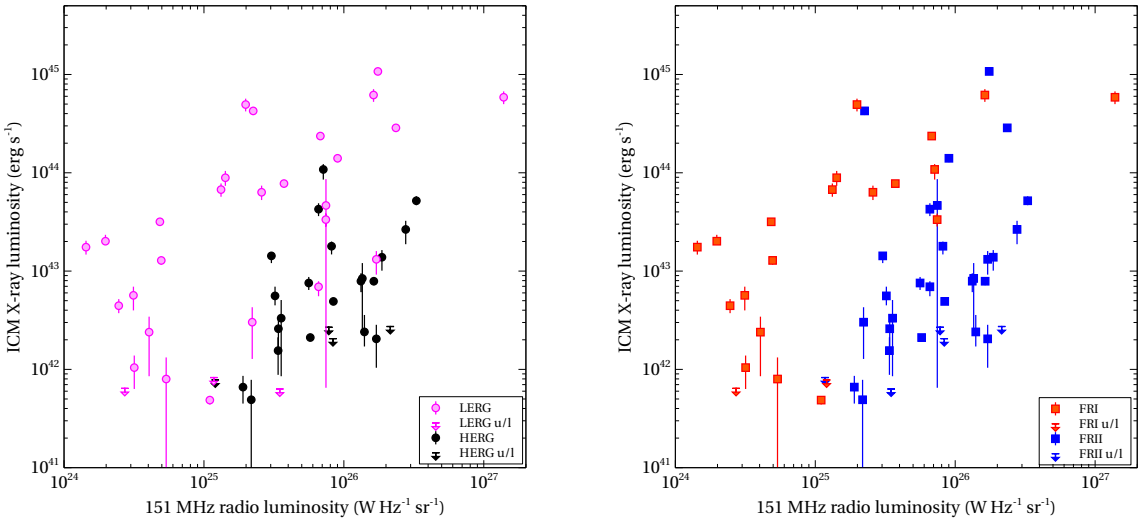

FIGURE 4.5: Radio luminosity vs ICM X-ray luminosity for the z0.1 sample, separated into excitation classes (left), and FRI and FRII galaxies (right). LERGs/FRIs are shown by magenta/red symbols and HERGs/FRIIs by black/blue symbols. Upper limits are shown by arrows in the corresponding colour.

For the FRI and FRII subsamples in Figure 4.5 (right), there appears to be a correlation between radio and ICM luminosity for both subsamples, and this is confirmed by the partial correlation tests (Table 4.5) ($> 2.5\sigma$ for both subsamples). Since the FRI and FRII subsamples contain both HERGs and LERGs, one would expect their correlation strengths to lie between those of the HERGs and LERGs, and this is the case.

4.5.1.2 Combined z0.1 and ERA samples

Figure 4.6 shows the radio vs ICM luminosities for the combined ERA and $z \sim 0.1$ samples for the LERGs (left) and HERGs (right). Both of the LERG samples occupy the same diagonal across the plot, with a similar amount of scatter, and the partial correlation test gives a strong correlation ($> 4\sigma$). The HERGs show a much weaker correlation ($> 2\sigma$) – looking at the positions of the sources from the two redshift samples in Figure 4.6 and remembering that there is no correlation for the HERGs at the individual redshifts, this correlation may be an artefact caused by the absence of low ICM luminosities for the ERA sources. See Section 4.5.1.3 below for a discussion of the lack of sources in this region.

As with the z0.1 sample alone, the partial correlation test results for the FRI and FRII subsamples lie between the HERG and LERG test results, reflecting the split of HERGs and LERGs between the FRI and FRII morphologies. This confirms that spectral type is the main contributor to the different relationship between radio and ICM luminosities.

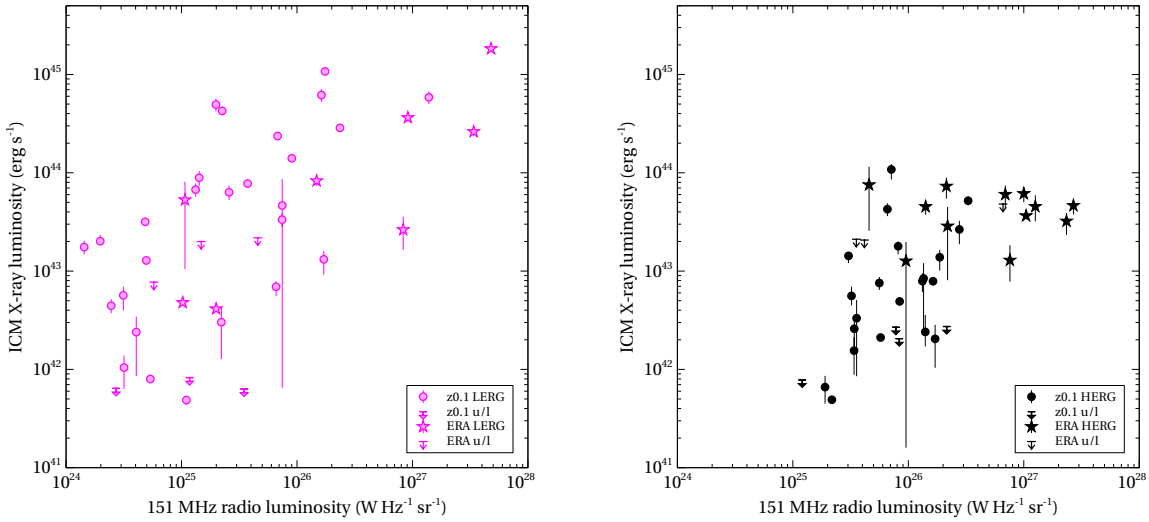

FIGURE 4.6: Radio luminosity vs ICM X-ray luminosity for the combined z0.1 and ERA samples, with LERGs on the left (magenta symbols) and HERGs on the right (black symbols). z0.1 sources are shown as circles and ERA sources as stars. z0.1 upper limits use triangles and ERA upper limits use arrows.

The z0.1 and ERA samples cover different ranges of radio luminosity. I therefore checked my result using subsamples matched in luminosity ranges: $5\times10^{24}-5\times10^{26}$ W Hz^{-1} sr^{-1} for the LERGs and $3\times10^{25}-3\times10^{26}$ W Hz^{-1} sr^{-1} for the HERGs (Table 4.5). In these subsamples, the strong LERG $L_X - L_R$ correlation is still present, but since the high radio luminosity HERGs are no longer in the sample, the partial correlation Kendall's τ test now showed no correlation for the HERGs. The reduced ERA samples are small and contain upper limits on the ICM luminosities so may affect the accuracy of the statistics; nevertheless, the difference between the HERG and LERG environments in both the complete and matched samples is striking.

4.5.1.3 Redshift evolution

Looking at Figure 4.7, there seems to be little difference between the LERG samples from the two epochs, suggesting that there has been no evolution of the environment since $z \sim 0.5$. The ERA HERG sample, however, occupies a narrower range of ICM luminosities than the z0.1 HERG sample, but with similar maximum values. This may indicate that there has been evolution of the HERG environments, as suggested by Harvanek et al. (2001) and Belsole et al. (2007).

I used Peto & Prentice generalised Wilcoxon tests (Feigelson and Nelson 1985) to look for differences in the median values of luminosity of the ERA and z0.1 LERG and HERG subsamples and FRI and FRII subsamples(Table 4.6; the medians are shown in Figure 4.7). The tests showed no difference between the two LERG subsamples, but a

strong difference between the HERG subsamples ($> 3\sigma$). The FRI and FRII test results lay between those of the LERGs and HERGs, again suggesting the spectral type is the main cause of the difference in results. I repeated the tests with the subsamples matched in radio luminosity (Figure 4.8), and found the same but weaker trends.

I therefore have no evidence of evolution of the LERG population since $z \sim 0.5$, but for the HERGs, although the maximum environment richness of the HERG population in the matched samples is the same at both redshifts, there are HERGs in poorer environments at $z \sim 0.1$ than at $z \sim 0.5$. Is this effect genuine, or is it due to non-detection of weak environments at high redshift?

I would need observations of almost 1000 ks to measure ICM luminosities of 10^{42} erg s^{-1} at the redshifts of the ERA sample, so I cannot know whether the lack of high redshift sources in this region of the plot is real or due to insufficient observation time. I have a hint that there might be at least occasional objects in this region from Ramos Almeida et al. (2013) – they obtained an extremely low galaxy-galaxy spatial covariance function (B_{gg}) for PKS1136−13, which has a radio luminosity of 2.7×10^{26} W Hz^{-1} sr^{-1}. If this source follows the expected correlation between L_X and B_{gg}, it would then lie well into the lower right portion of the $L_X - L_R$ plot. However, extended emission is just visible in the 80 ks X-ray observation of this source, giving it an ICM luminosity of $\sim 10^{43}$ erg s^{-1}. This is the only 2Jy source in the high redshift range with such a low B_{gg} — the others have B_{gg} values that should place them in environments around and above 10^{43} erg s^{-1}. I also have only three upper limits in the ERA sample HERGs, and two of these are from short observations, so if there are weak environment sources at these redshifts then they are rare and are unlikely to have a dramatic effect on the sample medians. I therefore conclude that evolution of the HERG environment is probable but not certain.

4.5.1.4 Cluster morphology

The distributions of β and core radius are shown in Figure 4.2. The HERG and LERG subsamples have slightly different β medians – 0.42 vs 0.52 – but a Wilcoxon-Mann-Whitney test shows no significant difference.

The median core radius for the full z0.1 sample is also different for the two subsamples – 17 kpc for the HERGs and 62 kpc for the LERGs. In this case, the distributions of the HERGs and LERGs are different, and this is confirmed by the Wilcoxon-Mann-Whitney test (z=2.41, p=0.008), suggesting that the HERGs may have a higher concentration of gas near the cluster centre. However, when the core radius was scaled by R_{500} the difference is no longer very significant (z=1.79, p=0.037), so the difference in core radius

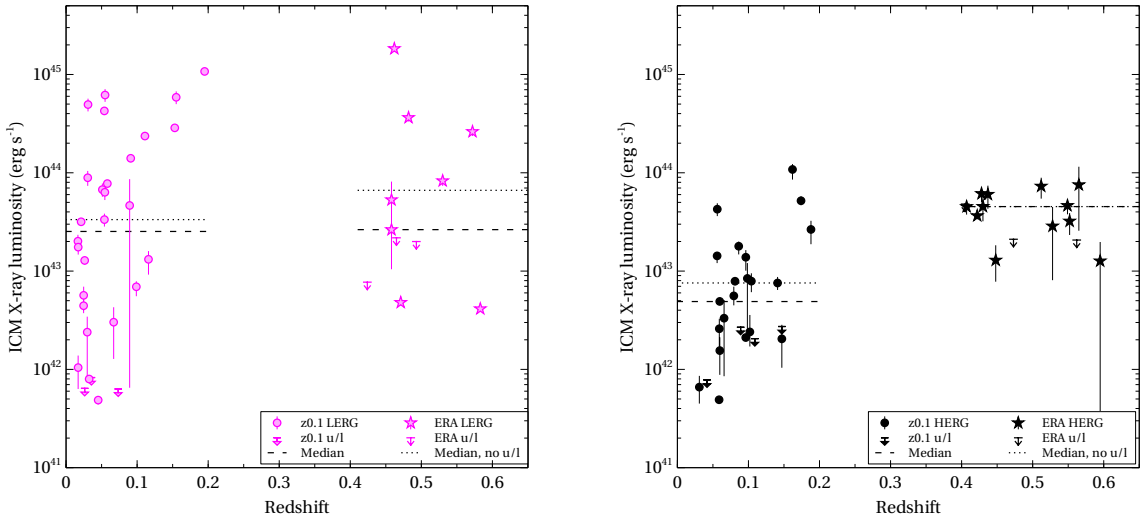

FIGURE 4.7: ICM X-ray luminosity vs redshift for the combined z0.1 and ERA samples, with LERGs on the left and HERGs on the right. Symbols as in Figure 4.6.

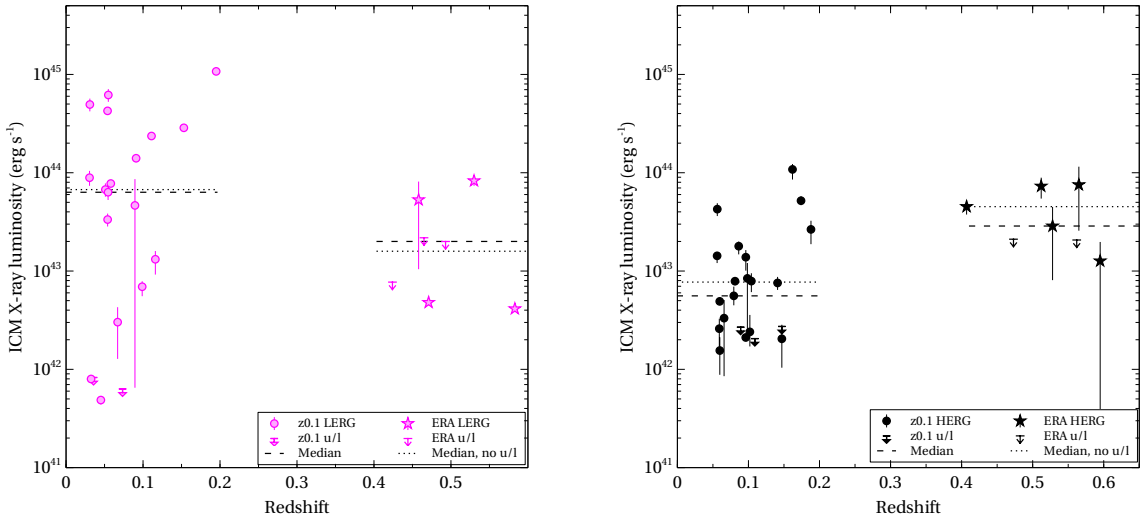

FIGURE 4.8: ICM X-ray luminosity vs redshift for subsamples matched in radio luminosity of the z0.1 and ERA samples, with LERGs on the left and HERGs on the right. Symbols as in Figure 4.6.

may be due to the difference in mass distributions between HERGs and LERGs rather than cluster shape.

4.5.1.5 Central density

If, as discussed in Section 1.1.2.5, LERGs follow a cycle fuelled by gas from the ICM and controlled by the central entropy of the system, I would expect the jet power to be related to the central conditions. I would also expect that, since ICM luminosity is related to cluster mass, ICM luminosity should also be related to the cluster central

density. I used the electron density n_e at $0.1R_{500}$ as an indicator of the central conditions and compared it with radio luminosity.

Figure 4.9 shows the electron densities at $0.1R_{500}$ plotted against ICM luminosity and radio luminosity for the HERGs (top), and the LERGs (bottom) for the z0.1 sample (I did not include the ERA sample as at their redshift the angular size of $0.1R_{500}$ was too close to the PSF to obtain reliable densities). As expected, the central density correlates strongly with ICM luminosity for both types of radio galaxy. In addition, there appears to be a relationship between L_R and n_e for the LERGs, but not for the HERGs, and this is confirmed at the 99.5 per cent confidence level by the Generalised Kendall's Tau tests comparing L_X and L_R with n_e in the presence of a common dependence on redshift (Table 4.5).

This result could simply be a reflection of the $L_R - L_X$ relationships for the two galaxy types, but if jet power is related to central density for the LERGs, this would also contribute to the $L_R - L_X$ relation. I therefore looked for a correlation between L_R and L_X in the presence of a common dependence on n_e. If the jet power is in a large part controlled by central density, this should remove the correlation; if jet power and central density are unrelated then the correlation should be unchanged. As can be seen from Table 4.5, the partial correlation test of $L_R - L_X$ in the presence of n_e shows no significant correlation. However, performing the inverse test of looking for a correlation between L_R and n_e in the presence of a common dependence on L_X also removed the correlation, suggesting that all three factors were well correlated.

In an attempt to find which of the three possible relationships ($L_R - L_X$, $L_R - n_e$ and $L_X - n_e$) was dominant, I did a Principal Components Analysis (PCA, Francis and Wills 1999) on the data with the upper limits excluded, having checked that this made little difference to the results of the Generalised Kendall's Tau tests. As can be seen from Table 4.7, the three factors all contribute in similar proportions to the main principal component PC1, suggesting that I cannot determine the dominant relationship from this data. This was confirmed using Spearman's ρ tests comparing the results of the full PCA with similar analyses on pairs of factors, which all gave similar and very strong correlations.

4.5.2 Comparison with general cluster and group environments

I assumed in my analysis that the cluster environments of my sample of radio-loud AGN do not differ markedly from those of clusters of similar luminosity without radio galaxies. I therefore compared my temperature-luminosity scaling relation with $L_X - T_X$ relations for other samples.

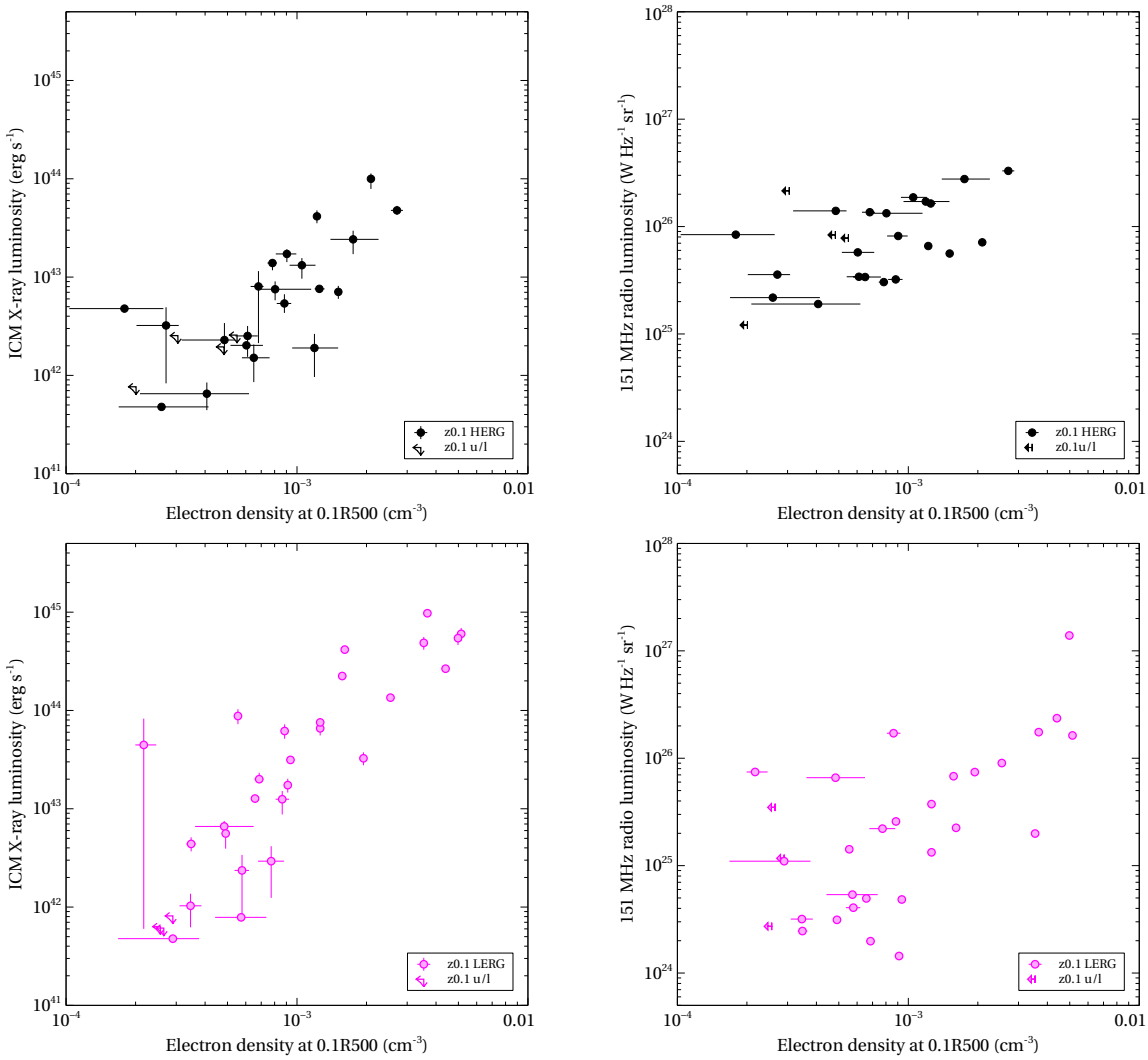

FIGURE 4.9: Density at $0.1R_{500}$ vs ICM X-ray luminosity(left) and radio luminosity (right) for the z0.1 sample. HERGs are at the top, LERGs below. Symbols as in Figure 4.6.

There is a very strong correlation between ICM temperature and luminosity (Table 4.5). Figure 4.10 shows ICM temperature plotted against luminosity for all sources in the z0.1 and ERA samples with temperatures obtained by spectral analysis. I used the orthogonal BCES method from Akritas and Bershady (1996) to calculate the regression line (solid line, $log_{10}L_X = (3.56 \pm 0.36) log_{10}T_X + (42.40 \pm 0.15)$).

The dashed line shows the Pratt et al. (2009) $L_X - T_X$ scaling relation for the REXCESS clusters, which I used to obtain the estimated temperatures. The slope from my sample is slightly higher (3.56 ± 0.36 vs 3.35 ± 0.32), but compatible. Also plotted in Figure 4.10 is the $L_X - T_X$ relation obtained by Stott et al. (2012) for clusters containing radio sources from the *XMM* Cluster Survey. Their slope of 2.91 ± 0.45 is lower than my result but consistent within the $1 - \sigma$ errors.

My sample contains both galaxy groups and clusters, both cool-core and non-cool-core environments and consists entirely of radio galaxies. These factors have all been found to modify the $L_X - T_X$ relation (e.g. Helsdon and Ponman 2000; Croston et al. 2005a; Chen et al. 2007; Magliocchetti and Brüggen 2007; Pratt et al. 2009; Eckmiller et al. 2011; Stott et al. 2012; Bharadwaj et al. 2015). In addition, selection biases (in particular the Malmquist bias, which ensures that for a given temperature, the most luminous objects are preferentially selected) can have a strong effect on the slope of the $L_X - T_X$ relation (e.g. Eckmiller et al. 2011; Bharadwaj et al. 2015), and the evolution parameter, which is usually assumed to be unity, is likely to be affected by the break in self-similarity in the $L_X - T_X$ relation (Maughan 2014).

My relation is likely to be affected by all the factors mentioned above, but since it lies near or within most of the ranges cited by the literature I concluded that my sample shows no evidence of being different from other cluster and group samples.

I also calculated entropy S within $0.1R_{200}$ for the sources from the z0.1 sample with temperatures obtained by spectral analysis. I used $h^{4/3}(z)S = kT/n_e^{2/3}$, where R_{200} is the radius at an overdensity of 200 (Arnaud et al. 2005), kT is the ICM temperature and n_e is the electron density. I calculated the electron density at $0.1R_{200}$ using the same method that I used for the central density (Section 4.4.1). The results are shown in Figure 4.11.

I obtained a regression line for the $S - T_X$ relation, again using the Akritas and Bershady (1996) orthogonal BCES method, and obtained a shallower slope than that of Pratt et al. (2010) (0.63 ± 0.13 vs 0.89 ± 0.15). My slope does however lie within the range of results from the literature cited by Pratt et al. (2010) (slopes of 0.49 to 0.92). If, as discussed in Section 1.1.2.5, interactions form part of the triggering process for HERGs, I would expect them to have high entropy for their temperature. Pratt et al. (2010) noted that disturbed clusters tend to have high entropy compared with relaxed clusters of the same temperature, and indeed all but one of my HERG sample lie above their regression line.

Overall, there is no systematic evidence that the luminosities of my sample of radio galaxies differ from those of galaxy groups and clusters that do not host radio-loud AGN, so my use of luminosity as a proxy for total cluster mass is reasonable. My entropies tend to be high, which is likely to be at least in part due to clusters being disturbed, but are still within the ranges cited in the literature.

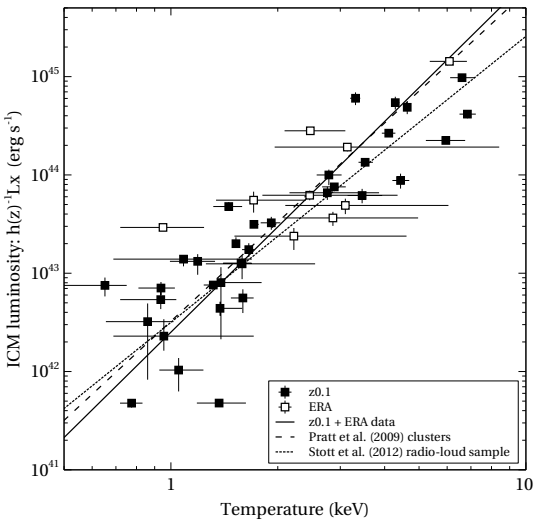

FIGURE 4.10: ICM luminosity vs temperature for the temperatures obtained by spectral analysis. Filled squares denote the z0.1 sample and empty squares the ERA sample. The solid line shows the $L_X - T_X$ relationship from the combined samples, and the dashed line shows Pratt et al. (2009)'s $L_X - T_X$ relation for clusters. Also shown is the relation from Stott et al. (2012) for their subsample of clusters containing radio galaxies (dotted line).

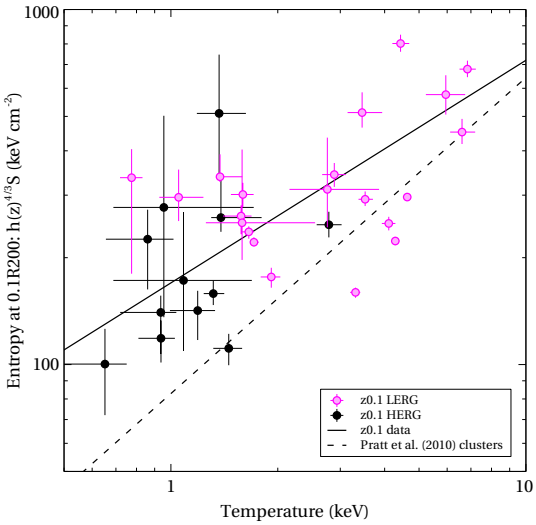

FIGURE 4.11: Entropy vs temperature for the z0.1 sample temperatures obtained by spectral analysis. Magenta circles are LERGs and black circles are HERGs. The solid line shows the $S - T_X$ relationship from the z0.1 sample and the dashed line shows Pratt et al. (2010)'s $S - T_X$ relation for clusters.

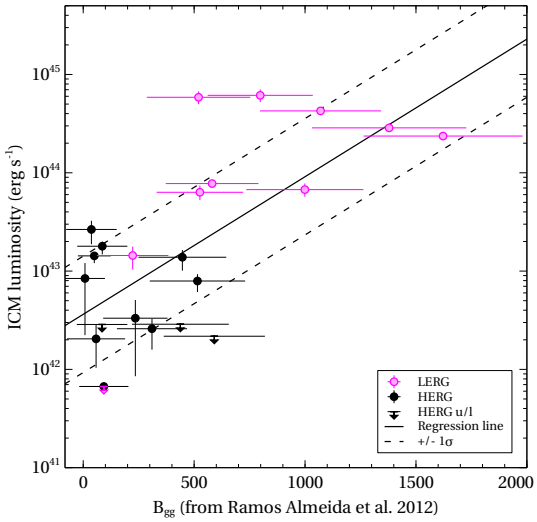

FIGURE 4.12: ICM luminosity vs galaxy-galaxy spatial covariance function B_{gg} for the 2Jy sources in the z0.1 sample. B_{gg} values were taken from Ramos Almeida et al. (2013). Magenta circles are LERGs and black circles are HERGs. The solid line shows the regression line for the data, and the dotted lines the 1σ scatter.

4.5.3 Comparison with optical measures

I would expect a correlation between different measures of cluster richness, though with a fair amount of scatter (e.g. Yee and Ellingson 2003; Ledlow et al. 2003, Section 3.5.3). Ramos Almeida et al. (2013) have calculated the galaxy-galaxy spatial covariance function (B_{gg}) for the 2Jy sample. I therefore compared these with the ICM luminosities for the 2Jy sources within my z0.1 sample (Figure 4.12). A Generalized Partial Kendall's τ test showed a correlation at the 3σ level (Table 4.5). I used the Buckley-James method (Isobe et al. 1986) to obtain a regression line including the upper limits in L_X; this gave $log_{10}L_X = (0.0014 \pm 0.0003)B_{gg} + (42.58 \pm 0.59)$. The amount of scatter compromises the relationship's utility as a scaling relation, and it should also be noted that the two measures were taken within different radii (170 kpc for B_{gg} and R_{500} (median 600 kpc) for L_X). However, the strength of the correlation shows that overall results from the two measures should be comparable.

4.5.4 Implications

My results add evidence of a difference in cluster environments to the increasing wealth of data supporting a dichotomy in the population of radio-loud AGN, and provide supporting evidence for models that involve the different accretion cycles of the high and low excitation sources.

4.5.4.1 LERG results

The strong correlations between radio luminosity, ICM luminosity and central density for LERGs supports the concept of some form of relationship between ICM properties and jet power. This could provide corroborative evidence for a stable, long-lasting feedback cycle as demonstrated in the simulations of Gaspari et al. (2012, 2013), in which matter is driven outwards by the jets and falls inwards from the ICM when the central conditions become favourable. The pressure of available gas in the ICM will affect the flow of gas into the nucleus, which will in turn affect the accretion rate and the jet power. There will be some variation as the central regions heat up and then cool again as the gas clumps accrete and disperse and are recharged, and this may be one of the several factors that could contribute to the scatter in the $L_R - L_X$ plot. Other possible factors that might add scatter to the relationship are discussed briefly in Section 3.5.4 – the scatter in the relationship between mechanical jet power and total radio luminosity (e.g. Bîrzan et al. 2008; Cavagnolo et al. 2010; Godfrey and Shabala 2013; Hardcastle and Krause 2013) and the effect of differences in central gas properties (which are not correlated with ICM luminosity, e.g. Croston et al. 2008b) on jet power. It might be that the cyclic variations suggested by Gaspari et al. (2012, 2013) could contribute to both these issues.

An alternative explanation for the correlation is that it results at least in part from 'environmental boosting' (e.g. Barthel and Arnaud 1996; Hardcastle and Krause 2013), where for a given jet power, a richer environment confines the plasma in a smaller region and so increases the radio luminosity. However, this effect should apply equally to both HERGs and LERGs. The fact that the individual HERG samples show no correlation suggests that an explanation based on fuelling mechanisms as described above is more likely. It also suggests that the environmental boosting may be counteracted by another mechanism. Entrainment reduces radio luminosity relative to jet power (eg Croston and Hardcastle 2014) and is expected to increase with environment density and so works in the opposite direction to environmental boosting.

4.5.4.2 HERG results

Turning to the HERGs, the lack of correlation between the radio luminosity and cluster properties for the individual samples suggests that the ICM does not have a major rôle to play either in powering the system or in controlling the luminosity of the lobes. This fits in with the theory that HERGs accrete at a relatively high rate from an accretion disc maintained by a local reservoir of cold gas, probably originating from galaxy interactions and mergers (e.g. Hardcastle et al. 2007a; Ramos Almeida et al. 2012; Tadhunter et al. 2014). Gas ingestion from the ICM as described by Gaspari et al. (2013) is sufficient to

fuel even the most powerful LERG jets, and is also sufficient to fuel low-power HERGs. It could not however maintain the accretion rates required to power the jets and nucleus of more powerful HERGs. The richness of the ICM would therefore be largely irrelevant and no correlation is to be expected.

If the difference between the HERG environments in the ERA and z0.1 environments does indicate evolution, then this is very interesting. At high redshifts ($z > 1$), radio galaxies are typically seen in richer environments than similar radio-quiet galaxies (Wylezalek et al. 2013; Hatch et al. 2014), but by $z \sim 0.5$ we are finding radio galaxies in groups and poor clusters. This may be due to cosmic downsizing — as the gas density in the vicinity of the black hole depletes as a result of AGN activity and star formation, then the conditions required for HERGs to be triggered, such as mergers bringing new gas into the host galaxy, occur in poorer environments as redshift reduces. However, although the minimum environment richness at $z \sim 0.1$ is lower than at $z \sim 0.5$ (as would be expected from cosmic downsizing) the maximum richness of the environments is the same. Thus there must be additional processes involved.

4.6 Conclusions

I have compared low frequency radio luminosity with the richness of the cluster environment for a sample of 55 radio-loud AGN lying in the redshift range $0.01 \leq z \leq 0.2$. The sample covered three decades of radio luminosity and contained 25 high excitation and 30 low excitation sources. I used the X-ray luminosity of the ICM as the measure of cluster richness. The X-ray observations were taken from the *Chandra* and *XMM-Newton* archives.

I found:

- For the complete z0.1 sample, a weak correlation between radio luminosity and cluster richness;
- For the LERG subsample, strong correlations between radio luminosity, cluster richness and central density;
- For the HERG subsample, no correlation between radio luminosity and cluster richness, or between radio luminosity and central density;
- The core radii of the LERGs were on average larger than those of the HERGs.

These results were similar to those obtained using the ERA sample (Chapter 3), which used a higher redshift band ($0.4 \leq z \leq 0.6$). I compared the results for $z \sim 0.1$ and $z \sim 0.5$, and found:

- For the two LERG samples, the slopes and normalisations of the radio luminosity–ICM richness relationships were very similar, giving a very strong correlation for the combined samples. This suggested that there had been no evolution with redshift since $z \sim 0.5$, and I found no significant difference between the cluster environments of the two samples;
- Although the HERGs in both samples had similar maximum environment richnesses, the lower redshift sample also included environments much weaker than any seen in the ERA sample, giving tentative evidence of evolution of the environment;
- The HERGs occupied groups and clusters with more compact central regions than the LERGs, suggesting that HERGs may have a greater concentration of gas near the host galaxy than LERGs;
- I found the luminosity-temperature relation for my samples to be compatible with the range of $L_X - T_X$ relations derived for general samples of clusters and groups, so my results show no evidence that environments occupied by radio-loud AGN are different from those of typical clusters.

The evidence of a difference between the HERG and LERG large-scale environments is now strong, as is the evidence for a relationship between radio luminosity and ICM richnesss for the LERGs. Since the underlying relationship between radio luminosity and jet power is a likely contributor to the scatter in the LERG $L_R - L_X$ relationship, in the next chapter I look at some of the factors likely to affect jet power.

4.7 Notes on the individual sources in the z0.1 sample

This section contains brief notes on the individual sources in the z0.1 sample, and compares my results with those of other researchers.

4.7.1 3CRR sources

3C 28 (A115-N, PKS 0053+26) is a LERG with FRII morphology. Its host is one of a pair of merging clusters and is highly asymmetric, and the disturbance is visible in the surface brightness profile. Both clusters are rich – Gutierrez and Krawczynski (2005) obtained values of around 5 keV for the individual clusters away from the merger and 8 keV for the plasma between the clusters. Because I was interested in the full environment around the host galaxy, I included parts of both regions and obtained a temperature of $6.61^{+0.59}_{-0.49}$ keV. This lies within the upper bound of the temperature of $5.35^{+1.28}_{-0.09}$ keV obtained by Shelton (2011).

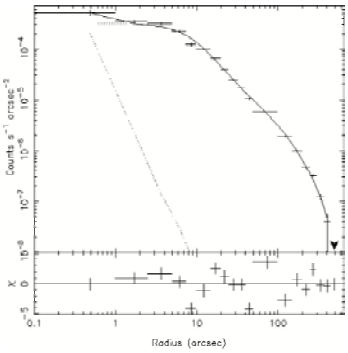

I obtained a luminosity very close to the value expected from the $L_X - T_X$ relation. It is higher than that obtained by Shelton (2011) — my surface brightness profile is substantially wider, perhaps because of my use of double background subtraction and double β modelling.

3C 31 (NGC 383) is a LERG with a massive central rotating disc of molecular gas (Okuda et al. 2005) and FRI morphology. My temperature of 1.53 ± 0.3 keV is consistent with the those obtained by Komossa and Böhringer (1999) and Croston and Hardcastle (2014). Hodges-Kluck et al. (2010) found a higher temperature ($2.0^{+0.5}_{-0.02}$ keV) in the central regions with a *Chandra* observation.

3C 33 (PKS 0106+13) is a Narrow Line Radio Galaxy (NLRG) with FRII morphology lying in a weak environment. The radio outburst is thought to be energetic enough to eject a significant fraction of the corona gas (Kraft et al. 2007). I detected very little emission beyond the host galaxy. The counts are low so I obtained an estimated temperature (1.1 keV). This is typical of a group environment.

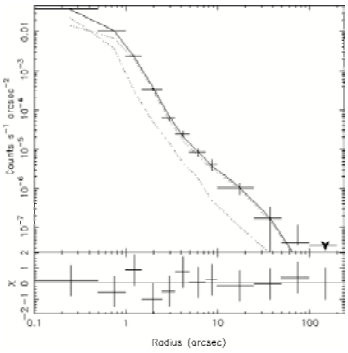

3C 35 is also an NLRG with FRII radio structure in a weak environment. Mannering et al. (2013) report a gas 'belt' lying around the source between the lobes and extending out to about 170 kpc – not far short of my detected radius of emission. I found a broad surface brightness profile and an estimated temperature of 1 keV, very similar to the spectral temperature obtained by Mannering et al. (2013) using combined *Chandra* and *XMM-Newton* observations.

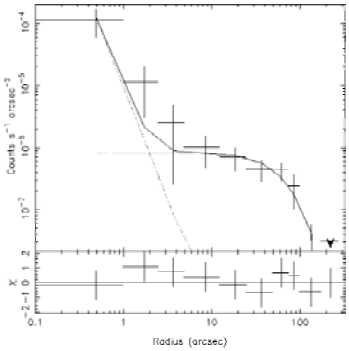

3C 66B is a LERG with FRI morphology. My temperature of 1.7 keV is compatible with that of Croston et al. (2008a), but I obtained a higher luminosity ($3.17^{+0.10}_{-0.12}$ vs $1.07^{+0.08}_{-0.24} \times 10^{43}$ erg s^{-1}). The reason for the discrepancy is not clear, but could relate to the use of an improved background subtraction method in this work.

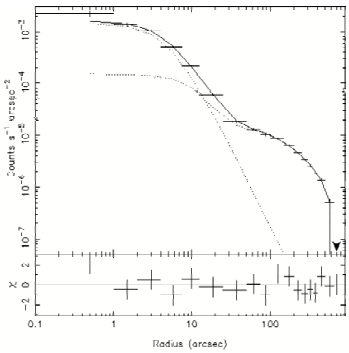

3C 76.1 is a LERG with FRI plumes spreading across a large proportion of the detected environment, which I found to be weak. Miller et al. (1999), using the *ROSAT* All-Sky Survey, did not detect any extended emission. Because of the low counts (this was a short observation), I could not fit a double-β model. I used an estimated temperature of 0.65 keV. This is lower than the $0.91^{+0.25}_{-0.14}$ keV obtained by Croston et al. (2008a) with an *XMM-Newton* observation; my luminosities are however compatible.

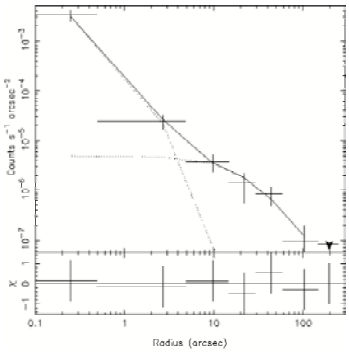

3C 98 (PKS 0356+10) is an NLRG with FRII morphology in a weak environment with the detected emission not extending far beyond the host galaxy. Again, Miller et al. (1999) did not detect extended emission. I used an estimated temperature of 0.62 keV. This was lower than the $1.1^{+0.3}_{-0.2}$ keV obtained by Hodges-Kluck et al. (2010) within a smaller radius.

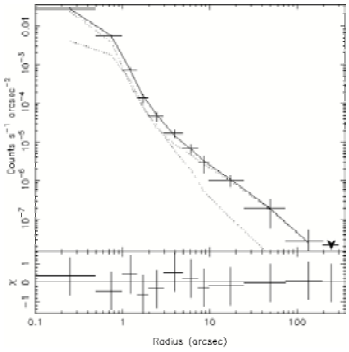

3C 192

(PKS 0802+24) is another NLRG with FRII morphology in a weak environment. This was a short observation, and although the emission extended beyond the host galaxy, there were insufficient counts to fit a double-β model. I used an estimated temperature (0.8 keV).

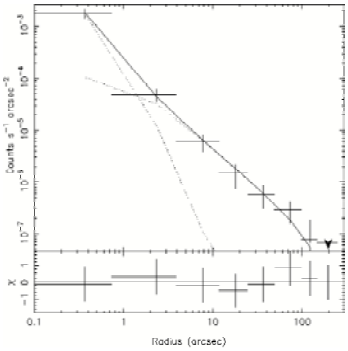

3C 219 is a Broad Line Radio Galaxy (BLRG) with FRII morphology. It may be recently re-triggered after a dormant period (Weil and Roberts 2014) as it has a small jet within a well-formed pair of lobes with a classical double structure.
The temperature (1.5 keV) and luminosity (5.2×10^{43} erg s^{-1}) are those of a group, and are compatible with those obtained by Shelton (2011).

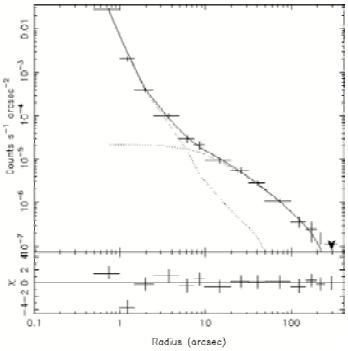

3C 236 is a LERG with massive FRII lobes extending well beyond the imaging chips. It is a double-double, with outer lobes of 4 Mpc in extent and inner lobes of 2 kpc (Tremblay et al. 2010). It is thought to have been reactivated about 10^5 years ago (Labiano et al. 2013). I found a weak environment, with insufficient counts for spectral analysis. My estimated temperature of 1.2 keV is that of a group environment.

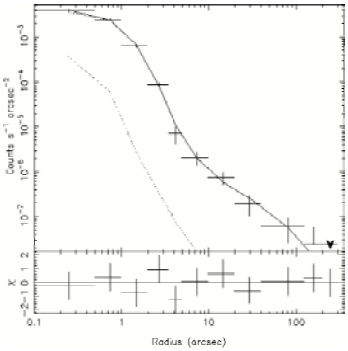

3C 285 is an NLRG with FRII morphology in a highly disturbed group environment. The host galaxy is also highly disturbed, probably as a result of a recent merger (Allen et al. 2002), and is currently interacting with another galaxy (Baum et al. 1988). I obtained a temperature of $0.94^{+0.10}_{-0.22}$ keV for the extended emission, consistent with Hodges-Kluck et al. (2010). Hardcastle et al. (2007b) obtained a lower temperature of 0.64 keV with a MEKAL model; I found compatible results when I replaced my APEC model with a MEKAL model.

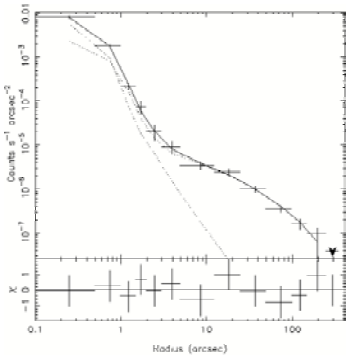

My surface brightness profile, generated with a double β model and double background subtraction, gave a wider profile than that obtained by Hardcastle et al. (2007b), and my luminosity is consequently higher – $0.56^{+0.14}_{-0.11}$ vs $0.19^{+0.1}_{-0.1} \times 10^{43}$ erg s^{-1}.

3C 293 is a LERG with FRI plumes in a weak environment. It is a double-double source with estimated ages of ~ 20 Myr for the outer lobes and $\lesssim 0.1$ Myr for the central source (Joshi et al. 2011), and has strong, jet-driven outflows of gas (Mahony et al. 2013; Lanz et al. 2015). I obtained a temperature of 0.78 keV – a weak group temperature. I found the emission to be under-luminous for its temperature.

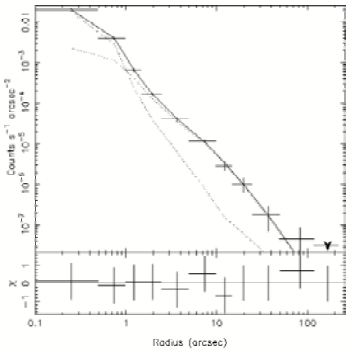

3C 296 (NGC 5532, PKS 1414+11) is a LERG with FRI morphology and occupies a group environment – Miller et al. (1999) found 4 galaxies in the group. The source is relatively near and the emission extends to just beyond the imaging chip. I therefore could not use double subtraction for modelling the profile, but were able to use one of the outer chips to model the background and so used double subtraction for the spectral analysis.

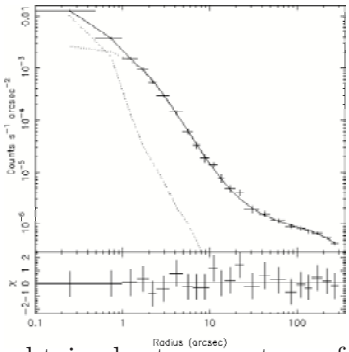

Croston et al. (2008a), using an *XMM-Newton* observation, obtained a temperature of 0.9 keV over a 50-600 arcsec region (larger than was available with my *Chandra* observation), but found that the temperature was higher (~ 1.4 keV), albeit with large errors, towards the centre. I also found that the temperature dropped gradually beyond around 150 arcsec, and so used the temperature within this region (1.6 keV). Hodges-Kluck et al. (2010) found the temperature to be 4 keV within a similar region, which is high compared with the results of Croston et al. (2008a) and my current work.

3C 303 is a BLRG with FRII structure at a steep angle to the viewer, and I found emission typical of a group environment. The observation had some pile-up, so I excluded the central 1.5 arcsec in the surface brightness profile. My temperature and luminosity are slightly lower than those obtained by Shelton (2011) – $0.94^{+0.09}_{-0.13}$ vs $1.86^{+3.00}_{-0.54}$ keV and $0.76^{+0.12}_{-0.11}$ vs $0.92 \pm 0.06 \times 10^{43}$ erg s^{-1}. My luminosity is a little high compared with the $L_X - T_X$ relation, but within the scatter.

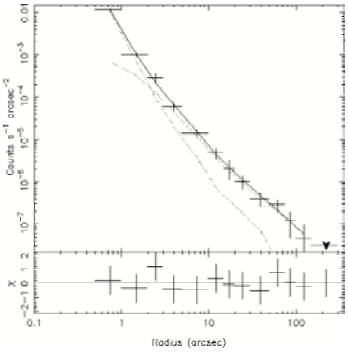

3C 305 is a NLRG with a halo around the host galaxy, probably of material being driven out by the jets (Hardcastle et al. 2012). It has unusual FRII lobes spreading at right-angles to the jets. In common with Hardcastle et al. (2012) and Miller et al. (1999), I found little evidence of ICM emission beyond the host galaxy, and so I derived upper limits for this source.

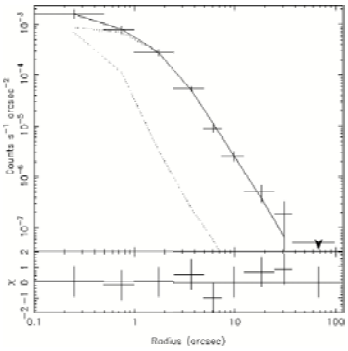

3C 310
(PKS 1502+26) is a LERG with wide FRI plumes and a disturbed environment containing a large cavity, filamentary structure and a shock front at about 180 kpc from the nucleus (Kraft et al. 2012). The emission extends beyond the observing chip, but I was able to use one of the outer chips to model the background for the spectral analysis. I obtained a temperature of 1.9 keV, typical of a strong group or weak cluster.

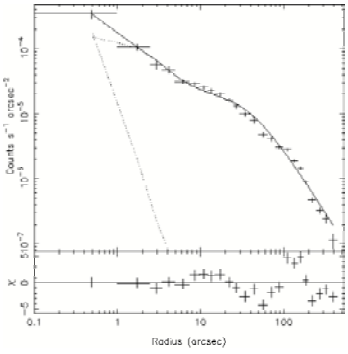

3C 321 (PKS 1529+24)
is an NLRG with FRII morphology in the process of merging with a neighbouring galaxy (Evans et al. 2008). The environment is weak and highly disturbed; I found little emission beyond the host galaxy and had low counts, so I used an estimated temperature of 0.87 keV.

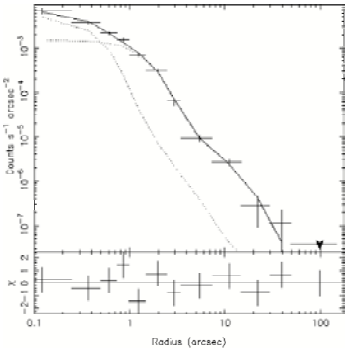

3C 326 (PKS 1550+20)
is a LERG with large FRII lobes extending beyond the imaging chip. It shows evidence of molecular reservoirs thought to be formed by positive feedback (Nesvadba et al. 2011). The host galaxy has a nearby companion. I found the environment to be wide and flat and fairly weak. I had insufficient counts for spectral analysis so used an estimated temperature of 1.9 keV.

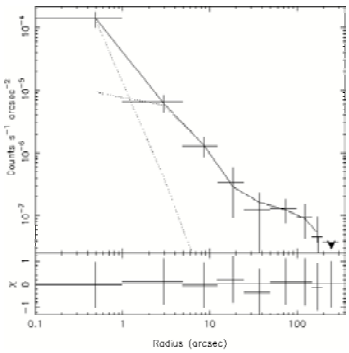

3C 338 (NGC 6166) is a LERG with FRI morphology, lying in the cluster Abell 2199. The cluster is highly disturbed, and Nulsen et al. (2013) discuss a variety of features in the cluster plasma including a shock front at 100 arcsec and a large plume extending to about 50 arcsec probably resulting from a cluster merger. These are visible in my surface brightness profile. The emission extends well beyond the imaging chip so double subtraction was not possible for either the profile or the spectral analysis. Nulsen et al. (2013) give a detailed temperature map of the centre of the cluster showing complex structure, and I obtained temperatures rising from a cooler centre in line with their results. My overall temperature of 4.63 ± 0.08 keV is consistent with those reported by Kaastra et al. (1999) (using a *ROSAT* observation) and Hodges-Kluck et al. (2010).

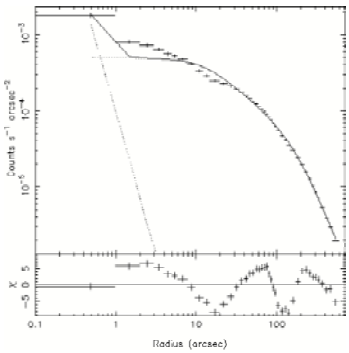

3C 346 (4C 17.70, PKS 1641+17) is an NLRG with FRI morphology lying in a weak cluster. My temperature of 2.8 keV is consistent with that of Shelton (2011). My profile shows the same features as that of Shelton (2011), but has a much larger detected radius and a shallower outer slope, perhaps due to improved background modelling from the double subtraction. My luminosity is therefore substantially higher (10.8 vs 0.65×10^{43} erg s^{-1}) and lies close to the $L_X - T_X$ relationship.

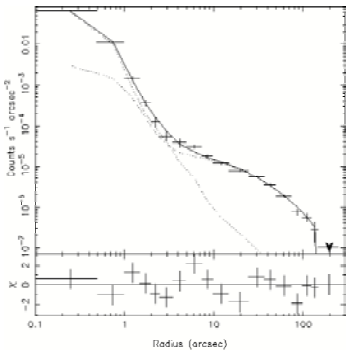

3C 386 (PKS 1836+17) is a LERG with broad $H\alpha$ lines in the spectrum (Simpson et al. 1996) and FRI lobes. The observation had low counts after background subtraction so I was unable to fit a double-β profile. There were insufficient counts left after subtraction of the *Chandra* blank sky files to obtain a background for the spectral analysis so I used single subtraction using a background from the observing chip to obtain the temperature, which was that of a group (1 keV).

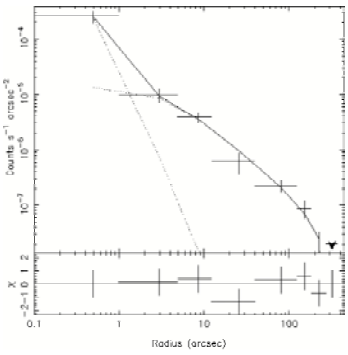

3C 388 is a LERG in a cluster with cavities around its FRII lobes and a sub-cluster to the east (Kraft et al. 2006). The emission extends beyond the imaging chips, but I was able to use a side chip to model the background. I found a cluster temperature of 3.5 keV. My temperature and metallicity for the extended ICM agree with the results of Kraft et al., but my temperature is slightly higher than that obtained by Hodges-Kluck et al. (2010); this is probably due to their use of a different (frozen) metallicity.

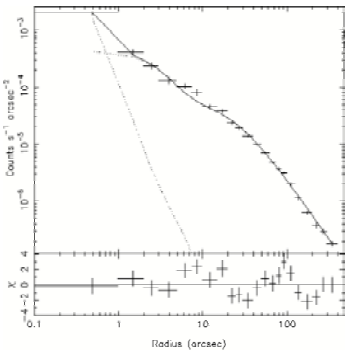

3C390.3. This BLRG has fast gas outflows from the central regions (Tombesi et al. 2010). It has FRII morphology and is in a strong environment. The ICM emission extends beyond the imaging chip, and the observation also suffers from considerable pileup. The temperature I obtained using single subtraction with the *Chandra* blank sky files was low for such bright emission (<1 keV). I had very few counts left after the *Chandra* blank sky subtraction and could not analyse a background spectrum, so it is possible that the blank sky files were not accurate for this region or that the effects of the pileup extended across a wide energy range. I therefore used an estimated temperature for this source.

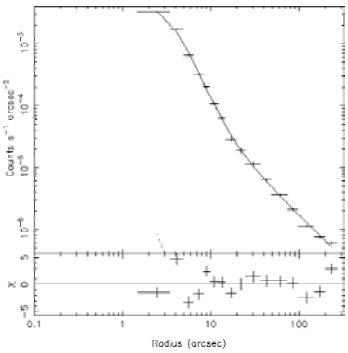

3C 433 (4C 24.54, PKS 2121+24)
is an NLRG with hybrid FRI/FRII morphology in a group environment. The northern lobe is very bent, perhaps due to interaction with the surrounding ICM (Hodges-Kluck et al. 2010). I obtained a temperature consistent with that of Hodges-Kluck et al. (2010), but slightly lower than that of Shelton (2011). My luminosity is higher than that of Shelton (2011) – $0.24^{+0.12}_{-0.07}$ vs $0.05 \pm 0.01 \times 10^{43}$ erg s^{-1} – but lies on the $L_X - T_X$ relationship. As with 3C 28, my modelling methods resulted in a much wider profile than that obtained by Shelton (2011).

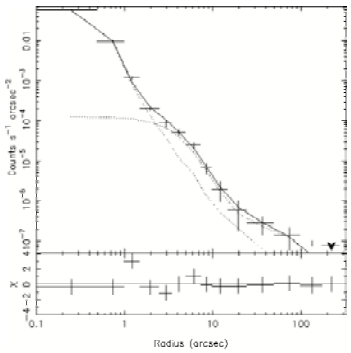

3C442A (PKS 2212+13) is a LERG with FRI plumes, hosted by the interacting galaxy pair NGC 7236/7237 (Worrall et al. 2007), with filaments from the interacting galaxies and a ridge structure between the plumes (Hardcastle et al. 2007b). Worrall et al. (2007) found no evidence of an active jet, and suggest that the jets may have been stopped by an excess of central gas pressure resulting from the merger. The system lies in a weak cluster, and extends beyond the imaging chip. I could not obtain a background from the outer chips so used the *Chandra* blank sky files for the background for the spectral analysis. I obtained a temperature consistent with that of Hardcastle et al. (2007b), and a luminosity close to the $L_X - T_X$ relation.

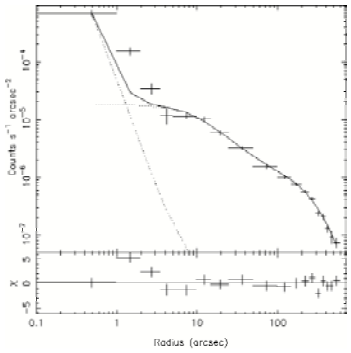

3C 449 is a LERG with FRI plumes extending well beyond the imaging chip, and is relatively close, so the environment emission extends beyond the chip. It has a 600 pc dust disk which, unusually, lies nearly parallel to the jet (Tremblay et al. 2006). The surface brightness profile is wide with an unusually shallow slope, though well constrained by the MCMC modelling.

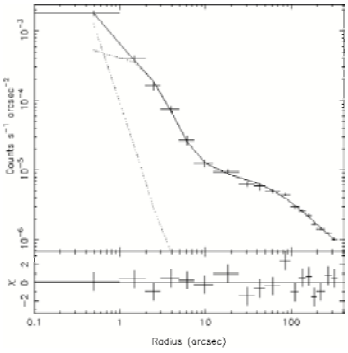

My temperature of $1.66^{+0.06}_{-0.07}$ keV is higher than that obtained from a *XMM-Newton* observation by Croston et al. (2008a) (0.98 ± 0.02 keV), but was measured over a smaller region. Hodges-Kluck et al. (2010) obtained a temperature of 1.58 ± 0.06 keV over a smaller region still; their modelling included the contribution of the host galaxy, which I excluded.

My luminosity of $1.75^{+0.28}_{-0.28} \times 10^{43}$ erg s^{-1} is slightly higher than that obtained by Croston et al. (2008a) ($1.20^{+0.12}_{-0.10} \times 10^{43}$ erg s^{-1}), but because of my higher temperature, my luminosity is calculated within a larger radius.

3C 452 is an NLRG with FRII morphology. There is a lot of X-ray emission associated with the radio structure, but beyond this the environment is poor. Having excluded the emission associated with the lobes, Shelton (2011) found a temperature of 1.18 ± 0.11 keV in the inner 160 arcsec, and $0.86^{+0.13}_{-0.05}$ keV beyond. I also found that the temperature dropped as the radius increased, but had a slightly higher temperature of $1.32^{+0.10}_{-0.08}$ keV in the central region.

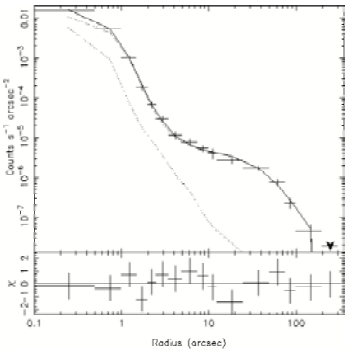

3C 465 is a LERG with large, bent FRI plumes lying in a cluster. The cluster has a cool core with the temperature increasing to around 5 keV before levelling off (Hardcastle et al. 2005). I obtained an overall temperature of $4.43^{+0.26}_{-0.23}$ keV, consistent with the results of Hardcastle et al. (2005) and Hodges-Kluck et al. (2010).

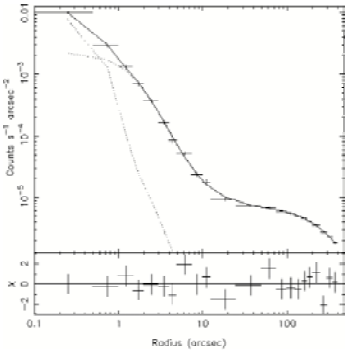

4C 73.08 is an NLRG with FRII morphology lying in a weak environment with unusual radio features (Strom et al. 2013). I did not detect much emission beyond the host galaxy and could only fit a single-β model. Chen et al. (2012) identified 9 group members. My temperature of 1.4 keV seems a little high for the weak environment, and I found the ICM under-luminous for the temperature compared with the $L_X - T_X$ relation.

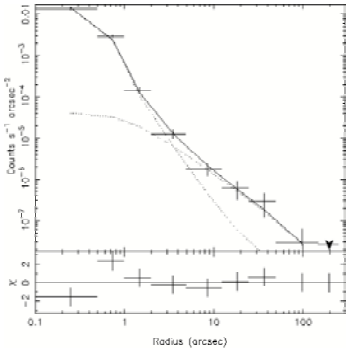

DA 240 is a LERG with large FRII lobes. Although it lies in a respectable group of more than 30 galaxies (Chen et al. 2011a), Miller et al. (1999) failed to detect any X-ray emission from the ICM with a *ROSAT* observation. I likewise detected no emission beyond the host galaxy, and so obtained upper limits on the temperature and luminosity.

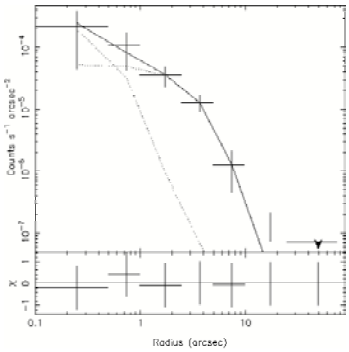

NGC 6109 (4C 35.40) is a LERG with a long narrow-angle-tail plume lying in a group of 13 galaxies (Miller et al. 1999). I found a weak environment beyond the host galaxy, but had insufficient counts to obtain a spectrum. I obtained an estimated temperature of 0.9 keV.

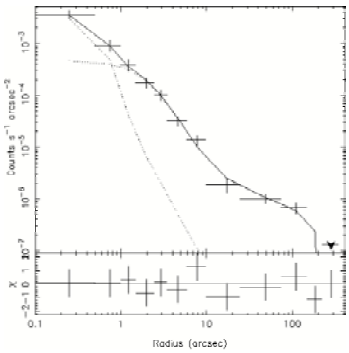

NGC 6251. This LERG has large FRI plumes extending beyond the imaging chip. It lies in a group of at least 20 galaxies (Chen et al. 2011b), and I detected emission extending beyond the chip. I could not model the background on the outer chips, so obtained the temperature using the single subtraction method with the *Chandra* blank sky files. I obtained a range of temperatures ranging from ~ 1 to ~ 2.5 keV from different regions, and used an intermediate result of $1.38^{+0.21}_{-0.03}$ keV, compatible with that found by Evans et al. (2005) using *XMM-Newton* observations.

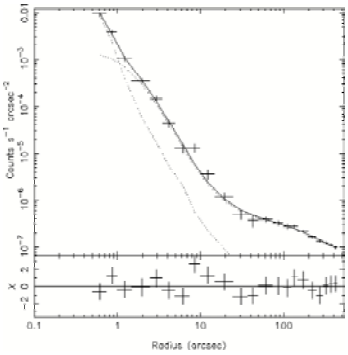

I found a much higher luminosity than Evans et al. (2005) (0.44 ± 0.07 vs $0.07 \pm 0.01 \times 10^{43}$ erg.s^{-1}), but a slightly lower luminosity than that which Chen et al. (2011b) estimated from the galaxy velocity dispersions ($\sim 0.57 \times 10^{43}$ erg.s^{-1}. My surface brightness profile was wider than that of Evans et al. (2005) and had a shallower β. This may be because my *Chandra* observation had a much smaller PSF than the *XMM-Newton* observation used by Evans et al. (2005), allowing a more detailed modelling of the surface brightness profile, or because the *Chandra* blank sky files underestimated the background emission. My result is however close to the $L_X - T_X$ relation.

NGC 7385 (4C 11.71) is a LERG with small FRI plumes. Miller et al. (1999) found a weak extended environment with a group of 17 galaxies; I found very few counts beyond the host galaxy emission and so obtained upper limits for the temperature and luminosity.

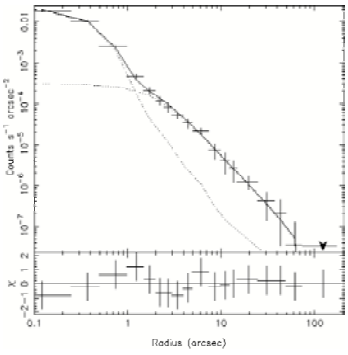

4.7.2 2Jy sources

PKS 0034−01 (3C 15) is a LERG with small FRII lobes in a weak environment ($B_{gg} \sim 90$ – Ramos Almeida et al. 2013). Like Rinn et al. (2005), I found insufficient evidence of ICM emission for analysis so I calculated upper limits for the temperature and luminosity.

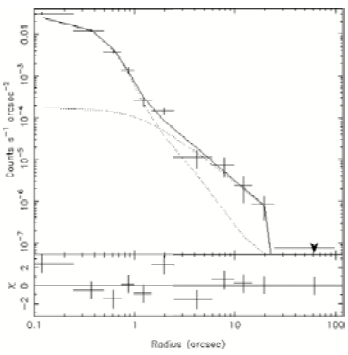

PKS 0038+09 (3C 18)
is a BLRG with small FRII lobes in a weak environment ($B_{gg} \sim 35$ – Ramos Almeida et al. 2013). The short observation time gave us insufficient counts for spectral analysis, so I used an estimated temperature of 1.8 keV.

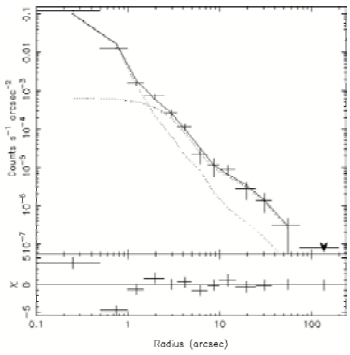

PKS 0043−42.
This is a spectroscopic LERG with FRII morphology lying in a weak cluster ($B_{gg} \sim 250$ – Ramos Almeida et al. 2013) and with evidence of a dusty torus (Ramos Almeida et al. 2011). The host galaxy was small in angular extent so I could not model it separately. I found a temperature typical of a group/weak cluster (1.6 keV).

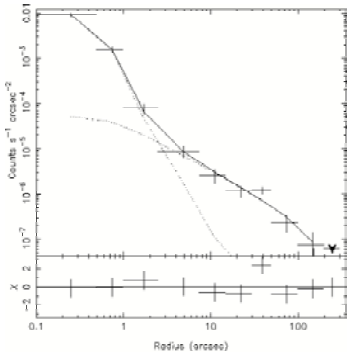

PKS 0213−13 (3C 62) is an NLRG
with small FRII lobes in a weak environment ($B_{gg} \sim 60$ – Ramos Almeida et al. 2013). I detected little emission beyond the host galaxy, and had insufficient counts for a double-β model or for spectral analysis. My estimated temperature of 0.85 keV is typical of a weak group.

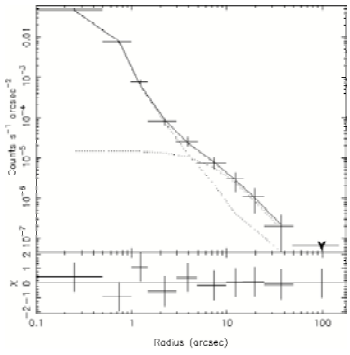

PKS 0349−27 is an NLRG with FRII morphology and extended regions of ionised gas (Grimberg et al. 1999), perhaps resulting from a previous merger. I found a temperature typical of a weak group environment (0.86 keV); Ramos Almeida et al. (2013) found a stronger B_{gg} than I would expect for that temperature ($B_{gg} \sim 200$).

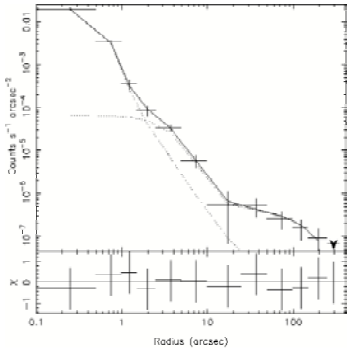

PKS 0404+03 (3C 105) is an NLRG with FRII morphology. Ramos Almeida et al. (2013) found that it lay in a weak environment ($B_{gg} \sim 80$). The observation time is short, and I found only very slight evidence of ICM emission beyond the host galaxy. I therefore derived upper limits for this source.

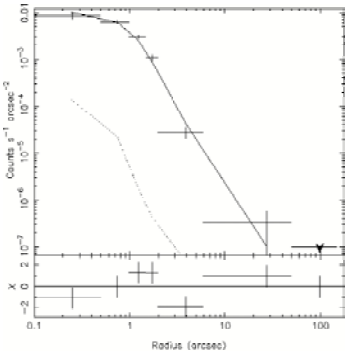

PKS 0442−28. This is also an NLRG with FRII morphology. I found no evidence of ICM emission beyond the host galaxy, so derived upper limits for this source. There are however several galaxies close to the host, and Ramos Almeida et al. (2013) found a B_{gg} of ~ 450.

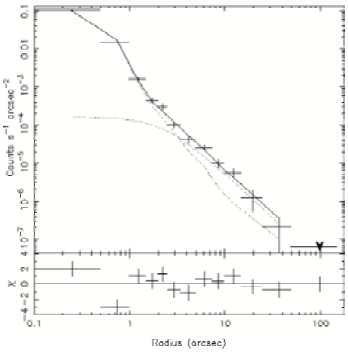

PKS 0620−52 is a LERG with FRI plumes lying at a steep angle to each other. It lies in a cluster ($B_{gg} \sim 900$ – Ramos Almeida et al. 2013). The emission extended beyond the imaging chips, and I was also unable to use a side chip to model the background. I used the *Chandra* blank sky files for the background for both the profile and the spectral analysis. My temperature of 2.8 keV is typical of a weak cluster.

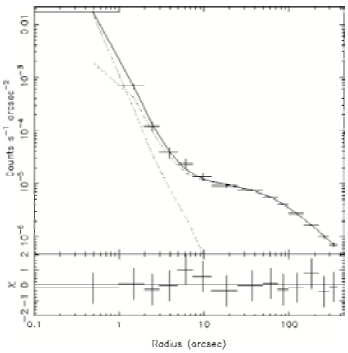

PKS 0625−35. This source has an optical classification of LERG, but is classified by Wills et al. (2004) as a possible BL Lac object and by Gliozzi et al. (2008) as a LERG. It has FRI morphology and lies in cluster A 3392 ($B_{gg} \sim 5000$ – Ramos Almeida et al. 2013). I obtained a cluster temperature (3.5 keV). The emission extended beyond the imaging chip so I used the *Chandra* blank sky files for the background for both the profile and the spectral analysis.

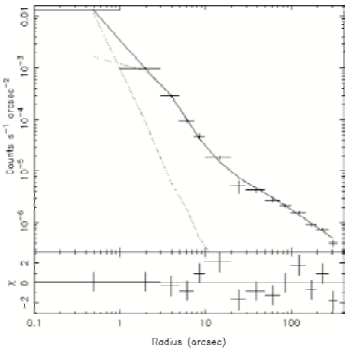

PKS 0625−53 is a LERG with a FRII morphology lying in a disturbed cluster (A 3391). The emission extended beyond the imaging chip but I was able to use the spectrum from one of the side chips to model the background. I obtained a higher temperature than Frank et al. (2013) ($6.84^{+0.38}_{-0.34}$ vs 5.21 ± 0.03 keV). This difference is in line with that expected from the reported difference between temperatures obtained using *Chandra* and *XMM-Newton* (Schellenberger et al. 2015). This is my hottest ICM, although not the most luminous, and it lies slightly below the $L_X - T_X$ relation – the *XMM-Newton* temperature of Frank et al. (2013) would bring the source onto the $L_X - T_X$ relation.

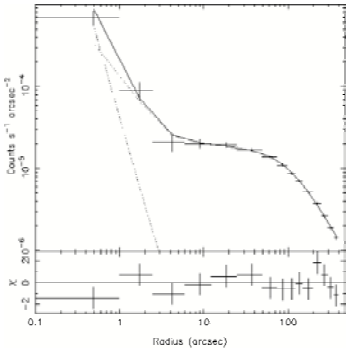

PKS 0806−10 (3C 195). The host galaxy of PKS 0806−10 may be interacting with a nearby galaxy (Inskip et al. 2010). It is an NLRG with FRII morphology. Although Ramos Almeida et al. (2013) found a strong group/weak cluster environment ($B_{gg} \sim 600$), I found little emission beyond the host galaxy so used an upper limit.

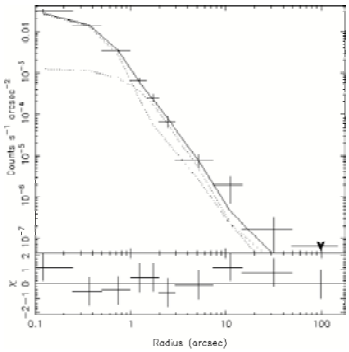

PKS 0915−11 (Hyd A, 3C 218) is a LERG with FRI morphology lying in cluster Abell 780 ($B_{gg} \sim 800$ – Ramos Almeida et al. 2013). There is a large shock at about 300 arcsec (Simionescu et al. 2009). The emission extended beyond the imaging chips, and I was also unable to use a side chip to model the background so I used the *Chandra* blank sky files for the background for both the profile and the spectral analysis. I obtained a temperature profile of a very similar shape to that reported by Simionescu et al. (2009) using an *XMM-Newton* observation, but with a higher temperature in line with the *Chandra* and *XMM-Newton* difference reported by Schellenberger et al. (2015). Hardcastle and Croston (2010) obtained a slightly higher temperature for a region nearer the nucleus, but it is compatible with my values for the temperature profile in that region.

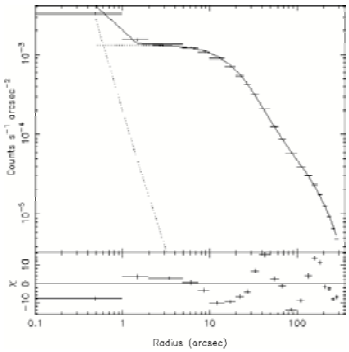

PKS 0945+07 (3C 227).

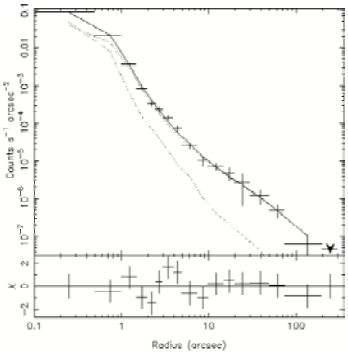

There is a dust torus around this BLRG extending to ~ 0.5 kpc (van der Wolk et al. 2010) and an emission line region extending to ~ 100 kpc (Prieto and Zhao 1997). It is an FRII lying in a weak environment ($B_{gg} \sim 80$ – Ramos Almeida et al. 2013). The detected emission does not extend far beyond the host galaxy, so I had insufficient counts for spectral analysis. My estimated temperature of 1.6 keV is that of a group environment.

PKS 1559+02 (3C 327) is an NLRG with a possible double nucleus and dust lanes (de Koff et al. 2000; Ramos Almeida et al. 2011). It has FRII radio morphology. Ramos Almeida et al. (2013) found a strong group environment ($B_{gg} \sim 500$), but I found the ICM emission to be weak with a temperature of only 0.65 keV. The surface brightness profile is very wide and shallow, and I fixed the β parameter at the lower limit. Perhaps because of this, I found the luminosity to be high for the temperature compared with that expected from the $L_X - T_X$ relation.

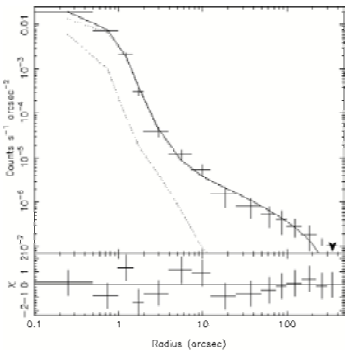

PKS 1648+05 (Her A, 3C 348) is a LERG with radio characteristics of both FRI and FRII morphologies (Sadun and Morrison 2002). It has a strong, disturbed environment, a secondary nucleus with a strong shock front (Nulsen et al. 2005), and entrained gas and dust filaments that may have come from a now stripped companion galaxy (O'Dea et al. 2013). The shock front is clearly visible in the surface brightness profile.

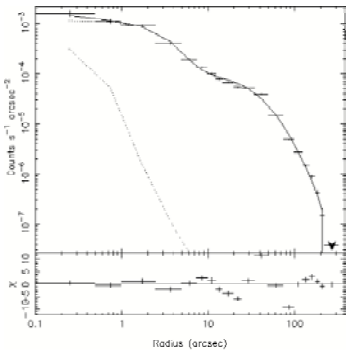

The emission extended beyond the imaging chip but I was able to use the spectrum from the outer regions to model the background. My temperature of 4.34 ± 0.11 keV is that of a moderate cluster, and is consistent with those reported by Nulsen et al. (2005) and Gizani and Leahy (2004) for the unshocked gas (using a shorter *Chandra* observation and a *ROSAT* observation respectively). Hardcastle and Croston (2010) obtained a slightly higher temperature from a smaller region nearer the nucleus and crossing the shock front; their temperature was compatible with a similar region in my temperature profile. Ramos Almeida et al. (2013) found that PKS 1648+05 is in a strong group ($B_{gg} \sim 500$) — a weaker environment than expected from my temperature.
Gizani and Leahy (2004) obtained a bolometric luminosity of 4.84×10^{44} erg s^{-1} within a radius of 500 kpc; I obtained a luminosity of 5.9×10^{44} erg s^{-1} within 938 kpc.

PKS 1733−56.
This source is a BLRG with FRII morphology lying in a disturbed environment and accreting gas from a merging galaxy (Bryant and Hunstead 2002). I found an unusually wide profile, perhaps a result of the disturbance, with a temperature typical of a group (1.4 keV). Ramos Almeida et al. (2013), however, found a very weak environment ($B_{gg} \sim 10$).

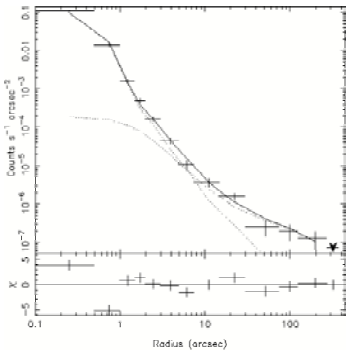

PKS 1839−48 is a LERG with a double nucleus (Ramos Almeida et al. 2011). It has FRI plumes and lies in a rich environment. Ramos Almeida et al. (2013) found a B_{gg} of around ~ 1600, and I obtained a correspondingly high ICM temperature (6 keV).

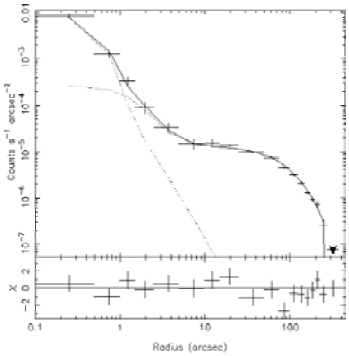

PKS 1949+02 (3C 403) is an NLRG with X-shaped, FRII morphology lying in a weak environment. I replicated the ISM temperature of 0.24 keV found by Hodges-Kluck et al. (2010), but had insufficient counts for spectral analysis of the extended emission. I therefore used an estimated temperature of $0.93^{+0.07}_{-0.12}$ keV. This is a little hotter than the ICM temperature of 0.6 ± 0.2 obtained by Hodges-Kluck et al. (2010). Ramos Almeida et al. (2013) obtained a group-type environment ($B_{gg} \sim 120 - 300$).

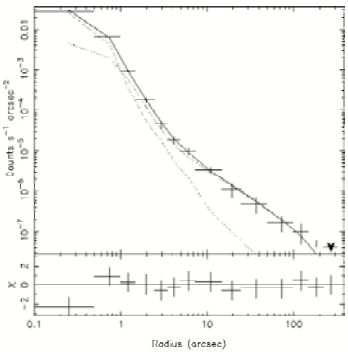

PKS 1954−55. This is a LERG with FRI morphology lying in a rich group environment ($B_{gg} \sim 500$ – Ramos Almeida et al. 2013). The emission extended beyond the imaging chips, but I was able to use a side chip to model the background for the spectral analysis. My temperature is that of a weak cluster (2.9 keV).

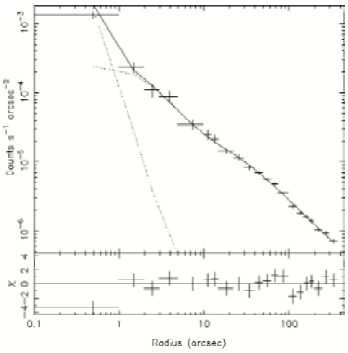

PKS 2211−17 (3C 444) is a LERG with cavities around its FRII lobes and a large-scale shock at about 200 kpc (Croston et al. 2011). It lies in a rich environment ($B_{gg} \sim 1300$ — Ramos Almeida et al. 2013). I obtained a similar temperature profile to that of Croston et al. (2011). For this work, I used a temperature within an annulus excluding the central temperature dip and extending across a wider region, and my temperature and luminosity are consequently a little higher ($4.11^{+0.18}_{-0.18}$ vs 3.5 ± 0.2 keV and $2.86^{+0.02}_{-0.03}$ vs 1.0×10^{44} erg s^{-1}).

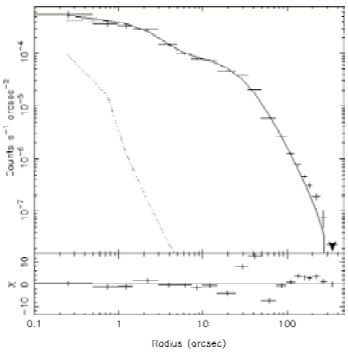

PKS 2221−02 (3C 445) is a BLRG with FRII morphology which is thought to have disc winds coming from the central regions (Braito et al. 2011). Ramos Almeida et al. (2013) found a weak environment ($B_{gg} \sim 50$). I had insufficient counts left after subtraction of the *Chandra* blank sky files to obtain a background for the spectral analysis, so I used single background subtraction for the temperature. My temperature is that of a group (1.1 keV), and is consistent with that found by Hodges-Kluck et al. (2010).

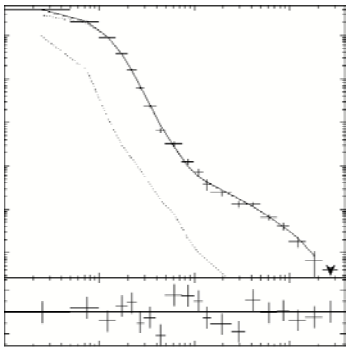

PKS 2356−61 is an NLRG with FRII lobes in a group environment ($B_{gg} \sim 450$ – Ramos Almeida et al. 2013). There were insufficient counts left after subtraction of the *Chandra* blank sky files to obtain a background for the spectral analysis. I therefore used single subtraction using a background from the observing chip to obtain the temperature, which was that of a group (1.2 keV). Hodges-Kluck et al. (2010) found a two-temperature ICM (3.0 and 0.9 keV) but used a much smaller radius for the spectrum. I could not fit a second thermal component with my wider region.

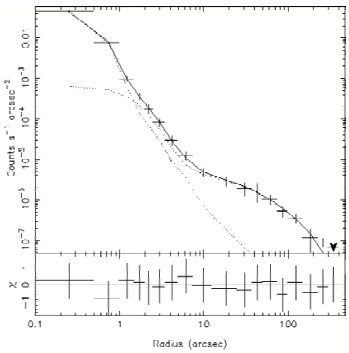

TABLE 4.1: The z0.1 sample.

Source	RA (J2000) Dec		Redshift	Scale	$\log_{10}$ L_{151}	Type	FR	nH
	h m s	deg min sec		kpc as^{-1}	W Hz^{-1} sr^{-1}		Class	x10^{20} cm^{-2}
3C 28	00 55 50.65	+26 24 37.3	0.195	3.23	26.24	LERG	2	5.39
3C 31	01 07 24.96	+32 24 45.2	0.017	0.34	24.30	LERG	1	5.36
3C 33	01 08 52.86	+13 20 14.2	0.060	1.15	25.93	HERG	2	3.90
3C 35	01 12 02.26	+49 28 35.5	0.067	1.28	25.34	LERG	2	13.00
3C 66B	02 23 11.41	+42 59 31.5	0.021	0.43	24.68	LERG	1	9.15
3C 76.1	03 03 14.99	+16 26 19.0	0.033	0.65	24.73	LERG	1	10.60
3C 98	03 58 54.43	+10 26 02.8	0.031	0.62	25.28	HERG	2	15.10
3C 192	08 05 35.01	+24 09 49.7	0.060	1.15	25.53	HERG	2	4.21
3C 219	09 21 08.63	+45 38 57.3	0.174	2.95	26.52	HERG	2	1.51
3C 236	10 06 01.76	+34 54 10.2	0.099	1.83	25.82	LERG	2	1.23
3C 285	13 21 17.86	+42 35 14.8	0.079	1.50	25.51	HERG	2	1.27
3C 293	13 52 17.80	+31 26 46.4	0.045	0.89	25.04	LERG	1	1.29
3C 296	14 16 52.98	+10 48 27.2	0.025	0.50	24.50	LERG	1	1.88
3C 303	14 43 02.76	+52 01 37.2	0.141	2.48	25.75	HERG	2	1.58
3C 305	14 49 21.64	+63 16 14.0	0.042	0.82	25.08	HERG	1	1.70
3C 310	15 04 57.11	+26 00 58.3	0.054	1.05	25.87	LERG	1	3.70
3C 321	15 31 43.46	+24 04 19.0	0.096	1.78	25.76	HERG	2	4.11
3C 326	15 52 09.10	+20 05 48.3	0.089	1.67	25.87	LERG	2	3.81
3C 338	16 28 38.29	+39 33 04.2	0.031	0.62	25.30	LERG	1	0.86
3C 346	16 43 48.60	+17 15 49.4	0.162	2.79	25.85	HERG	1	5.67
3C 386	18 38 26.22	+17 11 50.2	0.017	0.35	24.50	LERG	1	18.10
3C 388	18 44 02.35	+45 33 29.6	0.091	1.70	25.95	LERG	2	6.47
3C 390.3	18 42 08.93	+79 46 17.2	0.056	1.09	25.82	HERG	2	4.27
3C 433	21 23 44.56	+25 04 28.0	0.102	1.88	26.15	HERG	1/2	11.90
3C 442A	22 14 46.88	+13 50 27.2	0.026	0.53	24.70	LERG	1	5.07

Source	RA (J2000)	Dec	Redshift	Scale	$\log_{10}$ L_{151}	Type	FR	nH
3C 449	22 31 20.62	+39 21 30.1	0.017	0.35	24.16	LERG	1	12.00
3C 452	22 45 48.75	+39 41 15.9	0.081	1.53	26.21	HERG	2	11.30
3C 465	23 38 29.36	+27 01 53.4	0.030	0.61	25.15	LERG	1	5.01
4C 73.08	09 49 45.78	+73 14 23.1	0.059	1.14	25.34	HERG	2	2.29
DA 240	07 48 36.82	+55 48 59.5	0.036	0.71	25.07	LERG	2	4.52
NGC 6109	16 17 40.56	+35 00 15.7	0.030	0.59	24.61	LERG	1	1.33
NGC 6251	16 32 31.95	+82 32 16.4	0.025	0.50	24.39	LERG	1	5.65
NGC 7385	22 49 54.59	+11 36 32.5	0.026	0.53	24.43	LERG	1	5.11
PKS 0034-01	00 37 49.18	-01 09 08.2	0.073	1.40	25.54	LERG	2	3.07
PKS 0038+09	00 40 50.53	+10 03 26.8	0.188	3.14	26.44	HERG	2	5.51
PKS 0043-42	00 46 17.75	-42 07 51.4	0.116	2.10	26.23	LERG	2	2.21
PKS 0213-13	02 15 37.5	-12 59 30.5	0.147	2.57	26.23	HERG	2	1.92
PKS 0349-27	03 51 35.81	-27 44 33.8	0.066	1.26	25.55	HERG	2	0.99
PKS 0404+03	04 07 16.49	+03 42 25.8	0.089	1.66	25.89	HERG	2	11.90
PKS 0442-28	04 44 37.67	-28 09 54.6	0.147	2.57	26.33	HERG	2	2.43
PKS 0620-52	06 21 43.29	-52 41 33.3	0.051	1.00	25.12	LERG	1	5.17
PKS 0625-35	06 27 6.65	-35 29 16.3	0.055	1.06	25.41	LERG	1	7.24
PKS 0625-53	06 26 20.44	-53 41 35.2	0.054	1.05	25.35	LERG	2	5.42
PKS 0806-10	08 08 53.600	-10 27 39.71	0.109	1.99	25.92	HERG	2	7.74
PKS 0915-11	09 18 05.67	-12 05 44.0	0.055	1.07	26.21	LERG	1	4.93
PKS 0945+07	09 47 45.15	+07 25 20.4	0.086	1.62	25.91	HERG	2	3.00
PKS 1559+02	16 02 27.38	+01 57 55.7	0.104	1.91	26.12	HERG	2	6.44
PKS 1648+05	16 51 08.16	+04 59 33.8	0.155	2.69	27.14	LERG	1/2	6.33
PKS 1733-56	17 37 35.80	-56 34 03.4	0.099	1.82	26.13	HERG	2	8.29
PKS 1839-48	18 43 14.64	-48 36 23.3	0.111	2.02	25.83	LERG	1	5.62
PKS 1949+02	19 52 15.77	+02 30 23.1	0.059	1.14	25.53	HERG	2	14.30
PKS 1954-55	19 58 16.64	-55 09 39.7	0.058	1.13	25.57	LERG	1	4.52
PKS 2211-17	22 14 25.78	-17 01 36.3	0.153	2.66	26.37	LERG	2	2.61

Source	RA (J2000)	Dec	Redshift	Scale	$\log_{10}$ L_{151}	Type	FR	nH
PKS 2221-02	22 23 49.57	-02 08 12.4	0.056	1.09	25.48	HERG	2	4.87
PKS 2356-61	23 59 04.50	-60 54 59.1	0.096	1.78	26.27	HERG	2	2.38

Column 1: source name; Cols. 2-3: right ascension and declination, J2000 coordinates; Col. 4: redshift; Col. 5: angular scale; Col. 6: 151 MHz radio luminosity; Col. 7: radio-loud AGN spectral class; Col. 8: AGN morphology; Col. 9: Column density.

TABLE 4.2: Observation data for the z0.1 sample.

Source	X-ray[a] Instrument	Observation ID	Exposure[b] time (ks)	Screened[b] time (ks)	Radio map freq. (GHz)	Resolution (arcsec)	Ref.
3C 28	C	3233	50.38	49.30	1.4	1.1×1.1	1
3C 31	XMM	551720101	50.00	24.00	0.61	52×29	1
3C 33	C	6910, 7200	39.83	39.61	1.5	4×4	1
3C 35	C	10240	25.63	25.63	1.4	14×12	1
3C 66B	XMM	0002970201	17.86	13.39	1.4	12×12	1
3C 76.1	C	9298	8.06	8.06	1.5	4.9×4.9	1
3C 98	C	10234	31.71	31.71	4.9	3.7×3.7	1
3C 192	C	9270	10.02	9.62	1.4	3.9×3.9	1
3C 219	C	827	19.24	16.79	1.5	1.4×1.4	1
3C 236	C	10249	40.50	40.50	0.61	28×28	1
3C 285	C	6911	39.62	39.61	1.5	5.5×5.5	1
3C 293	C	12712	67.81	67.22	1.5	7.6×7.6	1
3C 296	C	3968	49.43	48.91	1.5	4.9×4.9	1
3C 303	C	1623	15.10	14.95	1.5	1.2×1.2	1
3C 305	C	12797, 13211	57.32	57.31	1.5	0.15×0.15	1
3C 310	C	11845	57.58	57.16	1.5	4×4	1
3C 321	C	3138	47.13	46.87	1.5	1.4×1.4	1
3C 326	C	10908, 10242	45.81	45.81	1.4	14×39	1
3C 338	C	10748	40.58	40.58	4.9	1×1	1
3C 346	C	3129	46.69	39.91	1.5	0.35×0.35	1
3C 386	C	10232	29.29	29.29	1.5	5.8×5.8	1
3C 388	C	5295	30.71	30.31	1.4	1.3×1.3	1
3C 390.3	C	830	33.97	28.60	1.6	2.8×2.8	1
3C 433	C	7881	38.19	37.15	8.5	0.75×0.75	1
3C 442A	C	5635, 6353	40.99	40.79	1.4	7.5×7.5	1

Source	Instrument	Obs. ID	Exposure time	Screened time	Radio map freq.	Resolution	Ref.
3C 449	C	4057	29.18	24.99	0.61	30×48	1
3C 452	C	2195	79.92	79.53	1.4	6×6	1
3C 465	C	4816	49.53	49.49	1.4	5.4×5.4	1
4C 73.08	C	10239	28.52	28.52	0.61	30×30	1
DA 240	C	10237	24.08	24.08	0.61	34×34	1
NGC 6109	C	3985	19.39	13.42	1.4	13×13	1
NGC 6251	C	847	37.44	30.67	0.33	55×55	1
NGC 7385	C	10233	39.33	39.33	4.9	4.9×3.6	2
PKS 0034-01	C	2178	27.52	26.54	4.9	4.5×3.7	3
PKS 0038+09	C	9293	7.94	7.94	4.9	4.4×3.4	3
PKS 0043-42	C	10319	18.38	18.38	8.6	1.2×0.88	4
PKS 0213-13	C	10320	19.89	19.89	4.9	5.9×3.4	3
PKS 0349-27	C	11497	19.89	19.89	1.5	11×8.9	2
PKS 0404+03	C	9299	8.07	8.07	8.4	2.2×2.2	5
PKS 0442-28	C	11498	19.79	19.79	4.9	9.3×2.1	3
PKS 0620-52	C	11499	19.80	19.80	4.7	2.6×1.5	3
PKS 0625-35	C	11500	19.79	19.79	4.9	4.7×3.2	2
PKS 0625-53	C	4943	18.45	16.67	4.8	2×1.6	4
PKS 0806-10	C	11501	19.79	19.79	4.9	6.8×1.6	2
PKS 0915-11	C	4970	98.82	98.42	1.4	2×1.5	2
PKS 0945+07	C	6842	29.78	29.78	1.5	4×4	6
PKS 1559+02	C	6841	39.65	39.62	8.5	2.2×2.2	5
PKS 1648+05	C	6257	49.52	49.52	1.5	1.4×1.4	7
PKS 1733-56	C	11502	19.86	19.66	4.7	2.2×1.3	3
PKS 1839-48	C	10321	19.79	19.79	4.7	2.6×1.7	3
PKS 1949+02	C	2968	49.47	45.66	1.5	4.5×4.1	8
PKS 1954-55	C	11505	20.65	20.45	4.8	2.4×1.3	4

Source	Instrument	Obs. ID	Exposure time	Screened time	Radio map freq.	Resolution	Ref.
PKS 2211-17	C	15091	164.38	163.17	4.9	7.6×3.1	3
PKS 2221-02	C	7869	45.60	45.60	8.2	2.4×2.4	5
PKS 2356-61	C	11507	19.79	19.79	1.5	7.2×6.9	9

References: (1) http://www.jb.man.ac.uk/atlas, (2) Made from the VLA archives, (3) Morganti et al. (1993), (4) Morganti et al. (1999), (5) Leahy et al. (1997), (6) Hardcastle et al. (2007a), (7) Gizani & Leahy (2003), (8) Dennett-Thorpe et al. (2002), (9) Made from the ATCA archives.

[a] C=*Chandra*, X=*XMM-Newton*. [b] pn camera times for *XMM-Newton* sources.

TABLE 4.3: Radial profile modelling for the z0.1 sample.

Source	Model,	D_{rad}[a]	Counts[b]	ICM (outer) model[c,d]			Host galaxy (inner) model[c,d]		
	Method	kpc		χ^2/dof	β	r_c (kpc)	χ^2/dof	β	r_c (kpc)
3C 28	$d\beta$, dsub	1432	14810	74/15	0.67 (0.55–0.85)	340 (437–253)	74/13	0.74 (0.62–0.90)	36 (47–27)
3C 31	$d\beta$, dsub	203	10827	104/62	0.30 (0.30–1.50)	39 (256–27)	104/62	0.79 (0.51–1.02)	1.3 (1.9–0.3)
3C 33	$d\beta$, dsub	113	2770	3.2/8	0.76 (0.30–1.20)	16 (112–1)	4.4/6	1.20 (0.85–2.00)	1.0 (2.0–0.5)
3C 35	$s\beta$, dsub	221	218	3.5/5	1.17 (0.30–1.20)	134 (384–2)			
3C 66B	$d\beta$, dsub	282	13788	13/14	0.35 (0.31–0.37)	46 (59–33)	42351	2.86 (1.09–3.00)	10 (12–4)
3C 76.1	$s\beta$, dsub	95	117	0.6/2	0.46 (0.30–1.20)	9.8 (64.6–0.8)			
3C 98	$d\beta$, dsub	121	1380	1.4/8	0.42 (0.30–1.20)	1.8 (58.1–1.0)	1.4/6	2.92 (0.77–3.00)	0.9 (1.3–0.2)
3C 192	$s\beta$, dsub	170	191	1.1/3	0.41 (0.30–0.91)	1.0 (10.6–1.0)			
3C 219	$s\beta$, dsub	726	2251	42266	0.40 (0.31–0.59)	28 (90–4)			
3C 236	$d\beta$, dsub	359	1057	4.2/7	0.39 (0.30–1.20)	26 (358–5)	4.2/5	1.20 (0.91–2.99)	2.4 (6.4–1.6)
3C 285	$d\beta$, dsub	368	1521	4.1/9	0.36 (0.32–0.70)	14 (82–5)	4.3/7	1.12 (1.00–3.00)	0.8 (4.1–0.5)
3C 293	$d\beta$, dsub	104	2421	1.4/7	0.69 (0.47–1.20)	5.7 (13.2–2.3)	1.6/5	0.98 (0.49–1.20)	0.7 (1.2–0.1)
3C 296	$d\beta$, ssub	>147	6862	6.4/19	0.70 (0.30–1.20)	188 (338–58)	7.1/17	0.64 (0.59–0.71)	0.7 (0.9–0.5)
3C 303	$s\beta$, dsub	366	2510	3.7/9	0.51 (0.44–0.70)	1.2 (10.3–1.0)			
3C 305	u/l		<797		*0.47*	*40.39*			
3C 310	$d\beta$, ssub	>465	9456	126/20	0.50 (0.46–0.54)	41 (53–32)	128/22	0.83 (0.56–2.00)	2.9 (8.9–1.7)
3C 321	$d\beta$, dsub	87	843	6.8/8	1.19 (0.31–1.20)	30 (55–5)	7.2/6	2.64 (1.07–3.50)	6.1 (8.3–2.8)
3C 326	$d\beta$, dsub	328	321	0.2/5	1.11 (0.30–1.20)	738 (1670–10)	0.2/3	0.95 (0.70–1.50)	10 (35–4)
3C 338	$d\beta$, ssub	>364	363864	1595/39	0.63 (0.61–0.65)	91 (94–85)	1625/37	0.58 (0.56–0.61)	11 (12–11)
3C 346	$d\beta$, dsub	411	5079	18/4	0.41 (0.33–0.64)	43 (102–19)	18/5	1.20 (1.20–1.20)	2.5 (4.4–1.0)
3C 386	$s\beta$, dsub	93	384	2.9/3	0.37 (0.30–0.52)	1.0 (4.2–1.0)			
3C 388	$d\beta$, ssub	>667	8149	45/18	0.52 (0.49–0.56)	40 (52–31)	48/16	1.26 (0.79–2.50)	7.5 (17.7–4.3)
3C 390.3	$d\beta$, ssub	>294	12647	65/12	0.40 (0.37–0.42)	13 (21–7)	65/10	1.07 (0.96–1.25)	5.3 (6.4–4.5)
3C 433	$d\beta$, dsub	323	3058	12.2/10	1.09 (0.30–1.20)	310 (593–3)	12.3/8	1.14 (0.50–1.20)	10 (16–1)
3C 442A	$d\beta$, ssub	>311	6344	44/14	1.11 (0.58–1.20)	212 (251–101)	44.5/12	0.53 (0.41–0.90)	6.2 (16.3–3.0)

Source	Model,	D_{rad}	Counts	ICM (outer) model			Host galaxy (inner) model		
	Method			χ^2/dof	β	r_c	χ^2/dof		r_c
3C 449	$d\beta$, ssub	>119	10260	17/14	0.36 (0.33–0.40)	18 (28–13)	17.3/12	0.95 (0.72–2.14)	1.0 (2.2–0.5)
3C 452	$d\beta$, dsub	300	3202	7.4/12	0.74 (0.42–1.20)	64 (125–21)	7.5/10	1.52 (0.96–3.00)	1.3 (2.5–0.6)
3C 465	$d\beta$, ssub	>240	37631	18/18	0.53 (0.45–0.74)	155 (216–122)	20/16	0.66 (0.61–0.73)	0.8 (1.1–0.6)
4C 73.08	$s\beta$, dsub	167	624	8.9/4	0.42 (0.31–1.20)	1.0 (68.3–1.0)			
DA 240	u/l		<433		*0.47*	*40.89*			
NGC 6109	$d\beta$, dsub	131	710	4.5/8	1.20 (0.30–1.20)	167 (579–24)	4.5/6	0.70 (0.47–1.00)	1.2 (3.3–0.2)
NGC 6251	$d\beta$, ssub	>220	2084	20/18	0.33 (0.30–0.55)	54 (152–27)	18/11	0.71 (0.57–0.88)	0.6 (1.1–0.3)
NGC 7385	u/l		<1122		*0.47*	*40.89*			
PKS 0034-01	u/l		<254		*0.47*	*40.90*			
PKS 0038+09	$d\beta$, dsub	231	1238	43/9	0.78 (0.30–1.20)	71 (975–3)	43/7	2.50 (0.96–2.50)	19 (25–8)
PKS 0043-42	$s\beta$, dsub	413	576	7.8/5	0.34 (0.30–0.44)	1.0 (20.7–1.0)			
PKS 0213-13	$s\beta$, dsub	126	1244	2.9/5	0.63 (0.30–1.20)	18 (81–4)			
PKS 0349-27	$d\beta$, dsub	310	839	1.0/8	0.30 (0.30–1.50)	97 (1256–39)	1.1/6	2.13 (0.45–2.50)	11 (23–1)
PKS 0404+03	u/l		<122		*0.47*	*40.89*			
PKS 0442-28	u/l		<126		*0.47*	*40.87*			
PKS 0620-52	$d\beta$, ssub	>368	8843	2.5/10	0.42 (0.37–0.48)	61 (89–41)	2.7/8	0.77 (0.61–1.12)	0.7 (1.0–0.2)
PKS 0625-35	$d\beta$, ssub	>365	5280	19/10	0.36 (0.31–0.67)	40 (168–15)	21/8	0.80 (0.66–0.99)	3.0 (4.3–1.9)
PKS 0625-53	$d\beta$, ssub	>412	28390	11/11	0.48 (0.43–0.53)	105 (132–85)	3.4/6	0.65 (0.39–0.80)	0.5 (1.3–0.1)
PKS 0806-10	u/l		<161		*0.47*	*40.99*			
PKS 0915-11	$d\beta$, ssub	>315	661760	1339/16	1.20 (0.68–1.20)	302 (417–142)	237/15	0.89 (0.56–1.44)	30 (40–21)
PKS 0945+07	$d\beta$, dsub	318	4404	10/13	0.40 (0.31–0.95)	7.0 (50.1–2.0)	11/11	0.86 (0.71–1.40)	0.6 (1.5–0.4)
PKS 1559+02	$d\beta$, dsub	564	1255	8.7/11	0.30 (0.30–1.20)	6.9 (1807.8–1.0)	9.0/9	2.99 (1.14–3.00)	3.3 (3.8–1.3)
PKS 1648+05	$d\beta$, ssub	>859	25027	538/16	0.63 (0.60–0.65)	93 (101–85)	538/14	2.32 (1.65–3.00)	19 (26–15)
PKS 1733-56	$d\beta$, dsub	492	4055	51/9	1.16 (0.30–1.20)	1165 (1813–18)	51/7	0.56 (0.30–1.27)	2.5 (10.7–0.2)
PKS 1839-48	$d\beta$, dsub	547	6934	21/14	0.66 (0.58–0.75)	191 (239–156)	21/12	0.79 (0.50–1.49)	3.0 (7.2–0.8)
PKS 1949+02	$d\beta$, dsub	252	2435	7.5/8	0.38 (0.30–1.20)	7.4 (112.0–1.8)	63/9	0.88 (0.61–1.94)	0.6 (1.3–0.4)
PKS 1954-55	$d\beta$, ssub	>415	7689	25/17	0.36 (0.33–0.41)	30 (51–13)	14/14	0.61 (0.47–1.14)	2.6 (8.7–1.8)

Source	Model, Method	D_{rad}	Counts	ICM (outer) model			Host galaxy (inner) model		
				χ^2/dof	β	r_c	χ^2/dof		r_c
PKS 2211-17	$d\beta$, dsub	784	31037	362/16	0.72 (0.69–0.74)	81 (87–76)	363/14	2.49 (1.58–2.50)	15 (17–10)
PKS 2221-02	$d\beta$, dsub	240	8775	22/16	0.35 (0.30–1.00)	16 (105–7)	28/14	1.15 (0.99–1.34)	1.5 (1.8–1.2)
PKS 2356-61	$d\beta$, dsub	526	1791	1.8/14	0.42 (0.30–1.20)	56 (279–12)	1.9/12	1.16 (0.64–2.00)	3.9 (9.4–1.1)

Column 1: source name. Col. 2: $d\beta$ is double β model, $s\beta$ is single β model, dsub is double background subtraction, ssub is single background subtraction, u/l is upper limit. Col. 3: maximum detected radius. Col. 4: net counts in the surface brightness profile. Col. 5: χ^2 and degrees of freedom for the ICM model. Col. 6: β for the ICM model. Col. 7: core radius for the ICM model. Col. 8: χ^2 and degrees of freedom for the inner model. Col. 9: β for the inner model. Col. 10: core radius for the inner model.

[a] Lower limits indicate that the detected ICM emission extended beyond the chip. [b] Counts for *XMM-Newton* sources are for the pn camera only. [c] Values for β and core radius r_c are best fit parameters. Ranges are the Bayesian credible intervals. [d] Italics indicate median values used for sources with low counts.

TABLE 4.4: ICM X-ray luminosity (L_X), central electron density (n_e) and ICM temperatures (T_X) for the z0.1 sample.

Source	$L_X(bol)$	R_{500}	$L_X(bol)$	$h(z)^{-1}L_X(bol)$	n_e	Method	Annulus	Z	T_X	χ^2/dof
	$\times10^{43}$ erg s^{-1}	kpc	$\times10^{43}$ erg s^{-1}	$\times10^{43}$ erg s^{-1}	m^{-3}		radii		keV	
	within D_{rad}		within R_{500}	within R_{500}	at $0.1R_{500}$		arcsec			
3C 28	$111.30^{+2.33}_{-2.12}$	1175	$107.40^{+1.79}_{-1.75}$	97.56	3667^{+27}_{-27}	Spectrum	24.60-246	0.30	$6.61^{+0.59}_{-0.49}$	106/143
3C 31	$0.63^{+0.06}_{-0.03}$	549	$2.01^{+0.33}_{-0.14}$	2.00	686^{+30}_{30}	Spectrum	60.00-600	0.30	$1.52^{+0.03}_{-0.03}$	2198/1430
3C 33	$0.49^{+0.02}_{-0.02}$	458	$0.49^{+0.02}_{-0.03}$	0.48	179^{+84}_{-75}	Estimate	2.46-98	0.30	$1.12^{+0.01}_{-0.02}$	
3C 35	$0.25^{+0.09}_{-0.10}$	420	$0.30^{+0.13}_{-0.17}$	0.29	772^{+105}_{-94}	Estimate	2.46-172	0.30	$0.97^{+0.10}_{-0.20}$	
3C 66B	$1.44^{+0.03}_{-0.03}$	601	$3.17^{+0.10}_{-0.12}$	3.14	936^{+10}_{-10}	Spectrum	50.00-600	$0.21^{+0.04}_{-0.03}$	$1.71^{+0.05}_{-0.04}$	711/691
3C 76.1	$0.04^{+0.02}_{-0.03}$	341	$0.08^{+0.05}_{-0.08}$	0.08	573^{+163}_{-131}	Estimate	2.46-147	0.30	$0.80^{+0.07}_{-0.12}$	
3C 98	$0.06^{+0.01}_{-0.02}$	330	$0.07^{+0.02}_{-0.02}$	0.07	407^{+212}_{-197}	Estimate	2.95-196	0.30	$0.62^{+0.04}_{-0.06}$	
3C 192	$0.11^{+0.03}_{-0.03}$	376	$0.16^{+0.06}_{-0.07}$	0.15	650^{+111}_{-72}	Estimate	1.48-147	0.30	$0.80^{+0.07}_{-0.12}$	
3C 219	$6.87^{+0.87}_{-1.03}$	501	$5.19^{+0.58}_{-0.51}$	4.77	2708^{+165}_{-159}	Spectrum	4.92-172	0.15	$1.46^{+0.13}_{-0.14}$	36/28
3C 236	$0.68^{+0.08}_{-0.11}$	475	$0.69^{+0.10}_{-0.14}$	0.66	484^{+164}_{-121}	Estimate	2.46-196	0.30	$1.24^{+0.05}_{-0.08}$	
3C 285	$0.52^{+0.12}_{-0.10}$	409	$0.56^{+0.13}_{-0.11}$	0.54	881^{+62}_{-64}	Spectrum	34.40-172	0.30	$0.94^{+0.10}_{-0.22}$	22/17
3C 293	$0.05^{+0.00}_{-0.00}$	373	$0.05^{+0.00}_{-0.00}$	0.05	290^{+86}_{-122}	Spectrum	2.46-73	0.30	$0.78^{+0.06}_{-0.06}$	18/12
3C 296	$0.23^{+0.03}_{-0.03}$	569	$0.57^{+0.13}_{-0.17}$	0.56	490^{+18}_{-17}	Spectrum	19.68-147	0.15	$1.59^{+0.12}_{-0.12}$	45/54
3C 303	$0.75^{+0.11}_{-0.11}$	397	$0.76^{+0.12}_{-0.11}$	0.71	1547^{+150}_{-107}	Spectrum	2.46-123	0.30	$0.94^{+0.09}_{-0.13}$	7.2/7
3C 305		*533*	<0.08	<0.08	<201	Upper limit	9.84-147	0.30	< 0.65	
3C 310	$3.00^{+0.45}_{-0.45}$	623	$3.34^{+0.50}_{-0.50}$	3.26	1940^{+27}_{-27}	Spectrum	9.84-246	$0.26^{+0.07}_{-0.06}$	$1.92^{+0.12}_{-0.13}$	135/134
3C 321	$0.21^{+0.01}_{-0.01}$	388	$0.21^{+0.01}_{-0.01}$	0.20	604^{+108}_{-88}	Estimate	2.46-49	0.30	$0.87^{+0.01}_{-0.02}$	
3C 326	$2.00^{+1.18}_{-1.93}$	617	$4.65^{+3.97}_{-4.58}$	4.46	216^{+28}_{-17}	Estimate	14.76-196	0.30	$1.94^{+0.40}_{-1.35}$	
3C 338	$40.14^{+5.94}_{-5.94}$	1041	$49.44^{+7.32}_{-7.32}$	48.75	3538^{+4}_{-4}	Spectrum	19.68-344	$0.44^{+0.04}_{-0.04}$	$4.63^{+0.08}_{-0.08}$	392/304
3C 346	$7.47^{+0.61}_{-0.91}$	731	$10.81^{+1.44}_{-2.28}$	9.99	2090^{+46}_{-55}	Spectrum	2.46-98	0.30	$2.79^{+0.24}_{-0.21}$	111/94
3C 386	$0.03^{+0.01}_{-0.01}$	450	$0.10^{+0.03}_{-0.04}$	0.10	345^{+39}_{-36}	Spectrum	2.46-270	0.30	$1.05^{+0.18}_{-0.12}$	12/15
3C 388	$13.05^{+1.14}_{-1.14}$	866	$14.04^{+1.24}_{-1.23}$	13.45	2538^{+25}_{-24}	Spectrum	9.84-344	$0.53^{+0.18}_{-0.15}$	$3.52^{+0.18}_{-0.15}$	141/167
3C 390.3	$3.16^{+0.47}_{-0.47}$	662	$4.26^{+0.64}_{-0.64}$	4.15	1223^{+23}_{-25}	Estimate	2.46-270	0.30	$2.14^{+0.01}_{-0.01}$	
3C 433	$0.24^{+0.10}_{-0.06}$	409	$0.24^{+0.12}_{-0.07}$	0.23	485^{+54}_{-168}	Spectrum	9.84-147	0.30	$0.96^{+0.76}_{-0.27}$	6.8/10

Source	$L_X(bol)$ within D_{rad}	R_{500}	$L_X(bol)$ within R_{500}	$h(z)^{-1}L_X(bol)$ within R_{500}	n_e at $0.1R_{500}$	Method	Annulus	Z	T_X	χ^2/dof
3C 442A	$1.13^{+0.10}_{-0.10}$	564	$1.28^{+0.12}_{-0.12}$	1.27	658^{+17}_{-14}	Spectrum	14.76-319	$0.24^{+0.12}_{-0.09}$	$1.58^{+0.11}_{-0.17}$	75/85
3C 449	$0.41^{+0.06}_{-0.06}$	583	$1.75^{+0.28}_{-0.28}$	1.74	911^{+14}_{-15}	Spectrum	14.76-147	$0.33^{+0.09}_{-0.08}$	$1.66^{+0.06}_{-0.07}$	63/77
3C 452	$0.77^{+0.04}_{-0.05}$	496	$0.79^{+0.05}_{-0.07}$	0.76	1250^{+66}_{-57}	Spectrum	9.84-147	0.30	$1.32^{+0.10}_{-0.08}$	45/46
3C 465	$3.47^{+0.51}_{-0.51}$	1016	$8.90^{+1.54}_{-1.54}$	8.78	554^{+4}_{-4}	Spectrum	9.84-295	$0.36^{+0.09}_{-0.08}$	$4.43^{+0.26}_{-0.23}$	255/259
4C 73.08	$0.04^{+0.02}_{-0.02}$	512	$0.05^{+0.03}_{-0.04}$	0.05	258^{+154}_{-90}	Spectrum	14.76-147	0.30	$1.37^{+0.26}_{-0.18}$	8.3/8
DA 240		*533*	<0.08	<0.08	<290	Upper limit	14.76-147	0.30	< 0.66	
NGC 6109	$0.14^{+0.04}_{-0.05}$	412	$0.24^{+0.10}_{-0.15}$	0.24	577^{+41}_{-41}	Estimate	9.84-221	0.30	$0.91^{+0.11}_{-0.24}$	
NGC 6251	$0.18^{+0.03}_{-0.03}$	523	$0.44^{+0.07}_{-0.07}$	0.44	348^{+17}_{-16}	Spectrum	34.44-246	0.30	$1.38^{+0.21}_{-0.03}$	30/25
NGC 7385		*533*	<0.06	<0.06	<256	Upper limit	4.92-147	0.30	< 0.61	
PKS 0034-01		*533*	<0.06	<0.06	<264	Upper limit	9.84-147	0.30	< 0.61	
PKS 0038+09	$2.42^{+0.46}_{-0.45}$	566	$2.65^{+0.60}_{-0.78}$	2.42	1754^{+504}_{-354}	Estimate	2.46-73	0.30	$1.82^{+0.12}_{-0.18}$	
PKS 0043-42	$1.02^{+0.20}_{-0.27}$	543	$1.32^{+0.28}_{-0.40}$	1.25	863^{+61}_{-55}	Spectrum	2.46-196	$0.41^{+0.69}_{-0.69}$	$1.59^{+0.96}_{-0.33}$	1.2/6
PKS 0213-13	$0.18^{+0.06}_{-0.08}$	375	$0.20^{+0.08}_{-0.10}$	0.19	1193^{+316}_{-237}	Estimate	4.92-49	0.30	$0.85^{+0.09}_{-0.15}$	
PKS 0349-27	$0.28^{+0.13}_{-0.19}$	392	$0.33^{+0.18}_{-0.25}$	0.32	270^{+36}_{-69}	Spectrum	2.95-246	0.30	$0.86^{+0.16}_{-0.20}$	15/13
PKS 0404+03		*533*	<0.27	<0.26	<549	Upper limit	19.68-147	0.30	< 0.93	
PKS 0442-28		*533*	<0.27	<0.25	<304	Upper limit	9.84-147	0.30	< 0.93	
PKS 0620-52	$3.94^{+0.59}_{-0.59}$	768	$6.74^{+1.05}_{-1.04}$	6.58	1261^{+18}_{-18}	Spectrum	19.68-246	$0.46^{+0.41}_{-0.19}$	$2.76^{+1.10}_{-0.60}$	115/137
PKS 0625-35	$3.15^{+0.48}_{-0.48}$	872	$6.33^{+1.07}_{-1.05}$	6.18	883^{+24}_{-27}	Spectrum	4.92-246	0.30	$3.46^{+0.48}_{-0.31}$	64/83
PKS 0625-53	$22.26^{+1.91}_{-1.92}$	1287	$42.61^{+3.93}_{-3.95}$	41.56	1609^{+16}_{-15}	Spectrum	24.60-295	0.30	$6.84^{+0.38}_{-0.34}$	171/188
PKS 0806-10		*533*	<0.21	<0.20	<482	Upper limit	19.68-147	0.30	< 0.86	
PKS 0915-11	$54.56^{+8.07}_{-8.07}$	851	$61.80^{+9.15}_{-9.15}$	60.25	5140^{+8}_{-11}	Spectrum	2.46-246	$0.30^{+0.02}_{-0.02}$	$3.31^{+0.10}_{-0.11}$	399/301
PKS 0945+07	$1.61^{+0.13}_{-0.17}$	562	$1.79^{+0.21}_{-0.31}$	1.72	903^{+89}_{-94}	Estimate	2.46-196	0.30	$1.64^{+0.06}_{-0.10}$	
PKS 1559+02	$1.04^{+0.23}_{-0.44}$	329	$0.79^{+0.16}_{-0.18}$	0.75	803^{+348}_{-110}	Spectrum	4.92-221	0.30	$0.65^{+0.10}_{-0.18}$	15/25
PKS 1648+05	$57.83^{+8.57}_{-8.57}$	995	$58.62^{+8.69}_{-8.69}$	54.37	4976^{+24}_{29}	Spectrum	14.76-196	$0.24^{+0.11}_{-0.10}$	$4.29^{+0.11}_{-0.11}$	200/239
PKS 1733-56	$0.83^{+0.35}_{-0.60}$	506	$0.84^{+0.37}_{-0.62}$	0.80	680^{+35}_{-51}	Spectrum	9.84-196	0.30	$1.38^{+0.42}_{-0.08}$	22/20
PKS 1839-48	$18.73^{+0.39}_{-0.45}$	1156	$23.64^{+0.67}_{-0.82}$	22.42	1570^{+26}_{-24}	Spectrum	4.92-147	0.30	$5.95^{+0.80}_{-0.72}$	89/102
PKS 1949+02	$0.22^{+0.04}_{-0.06}$	411	$0.26^{+0.07}_{-0.10}$	0.25	610^{+65}_{-70}	Estimate	4.92-221	0.30	$0.93^{+0.07}_{-0.12}$	

Source	$L_X(bol)$ within D_{rad}	R_{500}	$L_X(bol)$ within R_{500}	$h(z)^{-1}L_X(bol)$ within R_{500}	n_e at $0.1R_{500}$	Method	Annulus	Z	T_X	χ^2/dof
PKS 1954-55	$4.50^{+0.11}_{-0.11}$	785	$7.77^{+0.32}_{-0.31}$	7.56	1262^{+23}_{-21}	Spectrum	4.92-246	0.30	$2.89^{+0.22}_{-0.22}$	172/121
PKS 2211-17	$28.36^{+0.23}_{-0.26}$	916	$28.64^{+0.24}_{-0.26}$	26.59	4397^{+23}_{-26}	Spectrum	24.60-196	0.30	$4.11^{+0.18}_{-0.18}$	165/134
PKS 2221-02	$1.17^{+0.06}_{-0.09}$	450	$1.43^{+0.13}_{-0.22}$	1.39	782^{+34}_{-38}	Spectrum	4.92-221	0.30	$1.09^{+0.60}_{-0.40}$	52/57
PKS 2356-61	$1.45^{+0.31}_{-0.42}$	465	$1.38^{+0.25}_{-0.37}$	1.32	1049^{+152}_{-120}	Spectrum	4.92-196	0.30	$1.19^{+0.14}_{-0.20}$	17/15

Column 1: source name. Col. 2: ICM bolometric X-ray luminosity L_X within the maximum detected radius D_{rad}. Col. 3: the R_{500} overdensity radius – italics indicate median value used for sources with low counts. Col. 4: L_X within the R_{500} overdensity radius. Col. 5: as Col 4, but scaled by $h^{-1}(z)$ to correct for the critical density evolution. Col. 6: electron density at $0.1R_{500}$. Col. 7: method used to calculate ICM temperature. Col. 8: annulus used for calculating ICM temperature. Col 9: Metallicity – metallicities without errors were used as fixed parameters. Col. 10: ICM temperature. Col. 11: χ^2 and degrees of freedom for temperatures measured using spectral analysis.

TABLE 4.5: Partial correlation analysis results, using Generalized Kendall's τ correlation tests in the presence of a correlation with a third factor.

Sample	Sub-sample	N	τ/σ	p
Radio luminosity vs ICM luminosity, with a redshift correlation				
z0.1	All	55	2.62	0.0088
	HERG	25	1.68	0.093
	LERG	30	3.39	0.0006
	FRI	22	2.96	0.0030
	FRII	33	2.91	0.0036
Radio luminosity vs redshift, with an ICM luminosity correlation				
	HERG	25	4.65	< 0.0001
Radio luminosity vs ICM luminosity, with a redshift correlation				
0.03<z<0.2	All	46	2.37	0.018
	HERG	25	1.68	0.093
	LERG	21	2.72	0.0066
Radio luminosity vs ICM luminosity, with a redshift correlation				
z0.1 and ERA	All	81	4.09	0.0001
	HERG	40	2.43	0.015
	LERG	41	5.08	< 0.0001
	FRI	27	3.79	0.0001
	FRII	54	3.44	0.0006
Radio luminosity vs ICM luminosity, with a redshift correlation				
Matched	HERG	28	0.79	0.43
z0.1 and ERA	LERG	27	4.69	< 0.0001
ICM luminosity vs temperature, with a redshift correlation				
z0.1	Spectrum	34	15.28	< 0.0001
z0.1 and ERA	Spectrum	44	18.35	< 0.0001
ICM luminosity vs B_{gg}, with a redshift correlation				
z0.1 and ERA	All	22	3.66	0.0002
Radio luminosity vs central density, with a redshift correlation				
z0.1	HERG	25	0.73	0.47
	LERG	30	2.84	0.0046
ICM luminosity vs central density, with a redshift correlation				
	HERG	25	5.09	< 0.0001
	LERG	30	7.79	< 0.0001
Radio luminosity vs ICM luminosity, with a central density correlation				
	HERG	25	1.32	0.19
	LERG	30	1.50	0.13
Radio luminosity vs central density, with an ICM luminosity correlation				
	HERG	25	1.14	0.25
	LERG	30	1.37	0.17

N is sample size; τ is the partial correlation statistic; σ is the standard deviation; p is probability under the null hypothesis.

TABLE 4.6: Tests for differences in sample median ICM luminosities, using the Peto-Prentice two-sample test.

Sample	Sub-sample	N1	N2	statistic	p
Full	All	55	26	1.88	0.061
	HERG	25	15	3.69	0.0002
	LERG	30	11	0.16	0.87
	FRI	22	5	1.18	0.24
	FRII	33	21	3.35	0.0008
Matched	HERG	22	7	2.28	0.023
	LERG	20	7	1.53	0.12
	FRI	11	5	2.07	0.039
	FRII	32	9	1.69	0.09

N1 and N2 are the sizes of the z0.1 and ERA sub-samples being compared; p is probability under the null hypothesis.

TABLE 4.7: Principal Component Analysis for radio luminosity, ICM luminosity and central density, using the $z0.1$ sample.

	PC1	PC2	PC3
Eigenvalue	1.924	0.487	0.205
Proportion	0.736	0.186	0.078
Cumulative	0.736	0.922	1.000
Variable	PC1	PC2	PC3
Radio luminosity	0.495	0.646	0.581
ICM luminosity	0.646	0.296	0.407
Central density	0.581	-0.703	0.705

PC1, PC2 and PC3 are the principal components in order of contribution to the total variance.

Chapter 5

FRII galaxy lobes and the intra-cluster medium

5.1 Introduction

The dynamics of the lobes of radio-loud AGN are dependent on their pressure relative to that of the surrounding ICM (Scheuer 1974). If they are highly over-pressured, they will expand at supersonic rates; if near pressure balance they will expand more gently and be moulded by the ICM. The lobes will put energy into the ICM as they displace the gas, but if the expansion is supersonic, the lobes will also input energy through shocks (eg Bîrzan et al. 2004; Hlavacek-Larrondo et al. 2012). Observational studies of lobe shocks have estimated Mach numbers ranging from 1.2 to 6 (eg Wilson et al. 2006; Bîrzan et al. 2008; Shelton et al. 2011; Croston et al. 2011; Worrall et al. 2012; Nulsen et al. 2013); the strongest known lobe shock is Mach 6 for Centaurus A (Croston et al. 2009). However, in many cases the uncertainties in the methods used to estimate Mach numbers mean that these are likely to be lower limits and so the true values could be higher. The rate of lobe expansion is therefore important in determining heat input into the ICM.

As described in Section 1.3.3, there have been a number of simulations and observational studies looking at radio lobes: how the internal conditions differ from equipartition; their particle content; how their internal pressure compares with that of the ICM; and how energy is transferred from the lobe to the ICM. There is now a good body of evidence that FRI lobes need particles beyond the minimum energy conditions to maintain pressure balance with the ICM and that these are likely to be supplied by entrainment of baryons from the ICM by the jet (eg Bîrzan et al. 2008; Hardcastle and Croston 2010; Croston and Hardcastle 2014).

FRII sources tend to more distant so there are fewer detailed studies, but as described in Section 1.3.3, the assumption of equipartition usually leaves the lobes underpressured compared with their environments. When the inverse Compton emission visible in X-ray observations is used to better model the electron energy density in the lobes, the calculated lobe pressures are then brought near to those of their environments, suggesting that the lobes are slightly electron-dominated. That the jets remain relativistic for great distances suggests that the overall expansion speed of the lobes is driven by both ram pressure and internal lobe pressure, and so shocks at the lobe tips are to be expected. For distant sources, the temperature variations across the shock cannot be isolated, but Mach numbers can be estimated from the ratio between internal end external lobe pressure (Sections 1.3.3 and 2.2.5). This method neglects the ram pressure, so Mach numbers obtained in this way should be regarded as lower limits, but, importantly, they allow limits to be set on the energy input from the lobes.

Until now there have not been enough high quality X-ray observations of FRII lobes to build a large enough sample for a systematic study of lobe particle content and dynamics by combining X-ray IC analysis of the internal lobe conditions with environmental measures of their of external conditions (as presented in Chapters 3 and 4 of this thesis). The samples used in my environmental analysis have radio and X-ray observations of sufficient quality to enable estimates of FRII lobe pressures and lobe tip Mach numbers to be made for a representative sample of FRII lobes for the first time. In this chapter I carry out an inverse Compton study of FRII radio lobes with well constrained environments in order to determine the radio lobe dynamics, to look for evidence of energy being input into the ICM, and to see whether the ICM in its turn has an effect on the development of the lobes.

5.2 Sample

The sample consists of the lobes of the FRII galaxies from the ERA and z0.1 samples used in Chapters 3 and 4 of this thesis. The ERA sample contains 21 FRII sources, ranging from 3.5×10^{25} to 4.8×10^{27} W Hz^{-1} sr^{-1} in radio luminosity. Of these, 15 are HERGs and 6 are LERGs. The z0.1 sample contains 33 FRII sources (23 HERGs and 10 LERGs), with radio luminosities between 1.2×10^{25} and 3.3×10^{26} W Hz^{-1} sr^{-1}.

A number of lobes were excluded from the analysis for practical reasons: because the lobe images were incomplete – partially off the chip or lying across chip boundaries; because they were small in angular extent and masked by nuclear emission or by a rich ICM; because the ICM was strong and highly disturbed the results were highly dependent on choice of background; or because the map was poor quality or low resolution and the

lobe shapes could not be defined with sufficient accuracy. In one case the lobes were so large that they extended well beyond both the maximum detected ICM radius and the R_{200} overdensity radius, making estimates of the ICM pressure problematic. Table 5.1 lists the lobes that were excluded, and the possible effects of the exclusions are discussed in Section 5.4.4.6 below.

The final sample contains 37 HERG lobes, of which 4 have upper limits for the ICM luminosity and pressures, and 12 LERG lobes, including 1 ICM upper limit. 9 of the HERGs and 3 of the LERGs are from the ERA sample (including 1 HERG upper limit).

The radio and X-ray observations are listed in Chapters 3 and 4, Tables 3.2 and 4.2.

5.3 Analysis

The aim of the analysis was to investigate the lobe dynamics and content by comparing the observed and minimum (equipartition) lobe pressures, and then to use these results to compare conditions within the radio lobes with those of the surrounding ICM. I needed therefore to find the internal lobe pressures, compare them with ICM pressures, and estimate a lower limit on the advance speeds of the lobe tips.

I used the radio maps listed in Tables 3.2 and 4.2 to find the positions of the lobe tips, the mid-point of the lobes and estimate the lobe shapes and volumes. I excluded the nucleus, jets and hot-spots (which will have different electron densities and magnetic field strengths from the lobes) and background X-ray sources from the lobe regions and volumes. I used these regions to measure the radio and X-ray fluxes within the lobes.

Where possible, I made separate flux measurements and volume estimates for the individual lobes. For the ERA sample, however, the X-ray flux was generally very low so I used fluxes for the combined lobes. Also, for some sources there was no clear division between the two lobes, so again I combined the lobes. These are listed in Table 5.2, together with the lobe tip positions, mid-lobe positions and volumes.

There was no consistent set of radio maps for the sources in the samples. When possible, I used the lowest available frequency maps to define the lobe shapes and volumes and to exclude the nucleus and hot-spots since the synchrotron radiation is dominant at low frequencies. However, if the low frequency maps were of low resolution, I used higher frequency maps to define the shapes, but checking with the low resolution maps to see if there were any regions of extended flux missing from the higher frequency maps.

Since my commonest map frequency was 1.4 GHz, I used these when available to obtain the radio flux. When I only had higher frequency maps I used published flux

measurements at lower frequencies (since the lower frequencies were less likely to be contaminated by nuclear and hot-spot emission), splitting the low flux measurements between the lobes in the same ratio as the flux from the higher frequency measurements as was done by Croston et al. (2005b). The details of the maps used to measure the radio fluxes are given in Table 5.3.

Having defined the lobe shapes, I obtained the ICM pressures using the method described in Section 2.2.2, using the β-model parameters from Tables 3.3 and 4.3 in Chapters 3 and 4. Table 5.2 contains the ICM mid-lobe and lobe tip pressures.

To obtain the X-ray fluxes, I prepared the data as described in Section 2.2.1. I used a power law to model the IC emission (Section 2.2.3.5), but also tried to fit a thermal model in case there was a contribution from the shocked ICM. This only gave an improved fit for one source – 3C 452. This source has been studied in detail by Shelton et al. (2011) using an *XMM-Newton* observation; I obtained compatible results.

For several of the sources with low counts, I could get an acceptable fit from either a power law or a thermal model, but the temperature from the thermal fit was always low – usually less than the ICM temperature – so could not be a contribution from shocked gas. In these cases I used the power law fit.

For many sources, there were insufficient counts to get a good fit for the power law. I followed Croston et al. (2005b) in assuming that the photon index for the power law should be in the region of 1.5. If the photon index from the fit was much different from this I fixed it at 1.5 and fitted the model to obtain the normalisation. If there were insufficient counts to fit the model, I used an unbinned spectrum with the photon index again fixed to 1.5. Finally, if the net counts in the lobe were less than three times the background error I used three times the background error as an upper limit on the counts and again used a photon index of 1.5 to obtain the normalisation. Table 5.3 contains the radio and X-ray fluxes for the sources, together with details of the power law fits for the X-ray emission.

I used the radio and X-ray fluxes, together with the lobe volumes, to obtain the equipartition and observed (inverse Compton) magnetic fields and electron energy densities. For this, I used the SYNCH code (Hardcastle et al. 1998a). SYNCH calculates the equipartition conditions from the radio flux and then uses the X-ray flux to calculate the IC contributions from the CMB and from SSC, assuming that the energetic particles are predominantly electrons (Section 2.2.4).

Table 5.4 contains the equipartition and observed magnetic fields and pressures within the lobes. The quoted errors on the observed field and pressure are derived from the X-ray flux error, so do not include the systematic errors discussed below (Section 5.4.4).

Finally, I used the Rankine-Hugoniot conditions for the conservation of mass, momentum and energy across a shock front to obtain the Mach number $\mathscr{M}$ in terms of the lobe pressure balance (Section 1.3.3, equation 1.34 and Section 2.2.5). As noted in that section, the jet ram pressure is not included in the calculation so $\mathscr{M}$ will be a lower limit. In addition, as discussed in Section 1.1.2.2, the pressure calculations assume that there are no protons in the lobes. If there were a significant proton population, this would also increase the internal pressure.

The Mach numbers are included in Table 5.4. I have excluded sources with upper limits for the external pressure. Note that because nearly $\frac{2}{3}$ of the low luminosity LERGs are FRI sources, I could only calculate Mach numbers for 8 of the LERGs, 4 of which are upper limits. In contrast, there are only two HERG FRI sources, and I have 31 HERG Mach numbers (including one upper limit).

5.4 Results and discussion

5.4.1 Deviation from equipartition

Figures 5.1 and 5.2 show the ratio between the observed (IC) and equipartition magnetic fields and lobe pressures for the sample, with and without the upper limits. The observed magnetic field is, as found by Hardcastle et al. (2002a) and Croston et al. (2005b), lower than the equipartition field for all sources suggesting that the lobes contain electron energy densities additional to the minimum energy condition. All but two lobes are however within one order of magnitude of equipartition and the median ratio of observed to equipartition fields is 0.4, similar to that reported by Croston et al. (2005b).

Similarly, the observed pressure is higher than the equipartition pressure and again all are within one order of magnitude of equipartition except the same two lobes. The median pressure ratio (P_{obs}/P_{eqp}) is 2.7. As with all the calculations in this chapter, these results assume that there are no protons in the lobes and that the lobes are completely filled with synchrotron-emitting particles. If there were protons in the lobes, the internal pressure would be higher.

5.4.2 Lobe pressure balance

Figure 5.3 shows the observed pressure plotted against the external pressure at the lobe tip and at mid-lobe. Pressure balance is shown as a dotted line. If the lobes are growing they should be overpressured at the tip, and this is the case for the majority of the

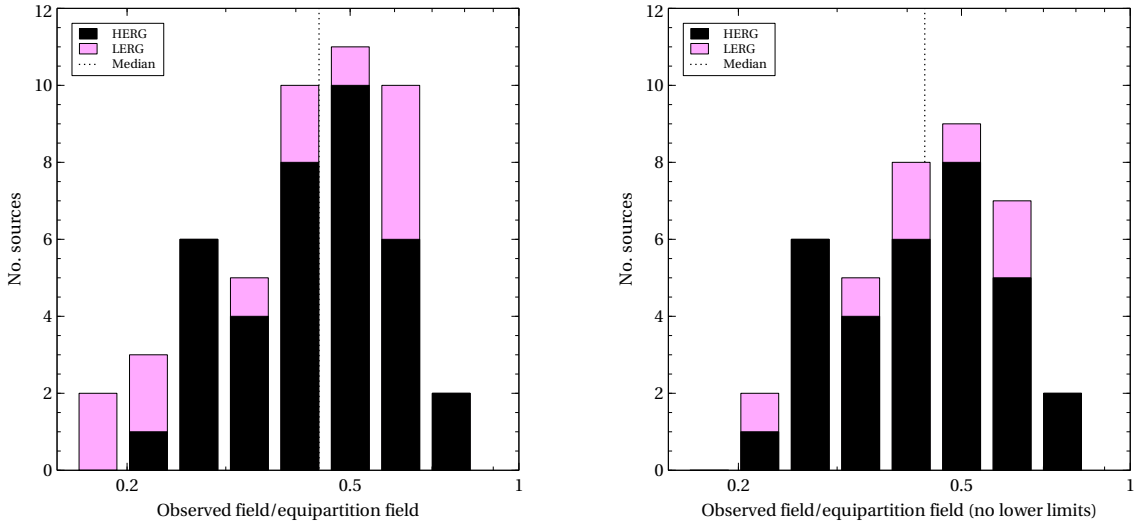

FIGURE 5.1: The ratio of observed (calculated from the IC emission) to equipartition magnetic fields, separated into excitation classes. HERGs are shown in black, LERGs in magenta. The left histogram includes all sources; the right histogram excludes lower limits.

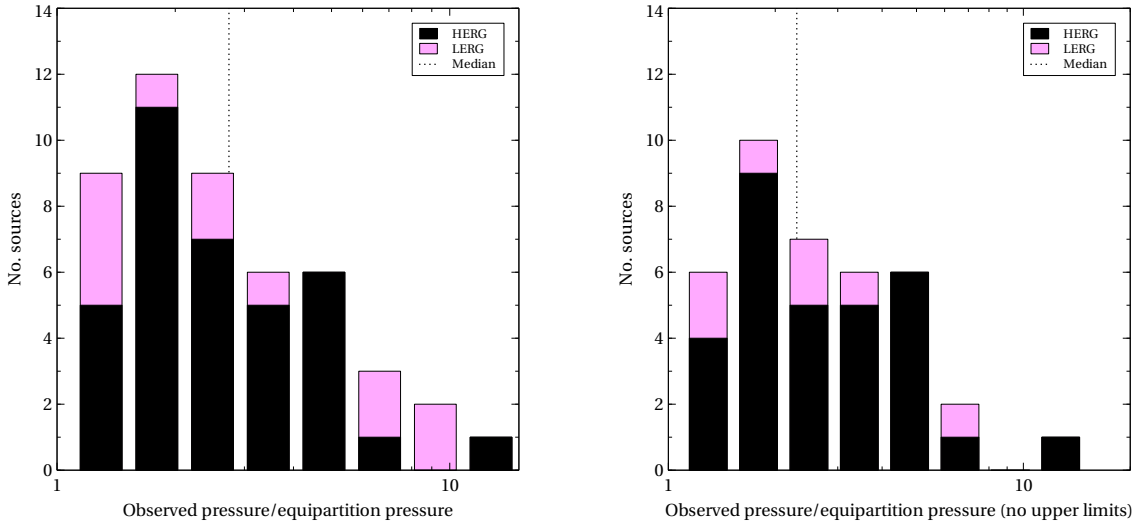

FIGURE 5.2: The ratio of observed (calculated from the IC emission) to equipartition lobe internal pressures, separated into excitation classes. HERGs are shown in black, LERGs in magenta. The left histogram includes all sources; the right histogram excludes upper limits.

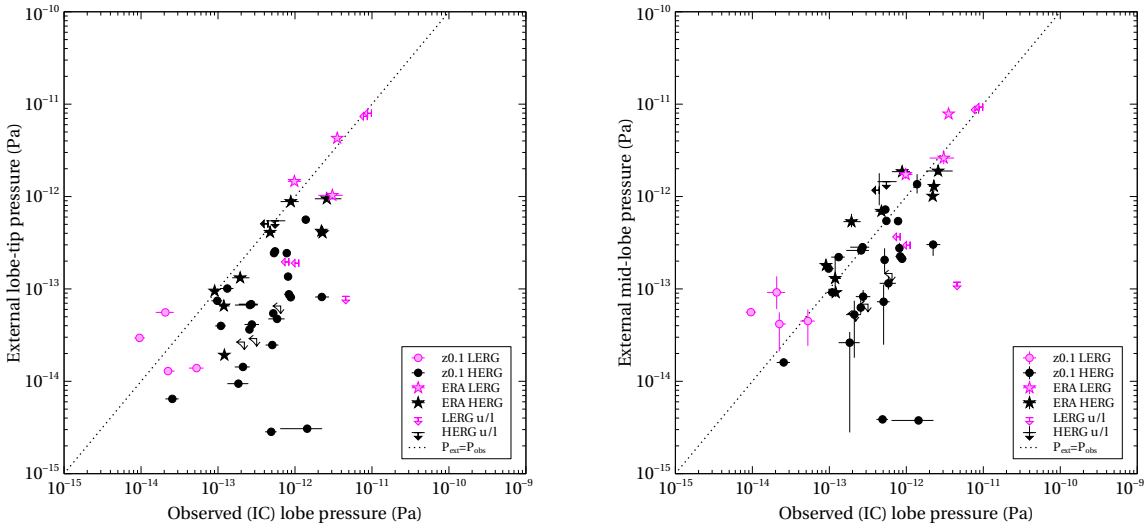

FIGURE 5.3: Internal lobe pressure vs external (ICM) pressure, at the lobe tip (left) and at mid-lobe (right). Magenta symbols are LERGs, black symbols are HERGs. Circles are z0.1 sources and stars are ERA sources. Arrows denote upper limits.

results. Since the effects of the jet ram pressure has not been included, the internal lobe-tip pressure will be higher than the observed lobe pressure calculated here, and so the observed pressures are lower limits at the tip. The true tip pressure is therefore likely to be above pressure balance for all the sources.

At mid-lobe, the lobes are distributed about the pressure balance line with a median P_{obs}/P_{ext} of 1.8, reflecting the results of Croston et al. (2005b) and Belsole et al. (2007). The lowest ratio of observed to external pressure is 0.17 for 3C 326 (the largest lobe in my sample by several hundred kpc), and there are only three lobes more than one order of magnitude above pressure balance. The lower limit PKS 0034-01 ($P_{obs}/P_{ext} = 39$) is an NLRG with small lobes (42 kpc long) so may be a young source. 3C 321, which has very high pressure ratios of over 100, has small lobes (50 and 90 kpc long) 280 kpc from the nucleus. It is merging with a neighbouring galaxy and is in a disturbed environment (Evans et al. 2008). The β-model has steep parameters, giving very low ICM pressures at mid-lobe. The parameters are very poorly constrained with large errors and so the extrapolation of the model to obtain the external lobe pressures is likely to be imprecise.

5.4.3 Lobe tip Mach number

The Mach numbers are plotted in Figure 5.4. As previously mentioned, there are two caveats on this calculation which mean that the Mach numbers should be regarded as lower limits. Firstly the calculation of internal lobe pressure assumes that the lobes contain no particles other than relativistic electrons/positrons. Any proton content will increase the pressure within the lobe, and consequently the Mach number. In addition,

the Mach number calculation is based on the lobe internal pressure and does not include the jet ram pressure and so inevitably underestimates the Mach number.

The two lobes with Mach numbers greater than 10 are both from 3C 321, which, as mentioned above, has very low, uncertain ICM pressures. I have not included 3C 321 in any further plots, but all statistics have been calculated with and without 3C 321.

Without 3C 321, the maximum Mach number is 4.7 and the median is 1.6, similar to the results of the studies mentioned in Section 5.1. My results are also compatible with those of Shelton et al. (2011) and Croston et al. (2011) who obtained Mach numbers of 1.6 and 1.7 for 3C 452 and PKS 2211−17 respectively. Perucho et al. (2014), in their simulations of relativistic jets, found high Mach numbers (5 to 30) during the early development of the lobes, but dropping rapidly after a few tens of Myr and reaching Mach 3 by 100 Myr. They then drop more gradually to less than Mach 2. My median therefore lies within their range of results for well developed lobes.

The HERG subsample has a wider range of Mach numbers than the LERG subsample, and the median Mach number for the LERGs is lower than that of the HERGs. However, a Median test does not reject the null hypothesis that the medians are the same ($p \sim 0.2$). Removing the high Mach numbers of 3C 321 from the Median test makes only a slight difference.

As stated before, these Mach numbers assume that the lobes do not contain protons. The presence of a significant proton population such as is thought to exist in FRI lobes would increase the lobe internal pressure substantially. I therefore looked at the effect of a ten-fold increase in internal pressure on my median Mach number and found that this would raise it to 5.5. The simulations of Perucho et al. (2014) only contain Mach numbers above 5 for sources less than about 70 Myr in age. It is unlikely that my samples would contain so many very young sources. This would suggest therefore that any proton content is low compared with that of FRI lobes.

It would be useful if the lobe dynamics, and consequently energetic input could be inferred directly from the radio and/or environment properties. Figure 5.5 shows radio luminosity (taken from Tables 3.1 and 4.1) plotted against Mach number. The plot shows no sign of a correlation between radio luminosity and Mach number, and this is confirmed by a partial correlation Kendall's τ test (Akritas and Siebert 1996) which looks for a correlation between the radio luminosity and Mach number in the presence of a dependency on redshift (Table 5.5).

I then compared Mach number with X-ray richness (Figure 5.6, left), using the ICM X-ray luminosities from Tables 3.4 and 4.4. In this case Mach number appears to decline with increasing ICM luminosity for the HERG subsample, while the LERG sources are

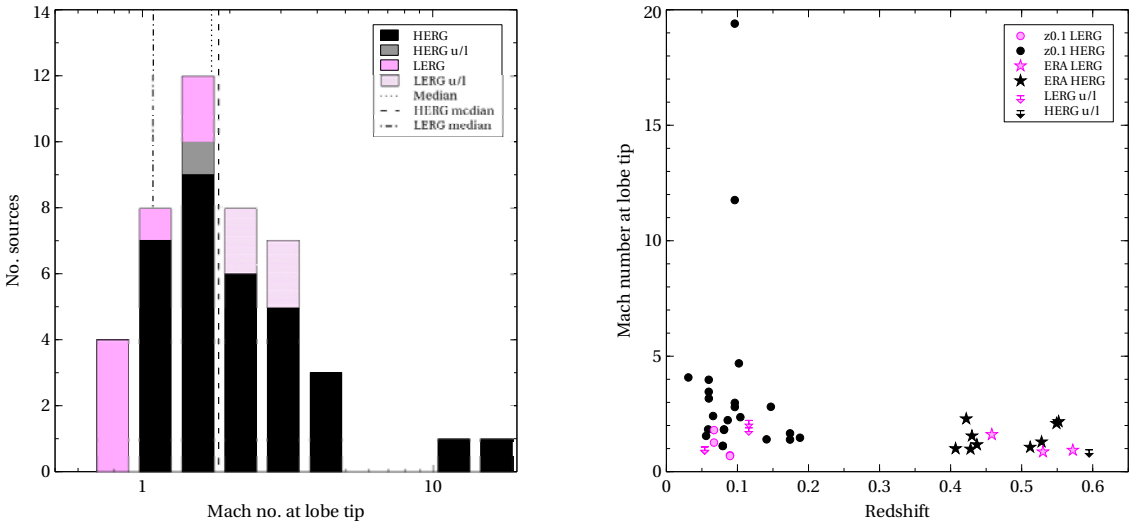

FIGURE 5.4: On the left, Mach number at the lobe tip. HERGs are shown in black and LERGs in magenta, HERG upper limits are grey, LERG upper limits are pale pink. On the right, Mach number at the lobe tip plotted against redshift. Symbols as in Figure 5.3. The two Mach numbers greater than 10 are from the lobes of 3C 321, discussed in Section 5.4.3

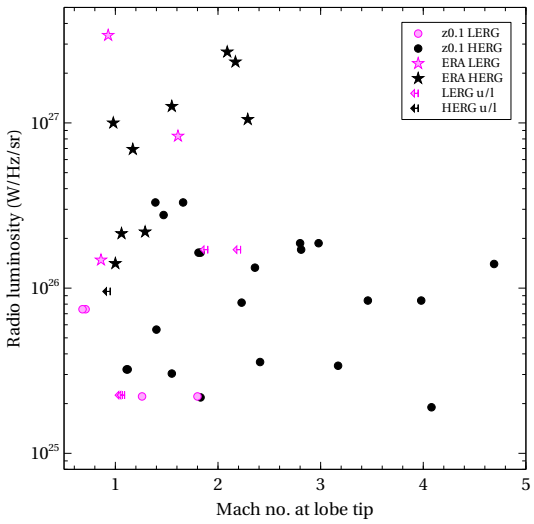

FIGURE 5.5: Radio luminosity plotted against Mach number. Symbols as in Figure 5.3.

limited to a band of ICM luminosities at low Mach number. The partial correlation Kendall's τ tests (Table 5.5) show a strong negative correlation for both the full sample and the HERG subsample. The correlation is weakened slightly when the uncertain 3C 321 Mach numbers are removed, but is still strong. There is quite substantial scatter – at least some of this is likely to be due to systematic errors which are discussed in Section 5.4.4 below.

It must be noted however that ICM external pressure was used in the Mach number estimates. As can be seen from the right-hand plot in Figure 5.6 and Table 5.5, lobe-tip

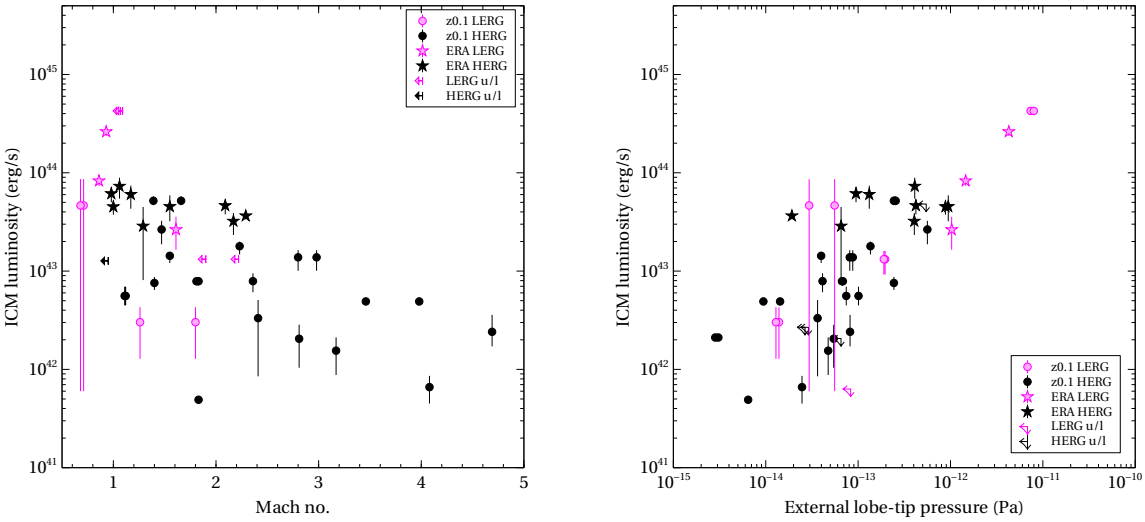

FIGURE 5.6: ICM X-ray luminosity plotted against Mach number (left) and lobe-tip pressure (right). Symbols as in Figure 5.3

external pressure correlates very strongly with ICM luminosity, so this is likely to be the factor driving the correlation between Mach number and ICM luminosity. However, ICM temperature is related to ICM luminosity and is also used in the pressure calculations so is a potential confounding factor. More work is therefore needed to check if this if the relationship is genuine.

If the anti-correlation between environment richness and Mach number is genuine, it may have contributed to the lack of high Mach number LERGs – since ICM luminosity correlates with radio luminosity for the LERGs and the low radio luminosity LERGs mostly have FRI morphology, the lobes remaining in the sample are for the most part in relatively rich environments and so will be expected to have low Mach numbers.

In order to see if lobe advance speed is related to age, I used distance to the lobe tip as an indication of the age of the source. Figure 5.7 shows Mach number plotted against the distance to the lobe tip. Although the plot gives a suggestion of a weak correlation for the HERGs, this is not reflected in the statistics (Table 5.5). Since viewing angle will have a strong effect on the distance to lobe tip, I tested the NLRGs in the HERG subsample (which will all have a viewing angle of more than 45°) rather than the full HERG subsample. There are however several other factors that would affect any such relationship, for instance the environment is weaker beyond the core radius so if there is a relationship between Mach number and ICM luminosity this would need to be taken into account. Again, this is an area that needs more detailed consideration.

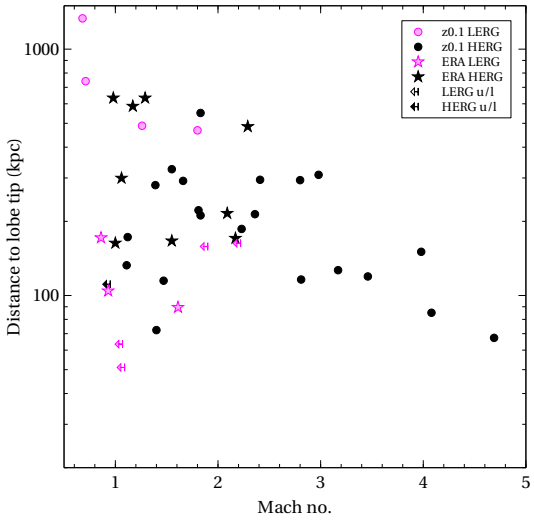

FIGURE 5.7: Mach number vs distance to lobe-tip. Symbols as in Figure 5.3

5.4.4 Systematic errors

I made a number of assumptions and approximations during the calculations which could impact on my findings. The following section looks at the likely size of the effects.

5.4.4.1 Lobe volumes

Since the electron density scales with lobe volume ($V^{-4/7}$, Hardcastle 2004 – assuming an electron index of 2), a potentially large source of error is the definition of the lobe shapes and the consequent flux measurements and volume calculations. I used the same shapes and exclusions for both the radio and X-ray flux measurements, and subtracted the exclusion volumes from the total volume. However, the shapes are of necessity simple, 2-dimensional shapes approximating a complex, 3-dimensional structure and gives scope for large inaccuracies.

I looked at the difference in using a cylindrical lobe instead of ellipsoidal for 3C 452; this increased the volume by 50% and reduced the observed pressure by 30%. Using an ellipsoidal lobe instead of cylindrical for 3C 35 reduced the volume by 40% and increased the observed pressure by 60%. An increase or decrease of 60% in the observed pressure would, for example, increase/decrease a Mach number of 5 to 6.3/3.2 or a Mach number of 1 to 1.2/0.7. Because the size of the change decreases with Mach number this is unlikely to make a significant difference to the results. Note that both these tests gave a visibly poor fit to the radio lobes so are likely to be over-estimating the potential errors.

I also looked at the effect of inaccuracies in exclusion sizes by doubling and halving my exclusion volume estimates for four sources. The exclusion volumes ranged from 5% to

15% of the total lobe volume and and gave similar percentage changes in the observed pressure. This size increase/decrease at Mach 5 would give a Mach number of 5.35/4.6, with the size of the change reducing with Mach number.

5.4.4.2 Low frequency spectral index

In previous inverse Compton studies (eg Hardcastle and Worrall 2000; Hardcastle et al. 2002a; Croston et al. 2005b), the electron energy distribution at low frequencies has been assumed to be a power law with an index of ∼2, steepening to ∼2.5 above a break frequency and then dropping exponentially at the cut-off frequency, following the theoretical work of Heavens and Meisenheimer (1987). However, recent LOFAR observations have allowed the low energy electron index to be measured precisely for some sources (eg Harwood et al. 2013, 2015, 2016), giving a steeper index in line with the index above the break. I therefore used an electron index of 2.4 (spectral index 0.7) to calculate the equipartition and observed lobe fields and energy densities for all sources.

If the index is too steep, the energy densities will be overestimated. I looked at the effect of a lower spectral index on the mid-lobe pressure ratio (and consequently the Mach number) for seven of the 3CRR sources with ratios of observed to external pressure ranging between 0.5 and 12. I found that reducing the electron energy index to 2.0 reduced the pressure balance by 25% to 30%. An increase/decrease of 30% would change Mach 5 to Mach 5.7/4.2 and Mach 1 to 1.1/0.9. As with the volume changes, the results are unlikely to be much affected by the index approximation.

5.4.4.3 Maximum and minimum energies

I followed Croston et al. (2005b) in using Lorentz factors of $\gamma_{min} = 10$ and $\gamma_{max} = 10^5$ to define the minimum and maximum electron energies for the inverse Compton calculations. As discussed in Croston et al. (2005b), it is the low energy population of electrons that scatter the CMB photons (which are responsible for the bulk of the lobe X-ray emission) to the observed X-ray frequencies, so varying γ_{max} makes little difference. They chose γ_{min} to be lower than had previously been observed in hot-spots, but found that varying it between 10 and 1000 gave the same results to within the $1-\sigma$ errors.

5.4.4.4 Radio observation properties

There was no consistent set of low frequency radio maps for the sources in the samples. Since the commonest map frequency was 1.4 GHz, when possible I used these to obtain the flux. For sources with maps at a higher frequency than 1.4 GHz, I used published flux measurements at lower frequencies as listed in Table 5.3, since the lower frequencies were less likely to be contaminated by nuclear and hot-spot emission.

There were also differences in the resolutions of the radio maps. As mentioned in Section 2.1.2, this could have an effect on the definition of the lobe shapes. In particular, high resolution maps are likely to have a small LAS and miss regions of diffuse gas.

Two-thirds of my radio observations fell into two groups – those with 1.4 GHz observations and resolutions between 1-5 arcsec (20 lobes) and those with 5 or 8.5 GHz observations again with resolutions between 1-5 arcsec (12 lobes). These two groups had almost identical ranges of source size (40 to 300 kpc) and similar medians (150 and 160 kpc respectively). I then looked at the ratio of observed to equipartition magnetic fields (B_{obs}/B_{eqp}). The 1.4 GHz subsample contained both the maximum and minimum B_{obs}/B_{eqp} from the full sample (median 0.33, range 0.07-0.83). The high frequency subsample had a median B_{obs}/B_{eqp} of 0.44 and a range of 0.18 to 0.67. A Kolmogorov-Smirnov test showed that there was no significant difference between the two distributions (D=0.25, p=0.62). Thus for the bulk of my sources the difference in frequency does not seem to be a problem.

Of the remaining lobes, five had 1.4 GHz observations at resolutions greater than 10 arcsec. These were large sources with lobe lengths from 290 to 1330 kpc. Their B_{obs}/B_{eqp} ratios were however similar to those of the two higher resolution samples (median 0.39, range 0.22 to 0.65). All but one of the remaining sources had frequencies and resolutions lying between those of the three groups already described. Their lobe lengths range between 67 and 310 kpc and their B_{obs}/B_{eqp} ratios have a median of 0.40, range 0.25 to 0.57. Again, there is nothing to distinguish their results from those of the other sources. The final source has low map frequency (610 MHz) and resolution (30 arcsec) and is large (550 kpc) but the B_{obs}/B_{eqp} ratio is near the median (0.41).

Overall, it seems unlikely that the range of frequencies and resolutions used in this study had much effect on the results.

5.4.4.5 Lobe viewing angle

We do not know the viewing angle of the radio lobe. NLRGs have viewing angles of greater than $\sim$45°; BLRGs and QSOs have viewing angle of less than $\sim$ 45°. A small

viewing angle will decrease the apparent volume of the lobe, increasing the calculated energy density and the observed lobe pressure. However, reducing the viewing angle also reduces the angular distance to mid-lobe and the lobe tip, so the ICM density will also be overestimated.

I looked at the effect of viewing angle on NLRG 3C 98 (N lobe) and BLRG PKS 0945+07 (W lobe). For 3C 98, I assumed a viewing angle of 45°, recalculated the volume, ICM pressures and lobe observed and equipartition pressures. This brought the lobe nearer equipartition (P_{obs}/P_{eqp} reduced from 3.1 to 2.6). The pressure balance was increased (by 16% at mid-lobe and 13% at the lobe tip). This size of change had only a slight effect on the Mach number, raising it from 4.1 to 4.4.

For PKS 0945+07 I assumed a viewing angle of 20°. Again, the effect of increasing the volume estimate brought the lobe nearer to equipartition (P_{obs}/P_{eqp} reduced from 5.7 to 3.2). In this case the pressure balance was almost unchanged, with the Mach number changing by less than 1%.

The relative changes in lobe and ICM pressures will depend on the environment richness and shape – both 3C 98 and PKS 0945+07 have low β-model parameters below the median so the ICM pressure will drop more slowly than for a steep β-model source. I therefore looked also at 3C 285, an NLRG with a steeper β-model than the median. The changes were smaller than for the shallow model, with only a 4% increase in pressure balance at the lobe tip. I therefore agreed with the conclusions of Hardcastle and Worrall (2000) and Croston et al. (2004), that the aspect ratio has similar impact on the calculated pressures in the lobe and the ICM. It will therefore have only a small effect on the calculation of the Mach number.

5.4.4.6 Excluded lobes

As mentioned in Section 5.2, results could not be calculated for a number of lobes. There were two main reasons for exclusion:

a) The lobes were so small in angular extent that they were masked by nuclear and/or central ICM emission. These lobes were either very young, in which case they may still be evolving rapidly and not be representative of the population of stable lobes (eg Hardcastle and Krause 2013), or they are at a shallow angle to the observer. In the latter case, the sample is large enough that it is unlikely that the lobes are different from the rest of the sample. A 1 Mpc lobe, for example, at a viewing angle of 20° would appear more than 300 kpc long. The largest of these excluded lobes was 75 kpc, so none of them could have been unusually large.

b) The lobes were only partially on the observing chip, or, in one case, were over a 4-chip join. These lobes are likely to be amongst the largest in angular extent, and potentially in physical extent and so might bias the sample. Of the five sources with off-chip lobes, only one had both lobes off chip so all the others had their second lobe in the sample. The source with both lobes off-chip was the largest of this group of excluded sources with lobes of ∼1 Mpc, but it also lay in a very weak ICM with upper limits on the external pressure so I could not have calculated the Mach number for this source.

I also excluded 3C 236 because the lobes were so large (2.7 and 1.9 Mpc) that I did not trust the extrapolation of the ICM β model to provide the pressures. This is by far the biggest source in the sample – the next largest lobe is 1.3 Mpc long. In all, only three of the 39 lobes for which I could calculate Mach numbers were longer than 0.5 Mpc, and only one lobe was longer than 1 Mpc. There is therefore the possibility of bias against large lobes; having said that, I have Mach numbers for lobes from 40 to 1300 kpc long, which is a wide range of lobe sizes, and the few large lobes in the sample do not stand out as being different from the rest of the sample.

5.4.4.7 Environment measurements

There are two causes for concern with the measurements of the external environment. Firstly, some environments had a maximum detected radius (D_{rad}) larger than the observing chip and so background subtraction was done using the *Chandra* blank files only (Section 2.2.3.2). These were mostly nearby FRI galaxies, so this applies to only one pair of FRII galaxy lobes in my sample (PKS 0625-53) and consequently is not a cause for concern.

The other potential problem comes from the extrapolation of the β model beyond D_{rad} for the ICM pressure calculations. There were 10 lobes where the lobe tip was greater than D_{rad}. These all have environments with poorly constrained β models and so their external pressures have large errors. 3C 321 has the largest lobes in the sample and was discussed in Section 5.4.3 – its lobes have unreasonably large Mach numbers and all statistics were calculated with and without these two lobes. 3C 326's lobes have the lowest Mach numbers (0.7) – again these are large lobes so extrapolation from an inaccurate β model could be overestimating the ICM pressure. 3C 33 has relatively small lobes but is in a weak environment. Its Mach numbers are quite high (4 and 3.5) but reasonable for such a weak environment and there are two others higher. The other 4 lobes all have Mach numbers near the median and so do not stand out in any way.

I am again a little concerned at possible errors involving large lobes – the highest and lowest Mach numbers come from the largest sources in the sample – but do not think that the overall results will be much affected.

5.4.4.8 Overall effect of systematics

Overall, the estimates of lobe volumes and the assumption of a constant low frequency spectral index are likely to be the biggest source of error in the results. Improved lobe volume estimates will need better resolution low frequency radio maps, but it would be possible to make estimates of spectral indices where data are available, look at the overall variation and make a better assessment of the impact of the assumption of a constant index of 0.7. However, the strength of the main result is such that it is unlikely that any of the systematic errors described here will modify it significantly.

5.4.5 Implications

As found by other researchers (eg Hardcastle et al. 2002a; Isobe et al. 2002; Croston et al. 2004; Isobe et al. 2005; Kataoka and Stawarz 2005; Croston et al. 2005b), the lobe pressures were near but slightly above equipartition, reflecting the contribution of a higher electron density than required by the minimum energy conditions. If there were a sizeable population of relativistic protons or if there were a large population of non-radiating particles in the lobes, we would expect the equipartition field and pressure to be different from those calculated for a dominant electron population (see Sections 1.3.3.1 and 1.3.3.2). The lobes were almost all within one decade of equipartition, which suggests both that there is not a large population of energetic protons and the filling factor must be close to unity.

The pressure difference between the lobes and their environment is important both for the advance speed of the lobe through the ICM and for determining the shape of the lobe. The lobe being near pressure balance with its environment means that the ICM can influence the shape of the lobe. The relatively high density in the inner regions of the cluster will compress the lobe near the nucleus, separating it into familiar double system and supporting model C in Scheuer (1974). Lobes near pressure balance can also be moulded by variations in the ICM, giving disturbances and asymmetries that are again familiar in observed systems.

The relationship between lobe tip Mach number and environment richness gives evidence both of the lobe expansion being affected by the ICM and of energy being injected into the ICM in addition to the energy required to displace the ICM. The lobes in rich

environments are subsonic or only slightly supersonic and so will not be putting much additional energy into the ICM, although they will still be disturbing the environment. Those in sparse environments however will be inputting larger amounts of energy, so group environments will be affected more than cluster environments.

The space density of HERGs increases with redshift (Best et al. 2014), so this energy injection is likely to have been occurring at intervals from relatively early in cluster formation when the proto-clusters were likely to have low density ICM. The energy input from the shocks driven by FRII lobes would then be relatively high, and may have contributed to the entropy excess seen particularly in low mass groups and clusters (eg Ponman et al. 1999) and which may be complicit in both the breaking of self-similarity in the cluster scaling relations and the commonly reported finding that the $L_X - T_X$ scaling relation is steeper for groups than for clusters (Section 1.2.2).

Because of the relationship between radio luminosity and cluster richness for the LERGs, this sample of FRII lobes only contains LERGs in rich environments. Thus there are not enough LERG lobes in this sample to see whether there is a genuine difference between the range of HERG and LERG Mach numbers or whether the lack of strong shocks in LERGs is due to sample bias – the latter seems more likely. However, since LERGs are thought to occur at the end of the galaxy evolutionary sequence they may also have contributed less to cluster evolution than the HERGs and so their input may be of less importance when looking at cluster development.

It was perhaps surprising that there was not a significant relationship between Mach number and the distance to the lobe tip, and consequently to source age. Although Figure 5.7 (right) hints that higher Mach numbers belong to shorter (younger) lobes, there is a wide range of lobe lengths at the lower Mach numbers. Although one would expect Mach number to reduce with age, the range of environment richnesses means that the same pressure ratio will be reached at different radii for similar age sources, which would add scatter to any relationship. Similarly the viewing angle will add scatter when using distance to lobe tip as a proxy for age.

5.5 Conclusions

I have examined the lobes of two samples of FRII radio galaxies, at redshifts 0.1 and 0.5. I have estimated the internal lobe pressures for equipartition (∼minimum energy condition) from the radio flux and the observed (inverse Compton) lobe pressures from the X-ray flux. I estimated external (ICM) pressures from the ICM temperatures using

the ICM surface brightness profiles and estimated Mach numbers for the lobe advance through the ICM.

I found the following:

- All lobe pressures were higher than those predicted by equipartition (in the absence of protons), although all lobes were within one order of magnitude of the equipartition prediction;
- Almost all lobes were calculated to be over-pressured at the tip compared with the ICM, as expected for expanding lobes, and were within one order of magnitude of the ICM pressure for all but three lobes;
- Lobe pressures at mid-lobe were near pressure balance with the ICM, allowing the ICM to shape the regions of the lobes near the nucleus as they expand outwards;
- Lobe tip Mach numbers were below 5 for all but one source, with a median of 1.8. Given that the Mach numbers are lower limits, it is likely that at least half the sample are driving strong shocks into the ICM;
- There was a suggestion of an inverse correlation between lobe-tip Mach numbers and ICM luminosity, but this result needs more work to eliminate potential confounding factors;

As discussed in Section 5.4.4, there are a number of potential systematic errors associated with the calculations, although because the size of the errors diminishes with Mach number they are unlikely to affect the gist of the results. LOFAR data is beginning to produce a consistent set of low frequency maps, and in future the systematics can be reduced by the use of more accurate low frequency spectra and estimates of the lobe volume.

Having calculated Mach numbers for the FRII sample, these results could now be used to estimate the total energy input to the ICM by the lobes from both gas displacement and shock heating, which would be useful for modelling cluster evolution. It would also be useful to look at the change in lobe aspect ratio as the lobes evolve (Hardcastle and Krause 2013), which is a potential indicator for distinguishing between models of lobe dynamics.

TABLE 5.1: FRII lobes excluded from lobe analysis

Source	Lobe	Reason for exclusion
3C 28	Both	Small lobes in a rich, disturbed environment
3C 98	South	Lobe is across a 4-chip join
3C 236	Both	Large lobes (2.7 and 1.9 Mpc) which extend substantially beyond both the maximum detected radius (0.3 Mpc) and the R_{200} overdensity radius (0.7 Mpc)
3C 388	Both	Lobes are in a strong, disturbed environment
3C 390.3	Both	Lobes are in a strong, disturbed environment
3C 433	North	North lobe has FRI morphology (van Breugel et al. 1983; Hodges-Kluck et al. 2010)
4C 73.08	East	Lobe is partially off the chip
DA 240	Both	Both lobes partially off the chip
PKS 0442-28	Both	Poor quality radio map which was not good enough to define the lobe shape
PKS 1559+02	West	Lobe is partially off the chip
PKS 2211-17	Both	Lobes are in a strong, disturbed environment
PKS 2221-17	North	Lobe is partially off the chip
7C 0223	Both	Low resolution map which was not good enough to define the lobe shape
7C 1731	Both	Lobes are less than 1 arcsec in extent
7C 0213	Both	Low resolution map which was not good enough to define the lobe shape
TOOT 1303+3334	Both	No lobe structure visible
6C 0850+3747	North	Lobe is over the nucleus
3C 19	Both	Small lobes (4 arcsec) in a strong environment
3C 295	Both	Small lobes (3.5 arcsec) in a strong environment

TABLE 5.2: FRII lobe sizes and ICM pressures.

Source	Lobe[a]	Lobe tip	Tip pressure	Mid-lobe	Mid-lobe pressure	Volume[b] (radius)
		kpc	$\times 10^{-14}$ Pa	kpc	$\times 10^{-12}$ Pa	kpc
3C 33	N	150	$0.943^{+0.127}_{-0.942}$	86	$2.62^{+0.80}_{-2.34}$	52
3C 33	S	119	$1.43^{+0.26}_{-1.43}$	59	$5.27^{+2.18}_{-3.47}$	50
3C 35	N	468	$1.39^{+0.28}_{-1.26}$	234	$4.49^{+1.50}_{-2.07}$	144
3C 35	S	488	$1.29^{+0.26}_{-1.17}$	244	$4.17^{+1.40}_{-2.06}$	144
3C 98	N	85	$2.47^{+0.91}_{-2.45}$	42	$7.26^{+3.89}_{-4.77}$	67
3C 192	C	126	$4.74^{+1.12}_{-1.03}$	63	$11.5^{+2.4}_{-1.7}$	55
3C 219	N	291	$24.4^{+1.1}_{-1.1}$	145	$54.2^{+2.2}_{-2.7}$	36
3C 219	S	280	$25.5^{+1.2}_{-1.2}$	145	$54.5^{+2.2}_{-2.7}$	36
3C 285	E	132	$10.1^{+0.6}_{-0.6}$	66	$22.1^{+1.4}_{-1.6}$	46
3C 285	W	172	$7.44^{+0.66}_{-0.52}$	86	$16.6^{+1.0}_{-1.1}$	56
3C 303	C	72	$24.4^{+3.1}_{-2.0}$	36	$72.3^{+7.0}_{-4.7}$	16
3C 321	N	272	$0.307^{+0.020}_{-0.281}$	246	$0.377^{+0.009}_{-0.338}$	9
3C 321	S	282	$0.284^{+0.023}_{-0.262}$	237	$0.387^{+0.009}_{-0.347}$	21
3C 326	E	741	$5.57^{+1.73}_{-5.56}$	370	$9.17^{+4.51}_{-3.12}$	181
3C 326	W	1333	$2.95^{+0.73}_{-2.95}$	736	$5.60^{+1.74}_{-5.60}$	206
3C 433	S	67	$8.18^{+2.52}_{-5.65}$	34	$30.2^{+2.1}_{-7.4}$	16
3C 452	E	211	$6.84^{+0.98}_{-1.31}$	105	$28.3^{+2.1}_{-1.8}$	61
3C 452	W	221	$6.69^{+0.99}_{-1.30}$	110	$26.1^{+1.9}_{-1.7}$	62
4C 73.08	W	550	$0.645^{+0.178}_{-0.645}$	275	$1.60^{+0.47}_{-1.60}$	208
PKS 0034-01	C	42	<8.30	21	<11.8	17
PKS 0038+09	C	114	$56.2^{+18.4}_{-11.9}$	57	136^{+38}_{-28}	23
PKS 0043-42	N	158	$19.6^{+1.8}_{-1.8}$	86	$36.6^{+2.7}_{-2.6}$	16
PKS 0043-42	S	162	$19.0^{+1.8}_{-1.8}$	105	$29.7^{+2.5}_{-2.1}$	13
PKS 0213-13	C	116	$5.44^{+1.99}_{-3.70}$	58	$20.6^{+6.9}_{-5.7}$	27
PKS 0349-27	S	294	$3.64^{+1.55}_{-1.71}$	159	$6.28^{+1.60}_{-0.92}$	63
PKS 0404+03	N	280	<2.90	149	<6.84	45
PKS 0404+03	S	298	<2.66	178	<5.41	44
PKS 0625-53	N	63	738^{+12}_{-10}	36	869^{+21}_{-19}	16
PKS 0625-53	S	51	796^{+14}_{-15}	23	928^{+24}_{-22}	15
PKS 0806-10	C	131	<6.53	65	<14.7	24
PKS 0945+07	W	186	$13.6^{+3.0}_{-2.1}$	107	$27.6^{+3.9}_{-3.5}$	39
PKS 1559+02	E	213	$4.12^{+0.99}_{-0.71}$	106	$8.25^{+1.48}_{-1.16}$	44
PKS 2221-02	S	325	$3.98^{+0.97}_{-0.52}$	162	$9.17^{+1.01}_{-0.76}$	91
PKS 2356-61	N	293	$8.75^{+1.33}_{-1.35}$	146	$22.5^{+1.9}_{-1.7}$	43
PKS 2356-61	S	308	$8.12^{+1.34}_{-1.37}$	154	$21.2^{+1.8}_{-1.7}$	43
7C 0219+3423	C	111	$50.6^{+35.1}_{-25.8}$	62	117^{+62}_{-36}	11
6C 0850+3747	S	163	$88.2^{+7.3}_{-8.7}$	95	185^{+14}_{-12}	11
6C 1200+3416	C	171	145^{+9}_{-8}	110	173^{+13}_{-17}	9
6C 1132+3439	C	299	$41.0^{+4.7}_{-3.6}$	176	$69.3^{+6.4}_{-5.7}$	14
6C 0857+3945	C	633	$6.54^{+5.15}_{-2.67}$	387	$13.0^{+8.6}_{-3.8}$	25
3C 16	C	218	<54.6	109	<145	16
3C 46	C	586	$13.2^{+3.9}_{-6.3}$	293	$53.5^{+11.5}_{-6.9}$	29
3C 200	C	89	103^{+32}_{-20}	50	261^{+56}_{-36}	7
3C 457	C	633	$9.49^{+1.15}_{-1.17}$	366	$18.0^{+1.7}_{-1.5}$	41
3C 274.1	C	485	$1.92^{+0.31}_{-0.71}$	274	$9.13^{+1.04}_{-0.95}$	35
3C 244.1	C	166	$94.6^{+15.9}_{-12.3}$	96	189^{+29}_{-18}	7
3C 228	C	170	$40.6^{+11.5}_{-10.8}$	98	129^{+22}_{-15}	9
3C 330	C	215	$42.2^{+6.4}_{-5.7}$	125	101^{+9}_{-8}	7
3C 427.1	C	104	428^{+18}_{-21}	60	784^{+40}_{-45}	6

[a] North, South, East, West and Combined lobes. [b] The quoted volume is the radius of a sphere of the same volume as the lobe.

TABLE 5.3: FRII lobe fluxes.

Source	Lobe	Radio Frequency GHz	Radio Flux Jy	Method[a]	Photon Index	1 keV X-ray flux nJy	χ^2/dof
3C 33	N	1.48	1.44	S	$1.14^{+0.71}_{-0.54}$	$3.83^{+1.44}_{-1.22}$	2.40/5
3C 33	S	1.48	1.61	S	$1.45^{+0.94}_{-0.77}$	$4.11^{+0.99}_{-0.99}$	6.09/4
3C 35	N	1.42	0.465	S	$1.77^{+0.43}_{-0.37}$	$27.2^{+6.3}_{-5.6}$	15.66/13
3C 35	S	1.42	0.532	C	$1.43^{+0.24}_{-0.23}$	$11.2^{+2.6}_{-0.1}$	1.77/6
3C 98	N	0.178	29.2	S	$1.97^{+0.46}_{-0.40}$	$12.6^{+2.6}_{-2.4}$	11.09/7
3C 192	C	1.41	4.09	S	$1.26^{+0.52}_{-0.45}$	$15.5^{+4.0}_{-3.7}$	4.89/5
3C 219	N	1.52	2.83	S	$1.64^{+0.14}_{-0.14}$	$16.1^{+1.4}_{-1.4}$	15.30/14
3C 219	S	1.52	2.99	S	$1.77^{+0.20}_{-0.19}$	$11.0^{+1.1}_{-1.1}$	7.53/8
3C 285	E	1.65	0.790	S	$1.53^{+0.62}_{-0.63}$	$2.48^{+0.56}_{-0.58}$	1.37/2
3C 285	W	1.65	0.857	S	$1.79^{+0.67}_{-0.72}$	$3.28^{+0.60}_{-0.62}$	0.17/2
3C 303	C	1.45	0.900	F	1.50	$0.846^{+0.404}_{-0.404}$	
3C 321	N	1.51	0.135	M	1.50	$0.311^{+0.177}_{-0.177}$	
3C 321	S	1.51	1.32	M	1.50	$1.12^{+0.23}_{-0.23}$	
3C 326	E	1.40	1.87	S	$1.41^{+0.68}_{-0.71}$	$26.2^{+8.4}_{-7.8}$	27.23/18
3C 326	W	1.40	1.44	F	1.50	$15.7^{+4.0}_{-4.0}$	
3C 433	S	0.178	53.9	S	$2.10^{+0.71}_{-0.54}$	$3.28^{+0.92}_{-0.76}$	1.69/3
3C 452	E	1.41	4.25	S	$1.47^{+0.15}_{-0.20}$	$12.8^{+3.0}_{-4.3}$	32.24/51
3C 452	W	1.41	3.97	S	$1.58^{+0.17}_{-0.26}$	$12.6^{+3.4}_{-4.9}$	61.07/50
4C 73.08	W	0.609	3.90	S	$1.44^{+0.45}_{-0.40}$	$33.4^{+7.4}_{-6.9}$	19.42/23
PKS 0034-01	C	0.408	9.74	S	$1.94^{+0.22}_{-0.21}$	$4.99^{+0.53}_{-0.53}$	6.33/5
PKS 0038+09	C	0.408	11.5	F	1.50	$7.88^{+1.52}_{-1.52}$	
PKS 0043-42	N	0.408	8.25	U	1.50	<0.940	
PKS 0043-42	S	0.408	7.40	U	1.50	<0.748	
PKS 0213-13	C	0.408	11.7	F	1.50	$3.48^{+0.93}_{-0.93}$	
PKS 0349-27	S	1.47	1.03	M	1.50	$10.7^{+1.1}_{-1.1}$	
PKS 0404+03	N	0.178	11.1	U	1.50	<4.54	
PKS 0404+03	S	0.178	8.27	U	1.50	<4.04	
PKS 0625-53	N	0.408	10.8	U	1.50	<5.62	
PKS 0625-53	S	0.408	9.40	U	1.50	<5.93	
PKS 0806-10	C	0.408	10.2	U	1.50	<2.58	
PKS 0945+07	W	1.43	2.29	S	$1.85^{+0.20}_{-0.19}$	$11.3^{+0.9}_{-1.0}$	19.29/15
PKS 1559+02	E	0.408	10.8	S	$1.56^{+0.45}_{-0.39}$	$5.83^{+1.62}_{-1.44}$	3.39/6
PKS 2221-02	S	1.42	3.40	S	$1.31^{+0.33}_{-0.31}$	$11.3^{+2.0}_{-2.0}$	23.22/23
PKS 2356-61	N	1.47	3.81	S	$1.58^{+0.25}_{-0.23}$	$17.1^{+2.4}_{-2.3}$	10.96/14
PKS 2356-61	S	1.47	5.40	S	$1.44^{+0.25}_{-0.24}$	$18.1^{+2.6}_{-2.5}$	13.03/16
7C 0219+3423	C	1.41	0.0847	U	1.50	<0.744	
6C 0850+3747	S	1.41	0.181	M	1.50	$1.02^{+0.28}_{-0.28}$	
6C 1200+3416	C	1.41	0.154	M	1.50	$0.841^{+0.195}_{-0.158}$	
6C 1132+3439	C	1.41	0.390	M	1.50	$1.46^{+0.28}_{-0.28}$	
6C 0857+3945	C	1.41	0.266	M	1.50	$1.72^{+0.45}_{-0.36}$	
3C 16	C	1.54	1.54	M	1.50	$1.93^{+0.93}_{-0.93}$	
3C 46	C	1.48	0.762	M	1.50	$4.20^{+1.56}_{-1.14}$	
3C 200	C	1.49	1.30	M	1.50	$1.48^{+0.58}_{-0.58}$	
3C 457	C	1.45	0.650	S	$1.59^{+0.18}_{-0.18}$	$5.25^{+0.90}_{-0.84}$	18.54/19
3C 274.1	C	1.44	1.10	S	$1.39^{+0.16}_{-0.16}$	$3.93^{+0.62}_{-0.60}$	8.74/11
3C 244.1	C	1.44	2.31	M	1.50	$1.29^{+0.86}_{-0.86}$	
3C 228	C	1.44	2.71	M	1.50	$2.60^{+0.47}_{-0.47}$	
3C 330	C	1.49	2.39	M	1.50	$0.897^{+0.197}_{-0.198}$	
3C 427.1	C	1.53	2.89	M	1.50	$1.50^{+0.27}_{-0.27}$	

[a] S = fitted index, C = fitted index from combined lobe spectra, F = fit with fixed index, M = modelled with unbinned data, U = upper limit

TABLE 5.4: FRII lobe equipartition and Inverse Compton fields and pressures

Source	Lobe[a]	B_{eqp}	B_{IC}	P_{eqp}	P_{IC}	Mach no.
		$\times10^{-10}$ T		$\times10^{-14}$ Pa		
3C 33	N	5.61	$2.40^{+0.61}_{-0.41}$	8.34	$18.4^{+6.4}_{-5.2}$	4.0
3C 33	S	5.88	$2.45^{+0.44}_{-0.29}$	9.17	$21.1^{+4.7}_{-4.6}$	3.5
3C 35	N	1.75	$0.390^{+0.056}_{-0.045}$	0.814	$5.26^{+1.22}_{-1.07}$	1.8
3C 35	S	1.82	$0.711^{+0.005}_{-0.081}$	0.879	$2.24^{+0.48}_{-0.03}$	1.3
3C 98	N	7.87	$2.73^{+0.36}_{-0.29}$	16.4	$50.7^{+10.2}_{-9.2}$	4.1
3C 192	C	6.97	$1.98^{+0.26}_{-0.30}$	12.9	$58.5^{+14.7}_{-13.5}$	3.2
3C 219	N	7.75	$2.03^{+0.11}_{-0.10}$	15.9	$78.1^{+6.7}_{-6.6}$	1.7
3C 219	S	7.91	$2.62^{+0.16}_{-0.15}$	16.6	$55.1^{+5.5}_{-5.0}$	1.4
3C 285	E	5.09	$2.39^{+0.40}_{-0.27}$	6.87	$13.2^{+2.7}_{-2.6}$	1.1
3C 285	W	4.44	$2.12^{+0.28}_{-0.20}$	5.24	$9.78^{+1.57}_{-1.58}$	1.1
3C 303	C	10.7	$5.36^{+1.17}_{-1.85}$	30.5	$53.4^{+1.4}_{-1.7}$	1.4
3C 321	N	10.7	$2.88^{+1.85}_{-0.67}$	30.6	144^{+81}_{-79}	19.4
3C 321	S	10.4	$5.23^{+0.75}_{-0.54}$	28.5	$49.1^{+8.6}_{-8.2}$	11.8
3C 326	E	2.02	$0.947^{+0.142}_{-0.219}$	1.08	$2.07^{+0.59}_{-0.52}$	0.7
3C 326	W	1.69	$1.10^{+0.20}_{-0.14}$	0.761	$0.956^{+0.164}_{-0.136}$	0.7
3C 433	S	22.7	$11.9^{+2.0}_{-1.6}$	137	223^{+53}_{-40}	4.7
3C 452	E	6.13	$2.31^{+0.62}_{-0.27}$	9.97	$27.0^{+6.0}_{-8.3}$	1.8
3C 452	W	5.97	$2.23^{+0.75}_{-0.30}$	9.46	$25.9^{+6.7}_{-9.3}$	1.8
4C 73.08	W	2.02	$0.833^{+0.121}_{-0.092}$	1.09	$2.55^{+0.52}_{-0.48}$	1.8
PKS 0034-01	C	17.1	$4.02^{+0.28}_{-0.23}$	77.5	456^{+47}_{-48}	
PKS 0038+09	C	12.8	$4.35^{+0.00}_{-0.00}$	43.3	138^{+0}_{-0}	1.5
PKS 0043-42	N	16.1	<10.8	68.7	<83.2	<1.9
PKS 0043-42	S	18.3	<11.8	88.7	<112	<2.2
PKS 0213-13	C	11.5	$6.42^{+0.00}_{-0.00}$	34.9	$52.2^{+0.0}_{-0.0}$	2.8
PKS 0349-27	S	4.31	$1.09^{+0.07}_{-0.06}$	4.92	$25.6^{+2.5}_{-2.5}$	2.4
PKS 0404+03	N	7.47	<3.26	14.8	<31.8	
PKS 0404+03	S	6.81	<3.35	12.3	<22.0	
PKS 0625-53	N	20.0	<3.86	106	<869	<1.1
PKS 0625-53	S	19.5	<3.41	101	<983	<1.1
PKS 0806-10	C	12.3	<6.50	40.2	<65.2	
PKS 0945+07	W	7.33	$1.76^{+0.09}_{-0.08}$	14.3	$81.3^{+6.7}_{-6.8}$	2.2
PKS 1559+02	E	7.85	$4.04^{+0.74}_{-0.54}$	16.4	$27.5^{+6.5}_{-5.4}$	2.4
PKS 2221-02	S	4.52	$2.05^{+0.25}_{-0.19}$	5.42	$10.9^{+1.8}_{-1.7}$	1.5
PKS 2356-61	N	7.71	$1.93^{+0.18}_{-0.14}$	15.8	$83.4^{+11.5}_{-11.3}$	2.8
PKS 2356-61	S	8.47	$2.30^{+0.21}_{-0.17}$	19.1	$88.1^{+12.2}_{-12.0}$	3.0
7C 0219+3423	C	8.32	<3.35	18.4	<44.5	<1.0
6C 0850+3747	S	9.78	$3.16^{+0.66}_{-0.42}$	25.4	$88.2^{+23.5}_{-23.3}$	1.0
6C 1200+3416	C	11.2	$4.00^{+0.52}_{-0.46}$	33.3	$98.2^{+21.9}_{-17.4}$	0.9
6C 1132+3439	C	9.94	$4.85^{+0.66}_{-0.48}$	26.2	$47.5^{+8.1}_{-7.7}$	1.1
6C 0857+3945	C	5.82	$3.59^{+0.52}_{-0.46}$	8.97	$11.9^{+2.3}_{-1.6}$	1.3
3C 16	C	12.6	$7.90^{+3.75}_{-1.64}$	42.2	$55.1^{+19.6}_{-12.9}$	
3C 46	C	6.64	$3.44^{+0.70}_{-0.58}$	11.7	$19.4^{+6.1}_{-4.1}$	1.2
3C 200	C	22.9	$9.84^{+3.33}_{-1.75}$	139	306^{+112}_{-105}	1.6
3C 457	C	4.78	$2.68^{+0.29}_{-0.24}$	0.605	$9.04^{+1.22}_{-1.08}$	1.0
3C 274.1	C	6.21	$4.26^{+0.44}_{-0.35}$	10.2	$12.1^{+1.1}_{-1.0}$	2.3
3C 244.1	C	25.8	$14.7^{+13.5}_{-3.8}$	177	259^{+141}_{-78}	1.5
3C 228	C	23.5	$12.8^{+1.6}_{-1.2}$	146	228^{+33}_{-31}	2.2
3C 330	C	28.4	$23.6^{+3.8}_{-2.6}$	214	220^{+16}_{-7}	2.1
3C 427.1	C	33.0	$22.0^{+2.8}_{-2.1}$	290	354^{+41}_{-35}	0.9

B_{eqp} and B_{IC} are the equipartition and observed magnetic fields; P_{eqp} and P_{IC} are the equipartition and observed lobe pressures.

[a] North, South, East, West and Combined lobes.

TABLE 5.5: Partial correlation analysis results for the FRII lobes, using Generalized Kendall's τ correlation tests in the presence of a correlation with a third factor.

Sample	Sub-sample	N	τ/σ	p
Mach no. vs Radio luminosity, with a redshift correlation				
z0.1 and ERA	All	44	1.55	0.12
	HERG	33	0.58	0.56
	no 3C 321	31	1.46	0.14
Mach no. vs ICM luminosity, with a redshift correlation				
z0.1 and ERA	All	44	-4.35	< 0.0001
	HERG	33	-3.17	0.002
	no 3C 321	31	-2.42	0.02
ICM luminosity vs lobe-tip external pressure, with a redshift correlation				
z0.1 and ERA	All	44	2.87	0.004
	HERG	33	3.12	0.002
	LERG	11	3.07	0.002
Mach no. vs lobe-tip distance, with a redshift correlation				
z0.1 and ERA	All	44	-1.03	0.30
	NLRG	27	-1.88	0.06
	no 3C 321	25	-1.09	0.28

N is sample size; τ is the partial correlation statistic; σ is the standard deviation; p is probability under the null hypothesis.

Chapter 6

AGN central properties and the cluster environment

6.1 Introduction

The low excitation samples of radio-loud AGN examined in Chapters 3 and 4 showed a strong correlation between radio luminosity (L_R) and environment richness (as characterised by the X-ray luminosity – L_X), but with scatter of between one and two orders of magnitude. If this correlation is indicative of a feedback connection between the hot gas fuel and jet production, then the relationship assumes that total radio luminosity is a proxy for jet power. Since jet power must be derived from the accretion of matter onto a black hole, the key determining parameters are thought to include black hole mass (M_{BH}), accretion rate ($\dot{m}$) and black hole spin (j). The mechanism for producing the jets is still unknown, but one class of models, initially proposed by Blandford and Znajek (1977) and which assumes a strong dependence on spin energy, gives the relationship for the jet power from a spinning black hole to be $Q_{jet} \propto j^2 B^2 M_{BH}^2$ (eg Daly and Sprinkle 2014), where B is the magnetic field strength. There is considerable uncertainty in the details of the model, but Q_{jet} is likely to related to M_{BH} in some manner, and since radio luminosity is also expected to be related to Q_{jet}, a potential confounding factor in my $L_R - L_X$ relation for the LERGs would be a relationship between the black hole mass of the AGN and cluster richness. It is plausible that such a relationship could arise during evolution.

A relationship between cluster richness and accretion rate for the HERGs would also be of interest – it is assumed that they are fuelled by local gas reservoirs (see Section 1.1.2.5), so there should be no such indications of fuelling from the ICM.

In this chapter therefore I look at whether black hole mass or accretion rate are related to cluster richness in order to address the following questions: is the $L_R - L_X$ relation for the LERGs independent of the central properties of the AGN, and is accretion rate for the HERGs independent of cluster environment, supporting the theory that HERG fuelling is a function of local processes.

As mentioned above, the $L_R - L_X$ relation for the LERGs implies a correlation between jet power and radio luminosity, so we would expect a correlation between radio luminosity and black hole mass. McLure et al. (2004), using black hole masses derived from the bulge luminosity, found that this was the case for the NLRG subsample, but that including the LERGs weakened the relationship. Gürkan et al. (2014), using mid-IR luminosity as a proxy for accretion rate, also found a strong correlation with radio luminosity for the HERGs, but not for the LERGs. There are however problems with the use of mid-IR as a proxy for accretion rate for LERGs – this is discussed in Section 6.2 below. Other recent studies show relationships between jet power and the central properties, but again with differences between the galaxy types. Chen et al. (2015) used virial black hole masses and calculated Eddington ratios from the [OIII] line. They found that Flat Spectrum Radio Quasars (FSRQs) and high excitation FRII radio galaxies showed a stronger relationship between black hole mass and jet power than High frequency peaked BL Lacs (HBLs) and low excitation LERG radio galaxies. Conversely, the HBLs and FRI/LERG radio galaxies showed a stronger relationship between accretion rate and jet power than the FSRQs and FRII/HERG radio galaxies. Daly (2016) on the other hand, again using the [OIII] line to obtain accretion rate, reports a strong relationship between beam power and accretion disk luminosity for high excitation sources, but a much weaker relationship for LERGs.

Thus I also look in this chapter for relationships between radio luminosity and accretion rate and black hole mass, since such relationships would strengthen the assumption of a relationship between jet power and total radio luminosity.

6.2 Sample

For this work, I used the radio and ICM X-ray luminosities of the ERA and z0.1 samples (Chapters 3 and 4).

McLure et al. (2004) calculated black hole masses from bulge masses using the $M_{BH} - M_{bulge}$ relation of McLure and Dunlop (2002) for the ERA sample, but I do not have black hole masses for all the sources in the z0.1 sample so cannot check directly for any relationship between M_{BH} and L_X for my combined samples. Neither do I have

accretion rates or spin. Two of the central properties – black hole mass and accretion rate – do however have proxies in the IR luminosities. Gürkan et al. (2014) made a detailed examination of the mid-IR properties of radio-loud AGN using *Wide Infrared Survey Explorer (WISE)* data (Wright et al. 2010). The near-IR emission (eg 3.4 μm) is dominated by emission from the old stellar population so, since bulge mass correlates with black hole mass (eg Magorrian et al. 1998), they can be used as an indicator of black hole mass. The mid-IR wavelengths are expected to be dominated, at least for the HERGs, by optical and UV emission from the nucleus re-radiated in the mid-IR by the dusty torus. Thus for sources fitting the unified model it can be used as an indicator of the power of the source and consequently as a proxy for accretion luminosity. Gürkan et al. (2014) found the 22 μm band to be the best indicator from the *WISE* data since it was less contaminated by stellar and polycarbon emission than the 12 μm band.

Accretion luminosity scales with accretion rate ($L_{acc} = \eta \dot{M} c^2$ – Section 1.1.2.4) where the accretion efficiency η is the same for black holes with the same spin. By equating gravitational and kinetic energy, $L_{acc} = GM_{BH}\dot{M}/R_{ISCO}$ where R_{ISCO} is the radius of the Innermost Stable Circular Orbit - the inner edge of the accretion disc. Thus $\eta \propto GM_{BH}/R_{ISCO}$ and since R_{ISCO} is dependent on M_{BH} and the spin of the black hole (Longair 2011, Section 13.11), η can be regarded as constant for black holes of similar spin.

I therefore used 3.4 μm IR luminosity as a proxy for black hole mass and 22 μm as a proxy for accretion rate (IR data for sources not included in Gürkan et al. (2014) were kindly supplied by G. Gürkan). The IR emission of quasars and BLRGs, which according to the unified theory are poorly screened by the dusty torus, is likely to be contaminated by nuclear emission so I used only NLRGs rather than the full HERG sample in this chapter, making a sample of 33 NLRGs and 41 LERGs. These include 26 FRI and 46 FRII galaxies, and two hybrid FRI/FRIIs. Table 6.1 contains the 151 MHz radio luminosities, ICM bolometric X-ray luminosities, 3.4 μm IR luminosities and 22 μm IR luminosities for the z0.1 and ERA samples.

The use of mid-IR luminosity as a proxy for accretion rate needs to be used with caution. Firstly, since the mid-IR luminosity comes from the torus, the LERG mid-IR emission must come from another source – Mingo et al. (2014) suggest that it might be associated with the jet and the old stellar population. Although the mid-IR emission for the LERGs does not relate directly to the nuclear emission in the same way as for the HERGs, it can still be regarded as an upper limit on the accretion rate.

The assumption of constant accretion efficiency for black holes of the same spin is valid if spin is independent of black hole mass. If however there is some depenedency of spin

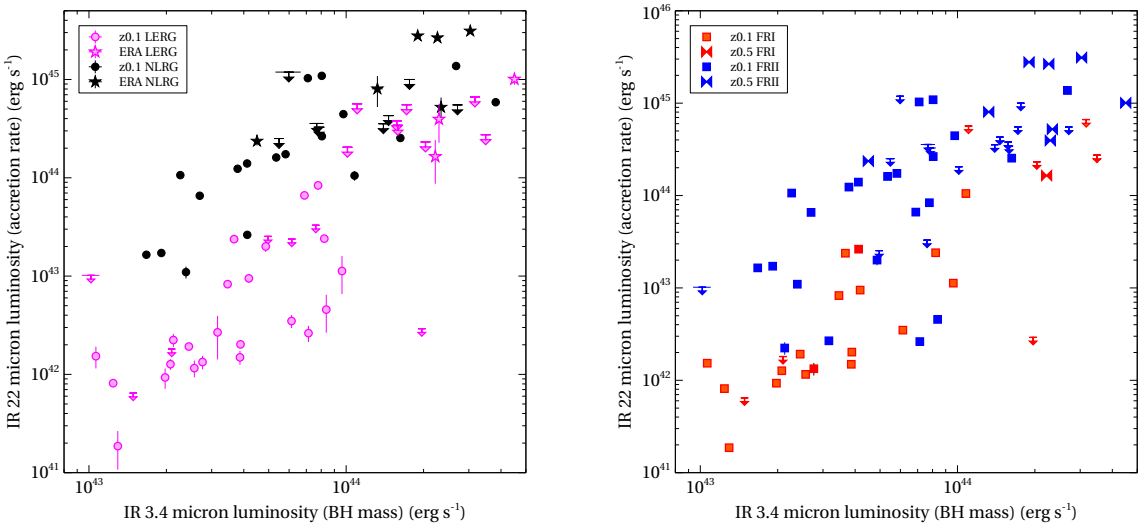

FIGURE 6.1: 3.4 vs 22 μm luminosity for the z0.1 and ERA samples. The left plot shows LERGs as magenta symbols and NLRGs as black symbols, z0.1 sources as circles and ERA sources as stars. The right plot show FRI galaxies as red symbols and FRII as blue symbols, z0.1 sources as squares and ERA sources as ties. Arrows are upper limits.

on mass, for example if more massive black holes have a higher maximum spin, then that assumption may be violated.

Figure 6.1 shows L_{acc} plotted against M_{BH} for the different classes of radio galaxy in my sample, and there does appear to be a correlation, particularly for the NLRGs and LERGs. The correlation for the NLRGs and LERGs was confirmed by partial correlation analysis tests, using generalized Kendall's τ tests for a correlation in the presence of a common correlation with redshift (see Table 6.3), but the tests showed that any apparent correlations for the full sample and for the FRI and FRII subsamples were due to the common redshift dependence from sample selection effects. The NLRG and LERG relationships appear to have different slopes, which since their IR luminosity comes from different sources is a reasonable result.

There are several possible reasons why the might be a correlation. It may be due to a dependence of η on black hole mass, or there may be other factors relating the two IR luminosities. For example, the near-IR luminosity is a measure of bulge mass, so it may also be an indicator of the amount of fuel available for accretion. The use of mid-IR luminosity as a proxy for accretion rate has therefore potential confounding factors, but provided these are borne in mind it is a useful exploratory tool.

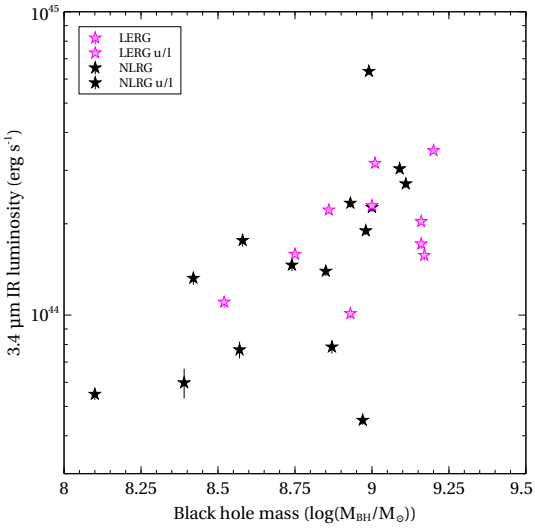

FIGURE 6.2: Black hole mass from McLure et al. (2004) vs 3.4 μm IR luminosity for the ERA sample. LERGs are shown in magenta and HERGs in black.

6.3 Black hole mass

In this section I look at the how black hole mass relates to redshift, radio luminosity and ICM luminosity and whether there are any differences between the LERG, HERG, FRI and FRII subsamples, with the specific aim of determining whether L_X is independent of black hole mass which, since jet power is expected to be related to black hole mass, is a potential confounding factor in the LERG $L_R - L_X$ relationship.

Although jet power is expected to be related to black hole mass, it has also been found that LERGs tend to occupy more massive galaxies that HERGs (e.g. Tasse et al. 2008; Smolčić 2009; Best and Heckman 2012), and so the relationship between bulge stellar mass and black hole mass implies that LERGs should tend to have higher black hole masses than HERGs. Since LERGs do not habitually have higher jet powers than HERGs, this suggests that any relationship between black hole mass and jet power should be different for the two galaxy types.

I first checked that the black hole masses from McLure et al. (2004) correlated with the 3.4 μm luminosities for the same objects (Figure 6.2). With the exception of two HERGs (3C 341 and 6C 0857) the correlation appears good and this was confirmed by a Kendall's τ test (Table 6.2).

6.3.1 3.4 μm magnitude and redshift

Gürkan et al. (2014) found a strong correlation between 3.4 μm magnitude and redshift, supporting theories that radio-loud AGN are hosted by mature giant galaxies with a

passively-evolving stellar population. They also found that the lower radio luminosity sources (the 6CE and 7CE objects) had lower 3.4 μm luminosity than the 3CRR and 2Jy sources, supporting the suggestion that radio jet power is related to black hole mass.

The top left plot in Figure 6.3 shows 3.4 μm luminosity and redshift for the LERGs and NLRGs in my samples, and alongside is the equivalent 151 MHz radio luminosity/redshift plot. Note that the apparent redshift correlation with redshift is a selection effect due to the a combination of flux limited samples and the relative scarcity of high luminosity sources. The radio surveys used for the ERA sample go to a lower flux limit than those used for the z0.1 sample.

An interesting difference between the two plots is that there are LERGs in both the z0.1 and ERA samples at lower radio luminosities than those of the NLRGs; there are no equivalent low luminosity LERGs in the 3.4 μm/redshift plot. These LERGs are all FRI sources. The five low radio luminosity ERA sources are LERGs from the TexOx-1000 sample – McLure et al. (2004) also found the TexOx-1000 LERGs had high black hole masses compared with the low radio luminosity sources from the other radio surveys contributing to his sample.

In the bottom of Figure 6.3 are the same plots split into FRI and FRII galaxy morphologies (the hybrid morphology sources 3C 433 and PKS 1648+05 have been excluded), and it appears that the FRI sources have a higher M_{BH}/L_R ratio than the FRIIs. This can be seen more clearly in Figure 6.5; the range of black hole masses is the same for both the FRI and FRII subsamples, despite their different ranges of radio luminosity. The median value of the M_{BH}/L_R ratios for the FRIs was 7 times that of the FRIIs, and a Kolmogorov-Smirnov test that they came from the same distribution showed a strong difference between the two sub-samples (D=0.74, p<0.000001). The difference between the NLRG and LERG distributions was also strong, but less than that for the FR morphologies (D=0.5, p<0.0001), which reflected the morphology content of the NLRG and LERG subsamples. Using the McLure et al. (2004) black hole masses for the ERA sample also gave a much stronger result for FRI vs FRII than for NLRG vs LERG (D=1.0, p=0.00003 for FFI/FRII; D=0.5, p=0.04 for NLRG/LERG). Note however that there are only five FRI sources in the ERA sample.

One possible explanation for the difference in the M_{BH}/L_R ratios could be the particle content of the different morphology jets. As discussed in Section 1.3.3.1, FRI jets are thought to entrain a significant quantity of protons from the ICM; these would absorb some of the jet's kinetic energy so that the radio luminosity from the radiating electrons would be reduced compared with the total jet power. Since the LERG subsample contains both FRI and FRII galaxies, a difference in the $Q_{jet} - L_R$ relation between FRI and FRII morphologies would add scatter to the $L_R - L_X$ relation for the LERGs.

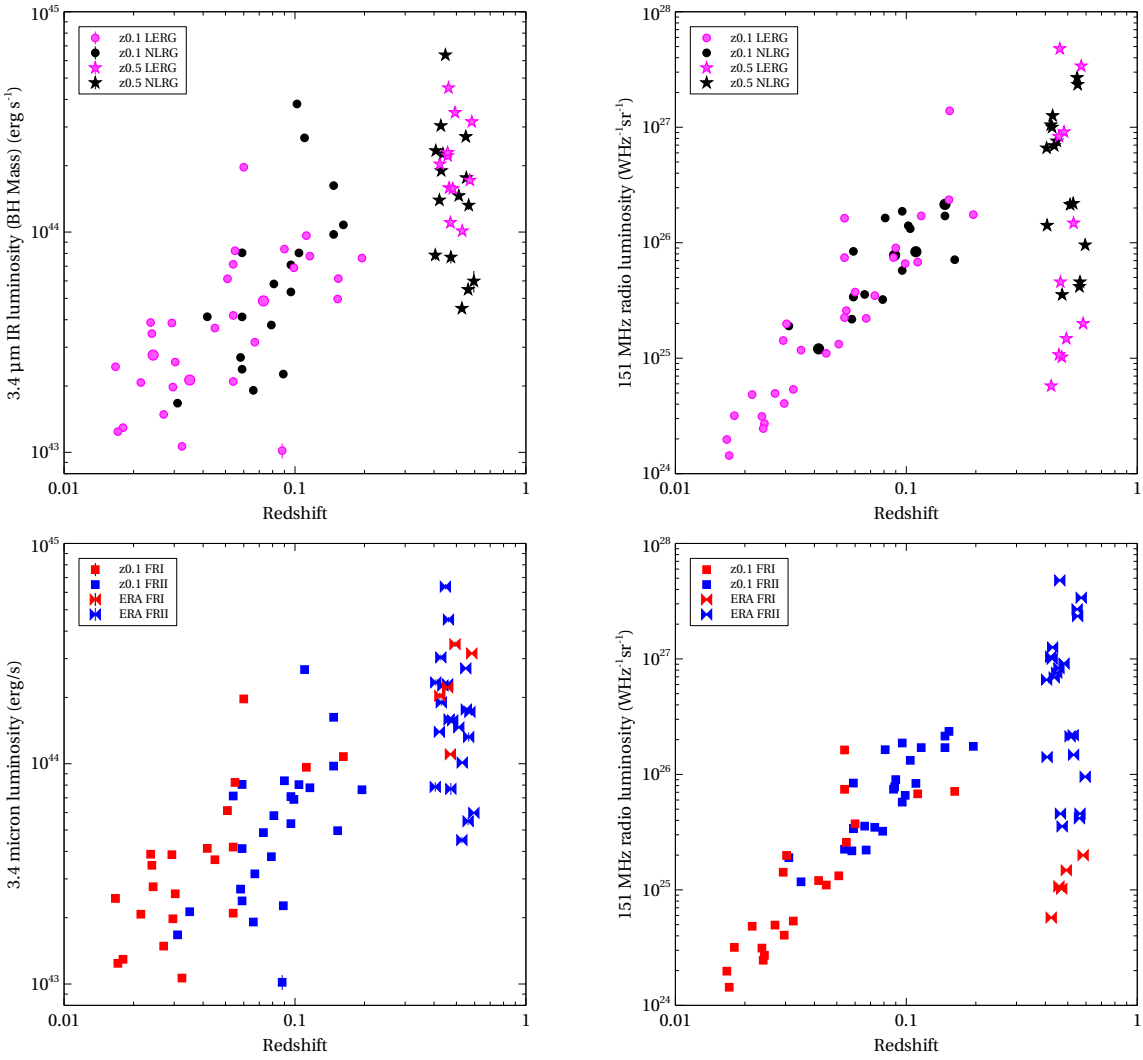

FIGURE 6.3: 3.4 μm luminosity (left) and 151 MHz radio luminosity (right) plotted against redshift for the z0.1 and ERA samples, split into LERGs and NLRGs (top) and FRI and FRII galaxies (bottom). The top shows LERGs as magenta symbols and NLRGs as black symbols, z0.1 sources as circles and ERA sources as stars. The bottom plots show FRI galaxies as red symbols and FRII as blue symbols, z0.1 sources as squares and ERA sources as ties.

6.3.2 3.4 μm and radio luminosities

It is expected that jet power, and consequently radio power, should be related to black hole mass. I first used the ERA sample black hole masses from McLure et al. (2004) to check for evidence of a relationship – Figure 6.4. Like McLure et al., I found a correlation between M_{BH} and L_R for the NLRGs in my ERA sample, but not for the LERGs (Table 6.2).

I then looked at the combined samples using 3.4 μm luminosity as a proxy for black hole mass: Figure 6.5 (top) shows 3.4 μm luminosity plotted against 151 MHz radio luminosity for NLRGs and LERGs respectively.

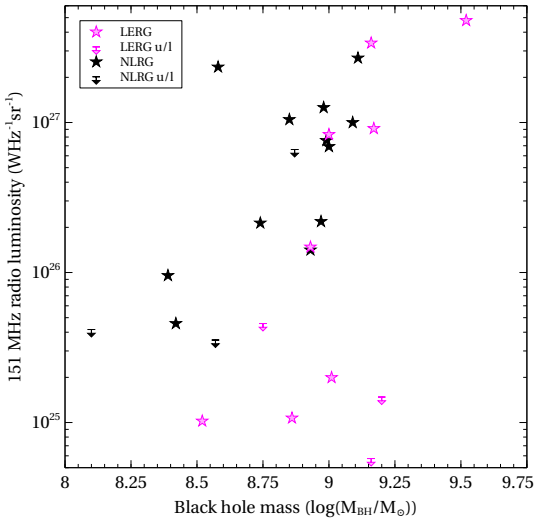

FIGURE 6.4: Black hole mass vs radio luminosity for the ERA sample. LERGs are shown in magenta and HERGs in black.

The NLRG plot shows the correlation between radio and near-IR luminosity suggested by Gürkan et al. (2014); this was confirmed by a partial correlation Kendall's τ test (Table 6.3) and reflects the result for the ERA sample using calculated black hole masses. The ERA sources dominate the high IR luminosities and the lowest 3.4 μm luminosity sources are from the z0.1 sample, reflecting their respective radio luminosities. Radio luminosity thus appears to be related to black hole mass for the NLRG sources.

In contrast, the LERG subsample does not appear to have a correlation with radio luminosity, again reflecting the result for the ERA sample with calculated black hole masses, and this is confirmed by the Kendall's τ test.

Given the apparent difference between the M_{BH}/L_R ratio for the FRIs and FRIIs, I also looked at the same plots for the different morphologies (Figure 6.5, bottom). However, the results reflect those of the NLRG/LERG results; I found no correlation for the low power FRI sources, which are mainly LERGs, and a strong correlation for the FRII sources, which are a mixture of NLRGs and LERGs. There is insufficient difference between the statistics for the pairs of subsamples to say whether morphology or spectral type is a dominant factor, but the redshift plots in Figure 6.3 suggest that morphology does make an important contribution. In addition, the differing proton contents of the FRI jets will also add scatter to any relationships with jet power, and consequently to relationships with L_R.

Thus it appears that radio luminosity is strongly related to black hole mass for NLRGs and FRIIs. Chen et al. (2015) also found a strong relationship between black hole mass and jet power for their sample of high excitation FRIIs. The use of L_R as a proxy for jet power therefore looks a reasonable assumption for these sources.

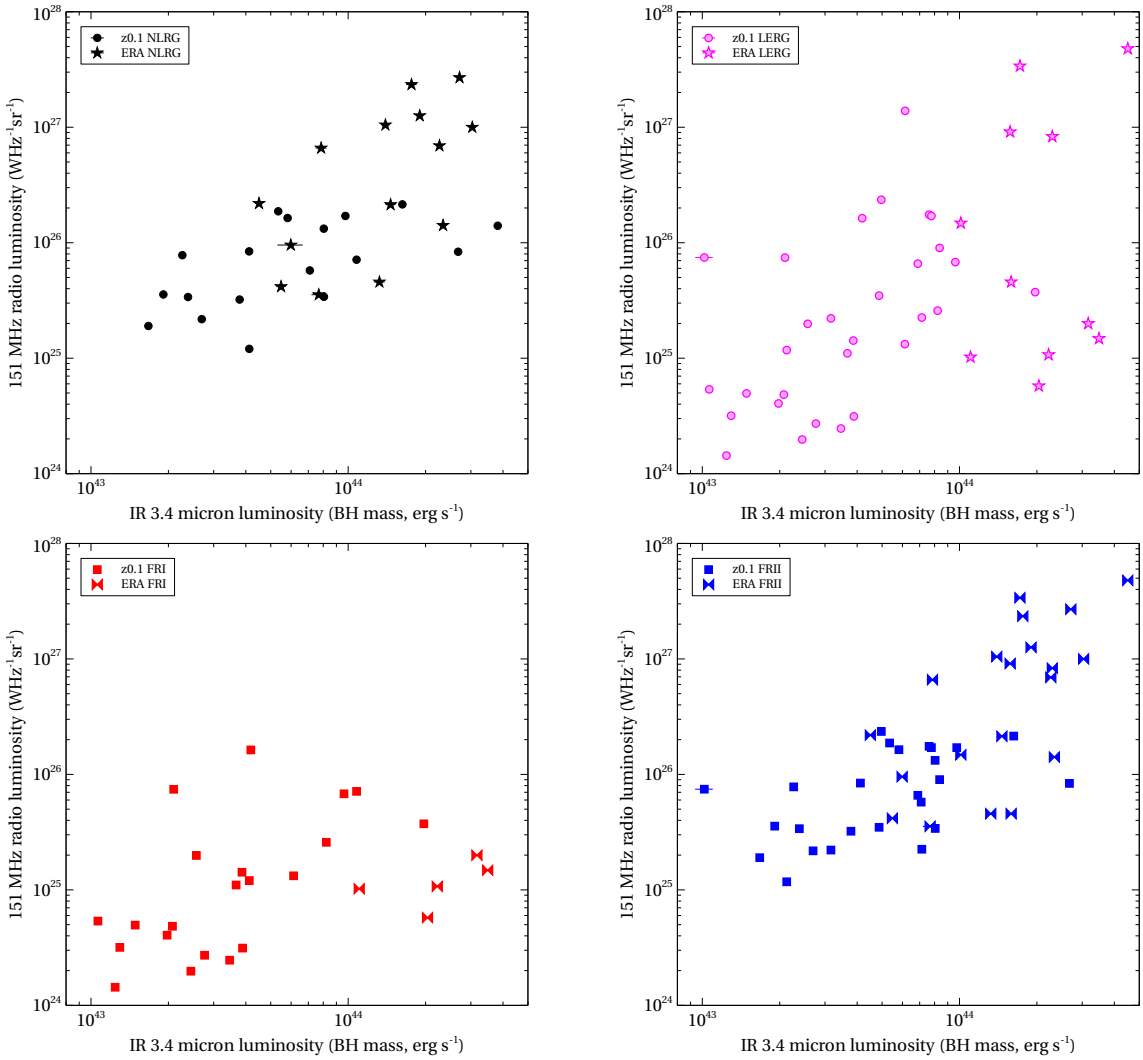

FIGURE 6.5: 3.4 μm luminosity vs 151 MHz radio luminosity for the z0.1 and ERA samples. The top two plots show NLRG sources (left) and LERGs (right). Below are the same plots for FRI galaxies (left) and FRII galaxies (right). Symbols as in Figure 6.3

.

For the LERGs, however, there does not appear to be a relationship between black hole mass and radio power – Chen et al. (2015) also found that the relationship was weaker for low excitation FRIs than the high excitation FRII sources. Given that my LERG sample contains both FRI and FRII morphologies, differences in the $Q_{jet} - L_R$ relations for FRIs and FRIIs and scatter from the different proton contents of the FRI galaxies will contaminate any such relationship, so my result is perhaps not surprising.

6.3.3 3.4 μm and ICM luminosities

Turning to the cluster richness, I then looked at whether it shows any relationship with black hole mass, in particular to check that the LERG $L_R - L_X$ relation is independent

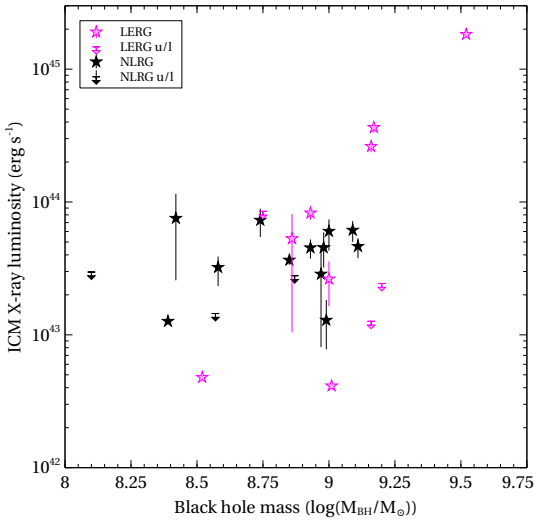

FIGURE 6.6: Black hole mass vs ICM X-ray luminosity for the ERA sample. LERGs are shown in magenta and HERGs in black.

of black hole mass. Again, I first looked at the ERA sample with the black hole masses from McLure et al. (2004) (Figure 6.6). I found no correlation between M_{BH} and L_X for either the NLRGs or the LERGs (Table 6.2).

For the combined samples, using 3.4 μm luminosity as a proxy for black hole mass, the results again reflect those for the ERA sample with the calculated black hole masses. Figure 6.7 shows 3.4 μm luminosity plotted against ICM X-ray luminosity for the NLRGs (top left) and LERGs (top right). The NLRG plot looks like a looser version of the HERG radio/ICM luminosity plot (Chapter 4, Figure 4.5 left) – which is unsurprising given the 3.4 μm/radio luminosity relationship discussed above. Since there is no correlation between radio and ICM luminosities for the high excitation sources, no correlation between ICM and 3.4 μm luminosities was expected. The partial correlation Kendall's τ tests in the presence of a common redshift dependence (Table 6.3) show no significant correlations (although the result for FRII subsample is not far short of significant at the 5% level) and this strengthens the case for fuelling from local reservoirs.

For the LERGs, there is a strong correlation between ICM and radio luminosities (Chapters 3 and 4) but none between radio and 3.4 μm luminosities. A correlation between 3.4 μm luminosity and ICM X-ray luminosity was therefore not expected, and this is confirmed in Figure 6.7 (right) and by the partial correlation Kendall's τ test (Table 6.3). Thus there is no evidence that black hole mass contributes to that relationship.

The 3.4 μm luminosity/ICM luminosity plots for the FRI/FRII subsamples are in the bottom of Figure 6.7. As with the NLRG/LERG subsamples, there is no correlation for either the FRI or FRII galaxies.

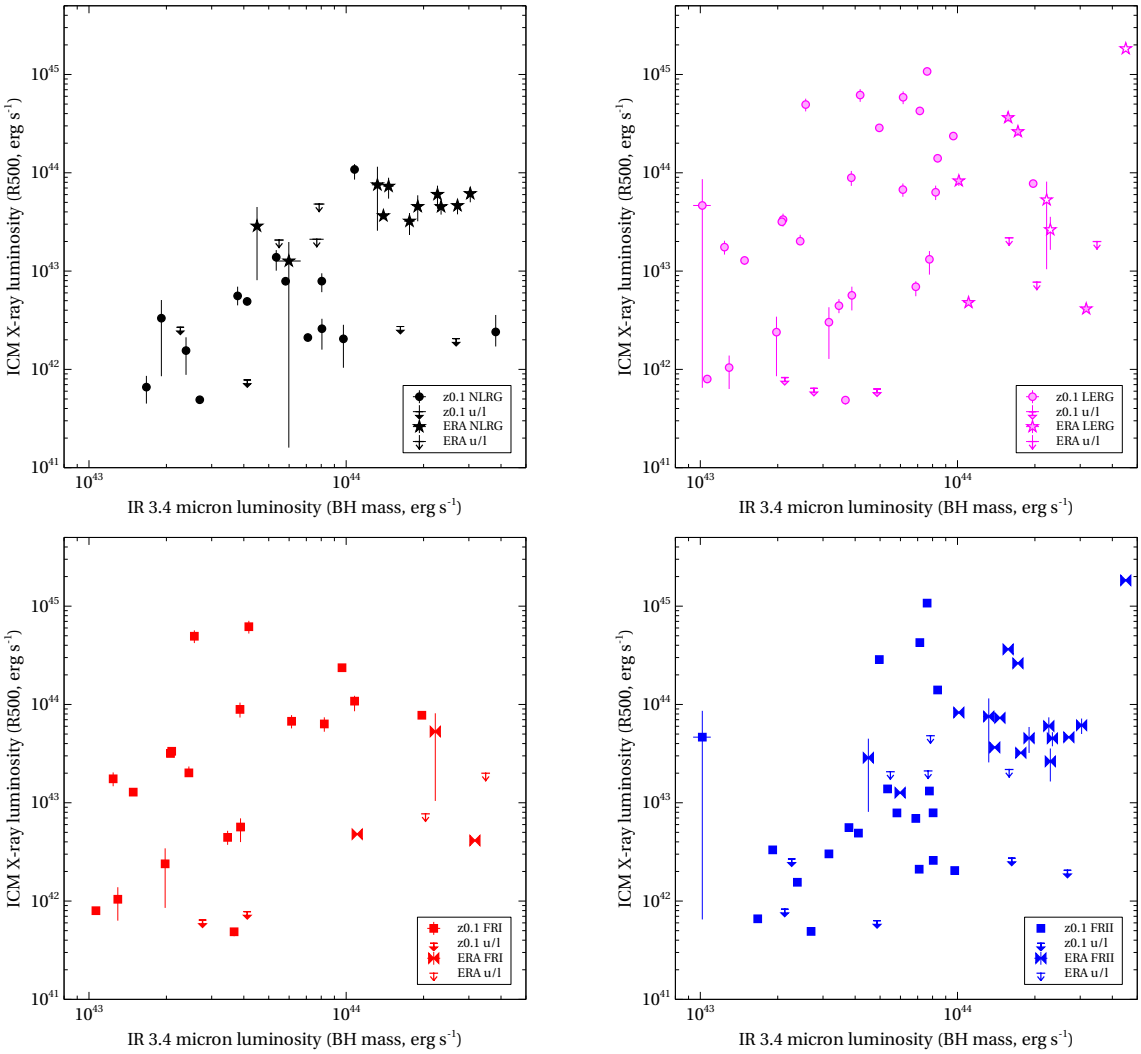

FIGURE 6.7: 3.4 μm luminosity vs ICM X-ray luminosity for the z0.1 and ERA samples. The top two plots show NLRG sources (left) and LERGs (right). Below are the same plots for FRI galaxies (left) and FRII galaxies (right). Symbols as in Figure 6.3

6.4 Accretion rate

In this section I look at the mid-IR data as a proxy for accretion luminosity and consequently for accretion rate, to see how accretion rate relates to the radio and ICM luminosity, and in particular whether accretion rate is independent of ICM luminosity for the high excitation sources. As discussed in Section 6.2, if there is a relationship between black hole mass and spin this could affect the results.

6.4.1 22 μm magnitude and redshift

Figure 6.8 shows 22 μm luminosity plotted against redshift for my samples, split into NLRG/LERG subsamples (left) and FRI/FRII subsamples (right). As found by Gürkan

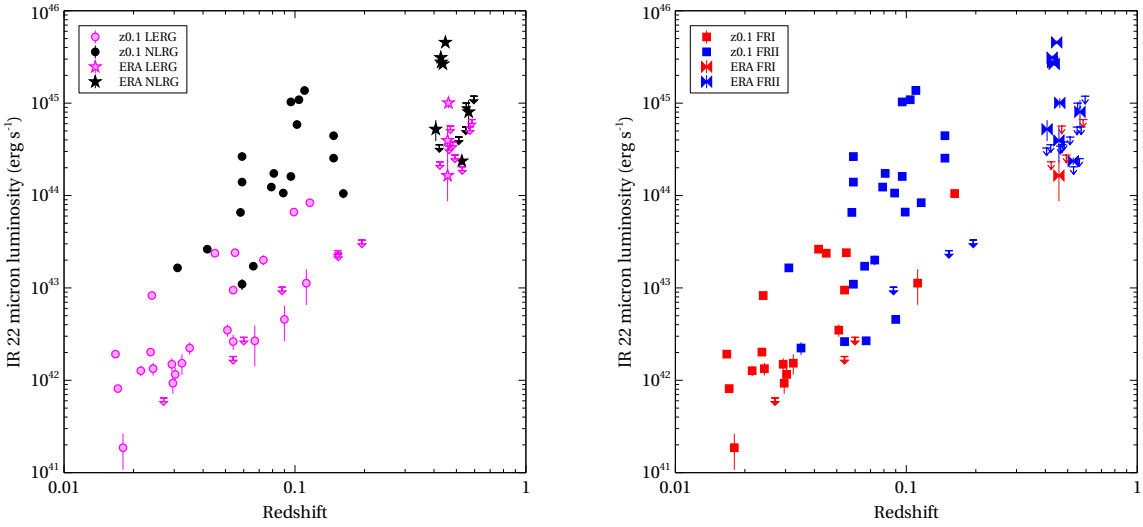

FIGURE 6.8: 22 μm luminosity plotted against redshift for the z0.1 and ERA samples, split into LERGs and NLRGs (left) and FRI and FRII galaxies (right). Symbols as in Figure 6.5.

et al. (2014), there appears to be a correlation between 22 μm IR luminosity and redshift. The paucity of low luminosity, low redshift LERGs found in the equivalent 3.4 μm plot (Figure 6.3, left) is not evident here, but again there appear to be anomalies in the low luminosity sources in the ERA sample. In this case, not only are the five TexOx-1000 sources high in the plot compared with the $L_R - z$ plot (Figure 6.3, right), but all the ERA sources, including the NLRGs, are compressed into a much narrower range of luminosities than would be expected from either the $L_R - z$ plot or the 3.4 $\mu m - z$ plot and from the scatter on the lower redshift sources in the 22 $\mu m - z$ plot. This suggests that there must be additional factors affecting any relationship between accretion rate and radio luminosity for the high excitation sources.

6.4.2 22 μm and radio luminosities

As discussed above, the mid-IR proxy for accretion rate is expected to be valid for the NLRG population, but not necessarily for the LERGs. In Gürkan et al. (2014), the plot of 22 μm vs 151 MHz radio luminosity for the full sample shows a continuous distribution with the bottom left of the plot dominated by LERGs. They found a strong correlation for their full sample and for their HERG subsample, but not for their LERGs.

Figure 6.9 shows the same plot for my samples, but separated into NLRGs (left) and LERGs (right). With the high proportion of upper limits, the statistics are likely to be unreliable, but the Kendall's τ tests (Table 6.3) show a weak correlation for the NLRGs and no correlation for the LERGs.

Again, the FRI/FRII results reflect the LERG/NLRG results. The correlation statistic for the FRII sources is stronger than for the NLRGs, but the sample is larger and extends over a larger luminosity range, so this does not necessarily indicate that the relationship is stronger for the FRIIs.

That the NLRGs have a weaker correlation with L_R for 22 μm luminosity than for 3.4 μm echoes the results of Chen et al. (2015), who found the jet powers for high excitation FRII sources showed a stronger relationship with black hole mass than with accretion rate. It must however be remembered that if accretion efficiency is also related to black hole mass, the correlation between L_R and 3.4 μm luminosity is potentially a confounding factor.

Chen et al. found a strong correlation between low excitation FRI jet powers and accretion rate, but neither Gürkan et al. (2014) nor I found a corresponding relationship between total radio power and 22 μm luminosity for the LERGs. Both the uncertain provenance of the LERG 22 μm luminosity and the possible disruption to the $Q_{jet} - L_R$ relation for FRIs by entrained material could be factors in this result.

6.4.3 22 μm and ICM luminosities

I look here in particular for any sign that environment richness has an effect on accretion rate for the NLRGs. Figure 6.10 shows no sign of a correlation between ICM X-ray luminosity and mid-IR luminosity for the NLRGs (top left), LERGs (top right), FRIs (bottom left) or FRIIs (bottom right). This is reflected in the Kendall's τ tests (Table 6.3), but again it should be noted that there is a high proportion of upper limits. The 3.4 μm/ICM luminosity results showed only a weak correlation for the FRII galaxies and no correlation for the other subsamples, so if accretion efficiency should have a dependence on black hole mass it is unlikely to contribute to any relationship between ICM luminosity and accretion rate. This result therefore provides further evidence that accretion in high excitation sources is independent of the large-scale environment.

6.5 Discussion and conclusions

6.5.1 High excitation sources

Overall, the NLRG sources follow the expected relationships, having a strong correlation between the radio and low-IR luminosities which is indicative of a correlation between black hole mass and jet power. I also found a weak correlation between radio and mid-IR luminosity, suggesting that there is also a correlation between accretion rate and

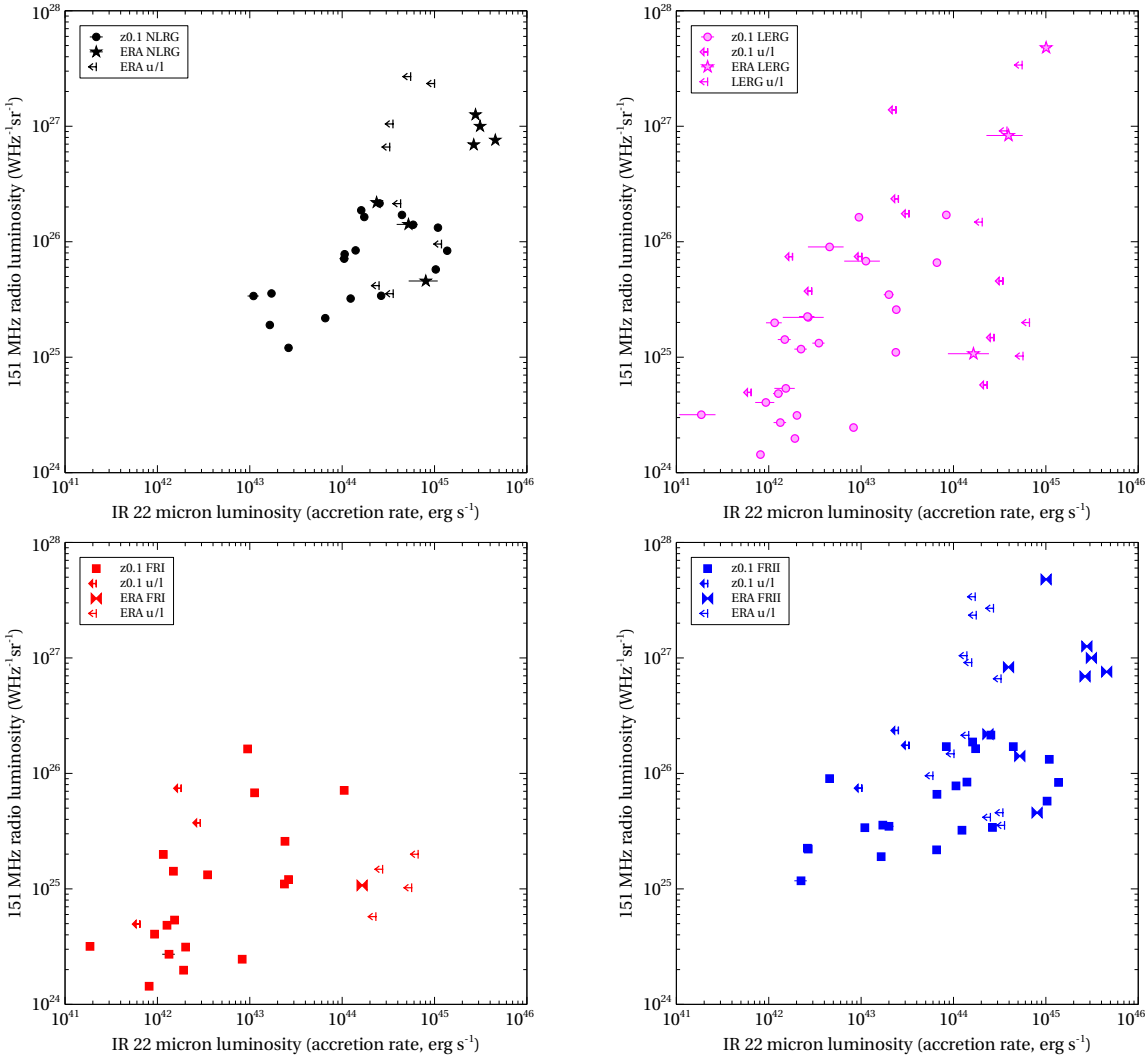

FIGURE 6.9: 22 μm luminosity vs 151 MHz radio luminosity for the z0.1 and ERA samples. The top two plots show NLRG sources (left) and LERGs (right). Below are the same plots for FRI galaxies (left) and FRII galaxies (right). Symbols as in Figure 6.3

jet power. My results reflect those of Chen et al. (2015), but Gürkan et al. (2014), with a much larger sample, found a much stronger correlation for mid-IR luminosity. If accretion efficiency is affected by black hole mass as well as accretion rate, it would be reasonable to have strong correlations for both factors. That the same accretion rate can occur over the full range of cluster environments for HERGs will contribute to the scatter in their $L_R - L_X$ plot (Figure 4.6, right).

Assuming the unified model is correct, these relationships would apply to all high excitation sources. They provide evidence that HERG accretion is fuelled by local reservoirs rather than the larger-scale environment, and that the use of total radio luminosity as a proxy for jet power is reasonable.

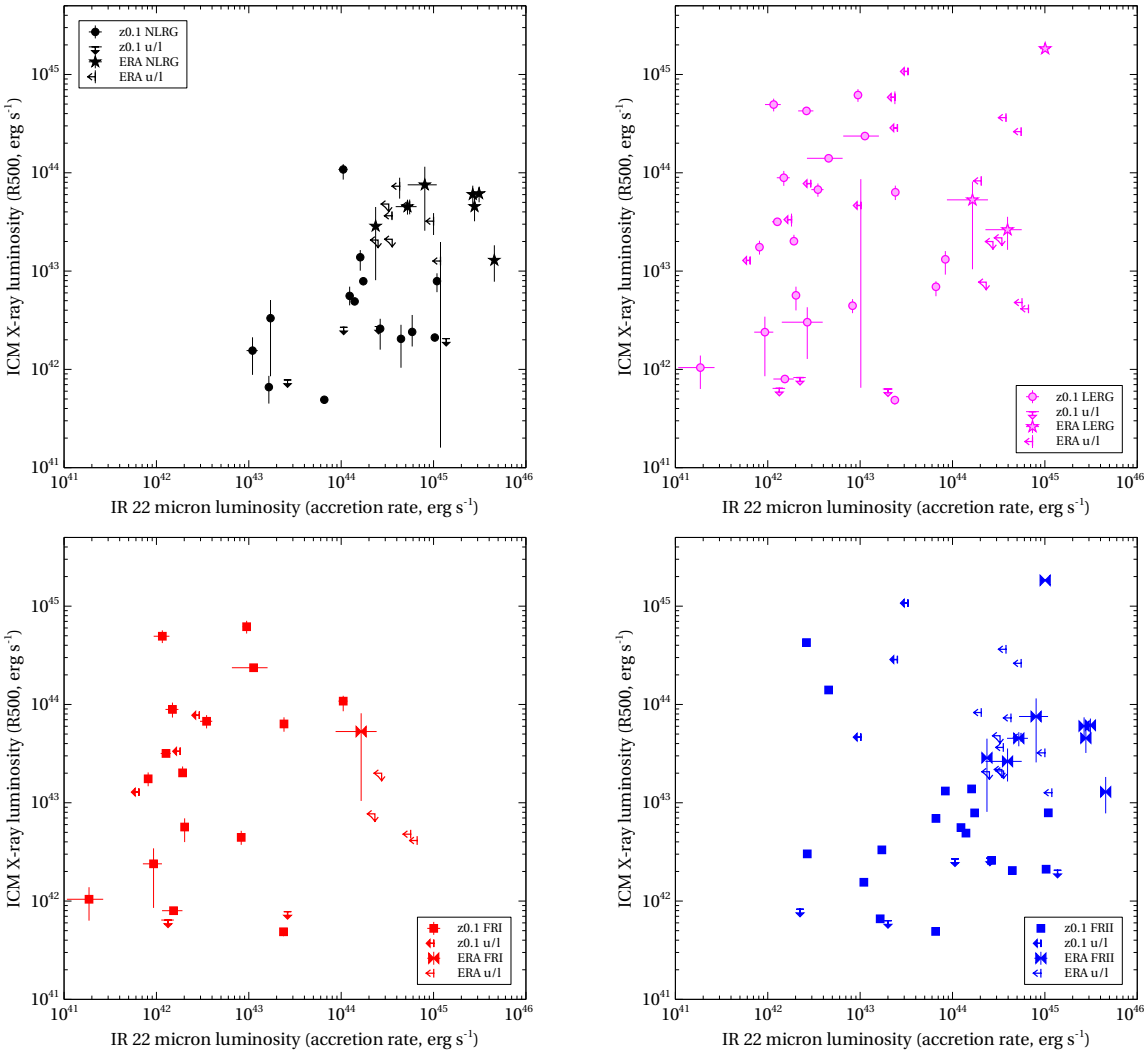

FIGURE 6.10: 22 μm luminosity vs ICM X-ray luminosity for NLRGs (left) and LERGs (right) in the z0.1 and ERA samples. Symbols as in Figure 6.3

6.5.2 Low excitation sources

The relationships do not seem to apply so strongly to the LERGs. Although the complete samples for both mid- and near-IR both show strong correlations with radio luminosity, the LERG subsample alone does not. This reflects the findings of both Gürkan et al. (2014) and Chen et al. (2015). It is unlikely that black hole mass is not a factor in determining accretion rate and consequently jet power, so there must be additional strong factors involved.

Bîrzan et al. (2008) and Godfrey and Shabala (2013) discuss ways that the environment could affect the $Q_{jet} - L_R$ relation in some detail, and several of these factors are related to the large-scale environment. Measuring jet power is difficult, requiring model-dependent assumptions, and for practical reasons, different methods are usually used for FRI and FRII galaxies. The differences between FRI and FRII jets make extrapolating

results across the two types of galaxy dubious. For example, if the two galaxy types have different particle content, this will affect their radiative efficiency. As discussed in Section 1.3.3, the plumes of FRI galaxies may have a significant contribution from entrained material. Entrainment would reduce radio luminosity for a given jet power, and since the amount of entrainment is dependent on both the richness of the ICM and the detailed morphology of the jets, the decrease in luminosity will differ between FRI galaxies. The lobes of FRII galaxies, on the other hand, appear to be electron-dominated (see Sections 1.3.3 and 5.4.2) and so luminosity reduction from entrainment would not apply to these galaxies.

The density of the external medium is also expected to affect the radio luminosity for either galaxy morphology (Barthel and Arnaud 1996; Hardcastle and Krause 2013), and shocks are known to affect the cavity power estimates often used for estimating FRI jet power (eg Bîrzan et al. 2008). Shabala and Godfrey (2013) also looked at the effect of aging, where the spectral index of the synchrotron emission steepens with age as the production of inverse Compton emission reduces the energy of the electron population. They found that the $Q_{jet} - L_R$ relation was sensitive to differences in source size (a proxy for age). The relationship between Q_{jet} and L_R is therefore complicated with many different potentially disruptive factors.

The accretion method could also be disruptive to the $Q_{jet} - L_R$ relation. For Bondi accretion of hot gas, the maximum power released from the black hole system is related to accretion rate, which is in turn related to black hole mass, giving $P_{Bondi} \propto M_{BH}^2$ (Allen et al. 2006). However, the simulations of chaotic accretion reported in Gaspari et al. (2013) describe a much more complicated picture, with the accretion rate a factor of 50-100 times higher than the Bondi rate but fluctuating by over $1 M_\odot$ per year. This in itself could disguise the rôle of the black hole mass for LERGs; the difference in the M_{BH}/L_R ratio for FRI and FRII galaxies discussed in Section 6.3.1 would further disrupt any remaining correlations.

That black hole mass and ICM richness appear to be independent strengthens the evidence for a relationship between radio luminosity and environment richness reported in Chapters 3 and 4, and consequently strengthens the evidence that LERGs are fuelled from the large-scale environment rather than locally.

The mechanism by which LERGs produce mid-IR luminosity is unknown, and its use as a proxy for accretion rate needs to be examined. If, as suggested by Mingo et al. (2014), jet power is at least partly responsible for the emission then it could be used as an indicator of jet power (with scatter added from the other IR sources) and so it may also be an indicator of accretion rate. That the LERG sources fall roughly in the regions of the plots of 22 μm vs redshift and radio luminosity that would be expected if they

have the same relationships as the HERGs suggests that there is some dependence on jet power, but the lack of correlation makes its use as anything more than an indicator unreliable.

The same size black hole appears to result in lower radio luminosities for FRI galaxies than for FRIIs. As discussed above, this may be due to the different particle content of the radio jets. It also might be that the different accretion modes of the HERGs and LERGs have different dependencies on black hole mass, which would add a further complication. This is an interesting result that will affect investigations of differences between HERGs and LERGs, and it would be useful to explore this further with a larger sample such as that used by Gürkan et al. (2014).

To summarise, I found:

- FRI galaxies produce less radio luminosity for a given black hole mass than FRII galaxies;
- For the NLRGs, radio luminosity is related to black hole mass and to accretion rate, suggesting that there is a strong relationship between radio luminosity and jet power;
- For the NLRGs, there was no correlation between ICM richness and black hole mass or accretion rate, suggesting that the central conditions of the AGN are independent of the large-scale environment;
- For the LERGs, there was no correlation between radio luminosity and black hole mass, suggesting that there must be additional factors influencing radio luminosity and jet power. The differences between FRI and FRII galaxies could be one such factor;
- For the LERGs, there was no correlation between black hole mass and environment richness, suggesting that black hole mass is not involved in their $L_R - L_X$ relationship.

TABLE 6.1: Radio, ICM and near- and mid-IR luminosities

Source	Type	FR Class	Redshift	L_{151} $\times 10^{25}$ W Hz^{-1} sr^{-1}	L_X $\times 10^{43}$ erg s^{-1}	$L_{3.4}$ $\times 10^{43}$ erg s^{-1}	L_{22} $\times 10^{43}$ erg s^{-1}
3C 28	LERG	FRII	0.195	17.50	$107.400^{+1.791}_{-1.753}$	7.619±0.221	<3.291
3C 31	LERG	FRI	0.017	0.20	$2.013^{+0.326}_{-0.141}$	2.446±0.062	0.192±0.008
3C 33	HERG	FRII	0.060	8.41	$0.491^{+0.020}_{-0.027}$	4.120±0.107	13.978±0.373
3C 35	LERG	FRII	0.067	2.21	$0.302^{+0.127}_{-0.174}$	3.163±0.082	0.268±0.126
3C 66B	LERG	FRI	0.021	0.48	$3.173^{+0.095}_{-0.119}$	2.075±0.051	0.127±0.016
3C 76.1	LERG	FRI	0.033	0.54	$0.080^{+0.052}_{-0.079}$	1.064±0.028	0.153±0.038
3C 98	HERG	FRII	0.031	1.90	$0.066^{+0.020}_{-0.021}$	1.672±0.042	1.648±0.070
3C 192	HERG	FRII	0.060	3.39	$0.155^{+0.057}_{-0.067}$	2.384±0.066	1.097±0.151
3C 219	HERG	FRII	0.174	32.96	$5.193^{+0.577}_{-0.513}$	16.136±0.419	21.619±1.547
3C 236	LERG	FRII	0.099	6.59	$0.693^{+0.095}_{-0.138}$	6.885±0.184	6.618±0.444
3C 285	HERG	FRII	0.079	3.22	$0.559^{+0.135}_{-0.111}$	3.784±0.101	12.348±0.368
3C 293	LERG	FRI	0.045	1.10	$0.049^{+0.003}_{-0.005}$	3.667±0.095	2.375±0.090
3C 296	LERG	FRI	0.025	0.31	$0.567^{+0.128}_{-0.168}$	3.884±0.098	0.202±0.013
3C 303	HERG	FRII	0.141	5.61	$0.757^{+0.115}_{-0.114}$	13.005±0.338	20.673±0.857
3C 305	HERG	FRI	0.042	1.21	<0.078	4.126±0.107	2.627±0.085
3C 310	LERG	FRI	0.054	7.43	$3.340^{+0.501}_{-0.501}$	2.097±0.054	<0.181
3C 321	HERG	FRII	0.096	5.75	$0.211^{+0.011}_{-0.013}$	7.096±0.190	103.068±2.446
3C 326	LERG	FRII	0.089	7.45	$4.650^{+3.966}_{-4.585}$	1.018±0.080	<1.017
3C 338	LERG	FRI	0.031	1.99	$49.440^{+7.319}_{-7.320}$	2.568±0.071	0.116±0.022
3C 346	HERG	FRI	0.162	7.13	$10.810^{+1.443}_{-2.280}$	10.784±0.296	10.519±1.183
3C 386	LERG	FRI	0.017	0.32	$0.104^{+0.034}_{-0.041}$	1.294±0.034	0.019±0.008
3C 388	LERG	FRII	0.091	9.02	$14.040^{+1.240}_{-1.230}$	8.371±0.224	0.456±0.190
3C 390.3	HERG	FRII	0.056	6.59	$4.262^{+0.637}_{-0.636}$	29.738±0.772	29.690±0.726
3C 433	HERG	FRII	0.102	14.03	$0.240^{+0.117}_{-0.069}$	38.145±0.934	58.707±1.436

Source	Type	FR	Redshift	L_{151}	L_X	$L_{3.4}$	L_{22}
3C 442A	LERG	FRI	0.026	0.50	$1.283^{+0.119}_{-0.121}$	1.486±0.039	<0.065
3C 449	LERG	FRI	0.017	0.14	$1.752^{+0.283}_{-0.280}$	1.242±0.033	0.081±0.007
3C 452	HERG	FRII	0.081	16.37	$0.788^{+0.052}_{-0.070}$	5.814±0.160	17.364±0.504
3C 465	LERG	FRI	0.030	1.42	$8.903^{+1.541}_{-1.541}$	3.865±0.095	0.149±0.024
4C 73.08	HERG	FRII	0.059	2.18	$0.049^{+0.029}_{-0.042}$	2.696±0.070	6.565±0.212
DA 240	LERG	FRII	0.036	1.17	<0.083	2.129±0.057	0.224±0.034
NGC 6109	LERG	FRI	0.030	0.41	$0.239^{+0.105}_{-0.154}$	1.977±0.050	0.093±0.022
NGC 6251	LERG	FRI	0.025	0.25	$0.444^{+0.074}_{-0.071}$	3.460±0.087	0.828±0.026
NGC 7385	LERG	FRI	0.026	0.27	<0.064	2.764±0.070	0.133±0.021
PKS 0034-01	LERG	FRII	0.073	3.48	<0.063	4.868±0.130	2.002±0.243
PKS 0038+09	HERG	FRII	0.188	27.67	$2.652^{+0.596}_{-0.776}$	20.408±0.545	54.953±2.469
PKS 0043-42	LERG	FRII	0.116	17.06	$1.317^{+0.282}_{-0.397}$	7.778±0.214	8.363±0.591
PKS 0213-13	HERG	FRII	0.147	17.06	$0.205^{+0.080}_{-0.101}$	9.756±0.253	44.408±1.468
PKS 0349-27	HERG	FRII	0.066	3.56	$0.332^{+0.176}_{-0.246}$	1.912±0.051	1.718±0.135
PKS 0404+03	HERG	FRII	0.089	7.80	<0.268	2.266±0.062	10.640±0.405
PKS 0442-28	HERG	FRII	0.147	21.48	<0.273	16.251±0.434	25.390±1.097
PKS 0620-52	LERG	FRI	0.051	1.32	$6.742^{+1.047}_{-1.036}$	6.133±0.159	0.349±0.053
PKS 0625-35	LERG	FRI	0.055	2.58	$6.334^{+1.067}_{-1.053}$	8.223±0.207	2.404±0.114
PKS 0625-53	LERG	FRII	0.054	2.25	$42.610^{+3.928}_{-3.945}$	7.138±0.185	0.263±0.049
PKS 0806-10	HERG	FRII	0.109	8.36	<0.206	26.771±0.715	137.066±3.453
PKS 0915-11	LERG	FRI	0.055	16.29	$61.800^{+9.146}_{-9.147}$	4.184±0.109	0.947±0.090
PKS 0945+07	HERG	FRII	0.086	8.17	$1.790^{+0.206}_{-0.313}$	16.188±0.445	16.253±0.498
PKS 1559+02	HERG	FRII	0.104	13.24	$0.790^{+0.160}_{-0.180}$	8.039±0.221	108.903±2.743
PKS 1648+05	LERG	FRI	0.155	138.68	$58.620^{+8.689}_{-8.687}$	6.147±0.178	<2.378
PKS 1733-56	HERG	FRII	0.099	13.55	$0.842^{+0.365}_{-0.618}$	9.127±0.237	11.812±0.480
PKS 1839-48	LERG	FRI	0.111	6.79	$23.640^{+0.665}_{-0.825}$	9.634±0.265	1.126±0.470
PKS 1949+02	HERG	FRII	0.059	3.40	$0.259^{+0.068}_{-0.100}$	8.049±0.209	26.438±0.747
PKS 1954-55	LERG	FRI	0.058	3.73	$7.767^{+0.323}_{-0.310}$	19.687±0.496	<0.291

Source	Type	FR	Redshift	L_{151}	L_X	$L_{3.4}$	L_{22}
PKS 2211-17	LERG	FRII	0.153	23.55	$28.640^{+0.238}_{-0.265}$	4.966±0.148	<2.534
PKS 2221-02	HERG	FRII	0.056	3.03	$1.428^{+0.128}_{-0.222}$	25.315±0.638	30.365±0.788
PKS 2356-61	HERG	FRII	0.096	18.71	$1.383^{+0.252}_{-0.373}$	5.347±0.139	16.092±0.613
TOOT 1301+3658	LERG	FRII	0.424	0.58	<0.772	20.352±0.656	<23.174
TOOT 1255+3556	LERG	FRII	0.471	1.02	$0.479^{+0.200}_{-0.470}$	11.040±0.468	<56.539
TOOT 1626+4523	LERG	FRII	0.458	1.07	$5.304^{+2.830}_{-4.260}$	22.214±0.645	16.455±7.750
TOOT 1630+4534	LERG	FRII	0.493	1.48	<1.998	34.870±0.985	<27.410
TOOT 1307+3639	LERG	FRII	0.583	2.00	$0.413^{+0.200}_{-0.410}$	31.671±1.100	<66.441
7C 0223+3415	HERG	FRII	0.473	3.55	<2.108	7.687±0.488	<35.685
7C 1731+6638	HERG	FRII	0.562	4.17	<2.069	5.484±0.228	<25.090
7C 0213+3418	LERG	FRII	0.465	4.57	<2.180	15.882±0.591	<34.243
TOOT 1303+3334	HERG	FRII	0.565	4.57	$7.544^{+3.980}_{-4.970}$	13.233±0.641	80.381±27.900
7C 0219+3423	HERG	FRII	0.595	9.55	$1.266^{+0.710}_{-1.250}$	5.984±0.673	<118.896
6C 0850+3747	HERG	FRII	0.407	14.13	$4.525^{+0.700}_{-0.770}$	23.391±0.773	52.214±13.295
6C 1200+3416	LERG	FRII	0.530	14.79	$8.277^{+0.950}_{-0.920}$	10.120±0.368	<20.474
6C 1132+3439	HERG	FRII	0.512	21.38	$7.299^{+1.610}_{-1.840}$	14.623±0.657	<42.931
6C 0857+3945	HERG	FRII	0.528	21.88	$2.868^{+1.620}_{-2.060}$	4.502±0.153	23.596±2.266
3C 16	HERG	FRII	0.405	66.07	<4.808	7.852±0.387	<32.709
3C 46	HERG	FRII	0.437	69.18	$6.026^{+1.370}_{-1.720}$	22.652±0.694	265.712±13.332
3C 341	HERG	FRII	0.448	75.86	$1.290^{+0.540}_{-0.510}$	63.644±1.798	455.103±19.660
3C 200	LERG	FRII	0.458	83.18	$2.636^{+0.930}_{-0.990}$	22.960±0.816	39.429±16.715
3C 19	LERG	FRII	0.482	91.20	$36.400^{+2.790}_{-3.140}$	15.737±0.613	<37.928
3C 457	HERG	FRII	0.428	100.00	$6.139^{+1.050}_{-1.130}$	30.380±0.931	311.160±16.161
3C 274.1	HERG	FRII	0.422	104.71	$3.655^{+0.350}_{-0.290}$	13.959±0.508	<35.467
3C 244.1	HERG	FRII	0.430	125.89	$4.542^{+1.360}_{-1.330}$	18.975±0.627	277.833±13.941
3C 228	HERG	FRII	0.552	234.42	$3.220^{+0.670}_{-0.890}$	17.633±0.808	<100.027
3C 330	HERG	FRII	0.549	269.15	$4.639^{+0.700}_{-0.860}$	27.101±0.852	<55.130
3C 427.1	LERG	FRII	0.572	338.84	$26.220^{+2.530}_{-2.510}$	17.181±0.669	<55.340

Source	Type	FR	Redshift	L_{151}	L_X	$L_{3.4}$	L_{22}
3C 295	LERG	FRII	0.462	478.63	$183.000^{+3.550}_{-3.660}$	45.112±1.240	100.713±12.244

Column 1: source name. Col.2: Spectral type. Col. 3: FR morphology. Col. 4: redshift. Col.5: 151 MHz radio luminosity. Col. 6: 3.4μm IR luminosity. Col. 7: 22μm IR luminosity.

TABLE 6.2: Generalized Kendall's τ correlation test results using the ERA black hole masses (M_{BH}) from McLure et al. (2004).

Sample	Sub-sample	N	τ/σ	p
M_{BH} vs 3.4 μm IR luminosity				
ERA	All	26	4.63	<0.0001
M_{BH} vs Radio luminosity				
ERA	NLRG	15	2.62	0.0087
	LERG	11	1.56	0.12
M_{BH} vs ICM luminosity				
ERA	NLRG	15	1.47	0.14
	LERG	11	1.20	0.23

N is sample size; τ is the partial correlation statistic; σ is the standard deviation; p is probability under the null hypothesis.

TABLE 6.3: Partial correlation analysis results for the IR data, using Generalized Kendall's τ correlation tests in the presence of a correlation with a third factor.

Sample	Sub-sample[a]	N	τ/σ	p
3.4 μm IR luminosity vs 22 μm IR luminosity, with a redshift correlation				
z0.1 and ERA	All	74	0.52	0.6
	NLRG	33	5.33	< 0.0001
	LERG	41	3.55	0.0004
	FRI	26	1.42	0.16
	FRII	46	0.08	0.94
3.4 μm IR luminosity vs Radio luminosity, with a redshift correlation				
z0.1 and ERA	NLRG	33	3.38	0.0007
	LERG	41	0.08	0.94
	FRI	26	-0.16	0.87
	FRII	46	3.45	0.0006
3.4 μm IR luminosity vs ICM luminosity, with a redshift correlation				
z0.1 and ERA	NLRG	33	1.37	0.17
	LERG	41	1.20	0.23
	FRI	26	1.10	0.27
	FRII	46	1.86	0.063
22 μm IR luminosity vs Radio luminosity, with a redshift correlation				
z0.1 and ERA	NLRG	33	2.00	0.044
	LERG	41	0.81	0.42
	FRI	26	-0.25	0.80
	FRII	46	2.47	0.014
22 μm IR luminosity vs ICM luminosity, with a redshift correlation				
z0.1 and ERA	NLRG	33	1.07	0.29
	LERG	41	0.11	0.91
	FRI	26	-0.14	0.89
	FRII	46	-0.15	0.88

N is sample size; τ is the partial correlation statistic; σ is the standard deviation; p is probability under the null hypothesis.

[a] Hybrid morphology sources have been removed from the FRI and FRII subsamples.

Chapter 7

Conclusions and further work

As described in Chapter 1, the aim of this research programme was to make the first large-scale, systematic and representative study of the large-scale environments of radio-loud AGN. I quantified environment richness using the X-ray luminosity of the ICM, and also calculated temperature, pressure and density. I used these properties for the following investigations:

- to investigate the relationship between radio luminosity and environment richness;
- to look for evidence of a change in environment with epoch;
- to look for differences in the results for different classes of radio galaxy – morphological (FRI and FRII) or spectral (HERG and LERG);
- to derive the best possible constraints to date on the dynamics and particle content of FRII radio lobes using the X-ray observations of the lobes;
- to establish whether any relationships between radio luminosity and environment richness are affected by black hole mass or accretion rate.

I also compared the properties of the AGN environments in my samples with those of general cluster and group environments, and looked at whether it would be possible to convert between ICM luminosity (the measure of cluster richness used in this thesis) and B_{gg} (a measure of cluster richness based on galaxy overdensity) for radio-loud AGN.

In this chapter I give a brief overview of the work presented in the previous chapters, summarise my main findings and discuss further work that would build on my results.

7.1 Relationship between radio luminosity and environment richness

In order to look at the relationship between radio and cluster properties, I compared low frequency radio luminosity with ICM X-ray luminosity. I controlled the effects of evolution by using two samples across narrow ranges of redshift; the ERA sample at $z \sim 0.5$ (26 sources) and the z0.1 sample at $z \sim 0.1$ (55 sources). Each sample covered about 3 decades in radio luminosity, with an overlap of about 2 decades. This is the first time that a sufficiently large sample has been available to control for evolution in this way.

Looking at the ERA and z0.1 samples individually (Chapters 3 and 4 respectively), I found a correlation between radio luminosity and cluster richness for the full samples, but with total scatter of about one order of magnitude in environment richness at a given radio luminosity.

At both redshifts there was evidence for a difference between high- and low-excitation sources. The HERGs at each redshift occupied a narrower range of cluster richnesses than the LERGs and showed no sign of a correlation between radio luminosity and cluster richness. The LERG subsamples, on the other hand, occupied a wider range of environments and showed a strong correlation between radio luminosity and cluster richness.

I also compared the results for sources with FRI and FRII morphologies. The strengths of the relationships between radio and ICM luminosity reflected the proportions of HERGs and LERGs within the two different morphologies, suggesting that the relationship was dependent on spectral rather than morphological galaxy type.

Previous studies have shown fundamental differences between HERGs and LERGs (Section 1.1.2.3); that they have different accretion methods and host galaxy properties. My results add to these by showing differences in their relationships with their large scale environments, and, as discussed in Sections 1.1.2.5 and 4.5.4, support theories of different fuelling mechanisms for HERGs and LERGs. If the LERGs, which show a strong relationship between radio luminosity and cluster richness, are fuelled by material falling in from the ICM then it is reasonable that their properties will be dependent on the properties of the central density and consequently the richness of the ICM. The HERGs, which show no such relationship, are thought to be fuelled by local gas reservoirs and so the results reflect the fact that they are not dependent on the ICM.

In common with other researchers, I found considerable scatter in the results, which may be a sign of more complex relationships between jet power and environment than are generally assumed.

I also found that the HERGs occupied groups and clusters with more compact central regions than the LERGs; this may indicate that HERGs have a greater concentration of gas near the host galaxy than LERGs or may simply reflect the fact that HERGs are hosted by less massive environments.

7.2 Evolution of the environment

In Section 4.5.1.3 I compared the results for the two redshifts to see if there had been any changes with epoch. I found that the LERG subsamples at the two redshifts had very similar radio luminosity–ICM richness relationships, suggesting that the relationship had remained the same between the two epochs. I found no significant difference between the cluster environments of the LERGs at the two redshifts. If the ICM is the main source of fuel, then since the fuelling requirements to produce a given radio luminosity would not change with time, so the corresponding environments should not change.

The HERG environments showed tentative evidence of evolution. Although the maximum environment richnesses were similar at both redshifts, the z0.1 sample included much weaker environments than the ERA sample and the difference between samples was significant. At present it is not possible to say whether this result is real or is due to selection effects. If there are ICM groups at $z \sim 0.5$ matching the weakest environments in the z0.1 sample, it would take X-ray observations of $\sim 10^7$ s to detect them so a different measure of environment will be required to look at evolution in more detail. However, a search for HERGs with low B_{gg} measurements at $z \sim 0.5$ found only one candidate with a sufficiently low galaxy overdensity to imply a very weak ICM environment.

Since radio galaxy feedback is thought to be an important aspect of cluster evolution, and since HERGs are the predominant type of radio galaxy at high redshifts, this potential change in HERG environments with redshift is important for both theory and simulation. It would therefore be very useful to extend this work back to higher redshifts.

7.3 FRII lobes and the environment

In Chapter 5 I compared the internal and external properties of FRII radio lobes in order to constrain the dynamics of the lobes. Assessing the impact of the lobes on their

environments is important for modelling feedback and galaxy and cluster evolution, and this is the first time a representative sample has been available for this work.

I estimated the internal lobe conditions from the radio and X-ray fluxes and the external conditions from the ICM surface brightness profiles and temperatures. I found that all the lobe pressures were higher than the pressures predicted by equipartition, although all were within one order of magnitude of the equipartition prediction. This confirms results from smaller studies that have suggested that the lobes were near equipartition, but that the lobes contain electron energy densities additional to the minimum energy condition.

Lobes were over-pressured at the tip compared with the ICM, showing that they were still expanding through the ICM, but at mid-lobe the lobes were near pressure balance with the ICM. These results support radio lobe models which have moderate pressures once the initial growth phase is over and contradicts models that assume supersonic expansion throughout the lobe.

I estimated lower limits for the Mach numbers at the lobe tips from the ratio of the internal and external pressures. These ranged from around 0.7 to 5 (with one outlier with lobes at Mach 12 and 19, but this source had unreliable pressure estimates) and with a median of 1.8. These results reflect those from detailed studies of individual sources and, given that the estimates are lower limits, suggest that at least half the lobes are driving strong shocks. The HERGs occupied a bigger range of Mach numbers than the LERGs, but there was no significant difference between the medians of the two subsamples. It should be noted that because of the correlation between radio power and ICM richness, most of the LERGs in weak environments are FRIs. The LERG FRII subsample is thus biassed towards high ICM pressures and consequently low Mach numbers.

I found an inverse correlation between Mach number and ICM luminosity for the HERGs, but since ICM pressure was used in the Mach number estimates, further work is needed to check whether this result is genuine. If it is, it would be a useful tool for calibrating simulations.

7.4 AGN central properties and the cluster environment

I found a correlation between total radio luminosity (L_R) and environment X-ray luminosity (L_X) for the LERGs in my samples, but not for the HERGs. Black hole mass is expected to be a factor in jet production and consequently in total radio luminosity; if

it is related to cluster richness, then this would be a confounding factor in the $L_R - L_X$ relation.

Since HERGs are expected to be fuelled locally rather than from the ICM, it was also of interest to check whether the central properties of the AGN had any relationship with the cluster richness for the HERGs. A lack of such relationships would support local fuelling theories.

In addition, theories of jet production relate jet power to black hole mass, accretion rate and spin; a strong relationship between the central properties and radio luminosity would thus be evidence of a strong $Q_{jet} - L_R$ relationship.

In Chapter 6 I compared radio and ICM luminosity with black hole mass and accretion rate, using the WISE 3.4 μm and 22 μm IR luminosities from Gürkan et al. (2014) respectively as proxies. Note that the 22 μm luminosity for the HERGs comes from the torus, but the provenance of the LERG mid-IR is uncertain so the validity of its use as a proxy for accretion rate is also uncertain.

I found no relationship between black hole mass and ICM luminosity for the LERGs, adding evidence that cluster richness and radio luminosity are related. I also found no relationship between black hole mass and radio luminosity – this was unexpected as it throws doubt on the LERG $Q_{jet} - L_R$ relation, suggesting that there are other factors involved. If LERGs are fuelled by chaotic accretion, then accretion rate, and consequently jet power, could be quite variable and add considerable scatter into the relationship.

For the HERGs, I found no relationships between ICM luminosity and black hole mass or accretion rate, supporting theories of local fuelling. I also found a strong relationship between black hole mass and radio luminosity and a weaker one between accretion rate and radio luminosity, suggesting a good relationship between radio luminosity and jet power.

An interesting finding, and one which might contribute to the lack of a $M_{BH} - L_R$ relationship for the LERGs, was that FRI and FRII galaxies appear to have very different ratios between M_{BH} and L_R, with the FRI galaxies having substantially lower radio luminosity for a given black hole mass than FRII galaxies. Since the LERG population contains both FRI and FRII galaxies, this would contribute scatter to their $L_R - L_X$ relation and also to the $Q_{jet} - L_R$ relation.

7.5 Comparison with environments of other AGN

I looked at the scaling relations between ICM luminosity and temperature for my sources. My results were compatible with published scaling relations for general samples of clusters and groups, suggesting that my results show no systematic evidence that the environments occupied by the radio-loud AGN in my samples are different from those of typical clusters. There are however a lot of different factors affecting the relationship (see Section 4.5.2), including factors present in some but not all of my sources, so it would require a much larger and more detailed study isolate any effect of radio luminosity.

Similarly, the entropy-temperature relations for my samples lay within the range of published scaling relations.

7.6 Comparison of measures of ICM richness

I used ICM X-ray luminosity as a measure of cluster richness, but many researchers use methods involving galaxy counts and overdensities. B_{gg} measurements are available for a number of my sources, so I compared the two methods both to check that results obtained using the two measurement methods are comparable and to see if it was possible to convert between ICM luminosity and B_{gg}.

I found a good correlation between the two methods, so results obtained with the two measurement methods should be comparable. There was however considerable scatter and the notes on individual sources (Section 4.7) contain several examples where the two methods give very different results for the same source. It would therefore be inadvisable to use the correlation to convert between the two measurement methods.

7.7 Further work

7.7.1 The LERG $L_R - L_X$ relationship

The relationship between radio luminosity and the large-scale environment for the LERGs appears to be a strong result, but could be extended. My work was based on samples from two discrete redshifts so that I could isolate any relationships from the effects of evolution. I found no evidence of evolution of the LERG environment, so the relationship could be strengthened by adding available data from other redshifts. In particular, because I was looking for samples with similar luminosity ranges of HERGs and LERGs, I used a lower redshift limit of 0.01 thus excluding the low luminosity local sources. If

ICM luminosities can be calculated for these sources, they could be added to the plot to ensure that the relationship continues down to the lowest radio luminosities. This relationship could then be used both to verify results of simulations and as a diagnostic tool for unusual sources. For example, it would be interesting to see where sources with short jets, such as the LERGs identified by Baldi et al. (2015), lie in relation to the rest of the LERGs. This might help ascertain whether they are newly triggered or naturally weak. It would also be of interest to see where the radio-quiet sources with weak jets (eg Gallimore et al. 2006) lie relative to the LERG population.

The differences found between FRI and FRII radio galaxies in Chapter 6 potentially contribute to the scatter in the $L_R - L_X$ relationship. A larger sample would make it possible to ascertain whether the two galaxy morphologies have a different $L_R - L_X$ relationship and/or whether differences in particle content contribute to the scatter in the relation.

7.7.2 Evolution of ICM environments

The suggestion of evolution of the HERG environments is an important result. The current result – a possible difference between the environments at $z \sim 0.1$ and $z \sim 0.5$ – could be strengthened by expanding the ERA sample. The ERA sample is a subsample of the ZP5 sample of McLure et al. (2004), who were looking at the host galaxies of the radio sources and so excluded BLRGs and QSOs. The 3CRR survey has four BLRGs and QSOs in the ERA redshift range with suitable X-ray observations that could be added to the sample, and there are also four 2Jy sources with X-ray observations; this would increase the number of HERGs at $z \sim 0.5$ to 23. These are all high luminosity sources, but since I found no correlation between radio and ICM luminosities this is not a cause for concern.

There are now a number of surveys going back to moderate redshift and covering a wide range of radio luminosities – the COSMOS survey, for example, goes down to the FRI/FRII divide (Baldi et al. 2014) – and a sample at $z \sim 0.9$ would make a suitable step between my existing samples and high redshift proto-clusters. However, X-ray luminosity is not currently a feasible measure of cluster richness at these redshifts so some work would be needed to look at ways of using optical measures to isolate differences between environments and to calculate overdensities for the existing samples to allow comparisons with higher redshift sources. As discussed in Sections 1.2.1 and 1.3.2, richness measures based on galaxy counts can give different results when calculated within large and small volumes. It would be useful to obtain B_{gg} measurements within different volumes for my samples to look for systematic differences and also to see if

the relationship between ICM luminosity and B_{gg} changes with epoch. This will be important both for extending my work to look at higher redshifts and when making comparisons of studies using different volumes for calculating galaxy overdensities.

Going further back, the CARLA (Clusters Around Radio-Loud AGN) programme (eg Wylezalek et al. 2013; Hatch et al. 2014) is looking at proto-clusters housing radio-loud AGN in the redshift range 1.2 to 3.2. Mapping the changing environments of HERGs through the epochs to the present day would be a fascinating project. It might also be possible to use cosmological simulations to look at the cluster environments of the host galaxies to see when the conditions for triggering a radiative AGN occur and to look for any differences between the conditions for triggering radio-loud and radio-quiet AGN.

The proportion of LERGs reduces as redshift increases; nevertheless there are some LERGs in the COSMOS sample at $z \sim 0.9$ and so it would be useful to check that they fit the $L_R - L_X$ relationship shown at lower redshifts. It should be noted however that if they are dependent on the ICM for fuel, the results may be affected by using a cluster richness measure based on galaxy overdensity rather than ICM luminosity.

7.7.3 Energy input by FRII lobes

As discussed in Section 5.4.4, there are a number of potential systematic errors associated with the calculation of lobe pressures. As LOFAR results become available, the systematics could be reduced by using the correct low frequency spectral indices in the calculations rather than an assumed value and by obtaining more accurate volumes of the radio lobes.

I have not yet looked at the effect of lobe aspect ratio – the simulations of Hardcastle and Krause (2013) found that lobes become more elongated as they expand (as expected from the pressure differences between the lobe and external environment at the lobe tip and along the lobe sides). This is helpful evidence for differentiating between the different models of lobe dynamics (Section 1.3.3), and it would be useful to provide observational corroboration for this result.

My pressure balance results from Chapter 5 could be used to calibrate hydrodynamical simulations. These could then be run in simulation suites to find the energy inputs from typical populations of radio galaxies.

7.7.4 Relationships between jet power and total radio luminosity

My finding of a relationship between radio luminosity and cluster richness for the LERGs implies a strong relationship between radio luminosity and jet power. The $Q_{jet} - L_R$ relation (eg Willott et al. 1999; Bîrzan et al. 2008; Cavagnolo et al. 2010; Godfrey and Shabala 2013) has been in use for some time and is widely used to estimate feedback.

Since the work for this thesis was completed, Godfrey and Shabala (2016) have discovered that the methods used to calibrate the $Q_{jet} - L_R$ relation have a strong dependence on luminosity distance. This paper questions the results of a lot of research dealing with jet powers (eg Bîrzan et al. 2008; Cavagnolo et al. 2010; Godfrey and Shabala 2013; Daly 2016). Once a correction for distance dependence has been applied, the empirical relationship for the FRI galaxies becomes substantially flatter in slope than the predicted relationship. Godfrey and Shabala (2016) discuss several reasons why observation might not match with theory. One possibility is that, since energy from shocks is not included in the observational estimates of jet power, Q_{jet} is underestimated for the higher luminosity sources. Godfrey & Shabala also discuss the effect of entrainment, which is higher in lower power systems, on Q_{jet} estimates.

In the case of the FRII galaxies, the observational data no longer provide a calibration for the $Q_{jet} - L_R$ relation. Godfrey & Shabala discuss theoretical models, which suggest a slope of $\sim$0.5. They note however that the models assume overpressured, self-similar lobe growth, which does not match with observation.

Since most FRI sources are low luminosity LERGs, and one of the main findings in this thesis is a relationship between radio luminosity and ICM richness for LERGs, the factors discussed by Godfrey and Shabala (2016) would be expected to add scatter to or affect the steepness of this relation. It would therefore be useful to convert total radio power to jet power using the separate FRI and FRII relations proposed by Godfrey & Shabala to see if this has an effect on the scatter in my $L_R - L_X$ relation.

There do not as yet seem to have been any investigations that look for differences in the $Q_{jet} - L_R$ relation for HERGs and LERGs. HERGs have a higher accretion rate and appear to be fuelled locally, so are independent of their large-scale environment. As described above, my results support a strong relationship between radio luminosity and black hole mass, and since jet power is thought to have a strong dependence on black hole mass this would imply a strong $Q_{jet} - L_R$ relation. The majority of HERGs are FRII galaxies, so the HERG relationship should reflect that of the FRIIs. Note that Q_{jet} is also thought to be influenced by magnetic field strength, accretion rate and black hole spin, so these additional factors would also affect the relationship.

LERGs, on the other hand, appear to be fuelled from the ICM. They have lower accretion rates, which may be quite variable, and their radio luminosity does not correlate well with black hole mass. This is likely to affect the $Q_{jet} - L_R$ relation. Also the LERG population contains both FRI and FRII galaxies, which are expected to have different $Q_{jet} - L_R$ relations. It would therefore be useful to look more closely at the $Q_{jet} - L_R$ relation for LERGs, to see how all these factors affect predictions of energy input into galaxy clusters.

7.8 Summary

I have made the first systematic investigation of the relationships between the properties of different types of radio-loud AGN and their large-scale environments at two distinct redshifts. I have found a strong relationship between radio luminosity and ICM richness for low-excitation AGN but not for high-excitation AGN, and I have found tentative evidence of evolution of the environment for HERGs, but not for LERGs. I examined the lobes of the FRII galaxies in my samples, finding them to be at higher pressures than predicted by equipartition, but not by large amounts, suggesting that the assumption that the lobes are dominated by relativistic leptons is correct. I found that the lobes tended to be overpressured compared with the environment, but again not by a large amount, and that the lobe tips expanded more rapidly in weaker environments.

I have also looked at the relationships between the central properties of the AGN and the radio and ICM luminosities. I have verified that black hole mass is not a factor in the LERG $L_R - L_X$ relationship, and found no evidence that HERG properties are affected by ICM richness, adding evidence for theories of local fuelling for HERGs. I found evidence that HERGs should have a strong relationship between jet power and radio luminosity, but that LERG jet power must be subject to factors beyond black hole mass. Finally, I found evidence that FRI and FRII galaxies have different relationships between radio luminosity and black hole mass.

I then described some areas where my work could be expanded to provide further input to models and simulations of cluster evolution, in particular to look more closely at evolutionary effects and at lobe dynamics.

Bibliography

Abell, G. O. (1958). The Distribution of Rich Clusters of Galaxies. *ApJS*, 3:211.

Achterberg, A., Gallant, Y. A., Kirk, J. G., and Guthmann, A. W. (2001). Particle acceleration by ultrarelativistic shocks: theory and simulations. *MNRAS*, 328:393–408.

Akritas, M. G. and Bershady, M. A. (1996). Linear Regression for Astronomical Data with Measurement Errors and Intrinsic Scatter. *ApJ*, 470:706.

Akritas, M. G. and Siebert, J. (1996). A test for partial correlation with censored astronomical data. *MNRAS*, 278:919–924.

Allen, M. G., Sparks, W. B., Koekemoer, A., Martel, A. R., O'Dea, C. P., Baum, S. A., Chiaberge, M., Macchetto, F. D., and Miley, G. K. (2002). Ultraviolet Hubble Space Telescope Snapshot Survey of 3CR Radio Source Counterparts at Low Redshift. *ApJS*, 139:411–438.

Allen, S. W., Dunn, R. J. H., Fabian, A. C., Taylor, G. B., and Reynolds, C. S. (2006). The relation between accretion rate and jet power in X-ray luminous elliptical galaxies. *MNRAS*, 372:21–30.

Allen, S. W., Taylor, G. B., Nulsen, P. E. J., Johnstone, R. M., David, L. P., Ettori, S., Fabian, A. C., Forman, W., Jones, C., and McNamara, B. (2001). Chandra X-ray observations of the 3C 295 cluster core. *MNRAS*, 324:842–858.

Andreon, S., Serra, A. L., Moretti, A., and Trinchieri, G. (2015). The amazing diversity in the hot gas content of an X-ray unbiased massive galaxy clusters sample. *ArXiv e-prints*.

Antonucci, R. (1993). Unified models for active galactic nuclei and quasars. *ARA&A*, 31:473–521.

Arnaud, M., Pointecouteau, E., and Pratt, G. W. (2005). The structural and scaling properties of nearby galaxy clusters. II. The M-T relation. *A&A*, 441:893–903.

Baade, W. and Minkowski, R. (1954). Identification of the Radio Sources in Cassiopeia, Cygnus A, and Puppis A. *ApJ*, 119:206.

Baganoff, F. (1999). ACIS On-orbit background rates and spectra from Chandra OAC Phase 1. `http://cxc.harvard.edu/cal/Acis/Cal_prods/bkgrnd/current/baganoff_acis_bg.ps.gz`.

Bahcall, N. A. (1977). X-ray clusters of galaxies - Correlations with optical morphology and galaxy density. *ApJ*, 217:L77–L82.

Baldi, R. D., Capetti, A., Chiaberge, M., and Celotti, A. (2014). The radio-loud AGN population at $z \gtrsim 1$ in the COSMOS field. I. selection and spectral energy distributions. *A&A*, 567:A76.

Baldi, R. D., Capetti, A., and Giovannini, G. (2015). Pilot study of the radio-emitting AGN population: the emerging new class of FR 0 radio-galaxies. *A&A*, 576:A38.

Balestra, I., Tozzi, P., Ettori, S., Rosati, P., Borgani, S., Mainieri, V., Norman, C., and Viola, M. (2007). Tracing the evolution in the iron content of the intra-cluster medium. *A&A*, 462:429–442.

Band, D. L. and Grindlay, J. E. (1985). The synchrotron-self-Compton process in spherical geometries. I - Theoretical framework. *ApJ*, 298:128–146.

Barthel, P. D. and Arnaud, K. A. (1996). Anomalous radio-loudness of Cygnus A and other powerful radio galaxies. *MNRAS*, 283:L45–L49.

Baum, S. A., Heckman, T. M., Bridle, A., van Breugel, W. J. M., and Miley, G. K. (1988). Extended optical-line-emitting gas in radio galaxies - Broad-band optical, narrow-band optical, and radio imaging of a representative sample. *ApJS*, 68:643–714.

Becker, R. H., White, R. L., and Helfand, D. J. (1995). The FIRST Survey: Faint Images of the Radio Sky at Twenty Centimeters. *ApJ*, 450:559.

Belsole, E., Worrall, D. M., Hardcastle, M. J., Birkinshaw, M., and Lawrence, C. R. (2004). XMM-Newton observations of three high-redshift radio galaxies. *MNRAS*, 352:924–938.

Belsole, E., Worrall, D. M., Hardcastle, M. J., and Croston, J. H. (2007). High-redshift Fanaroff-Riley type II radio sources: large-scale X-ray environment. *MNRAS*, 381:1109–1126.

Best, P. N. (2004). The environmental dependence of radio-loud AGN activity and star formation in the 2dFGRS. *MNRAS*, 351:70–82.

Best, P. N. and Heckman, T. M. (2012). On the fundamental dichotomy in the local radio-AGN population: accretion, evolution and host galaxy properties. *MNRAS*, 421:1569–1582.

Best, P. N., Ker, L. M., Simpson, C., Rigby, E. E., and Sabater, J. (2014). The cosmic evolution of radio-AGN feedback to z = 1. *MNRAS*, 445:955–969.

Bharadwaj, V., Reiprich, T. H., Lovisari, L., and Eckmiller, H. J. (2015). Extending the L_X - T relation from clusters to groups. Impact of cool core nature, AGN feedback, and selection effects. *A&A*, 573:A75.

Birkinshaw, M. and Worrall, D. M. (1993). The X-ray structure and spectrum of NGC 6251. *ApJ*, 412:568–585.

Bîrzan, L., McNamara, B. R., Nulsen, P. E. J., Carilli, C. L., and Wise, M. W. (2008). Radiative Efficiency and Content of Extragalactic Radio Sources: Toward a Universal Scaling Relation between Jet Power and Radio Power. *ApJ*, 686:859–880.

Bîrzan, L., Rafferty, D. A., McNamara, B. R., Wise, M. W., and Nulsen, P. E. J. (2004). A Systematic Study of Radio-induced X-Ray Cavities in Clusters, Groups, and Galaxies. *ApJ*, 607:800–809.

Blandford, R. D. and Znajek, R. L. (1977). Electromagnetic extraction of energy from Kerr black holes. *MNRAS*, 179:433–456.

Böhringer, H., Dolag, K., and Chon, G. (2012). Modelling self-similar appearance of galaxy clusters in X-rays. *A&A*, 539:A120.

Bolton, J. G., Stanley, G. J., and Slee, O. B. (1949). Positions of Three Discrete Sources of Galactic Radio-Frequency Radiation. *Nature*, 164:101–102.

Bondi, H. (1952). On spherically symmetrical accretion. *MNRAS*, 112:195.

Braito, V., Reeves, J. N., Sambruna, R. M., and Gofford, J. (2011). Evidence for a circumnuclear and ionized absorber in the X-ray obscured broad-line radio galaxy 3C 445. *MNRAS*, 414:2739–2750.

Brunetti, G. (2000). Anisotropic inverse Compton scattering from the trans-relativistic to the ultra-relativistic regime and application to the radio galaxies. *Astropart. Phys.*, 13:107–125.

Bryant, J. J. and Hunstead, R. W. (2002). SPIRAL observations of the radio galaxy MRC B1733-565. *MNRAS*, 337:861–868.

Burbidge, G. R. (1956). On Synchrotron Radiation from Messier 87. *ApJ*, 124:416.

Buttiglione, S., Capetti, A., Celotti, A., Axon, D. J., Chiaberge, M., Macchetto, F. D., and Sparks, W. B. (2009). An optical spectroscopic survey of the 3CR sample of radio galaxies with z < 0.3. I. Presentation of the data. *A&A*, 495:1033–1060.

Canvin, J. R. and Laing, R. A. (2004). Relativistic models of two low-luminosity radio jets: B2 0326+39and B2 1553+24. *MNRAS*, 350:1342–1365.

Cavagnolo, K. W., McNamara, B. R., Nulsen, P. E. J., Carilli, C. L., Jones, C., and Bîrzan, L. (2010). A Relationship Between AGN Jet Power and Radio Power. *ApJ*, 720:1066–1072.

Cavaliere, A. and Fusco-Femiano, R. (1976). X-rays from hot plasma in clusters of galaxies. *A&A*, 49:137–144.

Chen, R., Peng, B., Strom, R. G., and Wei, J. (2011a). Group galaxies around giant radio galaxy NGC 6251. *MNRAS*, 412:2433–2444.

Chen, R., Peng, B., Strom, R. G., and Wei, J. (2012). Group of galaxies around the giant radio galaxy 4C 73.08. *MNRAS*, 422:3004–3009.

Chen, R., Peng, B., Strom, R. G., Wei, J., and Zhao, Y. (2011b). Giant radio galaxy DA 240 group: content and environment. *A&A*, 529:A5.

Chen, Y., Reiprich, T. H., Böhringer, H., Ikebe, Y., and Zhang, Y.-Y. (2007). Statistics of X-ray observables for the cooling-core and non-cooling core galaxy clusters. *A&A*, 466:805–812.

Chen, Y.-Y., Zhang, X., Xiong, D., and Yu, X. (2015). Black Hole Mass, Jet Power, and Accretion in AGNs. *AJ*, 150:8.

Croston, J. (2007). The environmental and epoch dependence of radio-loud AGN feedback. XMM-Newton Proposal.

Croston, J. (2009). The environmental and epoch dependence of radio-loud AGN feedback. Chandra Proposal.

Croston, J. H., Birkinshaw, M., Hardcastle, M. J., and Worrall, D. M. (2004). X-ray emission from the nuclei, lobes and hot-gas environments of two FR II radio galaxies. *MNRAS*, 353:879–889.

Croston, J. H. and Hardcastle, M. J. (2014). The particle content of low-power radio galaxies in groups and clusters. *MNRAS*, 438:3310–3321.

Croston, J. H., Hardcastle, M. J., and Birkinshaw, M. (2005a). Evidence for radio-source heating of groups. *MNRAS*, 357:279–294.

Croston, J. H., Hardcastle, M. J., Birkinshaw, M., Worrall, D. M., and Laing, R. A. (2008a). An XMM-Newton study of the environments, particle content and impact of low-power radio galaxies. *MNRAS*, 386:1709–1728.

Croston, J. H., Hardcastle, M. J., Harris, D. E., Belsole, E., Birkinshaw, M., and Worrall, D. M. (2005b). An X-Ray Study of Magnetic Field Strengths and Particle Content in the Lobes of FR II Radio Sources. *ApJ*, 626:733–747.

Croston, J. H., Hardcastle, M. J., Mingo, B., Evans, D. A., Dicken, D., Morganti, R., and Tadhunter, C. N. (2011). A Large-scale Shock Surrounding a Powerful Radio Galaxy? *ApJ*, 734:L28.

Croston, J. H., Kraft, R. P., Hardcastle, M. J., Birkinshaw, M., Worrall, D. M., Nulsen, P. E. J., Penna, R. F., Sivakoff, G. R., Jordán, A., Brassington, N. J., Evans, D. A., Forman, W. R., Gilfanov, M., Goodger, J. L., Harris, W. E., Jones, C., Juett, A. M., Murray, S. S., Raychaudhury, S., Sarazin, C. L., Voss, R., and Woodley, K. A. (2009). High-energy particle acceleration at the radio-lobe shock of Centaurus A. *MNRAS*, 395:1999–2012.

Croston, J. H., Pratt, G. W., Böhringer, H., Arnaud, M., Pointecouteau, E., Ponman, T. J., Sanderson, A. J. R., Temple, R. F., Bower, R. G., and Donahue, M. (2008b). Galaxy-cluster gas-density distributions of the representative XMM-Newton cluster structure survey (REXCESS). *A&A*, 487:431–443.

Croton, D. J., Springel, V., White, S. D. M., De Lucia, G., Frenk, C. S., Gao, L., Jenkins, A., Kauffmann, G., Navarro, J. F., and Yoshida, N. (2006). The many lives of active galactic nuclei: cooling flows, black holes and the luminosities and colours of galaxies. *MNRAS*, 365:11–28.

Daly, R. A. (2016). Spin Properties of Supermassive Black Holes with Powerful Outflows. *ArXiv e-prints*.

Daly, R. A. and Sprinkle, T. B. (2014). Black hole spin properties of 130 AGN. *MNRAS*, 438:3233–3242.

Davis, J. E. (2001). Event Pileup in Charge-coupled Devices. *ApJ*, 562:575–582.

Davis, J. E. (2007). Pile-up Fractions and Count Rates. `http://cxc.harvard.edu/csc/memos/files/Davis_pileup.pdf`.

de Koff, S., Best, P., Baum, S. A., Sparks, W., Röttgering, H., Miley, G., Golombek, D., Macchetto, F., and Martel, A. (2000). The Dust-Radio Connection in 3CR Radio Galaxies. *ApJS*, 129:33–59.

Dicken, D., Tadhunter, C., Morganti, R., Buchanan, C., Oosterloo, T., and Axon, D. (2008). The Origin of the Infrared Emission in Radio Galaxies. I. New Mid- to Far-Infrared and Radio Observations of the 2 Jy Sample. *ApJ*, 678:712–728.

Dickey, J. M. and Lockman, F. J. (1990). H I in the Galaxy. *ARA&A*, 28:215–261.

Duffy, R. T., Worrall, D. M., Birkinshaw, M., and Kraft, R. P. (2016). Buoyancy-driven inflow to a relic cold core: the gas belt in radio galaxy 3C 386. *MNRAS*, 459:4508–4517.

Dunn, R. J. H. and Fabian, A. C. (2006). Investigating AGN heating in a sample of nearby clusters. *MNRAS*, 373:959–971.

Dunn, R. J. H., Fabian, A. C., and Taylor, G. B. (2005). Radio bubbles in clusters of galaxies. *MNRAS*, 364:1343–1353.

Eales, S., Rawlings, S., Law-Green, D., Cotter, G., and Lacy, M. (1997). A first sample of faint radio sources with virtually complete redshifts. I - Infrared images, the Hubble diagram and the alignment effect. *MNRAS*, 291:593.

Eckmiller, H. J., Hudson, D. S., and Reiprich, T. H. (2011). Testing the low-mass end of X-ray scaling relations with a sample of Chandra galaxy groups. *A&A*, 535:A105.

Evans, D. A., Fong, W.-F., Hardcastle, M. J., Kraft, R. P., Lee, J. C., Worrall, D. M., Birkinshaw, M., Croston, J. H., and Muxlow, T. W. B. (2008). A Radio through X-Ray Study of the Jet/Companion-Galaxy Interaction in 3C 321. *ApJ*, 675:1057–1066.

Evans, D. A., Hardcastle, M. J., Croston, J. H., Worrall, D. M., and Birkinshaw, M. (2005). Chandra and XMM-Newton observations of NGC 6251. *MNRAS*, 359:363–382.

Fabian, A. C., Sanders, J. S., Allen, S. W., Crawford, C. S., Iwasawa, K., Johnstone, R. M., Schmidt, R. W., and Taylor, G. B. (2003). A deep Chandra observation of the Perseus cluster: shocks and ripples. *MNRAS*, 344:L43–L47.

Falder, J. T., Stevens, J. A., Jarvis, M. J., Hardcastle, M. J., Lacy, M., McLure, R. J., Hatziminaoglou, E., Page, M. J., and Richards, G. T. (2010). The environments of z $\sim$ 1 active galactic nuclei at 3.6μm. *MNRAS*, 405:347–358.

Fanaroff, B. L. and Riley, J. M. (1974). The morphology of extragalactic radio sources of high and low luminosity. *MNRAS*, 167:31P–36P.

Feigelson, E. D. and Nelson, P. I. (1985). Statistical methods for astronomical data with upper limits. I - Univariate distributions. *ApJ*, 293:192–206.

Fernandes, C. A. C., Jarvis, M. J., Martínez-Sansigre, A., Rawlings, S., Afonso, J., Hardcastle, M. J., Lacy, M., Stevens, J. A., and Vardoulaki, E. (2015). Black hole masses, accretion rates and hot- and cold-mode accretion in radio galaxies at z $\sim$ 1. *MNRAS*, 447:1184–1203.

Forman, W., Nulsen, P., Heinz, S., Owen, F., Eilek, J., Vikhlinin, A., Markevitch, M., Kraft, R., Churazov, E., and Jones, C. (2005). Reflections of Active Galactic Nucleus Outbursts in the Gaseous Atmosphere of M87. *ApJ*, 635:894–906.

Francis, P. J. and Wills, B. J. (1999). Introduction to Principal Components Analysis. In Ferland, G. and Baldwin, J., editors, *Quasars and Cosmology*, volume 162 of *Astronomical Society of the Pacific Conference Series*, page 363.

Frank, K. A., Peterson, J. R., Andersson, K., Fabian, A. C., and Sanders, J. S. (2013). Characterization of Intracluster Medium Temperature Distributions of 62 Galaxy Clusters with XMM-Newton. *ApJ*, 764:46.

Fujita, Y., Kawakatu, N., and Shlosman, I. (2014). AGN jet power and feedback controlled by Bondi accretion in brightest cluster galaxies. *ArXiv e-prints*.

Gallimore, J. F., Axon, D. J., O'Dea, C. P., Baum, S. A., and Pedlar, A. (2006). A Survey of Kiloparsec-Scale Radio Outflows in Radio-Quiet Active Galactic Nuclei. *AJ*, 132:546–569.

Garofalo, D., Evans, D. A., and Sambruna, R. M. (2010). The evolution of radio-loud active galactic nuclei as a function of black hole spin. *MNRAS*, 406:975–986.

Gaspari, M., Melioli, C., Brighenti, F., and D'Ercole, A. (2011). The dance of heating and cooling in galaxy clusters: three-dimensional simulations of self-regulated active galactic nuclei outflows. *MNRAS*, 411:349–372.

Gaspari, M., Ruszkowski, M., and Oh, S. P. (2013). Chaotic cold accretion on to black holes. *MNRAS*, 432:3401–3422.

Gaspari, M., Ruszkowski, M., and Sharma, P. (2012). Cause and Effect of Feedback: Multiphase Gas in Cluster Cores Heated by AGN Jets. *ApJ*, 746:94.

Gendre, M. A., Best, P. N., Wall, J. V., and Ker, L. M. (2013). The relation between morphology, accretion modes and environmental factors in local radio AGN. *MNRAS*, 430:3086–3101.

Gitti, M., Brighenti, F., and McNamara, B. R. (2012). Evidence for AGN Feedback in Galaxy Clusters and Groups. *Advances in Astronomy*, 950641.

Gizani, N. A. B. and Leahy, J. P. (2004). A multiband study of Hercules A - I. ROSAT observations of the intracluster medium. *MNRAS*, 350:865–878.

Gliozzi, M., Foschini, L., Sambruna, R. M., and Tavecchio, F. (2008). The polyhedral nature of LINERs: an XMM-Newton view of LINERs in radio galaxies. *A&A*, 478:723–737.

Godfrey, L. E. H. and Shabala, S. S. (2013). AGN Jet Kinetic Power and the Energy Budget of Radio Galaxy Lobes. *ApJ*, 767:12.

Godfrey, L. E. H. and Shabala, S. S. (2016). Mutual distance dependence drives the observed jet-power-radio-luminosity scaling relations in radio galaxies. *MNRAS*, 456:1172–1184.

Greenstein, J. L. and Matthews, T. A. (1963). Redshift of the Radio Source 3C 48. *AJ*, 68:279.

Grimberg, B. I., Sadler, E. M., and Simkin, S. M. (1999). Extended Emission Line Gas in Radio Galaxies: PKS 0349-27. *ApJ*, 521:121–133.

Gürkan, G., Hardcastle, M. J., and Jarvis, M. J. (2014). The Wide-field Infrared Survey Explorer properties of complete samples of radio-loud active galactic nucleus. *MNRAS*, 438:1149–1161.

Gutierrez, K. and Krawczynski, H. (2005). The Off-Axis Galaxy Cluster Merger A115. *ApJ*, 619:161–168.

Hardcastle, M. J. (2004). B_{gg} revisited: The environments of low-excitation radio galaxies and unified models. *A&A*, 414:927–929.

Hardcastle, M. J., Birkinshaw, M., Cameron, R. A., Harris, D. E., Looney, L. W., and Worrall, D. M. (2002a). Magnetic Field Strengths in the Hot Spots and Lobes of Three Powerful Fanaroff-Riley Type II Radio Sources. *ApJ*, 581:948–973.

Hardcastle, M. J., Birkinshaw, M., and Worrall, D. M. (1998a). Magnetic field strengths in the hotspots of 3C 33 and 111. *MNRAS*, 294:615.

Hardcastle, M. J., Birkinshaw, M., and Worrall, D. M. (2001). Chandra observations of the X-ray jet in 3C 66B. *MNRAS*, 326:1499–1507.

Hardcastle, M. J., Ching, J. H. Y., Virdee, J. S., Jarvis, M. J., Croom, S. M., Sadler, E. M., Mauch, T., Smith, D. J. B., Stevens, J. A., Baes, M., Baldry, I. K., Brough, S., Cooray, A., Dariush, A., De Zotti, G., Driver, S., Dunne, L., Dye, S., Eales, S., Hopwood, R., Liske, J., Maddox, S., Michałowski, M. J., Rigby, E. E., Robotham, A. S. G., Steele, O., Thomas, D., and Valiante, E. (2013). Herschel-ATLAS/GAMA:

a difference between star formation rates in strong-line and weak-line radio galaxies. *MNRAS*, 429:2407–2424.

Hardcastle, M. J. and Croston, J. H. (2010). Searching for the inverse-Compton emission from bright cluster-centre radio galaxies. *MNRAS*, 404:2018–2027.

Hardcastle, M. J., Evans, D. A., and Croston, J. H. (2006). The X-ray nuclei of intermediate-redshift radio sources. *MNRAS*, 370:1893–1904.

Hardcastle, M. J., Evans, D. A., and Croston, J. H. (2007a). Hot and cold gas accretion and feedback in radio-loud active galaxies. *MNRAS*, 376:1849–1856.

Hardcastle, M. J., Harris, D. E., Worrall, D. M., and Birkinshaw, M. (2004). The Origins of X-Ray Emission from the Hot Spots of FR II Radio Sources. *ApJ*, 612:729–748.

Hardcastle, M. J., Kraft, R. P., Worrall, D. M., Croston, J. H., Evans, D. A., Birkinshaw, M., and Murray, S. S. (2007b). The Interaction between Radio Lobes and Hot Gas in the Nearby Radio Galaxies 3C 285 and 3C 442A. *ApJ*, 662:166–181.

Hardcastle, M. J. and Krause, M. G. H. (2013). Numerical modelling of the lobes of radio galaxies in cluster environments. *MNRAS*, 430:174–196.

Hardcastle, M. J., Massaro, F., Harris, D. E., Baum, S. A., Bianchi, S., Chiaberge, M., Morganti, R., O'Dea, C. P., and Siemiginowska, A. (2012). The nature of the jet-driven outflow in the radio galaxy 3C 305. *MNRAS*, 424:1774–1789.

Hardcastle, M. J., Sakelliou, I., and Worrall, D. M. (2005). A Chandra and XMM-Newton study of the wide-angle tail radio galaxy 3C465. *MNRAS*, 359:1007–1021.

Hardcastle, M. J. and Worrall, D. M. (2000). The environments of FRII radio sources. *MNRAS*, 319:562–572.

Hardcastle, M. J., Worrall, D. M., and Birkinshaw, M. (1998b). Dynamics of the radio galaxy 3C449. *MNRAS*, 296:1098–1104.

Hardcastle, M. J., Worrall, D. M., Birkinshaw, M., Laing, R. A., and Bridle, A. H. (2002b). A Chandra observation of the X-ray environment and jet of 3C 31. *MNRAS*, 334:182–192.

Harvanek, M., Ellingson, E., Stocke, J. T., and Rhee, G. (2001). A Study of 3CR Radio Galaxies from z =0.15 to z =0.65. I. Evidence for an Evolutionary Relationship Between Quasars and Radio Galaxies. *AJ*, 122:2874–2892.

Harwood, J. J., Croston, J. H., Intema, H. T., Stewart, A. J., Ineson, J., Hardcastle, M. J., Godfrey, L., Best, P., Brienza, M., Heesen, V., Mahony, E. K., Morganti,

R., Murgia, M., Orrú, E., Röttgering, H., Shulevski, A., and Wise, M. W. (2016). FR II radio galaxies at low frequencies - I. Morphology, magnetic field strength and energetics. *MNRAS*, 458:4443–4455.

Harwood, J. J., Hardcastle, M. J., and Croston, J. H. (2015). Spectral ageing in the lobes of cluster-centre FR II radio galaxies. *MNRAS*, 454:3403–3422.

Harwood, J. J., Hardcastle, M. J., Croston, J. H., and Goodger, J. L. (2013). Spectral ageing in the lobes of FR-II radio galaxies: new methods of analysis for broad-band radio data. *MNRAS*, 435:3353–3375.

Hatch, N. A., Wylezalek, D., Kurk, J. D., Stern, D., De Breuck, C., Jarvis, M. J., Galametz, A., Gonzalez, A. H., Hartley, W. G., Mortlock, A., Seymour, N., and Stevens, J. A. (2014). Why z $>$ 1 radio-loud galaxies are commonly located in proto-clusters. *MNRAS*, 445:280–289.

Heavens, A. F. and Meisenheimer, K. (1987). Particle acceleration in extragalactic sources - The role of synchrotron losses in determining the spectrum. *MNRAS*, 225:335–353.

Heckman, T. M. and Best, P. N. (2014). The Coevolution of Galaxies and Supermassive Black Holes: Insights from Surveys of the Contemporary Universe. *ARA&A*, 52:589–660.

Heinz, S. (2003). The interaction of relativistic jets with their environment. *New Astronomy Reviews*, 47:565–567.

Helsdon, S. F. and Ponman, T. J. (2000). The intragroup medium in loose groups of galaxies. *MNRAS*, 315:356–370.

Herbert, P. D. Jarvis, M. J., J., M., Willott, C. J., Hardcastle, M. J., Rawlings, S., Hill, G. J., and Dunlop, J, S. (2015). The environments of z$\sim$0.5 radio galaxies. Submitted to MNRAS.

Herbert, P. D., Jarvis, M. J., Willott, C. J., McLure, R. J., Mitchell, E., Rawlings, S., Hill, G. J., and Dunlop, J. S. (2010). Evidence of different star formation histories for high- and low-luminosity radio galaxies. *MNRAS*, 406:1841–1847.

Hill, G. J. and Lilly, S. J. (1991). A change in the cluster environments of radio galaxies with cosmic epoch. *ApJ*, 367:1–18.

Hill, G. J. and Rawlings, S. (2003). The TOOT survey: status and early results. *NewAR*, 47:373–377.

Hine, R. G. and Longair, M. S. (1979). Optical spectra of 3CR radio galaxies. *MNRAS*, 188:111–130.

Hlavacek-Larrondo, J., Fabian, A. C., Edge, A. C., Ebeling, H., Sanders, J. S., Hogan, M. T., and Taylor, G. B. (2012). Extreme AGN feedback in the MAssive Cluster Survey: a detailed study of X-ray cavities at z>0.3. *MNRAS*, 421:1360–1384.

Hobson, M. P. and Baldwin, J. E. (2004). Markov-Chain Monte Carlo Approach to the Design of Multilayer Thin-Film Optical Coatings. *ApOpt*, 43:2651–2660.

Hodges-Kluck, E. J., Reynolds, C. S., Cheung, C. C., and Miller, M. C. (2010). The Chandra View of Nearby X-Shaped Radio Galaxies. *ApJ*, 710:1205–1227.

Hopkins, P. F., Hernquist, L., Cox, T. J., and Kereš, D. (2008). A Cosmological Framework for the Co-Evolution of Quasars, Supermassive Black Holes, and Elliptical Galaxies. I. Galaxy Mergers and Quasar Activity. *ApJS*, 175:356–389.

Ineson, J., Croston, J. H., Hardcastle, M. J., Kraft, R. P., Evans, D. A., and Jarvis, M. (2013). Radio-loud Active Galactic Nucleus: Is There a Link between Luminosity and Cluster Environment? *ApJ*, 770:136.

Ineson, J., Croston, J. H., Hardcastle, M. J., Kraft, R. P., Evans, D. A., and Jarvis, M. (2015). The link between accretion mode and environment in radio-loud active galaxies. *MNRAS*, 453:2682–2706.

Inskip, K. J., Tadhunter, C. N., Morganti, R., Holt, J., Ramos Almeida, C., and Dicken, D. (2010). A near-IR study of the host galaxies of 2 Jy radio sources at $0.03 <\sim z <\sim 0.5$ - I. The data. *MNRAS*, 407:1739–1766.

Ishibashi, W. and Fabian, A. C. (2012). Active galactic nucleus feedback and triggering of star formation in galaxies. *MNRAS*, 427:2998–3005.

Isobe, N., Makishima, K., Tashiro, M., and Hong, S. (2005). The XMM-Newton Detection of Diffuse Inverse Compton X-Rays from Lobes of the FR II Radio Galaxy 3C 98. *ApJ*, 632:781–787.

Isobe, N., Tashiro, M., Makishima, K., Iyomoto, N., Suzuki, M., Murakami, M. M., Mori, M., and Abe, K. (2002). A Chandra Detection of Diffuse Hard X-Ray Emission Associated with the Lobes of the Radio Galaxy 3C 452. *ApJ*, 580:L111–L115.

Isobe, T., Feigelson, E. D., and Nelson, P. I. (1986). Statistical methods for astronomical data with upper limits. II - Correlation and regression. *ApJ*, 306:490–507.

Jansky, K. G. (1935). A note on the source of interstellar interference. *Proc. IRE*, 21:1158.

Janssen, R. M. J., Röttgering, H. J. A., Best, P. N., and Brinchmann, J. (2012). The triggering probability of radio-loud AGN. A comparison of high and low excitation radio galaxies in hosts of different colors. *A&A*, 541:A62.

Jennison, R. C. and Das Gupta, M. K. (1953). Fine Structure of the Extra-terrestrial Radio Source Cygnus I. *Nature*, 172:996–997.

Jones, C. and Forman, W. (1984). The structure of clusters of galaxies observed with Einstein. *ApJ*, 276:38–55.

Joshi, S. A., Nandi, S., Saikia, D. J., Ishwara-Chandra, C. H., and Konar, C. (2011). A radio study of the double-double radio galaxy 3C293. *MNRAS*, 414:1397–1404.

Kaastra, J. S., Lieu, R., Mittaz, J. P. D., Bleeker, J. A. M., Mewe, R., Colafrancesco, S., and Lockman, F. J. (1999). High- and Low-Energy Nonthermal X-Ray Emission from the Abell 2199 Cluster of Galaxies. *ApJ*, 519:L119–L122.

Kahn, F. D. and Woltjer, L. (1959). Intergalactic Matter and the Galaxy. *ApJ*, 130:705.

Karovska, M., Fabbiano, G., Nicastro, F., Elvis, M., Kraft, R. P., and Murray, S. S. (2002). X-Ray Arc Structures in Chandra Images of NGC 5128 (Centaurus A). *ApJ*, 577:114–119.

Kataoka, J. and Stawarz, Ł. (2005). X-Ray Emission Properties of Large-Scale Jets, Hot Spots, and Lobes in Active Galactic Nuclei. *ApJ*, 622:797–810.

Kauffmann, G., White, S. D. M., Heckman, T. M., Ménard, B., Brinchmann, J., Charlot, S., Tremonti, C., and Brinkmann, J. (2004). The environmental dependence of the relations between stellar mass, structure, star formation and nuclear activity in galaxies. *MNRAS*, 353:713–731.

Kellermann, K. I. (2015). The road to quasars. In Massaro, F., Cheung, C. C., Lopez, E., and Siemiginowska, A., editors, *IAU Symposium*, volume 313 of *IAU Symposium*, pages 190–195.

Kellermann, K. I., Sramek, R., Schmidt, M., Shaffer, D. B., and Green, R. (1989). VLA observations of objects in the Palomar Bright Quasar Survey. *AJ*, 98:1195–1207.

King, I. (1962). The structure of star clusters. I. an empirical density law. *AJ*, 67:471.

King, I. R. (1972). Density Data and Emission Measure for a Model of the Coma Cluster. *ApJ*, 174:L123.

Komossa, S. and Böhringer, H. (1999). X-ray study of the NGC 383 group of galaxies and the source 1E 0104+3153. *A&A*, 344:755–766.

Konar, C., Hardcastle, M. J., Croston, J. H., and Saikia, D. J. (2009). The dynamics of the giant radio galaxy 3C457. *MNRAS*, 400:480–491.

Kraft, R. P., Azcona, J., Forman, W. R., Hardcastle, M. J., Jones, C., and Murray, S. S. (2006). The Hot Gas Environment of the Radio Galaxy 3C 388: Quenching the Accumulation of Cool Gas in a Cluster Core by a Nuclear Outburst. *ApJ*, 639:753–760.

Kraft, R. P., Birkinshaw, M., Hardcastle, M. J., Evans, D. A., Croston, J. H., Worrall, D. M., and Murray, S. S. (2007). A Radio through X-Ray Study of the Hot Spots, Active Nucleus, and Environment of the Nearby FR II Radio Galaxy 3C 33. *ApJ*, 659:1008–1021.

Kraft, R. P., Birkinshaw, M., Nulsen, P. E. J., Worrall, D. M., Croston, J. H., Forman, W. R., Hardcastle, M. J., Jones, C., and Murray, S. S. (2012). An Active Galactic Nucleus Driven Shock in the Intracluster Medium around the Radio Galaxy 3C 310. *ApJ*, 749:19.

Kraft, R. P., Vázquez, S. E., Forman, W. R., Jones, C., Murray, S. S., Hardcastle, M. J., Worrall, D. M., and Churazov, E. (2003). X-Ray Emission from the Hot Interstellar Medium and Southwest Radio Lobe of the Nearby Radio Galaxy Centaurus A. *ApJ*, 592:129–146.

Labiano, A., García-Burillo, S., Combes, F., Usero, A., Soria-Ruiz, R., Tremblay, G., Neri, R., Fuente, A., Morganti, R., and Oosterloo, T. (2013). Fueling the central engine of radio galaxies. II. The footprints of AGN feedback on the ISM of 3C 236. *A&A*, 549:A58.

Lacy, M., Rawlings, S., Hill, G. J., Bunker, A. J., Ridgway, S. E., and Stern, D. (1999). Optical spectroscopy of two overlapping, flux-density-limited samples of radio sources in the North Ecliptic Cap, selected at 38 and 151MHz. *MNRAS*, 308:1096–1116.

Laing, R. A., Jenkins, C. R., Wall, J. V., and Unger, S. W. (1994). Spectrophotometry of a Complete Sample of 3CR Radio Sources: Implications for Unified Models. In Bicknell, G. V., Dopita, M. A., and Quinn, P. J., editors, *The Physics of Active Galaxies*, volume 54 of *Astronomical Society of the Pacific Conference Series*, page 201.

Laing, R. A., Riley, J. M., and Longair, M. S. (1983). Bright radio sources at 178 MHz - Flux densities, optical identifications and the cosmological evolution of powerful radio galaxies. *MNRAS*, 204:151–187.

Lanz, L., Ogle, P. M., Evans, D., Appleton, P. N., Guillard, P., and Emonts, B. (2015). Jet-ISM Interaction in the Radio Galaxy 3C 293: Jet-driven Shocks Heat ISM to Power X-Ray and Molecular H_2 Emission. *ApJ*, 801:17.

Lawrence, C. R., Zucker, J. R., Readhead, A. C. S., Unwin, S. C., Pearson, T. J., and Xu, W. (1996). Optical Spectra of a Complete Sample of Radio Sources. I. The Spectra. *ApJS*, 107:541.

Ledlow, M. J., Voges, W., Owen, F. N., and Burns, J. O. (2003). The X-Ray Properties of Nearby Abell Clusters from the ROSAT All-Sky Survey: The Sample and Correlations with Optical Properties. *AJ*, 126:2740–2751.

Longair, M. S. (2011). *High Energy Astrophysics*. Cambridge University Press, Cambridge, UK.

Longair, M. S. and Seldner, M. (1979). The clustering of galaxies about extragalactic radio sources. *MNRAS*, 189:433–453.

Lumb, D. H., Warwick, R. S., Page, M., and De Luca, A. (2002). X-ray background measurements with XMM-Newton EPIC. *A&A*, 389:93–105.

Magliocchetti, M. and Brüggen, M. (2007). The interplay between radio galaxies and cluster environment. *MNRAS*, 379:260–274.

Magorrian, J., Tremaine, S., Richstone, D., Bender, R., Bower, G., Dressler, A., Faber, S. M., Gebhardt, K., Green, R., Grillmair, C., Kormendy, J., and Lauer, T. (1998). The Demography of Massive Dark Objects in Galaxy Centers. *AJ*, 115:2285–2305.

Mahony, E. K., Morganti, R., Emonts, B. H. C., Oosterloo, T. A., and Tadhunter, C. (2013). The location and impact of jet-driven outflows of cold gas: the case of 3C 293. *MNRAS*, 435:L58–L62.

Majerowicz, S., Neumann, D. M., and Reiprich, T. H. (2002). XMM-NEWTON observation of Abell 1835: Temperature, mass and gas mass fraction profiles. *A&A*, 394:77–87.

Mannering, E., Worrall, D. M., and Birkinshaw, M. (2013). Galaxy gas ejection in radio galaxies: the case of 3C 35. *MNRAS*, 431:858–873.

Markevitch, M. (2002). On the discrepancy between Chandra and XMM temperature profiles for A1835. *ArXiv Astrophysics e-prints, astro-ph/0205333*.

Markevitch, M., Bautz, M. W., Biller, B., Butt, Y., Edgar, R., Gaetz, T., Garmire, G., Grant, C. E., Green, P., Juda, M., Plucinsky, P. P., Schwartz, D., Smith, R., Vikhlinin, A., Virani, S., Wargelin, B. J., and Wolk, S. (2003). Chandra Spectra of the Soft X-Ray Diffuse Background. *ApJ*, 583:70–84.

Matthews, T. A., Morgan, W. W., and Schmidt, M. (1964). A Discussion of Galaxies Indentified with Radio Sources. *ApJ*, 140:35.

Maughan, B. J. (2014). PICACS: self-consistent modelling of galaxy cluster scaling relations. *MNRAS*, 437:1171–1186.

McLure, R. J. and Dunlop, J. S. (2001). The cluster environments of powerful radio-loud and radio-quiet active galactic nuclei. *MNRAS*, 321:515–524.

McLure, R. J. and Dunlop, J. S. (2002). On the black hole-bulge mass relation in active and inactive galaxies. *MNRAS*, 331:795–804.

McLure, R. J., Willott, C. J., Jarvis, M. J., Rawlings, S., Hill, G. J., Mitchell, E., Dunlop, J. S., and Wold, M. (2004). A sample of radio galaxies spanning three decades in radio luminosity - I. The host galaxy properties and black hole masses. *MNRAS*, 351:347–361.

McNamara, B. R. and Nulsen, P. E. J. (2007). Heating Hot Atmospheres with Active Galactic Nuclei. *ARA&A*, 45:117–175.

Mezcua, M. and Prieto, M. A. (2014). Evidence of Parsec-scale Jets in Low-luminosity Active Galactic Nuclei. *ApJ*, 787:62.

Miller, N. A., Owen, F. N., Burns, J. O., Ledlow, M. J., and Voges, W. (1999). An X-Ray and Optical Investigation of the Environments around Nearby Radio Galaxies. *AJ*, 118:1988–2001.

Mingo, B., Hardcastle, M. J., Croston, J. H., Dicken, D., Evans, D. A., Morganti, R., and Tadhunter, C. (2014). An X-ray survey of the 2 Jy sample - I. Is there an accretion mode dichotomy in radio-loud AGN? *MNRAS*, 440:269–297.

Minkowski, R. (1960). A New Distant Cluster of Galaxies. *ApJ*, 132:908–910.

Mitchell, E. (2005). . PhD thesis, University of Oxford.

Mitchell, R. J., Culhane, J. L., Davison, P. J. N., and Ives, J. C. (1976). Ariel 5 observations of the X-ray spectrum of the Perseus Cluster. *MNRAS*, 175:29P–34P.

Mulchaey, J. S. (2000). X-ray Properties of Groups of Galaxies. *ARA&A*, 38:289–335.

Mulchaey, J. S., Davis, D. S., Mushotzky, R. F., and Burstein, D. (1993). Diffuse X-ray emission from the NGC 2300 group of galaxies - Implications for dark matter and galaxy evolution in small groups. *ApJ*, 404:L9–L12.

Muldrew, S. I., Croton, D. J., Skibba, R. A., Pearce, F. R., Ann, H. B., Baldry, I. K., Brough, S., Choi, Y.-Y., Conselice, C. J., Cowan, N. B., Gallazzi, A., Gray, M. E., Grützbauch, R., Li, I.-H., Park, C., Pilipenko, S. V., Podgorzec, B. J., Robotham, A. S. G., Wilman, D. J., Yang, X., Zhang, Y., and Zibetti, S. (2012). Measures of galaxy environment - I. What is 'environment'? *MNRAS*, 419:2670–2682.

Mullin, L. M. and Hardcastle, M. J. (2009). Bayesian inference of jet bulk-flow speeds in Fanaroff-Riley type II radio sources. *MNRAS*, 398:1989–2004.

Mullin, L. M., Riley, J. M., and Hardcastle, M. J. (2008). Observed properties of FRII quasars and radio galaxies at z $<$ 1.0. *MNRAS*, 390:595–621.

Narayan, R. and Yi, I. (1994). Advection-dominated accretion: A self-similar solution. *ApJ*, 428:L13–L16.

Nesvadba, N. P. H., Boulanger, F., Lehnert, M. D., Guillard, P., and Salome, P. (2011). Dense gas without star formation: the kpc-sized turbulent molecular disk in 3C 326 N. *A&A*, 536:L5.

Netzer, H. (2006). Active Galactic Nuclei: Basic Physics and Main Components. In Alloin, D., editor, *Physics of Active Galactic Nuclei at all Scales*, volume 693 of *Lecture Notes in Physics, Berlin Springer Verlag*, page 1.

Nevalainen, J., David, L., and Guainazzi, M. (2010). Cross-calibrating X-ray detectors with clusters of galaxies: an IACHEC study. *A&A*, 523:A22.

Nulsen, P. E. J., Hambrick, D. C., McNamara, B. R., Rafferty, D., Birzan, L., Wise, M. W., and David, L. P. (2005). The Powerful Outburst in Hercules A. *ApJ*, 625:L9–L12.

Nulsen, P. E. J., Li, Z., Forman, W. R., Kraft, R. P., Lal, D. V., Jones, C., Zhuravleva, I., Churazov, E., Sanders, J. S., Fabian, A. C., Johnson, R. E., and Murray, S. S. (2013). Deep Chandra Observations of A2199: The Interplay between Merger-induced Gas Motions and Nuclear Outbursts in a Cool Core Cluster. *ApJ*, 775:117.

O'Dea, C. P., Baum, S. A., Tremblay, G. R., Kharb, P., Cotton, W., and Perley, R. (2013). Hubble Space Telescope Observations of Dusty Filaments in Hercules A: Evidence for Entrainment. *ApJ*, 771:38.

Oke, J. B. and Sargent, W. L. W. (1968). The Nucleus of the Seyfert Galaxy NGC 4151. *ApJ*, 151:807.

Okuda, T., Kohno, K., Iguchi, S., and Nakanishi, K. (2005). Rotating Molecular Gas Associated with a Silhouette Disk at the Center of the Radio Galaxy 3C 31. *ApJ*, 620:673–679.

Owen, F. N. and Ledlow, M. J. (1994). The FRI/II Break and the Bivariate Luminosity Function in Abell Clusters of Galaxies. In Bicknell, G. V., Dopita, M. A., and Quinn, P. J., editors, *The Physics of Active Galaxies*, volume 54 of *Astronomical Society of the Pacific Conference Series*, page 319.

Perley, R. A., Bridle, A. H., and Willis, A. G. (1984). High-resolution VLA observations of the radio jet in NGC 6251. *ApJS*, 54:291–334.

Perucho, M., Martí, J.-M., Quilis, V., and Ricciardelli, E. (2014). Large-scale jets from active galactic nuclei as a source of intracluster medium heating: cavities and shocks. *MNRAS*, 445:1462–1481.

Peterson, J. R. and Fabian, A. C. (2006). X-ray spectroscopy of cooling clusters. *Phys. Rep.*, 427:1–39.

Peterson, J. R., Kahn, S. M., Paerels, F. B. S., Kaastra, J. S., Tamura, T., Bleeker, J. A. M., Ferrigno, C., and Jernigan, J. G. (2003). High-Resolution X-Ray Spectroscopic Constraints on Cooling-Flow Models for Clusters of Galaxies. *ApJ*, 590:207–224.

Pizzolato, F. and Soker, N. (2005). On the Nature of Feedback Heating in Cooling Flow Clusters. *ApJ*, 632:821–830.

Ponman, T. J. and Bertram, D. (1993). Hot gas and dark matter in a compact galaxy group. *Nature*, 363:51–54.

Ponman, T. J., Cannon, D. B., and Navarro, J. F. (1999). The thermal imprint of galaxy formation on X-ray clusters. *Nature*, 397:135–137.

Potter, W. J. and Cotter, G. (2013). Synchrotron and inverse-Compton emission from blazar jets - II. An accelerating jet model with a geometry set by observations of M87. *MNRAS*, 429:1189–1205.

Pratt, G. W., Arnaud, M., Piffaretti, R., Böhringer, H., Ponman, T. J., Croston, J. H., Voit, G. M., Borgani, S., and Bower, R. G. (2010). Gas entropy in a representative sample of nearby X-ray galaxy clusters (REXCESS): relationship to gas mass fraction. *A&A*, 511:A85.

Pratt, G. W., Arnaud, M., and Pointecouteau, E. (2006). Structure and scaling of the entropy in nearby galaxy clusters. *A&A*, 446:429–438.

Pratt, G. W., Croston, J. H., Arnaud, M., and Böhringer, H. (2009). Galaxy cluster X-ray luminosity scaling relations from a representative local sample (REXCESS). *A&A*, 498:361–378.

Prestage, R. M. and Peacock, J. A. (1988). The cluster environments of powerful radio galaxies. *MNRAS*, 230:131–160.

Prieto, M. A. and Zhao, H. (1997). The giant nebulae associated with 3C 227: emission-line profiles and kinematic modelling. *MNRAS*, 290:34–40.

Rafferty, D. A., McNamara, B. R., Nulsen, P. E. J., and Wise, M. W. (2006). The Feedback-regulated Growth of Black Holes and Bulges through Gas Accretion and Starbursts in Cluster Central Dominant Galaxies. *ApJ*, 652:216–231.

Ramos Almeida, C., Bessiere, P. S., Tadhunter, C. N., Inskip, K. J., Morganti, R., Dicken, D., González-Serrano, J. I., and Holt, J. (2013). The environments of luminous radio galaxies and type-2 quasars. *MNRAS*, 436:997–1016.

Ramos Almeida, C., Bessiere, P. S., Tadhunter, C. N., Pérez-González, P. G., Barro, G., Inskip, K. J., Morganti, R., Holt, J., and Dicken, D. (2012). Are luminous radio-loud active galactic nuclei triggered by galaxy interactions? *MNRAS*, 419:687–705.

Ramos Almeida, C., Tadhunter, C. N., Inskip, K. J., Morganti, R., Holt, J., and Dicken, D. (2011). The optical morphologies of the 2 Jy sample of radio galaxies: evidence for galaxy interactions. *MNRAS*, 410:1550–1576.

Rawlings, S., Eales, S., and Lacy, M. (2001). A sample of 6C radio sources with virtually complete redshifts - II. Optical spectroscopy. *MNRAS*, 322:523–535.

Read, A. M. and Ponman, T. J. (2003). The XMM-Newton EPIC background: Production of background maps and event files. *A&A*, 409:395–410.

Reber, G. (1940). Notes: Cosmic Static. *ApJ*, 91:621–624.

Rinn, A. S., Sambruna, R. M., and Gliozzi, M. (2005). An X-Ray View of Weak-Line Radio Galaxies/LINERs. *ApJ*, 621:167–175.

Russell, H. R., McNamara, B. R., Edge, A. C., Hogan, M. T., Main, R. A., and Vantyghem, A. N. (2013). Radiative efficiency, variability and Bondi accretion on to massive black holes: the transition from radio AGN to quasars in brightest cluster galaxies. *MNRAS*, 432:530–553.

Rybicki, G. B. and Lightman, A. P. (1979). *Radiative processes in astrophysics*. John Wiley & Sons, Inc., New York.

Sadun, A. C. and Morrison, P. (2002). Hercules A (3C 348): Phenomenology of an Unusual Active Galactic Nucleus. *AJ*, 123:2312–2320.

Salpeter, E. E. (1964). Accretion of Interstellar Matter by Massive Objects. *ApJ*, 140:796–800.

Sanders, J. S. and Fabian, A. C. (2007). A deeper X-ray study of the core of the Perseus galaxy cluster: the power of sound waves and the distribution of metals and cosmic rays. *MNRAS*, 381:1381–1399.

Sarazin, C. L. (1986). X-ray emission from clusters of galaxies. *Reviews of Modern Physics*, 58:1–115.

Schellenberger, G., Reiprich, T., and Lovisari, L. (2012). Individual mass determination of the HIFLUGCS Clusters. In Ness, J.-U., editor, *Galaxy Clusters as Giant Cosmic Laboratories*, page 54.

Schellenberger, G., Reiprich, T. H., Lovisari, L., Nevalainen, J., and David, L. (2015). XMM-Newton and Chandra cross-calibration using HIFLUGCS galaxy clusters . Systematic temperature differences and cosmological impact. *A&A*, 575:A30.

Scheuer, P. A. G. (1974). Models of extragalactic radio sources with a continuous energy supply from a central object. *MNRAS*, 166:513–528.

Schmidt, R. W., Allen, S. W., and Fabian, A. C. (2001). Chandra observations of the galaxy cluster Abell 1835. *MNRAS*, 327:1057–1070.

Seldner, M. and Peebles, P. J. E. (1978). Statistical analysis of catalogs of extragalactic objects. X - Clustering of 4C radio sources. *ApJ*, 225:7–20.

Shabala, S. S. and Godfrey, L. E. H. (2013). Size Dependence of the Radio-luminosity-Mechanical-power Correlation in Radio Galaxies. *ApJ*, 769:129.

Shakura, N. I. and Sunyaev, R. A. (1973). Black holes in binary systems. Observational appearance. *A&A*, 24:337–355.

Shelton, D. L. (2011). The X-ray Environments of Radio Galaxies. Master's thesis, University of Hertfordshire.

Shelton, D. L., Hardcastle, M. J., and Croston, J. H. (2011). The dynamics and environmental impact of 3C 452. *MNRAS*, 418:811–819.

Shields, G. A. (1999). A Brief History of Active Galactic Nuclei. *PASP*, 111:661.

Simionescu, A., Roediger, E., Nulsen, P. E. J., Brüggen, M., Forman, W. R., Böhringer, H., Werner, N., and Finoguenov, A. (2009). The large-scale shock in the cluster of galaxies Hydra A. *A&A*, 495:721–732.

Simpson, C., Ward, M., Clements, D. L., and Rawlings, S. (1996). Emission-line ratios in a radio-selected sample of active galactic nuclei. *MNRAS*, 281:509–521.

Smith, E. P., Heckman, T. M., Bothun, G. D., Romanishin, W., and Balick, B. (1986). On the nature of QSO host galaxies. *ApJ*, 306:64–89.

Smith, R. K., Brickhouse, N. S., Liedahl, D. A., and Raymond, J. C. (2001). Collisional Plasma Models with APEC/APED: Emission-Line Diagnostics of Hydrogen-like and Helium-like Ions. *ApJ*, 556:L91–L95.

Smolčić, V. (2009). The Radio AGN Population Dichotomy: Green Valley Seyferts Versus Red Sequence Low-Excitation Active Galactic Nuclei. *ApJ*, 699:L43–L47.

Snowden, S. L., Egger, R., Freyberg, M. J., McCammon, D., Plucinsky, P. P., Sanders, W. T., Schmitt, J. H. M. M., Trümper, J., and Voges, W. (1997). ROSAT Survey Diffuse X-Ray Background Maps. II. *ApJ*, 485:125–135.

Son, D., Woo, J.-H., Kim, S. C., Fu, H., Kawakatu, N., Bennert, V. N., Nagao, T., and Park, D. (2012). Accretion Properties of High- and Low-excitation Young Radio Galaxies. *ApJ*, 757:140.

Stott, J. P., Hickox, R. C., Edge, A. C., Collins, C. A., Hilton, M., Harrison, C. D., Romer, A. K., Rooney, P. J., Kay, S. T., Miller, C. J., Sahlén, M., Lloyd-Davies, E. J., Mehrtens, N., Hoyle, B., Liddle, A. R., Viana, P. T. P., McCarthy, I. G., Schaye, J., and Booth, C. M. (2012). The XMM Cluster Survey: the interplay between the brightest cluster galaxy and the intracluster medium via AGN feedback. *MNRAS*, 422:2213–2229.

Strom, R. G., Chen, R., Yang, J., and Peng, B. (2013). Structure and environment of the giant radio galaxy 4C 73.08. *MNRAS*, 430:2090–2096.

Strüder, L., Briel, U., Dennerl, K., Hartmann, R., Kendziorra, E., Meidinger, N., Pfeffermann, E., Reppin, C., Aschenbach, B., Bornemann, W., Bräuninger, H., Burkert, W., Elender, M., Freyberg, M., Haberl, F., Hartner, G., Heuschmann, F., Hippmann, H., Kastelic, E., Kemmer, S., Kettenring, G., Kink, W., Krause, N., Müller, S., Oppitz, A., Pietsch, W., Popp, M., Predehl, P., Read, A., Stephan, K. H., Stötter, D., Trümper, J., Holl, P., Kemmer, J., Soltau, H., Stötter, R., Weber, U., Weichert, U., von Zanthier, C., Carathanassis, D., Lutz, G., Richter, R. H., Solc, P., Böttcher, H., Kuster, M., Staubert, R., Abbey, A., Holland, A., Turner, M., Balasini, M., Bignami, G. F., La Palombara, N., Villa, G., Buttler, W., Gianini, F., Lainé, R., Lumb, D., and Dhez, P. (2001). The European Photon Imaging Camera on XMM-Newton: The pn-CCD camera. *A&A*, 365:L18–L26.

Sun, M. (2009). Every BCG with a Strong Radio Agn has an X-Ray Cool Core: Is the Cool Core-Noncool Core Dichotomy Too Simple? *ApJ*, 704:1586–1604.

Sun, M. (2012). Hot gas in galaxy groups: recent observations. *New J. Phys.*, 14(4):045004.

Tadhunter, C., Dicken, D., Morganti, R., Konyves, V., Ysard, N., Nesvadba, N., and Ramos Almeida, C. (2014). The dust masses of powerful radio galaxies: clues to the triggering of their activity. *MNRAS*, 445:L51–L55.

Tadhunter, C. N., Morganti, R., di Serego-Alighieri, S., Fosbury, R. A. E., and Danziger, I. J. (1993). Optical Spectroscopy of a Complete Sample of Southern 2-JY Radio Sources. *MNRAS*, 263:999.

Tasse, C., Best, P. N., Röttgering, H., and Le Borgne, D. (2008). Radio-loud AGN in the XMM-LSS field. II. A dichotomy in environment and accretion mode? *A&A*, 490:893–904.

Tombesi, F., Sambruna, R. M., Reeves, J. N., Braito, V., Ballo, L., Gofford, J., Cappi, M., and Mushotzky, R. F. (2010). Discovery of Ultra-fast Outflows in a Sample of Broad-line Radio Galaxies Observed with Suzaku. *ApJ*, 719:700–715.

Tremblay, G. R., O'Dea, C. P., Baum, S. A., Koekemoer, A. M., Sparks, W. B., de Bruyn, G., and Schoenmakers, A. P. (2010). Episodic Star Formation Coupled to Reignition of Radio Activity in 3C 236. *ApJ*, 715:172–185.

Tremblay, G. R., Quillen, A. C., Floyd, D. J. E., Noel-Storr, J., Baum, S. A., Axon, D., O'Dea, C. P., Chiaberge, M., Macchetto, F. D., Sparks, W. B., Miley, G. K., Capetti, A., Madrid, J. P., and Perlman, E. (2006). The Warped Nuclear Disk of Radio Galaxy 3C 449. *ApJ*, 643:101–111.

Urry, C. M. and Padovani, P. (1995). Unified Schemes for Radio-Loud Active Galactic Nuclei. *PASP*, 107:803.

van Breugel, W., Balick, B., Heckman, T., Miley, G., and Helfand, D. (1983). The peculiar radio galaxy 3C 433. *AJ*, 88:40–54.

van der Wolk, G., Barthel, P. D., Peletier, R. F., and Pel, J. W. (2010). Dust tori in radio galaxies. *A&A*, 511:A64.

Varano, S., Chiaberge, M., Macchetto, F. D., and Capetti, A. (2004). The nuclear radio-optical properties of intermediate-redshift FR II radio galaxies and quasars. *A&A*, 428:401–408.

Vikhlinin, A., Kravtsov, A., Forman, W., Jones, C., Markevitch, M., Murray, S. S., and Van Speybroeck, L. (2006). Chandra Sample of Nearby Relaxed Galaxy Clusters: Mass, Gas Fraction, and Mass-Temperature Relation. *ApJ*, 640:691–709.

Voit, G. M. and Donahue, M. (2015). Cooling Time, Freefall Time, and Precipitation in the Cores of ACCEPT Galaxy Clusters. *ApJ*, 799:L1.

Wall, J. V. and Peacock, J. A. (1985). Bright extragalactic radio sources at 2.7 GHz. III - The all-sky catalogue. *MNRAS*, 216:173–192.

Weil, K. and Roberts, D. H. (2014). Optical Spectroscopy of the Restarting Radio Galaxy 3C 219. In *American Astronomical Society Meeting Abstracts #224*, volume 224 of *American Astronomical Society Meeting Abstracts*, page 221.16.

Willott, C. J., Rawlings, S., Blundell, K. M., and Lacy, M. (1999). The emission line-radio correlation for radio sources using the 7C Redshift Survey. *MNRAS*, 309:1017–1033.

Willott, C. J., Rawlings, S., Jarvis, M. J., and Blundell, K. M. (2003). Near-infrared imaging and the K-z relation for radio galaxies in the 7C Redshift Survey. *MNRAS*, 339:173–188.

Wills, K. A., Morganti, R., Tadhunter, C. N., Robinson, T. G., and Villar-Martin, M. (2004). Emission lines and optical continuum in low-luminosity radio galaxies. *MNRAS*, 347:771–786.

Wilson, A. S. and Colbert, E. J. M. (1995). The difference between radio-loud and radio-quiet active galaxies. *ApJ*, 438:62–71.

Wilson, A. S., Smith, D. A., and Young, A. J. (2006). The Cavity of Cygnus A. *ApJ*, 644:L9–L12.

Wold, M., Lacy, M., Lilje, P. B., and Serjeant, S. (2000). Clustering of galaxies around radio quasars at $0.5 <= z <= 0.8$. *MNRAS*, 316:267–282.

Worrall, D. M. and Birkinshaw, M. (2000). X-Ray-emitting Atmospheres of B2 Radio Galaxies. *ApJ*, 530:719–732.

Worrall, D. M. and Birkinshaw, M. (2006). Multiwavelength Evidence of the Physical Processes in Radio Jets. In Alloin, D., editor, *Physics of Active Galactic Nuclei at all Scales*, volume 693 of *Lecture Notes in Physics, Berlin Springer Verlag*, page 39.

Worrall, D. M., Birkinshaw, M., Kraft, R. P., and Hardcastle, M. J. (2007). The Effect of a Chandra-measured Merger-related Gas Component on the Lobes of a Dead Radio Galaxy. *ApJ*, 658:L79–L82.

Worrall, D. M., Birkinshaw, M., Young, A. J., Momtahan, K., Fosbury, R. A. E., Morganti, R., Tadhunter, C. N., and Verdoes Kleijn, G. (2012). The jet-cloud interacting radio galaxy PKS B2152-699 - I. Structures revealed in new deep radio and X-ray observations. *MNRAS*, 424:1346–1362.

Wright, E. L., Eisenhardt, P. R. M., Mainzer, A. K., Ressler, M. E., Cutri, R. M., Jarrett, T., Kirkpatrick, J. D., Padgett, D., McMillan, R. S., Skrutskie, M., Stanford, S. A., Cohen, M., Walker, R. G., Mather, J. C., Leisawitz, D., Gautier, III, T. N.,

McLean, I., Benford, D., Lonsdale, C. J., Blain, A., Mendez, B., Irace, W. R., Duval, V., Liu, F., Royer, D., Heinrichsen, I., Howard, J., Shannon, M., Kendall, M., Walsh, A. L., Larsen, M., Cardon, J. G., Schick, S., Schwalm, M., Abid, M., Fabinsky, B., Naes, L., and Tsai, C.-W. (2010). The Wide-field Infrared Survey Explorer (WISE): Mission Description and Initial On-orbit Performance. *AJ*, 140:1868–1881.

Wylezalek, D., Galametz, A., Stern, D., Vernet, J., De Breuck, C., Seymour, N., Brodwin, M., Eisenhardt, P. R. M., Gonzalez, A. H., Hatch, N., Jarvis, M., Rettura, A., Stanford, S. A., and Stevens, J. A. (2013). Galaxy Clusters around Radio-loud Active Galactic Nuclei at $1.3 < z < 3.2$ as Seen by Spitzer. *ApJ*, 769:79.

Yee, H. K. C. and Ellingson, E. (2003). Correlations of Richness and Global Properties in Galaxy Clusters. *ApJ*, 585:215–226.

Zanni, C., Murante, G., Bodo, G., Massaglia, S., Rossi, P., and Ferrari, A. (2005). Heating groups and clusters of galaxies: The role of AGN jets. *A&A*, 429:399–415.

Zeldovich, Y. B. (1964). *Dokl. Akad. Nauk SSSR*, 155:67.

Zwicky, F. (1937). On the Masses of Nebulae and of Clusters of Nebulae. *ApJ*, 86:217.